Mars Gravity Inversion

Investigating the lateral density variations of the Martian lithosphere.

B. van Brummen

Delft University of Technology

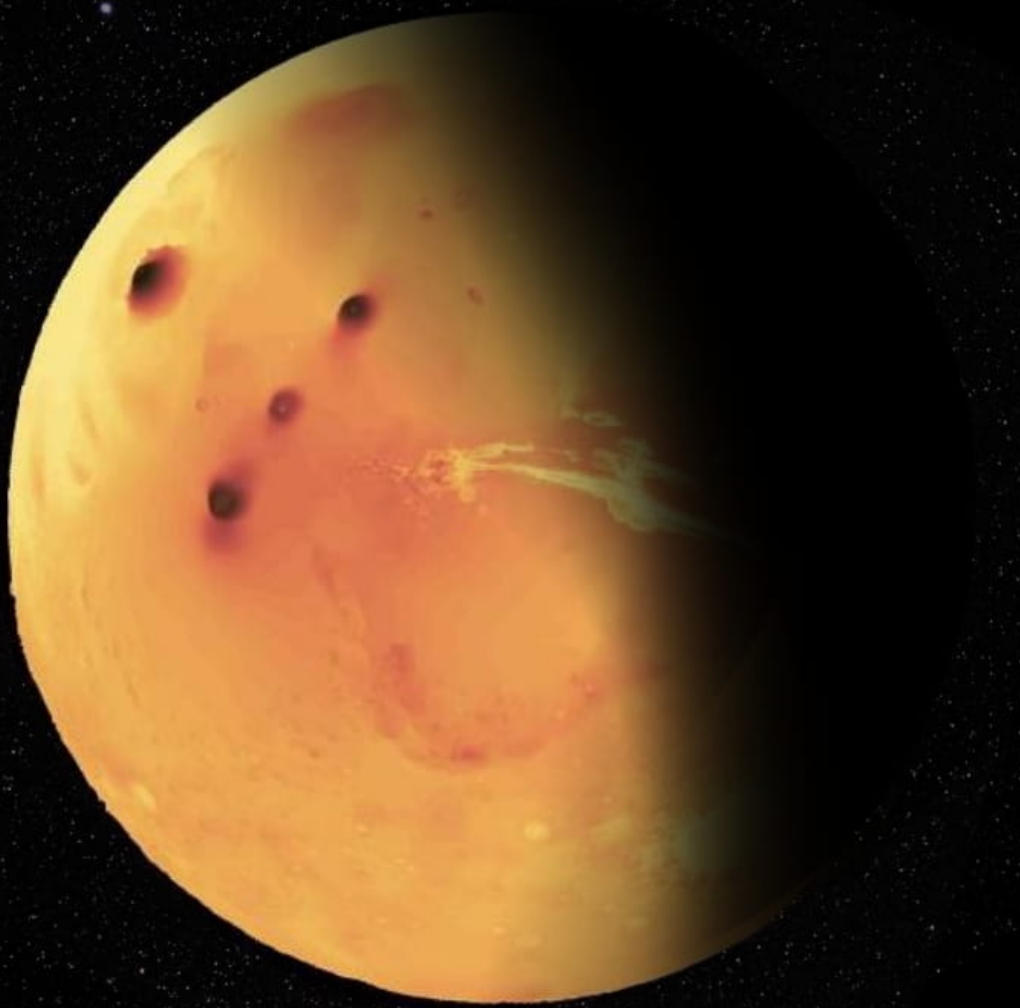

TU Delft Delft University of Technology

Mars Gravity Inversion

Investigating the lateral density variations of the Martian lithosphere.

by

B. van Brummen

to obtain the degree of Master of Science
at the Delft University of Technology,
to be defended publicly on June the 17th, 2022 at 14:15.

Student number:	4454405	
Project duration:	June 21, 2021 – June 17, 2022	
Committee:	Dr. ir. B. C. Root,	Delft University of Technology, Supervisor
	Dr. ir. W. van der Wal,	Delft University of Technology, Chair
	Dr. R. E. M. Riva,	Delft University of Technology

An electronic version of this thesis is available at http://repository.tudelft.nl/.

TU Delft Delft University of Technology

Abstract

In 2018 the InSight mission was launched with the main objective of providing accurate 3D models of Mars's interior. This was done by placing a seismometer on the surface of Mars to measure seismic activity. In 2021 three studies were published, one dedicated to the Martian core, one to the Martian mantle, and the last one focused on the Martian crust. Based on this seismic data, Khan et al. [2021] obtained a lithospheric thickness between the 400 and 600 km. The average Martian crust was found to lie between 24 to 72 kilometers. A restrictive range of crustal densities between 2700 to 3100 kg/m^3 was used. The mantle extended up to 1560 km below the surface of Mars. The core is molten and has a radius of 1830 km. Before seismic data was available, the method to learn more about the interior of a planet was to study the topography and gravity data. This is still, on Mars, the only way to get a global picture of the subsurface. Only one seismometer is currently available on Mars, making it difficult to currently obtain full planet 3D maps from seismology alone.

The objective of this research is to study the lateral density variations within the Martian lithosphere. The lithosphere is the planet's outermost shell, defined by its rigid mechanical properties. It is thought that the lithosphere of Mars consists of the crust and the outer part of the mantle. In previous research, the density of the Martian crust is most often taken as uniform. However, density variations exist at a small scale and potentially even at the largest Martian scale [Beuthe et al., 2012]. The thesis project aims to study these density variations within the Martian crust and upper mantle.

To study the lateral density variations in the crust and mantle, the MRO120D gravity data and MOLA topography data are used as input. The crust-mantle boundary is created based on thin shell isostasy [Qin, 2021]. A lower boundary of the lithosphere is chosen to be equal to 500 km. A mantle plume underneath Tharsis is added, based on the findings from van der Tang [2021]. This plume reached from a depth of 800 km up to a depth of 900 km and was centered around [110°W 3°N] and had a density variation of 400 kg/m^3 with respect to the surrounding mantle. An inversion was performed from which the density of both the crust and the mantle was obtained. In this calculation, two assumptions are made. First of all, it is assumed that the mass of each column is equal. The second assumption is that the obtained gravity for the column can be split into 2 point mass sources, one corresponding to the mass of the crust, located in the center of mass of the crust, and one corresponding to the mass of the mantle, located in the center of mass of the mantle.

A reference planet with T_e = 400 km, C = 105 km, $\rho_{c,ref}$ = 2700 kg/m^3, and $\rho_{m,ref}$ = 3800 kg/m^3, resulted in the smallest density differences within the crust, as well as the smallest gravitational tensor residual. When these input parameters were used for the inversion, a final density difference of approximately 1000 kg/m^3 between the crust and mantle was obtained after the inversion. A mean crustal density of approximately 2750 kg/m^3 and a mean mantle density of approximately 3750 kg/m^3 were found. The density variations in the crust varied from -424 up to 618 kg/m^3 around the mean crustal density and -228 and 133 kg/m^3 around the mean mantle density. The optimal elastic thickness obtained through the inversion lies between the 450$\pm$50 km and the uniform crustal thickness between 100 $\pm$ 10 km.

For the large impact craters, high crustal densities were found compared to the mean crustal density of Mars. Densities for Hellas and Utopia lay between the 3200 and 3345 kg/m^3, and for Isidis Basin, a slightly smaller impact crater, a crustal density of around 2870 kg/m^3 was found. These large crustal densities, together with the large elastic thickness and density difference between the crust and mantle, resulted in the conclusion that the large impact craters may be compensated using a different isostasy method. For this study, the crust-mantle boundary was obtained by applying the flexural response function to the crust-mantle boundary obtained using Airy isostasy. A boundary based on Pratt isostasy, instead of the thin shell isostasy boundary used currently, might be a better fit for the larger impact craters. The volcanoes outside the Tharsis region were found to be well compensated using the thin shell method, and small densities were found compared to the volcanoes in the Tharsis region, as well as what has been found in previous literature. The smaller densities for these stand-alone volcanoes might have to do with the compensation of these volcanoes due to the curvature of the planet, which is taken into account with the thin shell isostasy model. The literature analyzed in this study used different isostasy methods. By studying the possibility of different isostasy methods for different regions on Mars, the current model

could be improved further.

This study showed that it is possible to use gravity inversion to gain insights into the lithosphere of a planet. With these density differences, the Martian power spectrum could be fitted up to spherical harmonic degree 40. But, due to the resolution of the current gravity model, it was only possible to calculate the Martian density difference at a larger scale. To also be able to study the density differences at a smaller scale, higher resolution gravity data needs to become available.

Preface

This MSc thesis marks the end of an amazing era as a student at Delft University of Technology. When I came here nearly 7 years ago, I was still a small girl, excited for everything to come in my student time. Now this time has ended, and I look back with great joy. During my time at Aerospace Engineering, I gained the belief that this generation will go beyond all the amazing things already achieved and be the first to expand our Earth-based civilization to a multi-planetary civilization on Mars.

With this thesis, I strive to contribute to further expand the understanding of Mars. Bart Root was my daily supervisor, who gave me endless amounts of guidance and enthusiasm for this work. Thank you so much for all your support Bart, you really made the thesis process so much more enjoyable, and I couldn't imagine a better supervisor. Doing your master's research in Covid times can be quite lonely, but Bart tried his hardest to connect all his masters and Ph.D. students. He created the Planetary Interior and Gravity Modeling group for his students with similar interests to be able to support each other in these times. Having this group of people who were going through similar times made the thesis process much more enjoyable. Thank you all, and a special thank you to Weilun and Youandi for reading my thesis and providing me with valuable feedback. I would also like to thank Godert and Huygen for reading my thesis and providing me with feedback from an outsider's perspective. Finally, I would like to thank my graduation committee for their time and efforts.

Bodjie van Brummen
Rotterdam, June 2022

Contents

Abstract iii

Preface v

List of Figures xi

List of Tables xvii

Abbreviations xxi

1 Introduction 1
- 1.1 An Introduction to Mars . . . 2
  - 1.1.1 Lithosphere Structure . . . 2
  - 1.1.2 Geological History . . . 3
- 1.2 Research Questions . . . 4

2 Theory 7
- 2.1 Isostasy . . . 7
  - 2.1.1 The Airy–Heiskanen Model . . . 8
  - 2.1.2 Pratt–Hayford Model . . . 8
  - 2.1.3 Regional/Flexural Isostasy . . . 9
  - 2.1.4 Infinite Plate Model . . . 9
  - 2.1.5 Thin Shell Model . . . 10
- 2.2 Martian Topography . . . 11
- 2.3 Martian Gravity . . . 11
  - 2.3.1 Gravity Representation . . . 12
  - 2.3.2 MRO120D and GMM-3 . . . 13
  - 2.3.3 Gravity Anomaly . . . 14
  - 2.3.4 Forward Gravity Modelling . . . 14
- 2.4 Power Spectrum . . . 14
  - 2.4.1 Gravity Power Spectrum . . . 14
  - 2.4.2 Topography Power Spectrum . . . 15

3 Methodology 17
- 3.1 Creation of the Synthetic Planets . . . 17
  - 3.1.1 The Matérn Covariance Function . . . 17
  - 3.1.2 Flexure modeling . . . 18
- 3.2 Inversion . . . 20
  - 3.2.1 Weighted Linear Least-Squares . . . 20
  - 3.2.2 Tikhonov Regularization . . . 20
  - 3.2.3 Inversion Implementation . . . 21
  - 3.2.4 Inversion Iterations . . . 23
  - 3.2.5 Two-Layer Inversion . . . 23
- 3.3 Density calculations . . . 24
  - 3.3.1 Flowchart . . . 26
- 3.4 Mars Inversion Modeling . . . 28
  - 3.4.1 Topography . . . 28
  - 3.4.2 Crust-Mantle Boundary . . . 28
  - 3.4.3 Lower Boundary - Lithosphere . . . 29
  - 3.4.4 Plume Modeling . . . 29

4 Verification and Validation 31
4.1 Data. . . . 31
4.1.1 Topography . . . 31
4.1.2 Gravity . . . 32
4.2 One-Layer Inversion . . . 32
4.2.1 Height/Depth Analysis . . . 33
4.2.2 Effect of Adding Topography and a Lower Boundary . . . 33
4.2.3 Model 1 - Uniform Layer . . . 34
4.2.4 Model 2 - Varying Topography . . . 34
4.2.5 Model 3 - Varying Topography and Lower Boundary . . . 35
4.2.6 One-Layer Inversion: $\lambda - \sigma$ Analyses . . . 36
4.3 Two-Layer Inversion . . . 36
4.3.1 Difference between Gravitational Potential, Vector, and Tensor . . . 36

5 Power Spectrum and Two-Layer Results 39
5.1 Power Spectrum Analysis for Varying Input Variables . . . 39
5.1.1 Synthetic Planets. . . . 39
5.1.2 Crustal Thickness Variations . . . 40
5.1.3 Input Parameters Matèrn Covariance Function of the Topography. . . . 41
5.1.4 Density Variations of the Mantle . . . 43
5.1.5 Mass Variations between columns . . . 43
5.1.6 Input Parameters of the Flexural Response Function. . . . 44
5.2 Two-Layer Inversion . . . 45
5.2.1 Inclusion of Deeper Mantle Density Variations. . . . 45
5.2.2 Variation in Reference Model Input Parameters . . . 47
5.2.3 Influence of Additional Crustal Mass. . . . 49
5.2.4 Influence of Additional Mantle Mass. . . . 50
5.2.5 Influence of Additional Mantle and Crustal Mass . . . 51

6 Mars Inversion Results & Discussion 53
6.1 Mars Parameter Analysis . . . 53
6.1.1 First Phase - General Analyses . . . 53
6.1.2 Second Phase - Crustal and Elastic Thickness Analysis. . . . 55
6.1.3 Third Phase - Crustal and Mantle Density Variations. . . . 55
6.1.4 Discussion on Variations in Elastic Thickness . . . 57
6.1.5 Discussion on Variations in Average Crustal Thickness. . . . 57
6.1.6 Discussion on Variations in Crustal and Mantle Density . . . 57
6.2 Optimal Inversion Results Mars, Smallest $\max(\Delta\rho_{c,\mathrm{inv}})$. . . . 58
6.3 Density and Crustal Thickness Analyses . . . 59
6.3.1 Hellas Basin, Utopia Basin, and other impact craters. . . . 60
6.3.2 Tharsis Region, Olympus Mons, and the other Large Volcanoes . . . 61
6.3.3 Cross-Sections . . . 62
6.4 Gravity of the Inversion Model . . . 63
6.4.1 Gravity Anomaly . . . 63
6.4.2 Gravitational Tensor . . . 64
6.4.3 Power Spectrum . . . 65
6.5 Model Assumptions . . . 66
6.6 Evolution of Mars Based on the Obtained Densities. . . . 67
6.6.1 Hellas Basin . . . 68
6.6.2 Argyre Basin . . . 68
6.6.3 Utopia Basin, Isidis Basin, and Vastitas Borealis . . . 68
6.6.4 Olympus Mons and the Tharsis region . . . 68
6.6.5 Arabia Terra down to the Noachis Terra . . . 69

7 Conclusions and Recommendations 71

A Appendix 75
A.1 One layer inversion - models 2 and 3 . . . 75
A.2 $\lambda - \sigma$ analyses . . . 76
A.2.1 Variation in layer thickness . . . 76
A.2.2 Variation in layer Centre of Mass . . . 76
A.2.3 Variation in both layer Centre of Mass and Thickness . . . 77
A.2.4 Variation in $\Delta\rho$ . . . 77
A.2.5 Variation in Seed Number . . . 77
A.2.6 Variation in κ . . . 78
A.3 Two-Layer Inversion - Input Type Analyses 50 iterations . . . 80
A.4 Plots Variation Input Parameters Reference Model . . . 82
A.4.1 Crustal Density Variation . . . 83
A.4.2 Mantle Density Variation. . . . 84
A.4.3 Elsatic Thickness Variation. . . . 85
A.4.4 Young's Modulus Variation . . . 86
A.4.5 Average crustal Thickness Variation . . . 87
A.5 Density and crust-mantle boundary results for minimum $max(\Delta\rho_{c,inv})$ . . . 88
A.6 Gravity Input Inversion . . . 89
A.7 Heatmap Results . . . 91
A.8 Geologic Map of Mars . . . 93

Bibliography 95

List of Figures

1.1 A global map of Martian topography, based on the MOLA data-set, with the major regions labeled. 2
1.2 Geological activity as a function of time on Mars. 4

2.1 General representation of Airy isostasy. 7
2.2 General representation of Pratt isostasy. 7
2.3 General representation of Vening Meinesz isostasy. 9
2.4 The flexural response function for the infinite plate model with varying values of the elastic thickness. 9
2.5 The flexural response function for the infinite plate model and thin shell model, with varying values of the elastic thickness. 11
2.6 A global map of a Martian gravity anomaly based on the MRO120D gravity model. 12
2.7 A power spectrum comparison of the GMM-3 and MRO120Dgravity data sets. 13
2.8 The gravitational tensor in the zz direction obtained from the MRO120D data set. The top plot shows the result from spherical harmonic degree 1 to 90 and the bottom plot shows the same plot, but with the spherical harmonic terms C_{00}, C_{10}, C_{11}, S_{11}, and C_{20} removed. 13

3.1 The chordal Matérn covariance function plotted for different values of ϵ. 18
3.2 The chordal Matérn covariance function plotted for different values of κ. 18
3.3 The left figure shows the crustal profile before application of the flexural response function. The right figure shows the same crustal profile after application of the flexural response function between GSHA and GSHS for the infinite plate model. 19
3.4 The left figure shows the crustal profile before application of the flexural response function. The right figure shows the same crustal profile after application of the flexural response function between GSHA and GSHS for the thin shell model. 19
3.5 The difference between the boundary profiles, after GSHA and GSHS, of the thin shell model and the infinite plate model. 19
3.6 The generic L-curve for standard-form Tikhonov regularization with $x_0 = 0$; the points marked by the circles correspond to the regularization parameters = 105, 104, 103, 102, 101 and 1. Figure obtained from [Hansen, 2005] 21
3.7 This figure shows 3 different L-curve plots corresponding to 3 different one-layer inversion models. In this figure the minimum RMS value between the obtained density variations of the inversion as well as the original density profile is given. 21
3.8 The sensitivity of the three different isotropic kernels for different angular distanced. A planetary radius of 3396 km is used, equal to the radius of Mars. The kernels are computed at a height of 250 km and a depth of 150 km and based on the closed form equations given in Equation 3.17. 22
3.9 A schematic representation of both the synthetic planet and the reference model in the two-layer inversion. 23
3.10 This figure shows how taking a grid from a planet with a crust, mantle and topography translates to the volumes of the crust and mantle. 25
3.11 A flowchart given a schematic representation of the two-layer iterative inversion process. 27
3.12 The power spectrum of the Martian gravity, the uncompensated topography, the crust mantle boundary obtained with local compensation (Airy) as well as with the infinite plate model and thin shell model. 28
3.13 The mantle plume used in the reference model to fit the low Spherical Harmonic degrees in the power spectrum. The plume is modeled from a depth of 800km up to a depth of 900km. This plume was centerd around [110°W 3°N] with a longitudinal radius of 32° and a latitudinal radius 30°. . . . 29

4.1 The global topography of Mars, which is derived from the spherical harmonic shape model MarsTopo2600, referenced to the geoid. This figure is in a Mollweide projection with a central meridian of 100° W longitude and is overlain by a gradient image derived from the topography model. [Wieczorek, 2007] 31
4.2 The global topography map is computed for the elevation difference between the planetary radius and the areoid. 31

4.3 The power spectrum of the topography of Mars, which is derived from the spherical harmonic shape model MarsTopo2600. [Wieczorek, 2007]. 32
4.4 The power spectrum of the topography of Mars for both the MOLA data set, used in this study, and the MarsTopo2600 data set, used in [Wieczorek, 2007]. 32
4.5 Variance spectra of signal and error for the Doppler-derived gravitational potential model MRO120d. [Gorski et al., 2018]. 32
4.6 The power spectrum of the MRO120D data set plotted together with its uncertainty. 32
4.7 A cross section for each of the 3 one-layer models to study the effect of adding varying topography and lower boundary layers. 33
4.8 The topographic boundary for the one-layer inversion model. This varying upper boundary is used in the second and third model. 34
4.9 The Lower boundary for the one-layer inversion model. This varying lower boundary is used in the third model. 34
4.10 Inversion results Model 1. This model is a 50 km layer with varying density, a constant upper boundary of 0 km, and a constant lower boundary of -50 km. 34
4.11 Inversion results Model 1 after multiple iterations. This model is a 50 km layer with varying density, a constant upper boundary of 0 km, and a constant lower boundary of -50 km. The left top plot shows the input density difference, the top right plot shows the output density difference, and the bottom plot shows the difference between the two top plots. 34
4.12 Inversion results Model 2. This model is approximately a 50 km layer with varying density, a varying upper boundary shown in Figure 4.8 and a constant lower boundary of -50 km. The left top plot shows the input density difference, the right top plot shows the output density difference, and the bottom plot shows the difference between the two top plots. 35
4.13 Inversion results Model 2 after multiple iterations. This model is approximately a 50 km layer with varying density, a varying upper boundary shown in Figure 4.8 and a constant lower boundary of -50 km. The left top plot shows the input density difference, the right top plot shows the output density difference, and the bottom plot shows the difference between the two top plots. 35
4.14 Inversion results Model 3. This model is approximately a 50 km layer with varying density, a varying upper boundary shown in Figure 4.8 and a varying lower boundary shown in Figure 4.9. The left top plot shows the input density difference, the right top plot shows the output density difference, and the bottom plot shows the difference between the two top plots. 35
4.15 Inversion results Model 3 after multiple iterations. This model is approximately a 50 km layer with varying density, a varying upper boundary shown in Figure 4.8 and a varying lower boundary shown in Figure 4.9. The left top plot shows the input density difference, the right top plot shows the output density difference, and the bottom plot shows the difference between the two top plots. 35
4.16 The power spectrum of the inversion planet obtained using the reference planet with the densities changed to the densities obtained from the inversion. Subplot (a) shows the results using the gravitational potential as input data for the inversion, (b) for the gravitational vector in the z direction, and (c) for the gravitational tensor in the zz direction. 37
4.17 For each subplot, the top plot shows the difference between the input crustal density, ρ_c input, and the crustal density obtained using the inversion method, ρ_c inverse. The bottom plot shows the same plot, but for the mantle density instead of the crustal density. Subplot (a) shows the results using the gravitational potential as input data for the inversion, (b) for the gravitational vector in the z direction, and (c) for the gravitational tensor in the zz direction. 38

5.1 Airy for lateral density variations within the crust and mantle, now referred to as Airy2. 40
5.2 The power spectrum plotted for different values of average crustal thickness, c, for the synthetic planet Airy1. 40
5.3 The power spectrum plotted for varying density differences between the crust and the mantle, $\Delta\rho$, for the synthetic planet Airy1. The crustal density was set to 2900 kg/m^3. This resulted into density variations between 400 and 800 kg/m^3. 40
5.4 The power spectrum plotted for only the crust of the synthetic planet and for a planet with a crust of 3380 km. 41
5.5 The power spectrum plotted for different values of the decorrelation distance, ϵ, for the synthetic planet Airy1. 41
5.6 The power spectrum plotted for different values of the square-root of the variance, σ, for the synthetic planet Airy1. 41

5.7 The power spectrum plotted for different values of the square-root of the variance, σ, and the for the decorrelation distance, ϵ, for synthetic planet Airy1. 42
5.8 The power spectrum plotted for different values of the smoothness parameter, κ, for the synthetic planet Airy1. 42
5.9 The effect of changing the input parameter ϵ of the Matèrn covariance function on the crust-mantle boundary. From the left to right, and top to bottom, these plots are obtained using $\epsilon = 1$, $\epsilon = 5$, $\epsilon = 10$, $\epsilon = 25$, and $\epsilon = 50$. 42
5.10 The effect of changing the input parameter κ of the Matèrn covariance function on the crust-mantle boundary. From the left to right, and top to bottom, these plots are obtained using $\kappa = 0.3$, $\kappa = 0.6$, $\kappa = 0.9$, $\kappa = 1.2$, $\kappa = 1.5$. 42
5.11 The power spectrum plotted for different values of the smoothness parameter for the density, κ, for the synthetic planet Airy2. 43
5.12 The power spectrum plotted for varying density differences within the crust, by changing σ, for the synthetic planet Airy2. 43
5.13 The power spectrum plotted for variations within both the crust and the mantle, with mass differences between the columns, plotted for the synthetic planet Airy3. 44
5.14 The power spectrum plotted for variations within both the crust and the mantle, with mass differences between the columns, plotted for the synthetic planet Airy3. 44
5.15 The power spectrum plotted for different values of the elastic thickness, T_e, for the synthetic planet TSM1. 44
5.16 The power spectrum plotted for different values of the Poisson ratio, ν, for the synthetic planet TSM1. 44
5.17 The power spectrum plotted for different values of the elastic modulus, E, for the synthetic planet TSM1. 44
5.18 The density variations which were added to the two deep mantle layers from a depth of 500 km up to the depth of 1800 km. 45
5.19 For each subplot, the top plot shows the difference between the input crustal density, ρ_c input, and the crustal density obtained using the inversion method, ρ_c inverse. The bottom plot shows the same plot, but for the mantle density instead of the crustal density. Deep mantle density variations were added to the input model reference planet. Subplot (a) shows the results using the gravitational potential as input data for the inversion, (b) for the gravitational vector in the z direction, and (c) for the gravitational tensor in the zz direction. 46
5.20 The effect of changing multiple input parameters for the reference model, on the obtained crustal and mantle density from the inversion. F0r subplot (a), the crustal density is varied, for (b), the mantle density is varied, for (c) the elastic thickness is varied, for (d), the Young's modulus is varied, and for (e), the average crustal thickness is varied. 48
5.21 Effect of adding extra density variations to the crust of the synthetic planet. 49
5.22 A closer look at the effect of adding extra density variations to the crust of the synthetic planet, equal to a maximum magnitude of 1.25% of the original density variations. The top left figure shows the difference between the density of the crust for the synthetic planet and the inversion results. The top right figure shows the same but for the mantle density variations. The bottom left figure shows the added density to the crust, and the bottom right figure shows the residual gravitational tensor (T_{zz}). 49
5.23 A closer look at the effect of adding extra density variations to the crust of the synthetic planet, equal to a maximum magnitude of 20% of the original density variations. The top left figure shows the difference between the density of the crust for the synthetic planet and the inversion results. The top right figure shows the same but for the mantle density variations. The bottom left figure shows the added density to the crust and the bottom right figure shows the residual gravitational tensor (T_{zz}). 49
5.24 Effect of adding extra density variations to the mantle of the synthetic planet. 50
5.25 A closer look at the effect of adding extra density variations to the mantle of the synthetic planet, equal to a maximum magnitude of 1.25% of the original density variations. The top left figure shows the difference between the density of the crust for the synthetic planet and the inversion results. The top right figure shows the same but for the mantle density variations. The bottom left figure shows the added density to the mantle, and the bottom right figure shows the residual gravitational tensor (T_{zz}). 51

5.26 A closer look at the effect of adding extra density variations to the mantle of the synthetic planet, equal to a maximum magnitude of 20% of the original density variations. The top left figure shows the difference between the density of the crust for the synthetic planet and the inversion results. The top right figure shows the same but for the mantle density variations. The bottom left figure shows the added density to the mantle and the bottom right figure shows the residual gravitational tensor (T_{zz}). 51
5.27 Analysis of the effect of adding extra density variations to both the crust and the mantle. These plots are plotted for variable mantle variations, and constant crustal density variations. The crustal maximum added crustal density variations are for subplot (a) 1.25%, (b) 2.5%, (c) 5%, (d) 10%, and (e) 20%. 52

6.1 The first analysis of the different combinations of input parameters for the initial reference planets. The average crustal thickness is plotted against the density differences in the crustal density, for variations in elastic thickness between the four subplots. From top left, to bottom right, these figures show the results for elastic thicknesses of T_e = 50 km, T_e = 150 km, T_e = 250 km, and T_e = 400 km. . 54
6.2 Results for a set density difference between the crustal and mantle density of the reference model of 900 kg/m^3, and variations in the average crustal thickness and elastic thickness. The elastic thickness is plotted against the density differences in the crustal, left subplot, and mantle, right subplot, density. 55
6.3 Results for a set average crustal thickness for the reference model of 105 km and variations in the elastic thickness and density difference between the crust and mantle of the reference model. The mantle reference density is plotted against the density differences in the crustal for different density differences. From left to right, subplot 1 shows the results for an elastic thickness of 400 km, subplot 2 for 425 km, subplot 3 for 450 km, and subplot 4 for 475 km. 56
6.4 Results for a set average crustal thickness for the reference model of 105 km and variations in the elastic thickness and density difference between the crust and mantle of the reference model. The crustal reference density is plotted against the density differences in the crustal for different density differences. From left to right, subplot 1 shows the results for an elastic thickness of 400 km, subplot 2 for 425 km, subplot 3 for 450 km, and subplot 4 for 475 km. 56
6.5 The crustal and mantle density and density variations obtained through the Martian inversion. For the inversion, a multiplication factor of 30 and 25 iterations were used. These results were obtained for a reference model with the topography and crust-mantle boundary shown in Figure 6.6, for the same subplots, respectively. 58
6.6 The topography and crust-mantle boundary used for the reference model for the Martian inversion. This is obtained with C = 105 km, E = 100 GPa, ν = 0.25, ρ_c = 2700 kg/m^3, ρ_m = 3800 kg/m^3, and T_e = 400 km. 59
6.7 A cross section of the reference model based on the densities given in Figure 6.5 and the boundaries given in Figure 6.6. The subplot shows the longitude line of (a) -134 degrees, (b) -114 degrees, (c) -44 degrees, (d) 80 degrees, (e) 120 degrees, and (f) 148 degrees. 63
6.8 A more zoomed in cross section of the reference model based on the densities given in Figure 6.5 and the boundaries given in Figure 6.6. The subplot shows the cross-section for (a) Hellas Basin and (b) Utopia Basin. 63
6.9 The top left figure shows the anomaly for Mars, the top right for the reference model with the obtained inversion densities, and the bottom figure shows the residual. 64
6.10 The top left figure shows the gravitational tensor in the zz direction for Mars, the top right for the reference model with the obtained inversion densities, and the bottom figure shows the residual. The two top plots are truncated for $T_{zz} = \pm$ 15 Eotvos and the bottom figure is truncated for $T_{zz} = \pm$ 1.5 Eotvos. 65
6.11 The power spectrum of the gravity of Mars, the reference model with uniform densities, ρ_c = 2700 kg/m^3 and ρ_m = 3800 kg/m^3, and the reference model with the density variations obtained through the inversion. 66
6.12 The crustal density obtained for the Martian inversion result, with T_e = 400 km, C = 105 km, $\rho_{\text{c,ref}}$ = 2700 kg/m^3 and $\rho_{\text{m,ref}}$ = 3800 kg/m^3. 67

A.1 The RMS between the input density minus the inversion density divided by the maximum input density plotted against the standard deviation between the input tensor and inversion tensor for 120 different 1-layer inversion models, both for model 2 and model 3. 75
A.2 $\lambda - \sigma$ analyses plot for variation in layer thickness. 76

A.3 L-curve for both variation in layer thickness. . . . 76
A.4 $\lambda - \sigma$ analyses plot for variation in CM depth. . . . 76
A.5 L-curve for both variation in CM depth. . . . 76
A.6 $\lambda - \sigma$ analyses plot for variation in both layer thickness and variation in CM depth. . . . 77
A.7 L-curve for both variation in layer thickness and CM depth. . . . 77
A.8 $\lambda - \sigma$ analyses plot for variation in the density differences within the 1-layer model. . . . 77
A.9 L-curve for variation in the maximum density variations of the inversion layer. . . . 77
A.10 The density variations corresponding to the different seed numbers, used in the Matèrn covariance function, to obtain the $\lambda - \sigma$ plots shown in Figure A.11. . . . 78
A.11 $\lambda - \sigma$ analyses plot for variation in seed numbers with which the density profile was obtained using the Matèrn covariance function. . . . 78
A.12 L-curve for variation in seed number for the Matèrn covariance function of the density variations, which influence the density pattern. . . . 78
A.13 The density variations corresponding to the different κ values, used in the Matèrn covariance function, to obtain the $\lambda - \sigma$ plots shown in Figure A.14. . . . 79
A.14 $\lambda - \sigma$ analyses plot for variation in kappa value, used to obtain the density difference for the Matèrn covariance function. . . . 79
A.15 L-curve for variation in κ for the Matèrn covariance function of the density variations, which influence the wavelength pattern of the density variations. . . . 79
A.16 The input crustal and mantle density variations. These density variations are used as input for the analyses of the different input gravity data types. . . . 80
A.17 The power spectrum of the inversion planet obtained using the reference planet with the densities changed to the densities obtained from the inversion. Subplot (a) shows the results using the gravitational potential as input data for the inversion, (b) for the gravitational vector in the z direction, and (c) for the gravitational tensor in the zz direction. . . . 80
A.18 For each subplot, the top plot shows the difference between the input crustal density, ρ_c input, and the crustal density obtained using the inversion method, ρ_c inverse. The bottom plot shows the same plot, but for the mantle density instead of the crustal density. Subplot (a) shows the results using the gravitational potential as input data for the inversion, (b) for the gravitational vector in the z direction, and (c) for the gravitational tensor in the zz direction. . . . 81
A.19 The left plots shows the input crustal and mantle density, and the left plots the obtained crustal and mantle density from the inversion with the correct input parameters for the reference model. . . . 82
A.20 Each subplot shows the input crustal and mantle density, as well as the obtained crustal and mantle density from the inversion. Subplot (a) shows the results for $\rho_c = 0.95\rho_{c,inp}$, and (b) shows the results for $\rho_c = 1.05\rho_{c,inp}$. . . . 83
A.21 Each subplot shows the input crustal and mantle density, as well as the obtained crustal and mantle density from the inversion. Subplot (a) shows the results for $\rho_m = 0.95 \cdot \rho_{m,inp}$, and (b) shows the results for $\rho_m = 1.4 \cdot \rho_{m,inp}$. . . . 84
A.22 Each subplot shows the input crustal and mantle density, as well as the obtained crustal and mantle density from the inversion. Subplot (a) shows the results for $T_e = 0.1T_{e,inp}$, and (b) shows the results for $T_e = 2T_{e,inp}$. . . . 85
A.23 Each subplot shows the input crustal and mantle density, as well as the obtained crustal and mantle density from the inversion. Subplot (a) shows the results for $E = 0.1E_{inp}$, and (b) shows the results for $E = 2E_{inp}$. . . . 86
A.24 Each subplot shows the input crustal and mantle density, as well as the obtained crustal and mantle density from the inversion. Subplot (a) shows the results for $C = 0.6C_{inp}$, and (b) shows the results for $C = 1.1C_{inp}$. . . . 87
A.25 The crustal and mantle density and density variations obtained through the Martian inversion. For the inversion a multiplication factor of 30 and 25 iterations were used. These results were obtained for a reference model with the topography and crust-mantle boundary shown in Figure 6.6, for the same subplots respectively. . . . 88
A.26 The topography and crust-mantle boundary used for the reference model for the Martian inversion. This is obtained with C = 105 km, E = 100 GPa, ν = 0.25, and varying elastic thickness for the subplots. Subplot (a), (b) and (d) use rho_c = 2700 kg/m^3, ρ_m = 3800 kg/m^3, and subplot (c) uses rho_c = 2650 kg/m^3, ρ_m = 3650. . . . 89
A.27 The top left figure shows the anomaly for Mars, the top right for the reference model with uniform densities, and the bottom figure shows the residual, which is used as the input data for the inversion. 89

A.28 The top left figure shows the gravitational tensor in the zz direction for Mars, the top right for the reference model with uniform densities, and the bottom figure shows the residual, which is used as the input data for the inversion. The two top plots are truncated for $T_z z = \pm$ 15 Eotvos and the bottom figure is truncated for $T_z z = \pm$ 1.5 Eotvos. 90
A.29 The heatmaps for the first analyses of the different combinations of input parameters for the initial reference planets. The average crustal thickness is plotted against the density differences in the crustal density, for variations in elastic thickness between the four subplots. From top left, to bottom right, these figures show the results for elastic thicknesses of T_e = 50 km, T_e = 150 km, T_e = 250 km, and T_e = 400 km. 91
A.30 The heatmaps showing the results for a set density difference between the crustal and mantle density of the reference model of 900 kg/m^3, and variations in the average crustal thickness and elastic thickness. The elastic thickness is plotted against the density differences in the crustal, left subplot, and mantle, right subplot, density. 91
A.31 The heatmaps showing the results for a set average crustal thickness for the reference model of 105 km and variations in the elastic thickness and density difference between the crust and mantle of the reference model. The mantle reference density is plotted against the density differences in the crustal for different density differences. From left to right, subplot 1 shows the results for an elastic thickness of 400 km, subplot 2 for 425 km, subplot 3 for 450 km, and subplot 4 for 475 km. 92
A.32 The heatmaps showing the results for a set average crustal thickness for the reference model of 105 km and variations in the elastic thickness and density difference between the crust and mantle of the reference model. The crustal reference density is plotted against the density differences in the crustal for different density differences. From left to right, subplot 1 shows the results for an elastic thickness of 400 km, subplot 2 for 425 km, subplot 3 for 450 km, and subplot 4 for 475 km. 92
A.33 "This global geologic map of Mars, which records the distribution of geologic units and landforms on the planet's surface through time, is based on unprecedented variety, quality, and quantity of remotely sensed data acquired since the Viking Orbiters. These data have provided morphologic, topographic, spectral, thermophysical, radar sounding, and other observations for integration, analysis, and interpretation in support of geologic mapping. In particular, the precise topographic mapping now available has enabled consistent morphologic portrayal of the surface for global mapping. Also, thermal infrared image bases used for this map tended to be less affected by atmospheric haze and thus are reliable for analysis of surface morphology and texture at even higher resolution than the topographic products." [Tanaka et al., 2014] 94

List of Tables

2.1 The flexural response function for the different isostasy models. Both for local, Airy and Pratt, as well as flexural, infinite plate model and thin shell model, isostasy models the flexural response function is given. . . . 10

3.1 A summary of the used/obtained crustal and mantle densities and crustal and lithospheric/elastic thicknesses . . . 30

4.1 The different input parameters used in the inversion, for the 3 different types of input data. . . . 37

6.1 The chosen range for each of the different input parameters for the thin shell model, which will be used as input for the different reference models. . . . 53
6.2 Combinations of crustal and mantle density as input for the reference model used in the analysis of Figure 6.3. . . . 56
6.3 The second set of combinations of crustal and mantle density as input for the reference model used in the analysis of Figure 6.3. . . . 56
6.4 The combination of input parameters for the minimum $\max(\Delta\rho_{c,inv})$ for each elastic thickness used in subsection 6.1.3. . . . 58
6.5 The mean crustal thickness, mean crustal density, and mean mantle density obtained for some of the Martian surface features, specifically basins and low elevation areas, for the Martian inversion result. . . . 61
6.6 The mean crustal thickness, mean crustal density, and mean mantle density obtained for some of the Martian surface features, specifically volcanoes and high elevation areas, for the Martian inversion result. . . . 62
6.7 A table relating the map units used in section A.8 by Tanaka et al. [2014], to the crustal densities found for the Martian inversion result, as shown in Figure 6.12. . . . 68

7.1 The mean crustal thickness, mean crustal density, and mean mantle density obtained for some of the Martian surface features. . . . 72

Nomenclature

Greek Symbols

α	Scale parameter	–
$\bar{\mathbf{\Gamma}}$	Gravitational gradient	Eotvos
$\bar{\varepsilon}$	Error	–
κ	Smoothness parameter	–
λ	Ridge parameter	–
ν	Poisson's ratio	–
Φ	Flexural response function	–
ϕ	Planetocentric longitude	$\circ$
ρ	Density	$\mathrm{kg\,m^{-3}}$
ρ_c	Crustal density	$\mathrm{kg\,m^{-3}}$
ρ_m	Mantle density	$\mathrm{kg\,m^{-3}}$
σ	Power spectrum (or degree variance)	–
σ	Variance	–
θ	Planetocentric co-latitude	$\circ$

Physics constants

G	Gravitational constant	$6.67430 \times 10^{-11}\,\mathrm{m^3\,kg^{-1}\,s^{-2}}$

Roman symbols

$\bar{P}_{nm}$	Legendre function after normalisation	–
$\bar{x}$	Parameter vector	–
$\bar{y}$	Observation data vector	–
A	Information-matrix	–
A_{lm}	Spherical harmonic coefficients	–
c	Crustal thickness	km
C_{nm}	Spherical harmonic coefficients	–
D	Flexural rigidity	$\mathrm{N\,m^{-2}}$
D_c	Depth of compensation	km
E	Young's Modulus	Pa
g	Gravitational acceleration	$\mathrm{m\,s^{-2}}$
g_r	Gravitational vector in the radial direction	$\mathrm{m\,s^{-2}}$
H	Topographic height	km

h	Topographic height/depth	km
J	Cost function	–
K	Isotropic kernels	–
M	Mass	kg
M	Matérn covariance function	–
m	Spherical harmonic order	–
M_{lm}	Spherical harmonic coefficients	–
n	Spherical harmonic degree	–
P_{nm}	De-normalized Legendre functions	–
P_{xx}	Parameter covariance matrix	–
R	Planetary radius	km
r	Radius	km
R_0	Reference radius	km
S_{nm}	Spherical harmonic coefficients	–
T_e	Elastic Thickness	km
T_{nm}	Spherical harmonic coefficients	–
T_{rr}	Gravitational tensor in the r r direction	Eotvos
U	Gravitational potential	J
V	Volume	km^3
Y_{nm}	Spherical harmonic coefficients	–
Z_{CM}	center of Mass depth	km

Abbreviations

CM	Centre of Mass
DEM	Digital Elevation Model
DSN	Deep Space Network
FRF	Flexural Response Function
GA	Gravity Anomaly
GMM-3	Goddard Mars Model-3
GSHA	Global Spherical Harmonic Analysis
GSHS	Global Spherical Harmonic Synthesis
HRSC	High-Resolution Stereo Camera
IPM	Infinite Plate Model
MGS	Mars Global Surveyor
MOLA	Mars Orbiter Laser Altimeter
MRO	Mars Reconnaissance Orbiter
NASA	National Aeronautics and Space Administration
RMS	Root Mean Square
SH	Spherical Harmonic

1

Introduction

Mars, nicknamed the "Red Planet", is the second smallest planet in our solar system. The nickname originates from its red color when observed from afar. The surface is composed of rocks overlain by highly oxidized weathering products, which creates the relatively bright dust and soils. Due to the presence of iron-bearing minerals in the oxidized surface layer, the Martian surface colors red [Zuber, 2001], where its nickname originates from. When observed from the Sun, it is the fourth planet, with Earth being the third planet. Mars is currently a hot topic with, among others, SpaceX, NASA, and the Indian Space Research Organisation planning manned missions to Mars. Mars has an average distance to the Sun of 228.5 million km and an average radius of 3396.0 km. In the past, there have been many missions to Mars. The first successful mission to Mars was launched in 1964, the Mariner 4 flyby mission. In the past 56 years, a lot has been learned about Mars, but even more, is still unknown.

The lithosphere is the planet's outermost shell, defined by its rigid mechanical properties. It is thought that the lithosphere of Mars consists of the crust and the outer part of the mantle, just like Earth's lithosphere, but is substantially thicker than the lithosphere of Earth and, therefore, capable of statically supporting larger surface loads. This is based on different observations, such as the heights of the youngest shield volcanoes [Comer et al., 1985]. The lithosphere of Mars could potentially give more insight into tectonics and stresses [Banerdt et al., 1992], the heat flow and internal dynamics [Solomon and Head, 1990] and the evolution of Mars.

In previous research, one or more of the following parameters have been set constant: the crustal thickness, upper mantle thickness, crustal density, or upper mantle density. Most often, the only non-uniform parameter was taken to be the crustal thickness, resulting in setting the density of both the crust and mantle as uniform. Density variations exist at a small scale and potentially even at the largest Martian scale, the hemispheric dichotomy [Beuthe et al., 2012]. The Martian dichotomy is the distinct topographic contrast between the Southern and the Northern hemispheres. The thesis project aims to study density variations within the Martian crust and upper mantle. These density variations, together with the obtained crust-mantle boundary, form the basis of the improved lithosphere model, which will be related to the geological map of Mars, presented by Tanaka et al. [2014]. From now on, the upper mantle will be referred to as the mantle of both Mars as well as for the synthetic planet. A synthetic planet is a fully modeled planet for which everything is known. In this case, this is the topography and the density and thickness of each layer, from which the gravity can be obtained. This synthetic planet will be used to test and understand the model, as well as to analyze the robustness of the model.

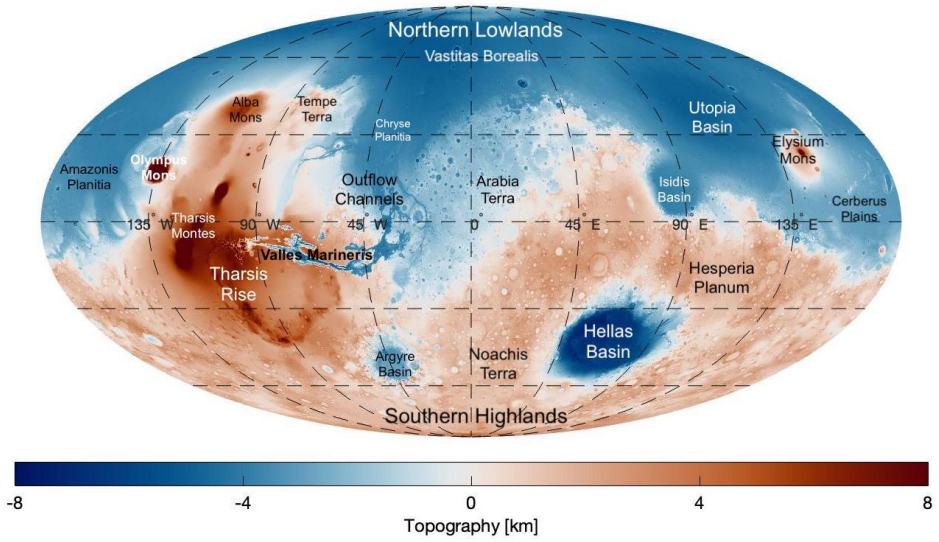

Figure 1.1: A global map of Martian topography, based on the MOLA data-set, with the major regions labeled. The colorbar is truncated at a topographic height and depth of 8 km. The MOLA data is obtained from https://pds-geosciences.wustl.edu/missions/mgs/megdr.html

1.1. An Introduction to Mars

Based on the data from previous missions, a topography map and a gravity anomaly map of Mars were created. The map of the topography of Mars is shown in Figure 1.1, and the gravity anomaly is given in Figure 2.6. The Martian topography has a few distinguishable features, which separate it from the rest of the planets in our solar system. The first feature is the Martian dichotomy. This dichotomy between the northern lowlands and the southern highlands is the oldest geologic event on Mars and is either expressed as differences in elevations, differences in crustal thickness, or differences in crater densities [Carr and Head III, 2010]. Another feature distinguishing Mars from other planets, is the high elevation area in the west of Mars, called the Tharsis region. This is also the region with the planet's most prominent volcanoes. The largest volcano on Mars is Olympus Mons, with an altitude of more than 21 km [Davies, 1974], making it the largest volcano in our solar system. Next to the Tharsis region, there is a smaller volcanic center to the west of Tharsis, Elysium, with different volcanoes with a maximum altitude of up to 14 km [Mouginis-Mark et al., 1982]. In the southwest of Mars, there is a low elevation area called the Hellas planitia. The Hellas planitia is an impact basin, therefore, also called the Hellas basin. The basin has a relief of 9 km and a diameter of about 2000 km [Leonard and Tanaka, 2001]. Some other large basins are Utopia basin, Isidis basin, and Argyre basin. The largest impact structure in the northern hemisphere is Utopia basin [Thomson and Head III, 2001]. It shows a 1–3 km deep depression and has a diameter of approximately 3200 km. Isidis basin and Argyre basin are slightly smaller impact craters, and both have a depression of approximately 3 km, as is shown in Figure 1.1.

Mars is known to have close to no atmosphere and an absence of oceans, vegetation, and complex life. Mars has a mass of $6.4171 \cdot 10^{23}$ kg, which is approximately 0.1 times the mass of Earth. This, together with its radius, results in the Martian mean density being approximately 0.7 that of Earth, equal to 3933 kg/m^3. The surface gravity of Mars is 3.71 m/s^2, approximately 0.4 times that of Earth. The atmospheric surface density is 0.020 kg/m^3, which can be neglected in calculations compared to the mean density of the planet. [1]

1.1.1. Lithosphere Structure

Insights into the lithosphere of a planet can be obtained by using the topography data as well as gravitational data and meteor analysis. Mars formed its crust, mantle, and core very quickly after its formation, within a few tens of millions of years of the Solar System formation, which is remarkably quick [Borg et al., 2003]. The core, mantle, and crust have different compositions. The exact crustal thickness of Mars is unknown, but different crustal models are available based on the topography and gravity data.

Zuber [2001] uses the most up-to-date topography and gravity fields from the Mars Global Surveyor mission. In

[1] https://nssdc.gsfc.nasa.gov/planetary/factsheet/marsfact.html.

these models, a crustal density of 2900 kg/m^3 and a mantle density of 3500 kg/m^3 are assumed. This is consistent with plausible crustal compositions and with bulk composition models [Dreibus and Wanke, 1985]. Wieczorek and Zuber [2004] related the geoid-to-topography ratios to an arbitrary model of crustal structure and compensation to obtain a crustal thickness larger than 29 km for crustal densities between 2700–3100 kg/m^3 and mantle densities between 3400–3550 kg/m^3. When more constrained densities between 2800–2900 kg/m^3 and 3300–3400 kg/m^3 for the crust and mantle respectively were used, a crustal thickness larger than 39 km was obtained. Another method used by Taylor et al. [2020] was to use Olympus Mons to study lithospheric flexure. In [Beuthe et al., 2012] localized spectral analysis of two different gravity data-sets was used to obtain a crustal density between 3000-3400 kg/m^3 for the large volcanoes. Belleguic et al. [2005] assumes that the surface and subsurface loads are elastically supported by the lithosphere. A crustal density of 3270 ± 150 kg/m^3 for the Elysium region was found, with an elastic thickness of 56 ± 20 to 105 ± 105 km. The elastic thickness is a mathematical interpretation of the lithosphere and is seen as the thickness of the outer layer of the planet, which can support loads in an elastic manner.

Next to the crust, the Martian lithosphere is another internal part of Mars that has been analyzed often in literature. Sometimes the elastic thickness instead of the lithospheric thickness is used in scientific papers, such as in [Zuber et al., 2000] and [Nimmo, 2002] because the elastic thickness is the calculated thickness that is needed to support the loads. Different results have revealed a significant variation in elastic thickness among the main crustal provinces. Zuber et al. [2000] found an elastic thickness in the southern highlands ranging from 0 to 20 km, the Alba Patera volcano displays an elastic thickness of 50 km, and Olympus Mons and the other volcanoes in the Tharsis region were found to have an elastic thickness larger than 100 km. There is a general trend visible between these different provinces: for the increasing age of the surface, the elastic thickness values generally decrease [Zuber, 2001].

Recently three papers were published about the Martian crust, mantle, and core, based on the new Insight seismic data [Khan et al., 2021]. These studies found that the average Martian crust lies somewhere between 24 to 72 km, with a lithosphere up to 500 km. A restrictive range of crustal densities between 2700 to 3100 kg/m^3 was used. It was found that the mantle extended up to 1560 km below the surface of Mars. The core was found to have a radius of 1830 km but was also found to be a molten core.

1.1.2. Geological History

The obtained density variations in the martian lithosphere will be compared to the geological history of Mars. Since 1996 different landers have touched down successfully on Mars. Also, a variety of different orbiters have been placed successfully into orbit. With the data collected by these missions, there now is a more detailed understanding of what it is like on Mars and how it evolved into its present state. The Martian surface features, based on the number of superimposed impact craters and the intersection relations, have been divided into three epochs: the Noachian, Hesperian, and Amazonian [Carr and Head III, 2010]. The terrain of the Noachian period dates from the heavy bombardment era and was named after the heavily cratered Noachis terra, see Figure 1.1, and estimated to have ended around 3.7 Gyr ago [Carr and Head III, 2010]. The remaining history of Mars was split into two periods: the Hesperian period, named after the Hesperia Planum, estimated to have ended around 2.9-3.3 Gyr ago, and the Amazonian period, named for the younger Amazonis Planitia [Carr and Head III, 2010].

Figure 1.2 shows the main geological activities as a function of time on Mars for the Noachian, Hesperian, and Amazonian periods. The oldest geologic event is the global dichotomy between the northern lowlands and the southern highlands, as visible in Figure 1.1. The Noachian period started around 4.1 Gyr ago. During the Noachian period, there were high rates of cratering, erosion, and valley formation. Also, the accumulation of most of Tharsis happened in this period, as well as widespread production of weathering products such as phyllosilicates, which was enabled by the surface conditions [Carr and Head III, 2010]. The Hesperian period was created to distinguish between the old post-Noachian plains and the younger plains and was later defined according to the number of superimposed craters. Therefore, based on the crater density, this period lasted from around 3.7 Gyr ago, the end of the Noachian period, to around 3 Gyr ago. During this period, the volcanism was forming extensive lava plains, and there were also high rates of canyon creation but low rates of valley formation. Due to the major deposition in the form of volcanism, lava plains, and erosion in the form of outflow channels and episodic seas, the northern plains were drastically reshaped during the Hesperian period [Tanaka and Kolb, 2001]. In this period, the Dorsa Argentea Formation (DAF) also occurred. The Dorsa Argentea are interpreted to be eskers in the south polar region of Mars which are formed due to discharge of melt-water from beneath either a moving or stagnant ice sheet [Tanaka and Kolb, 2001]. Also, in the soil of all the currently visited landing sites, except for Phoenix, abundant

sulfates have been observed. The age of the sulfate-rich Meridiani deposits is believed to be of Noachian age due to the number of craters. However, the sulfate-rich deposits in depressions are poorly constrained and could be much younger in age [Carr and Head III, 2010]. These sulfate minerals could have been formed directly by the weathering of basalts by acidic sulfate-rich fluids, but they could also have been formed by evaporation of waters derived from the weathering. Due to the possibility that these sulfates have been repeatedly eroded and deposited by the wind over tens to hundreds of millions of years, the present locations could have little relation to the original sources.

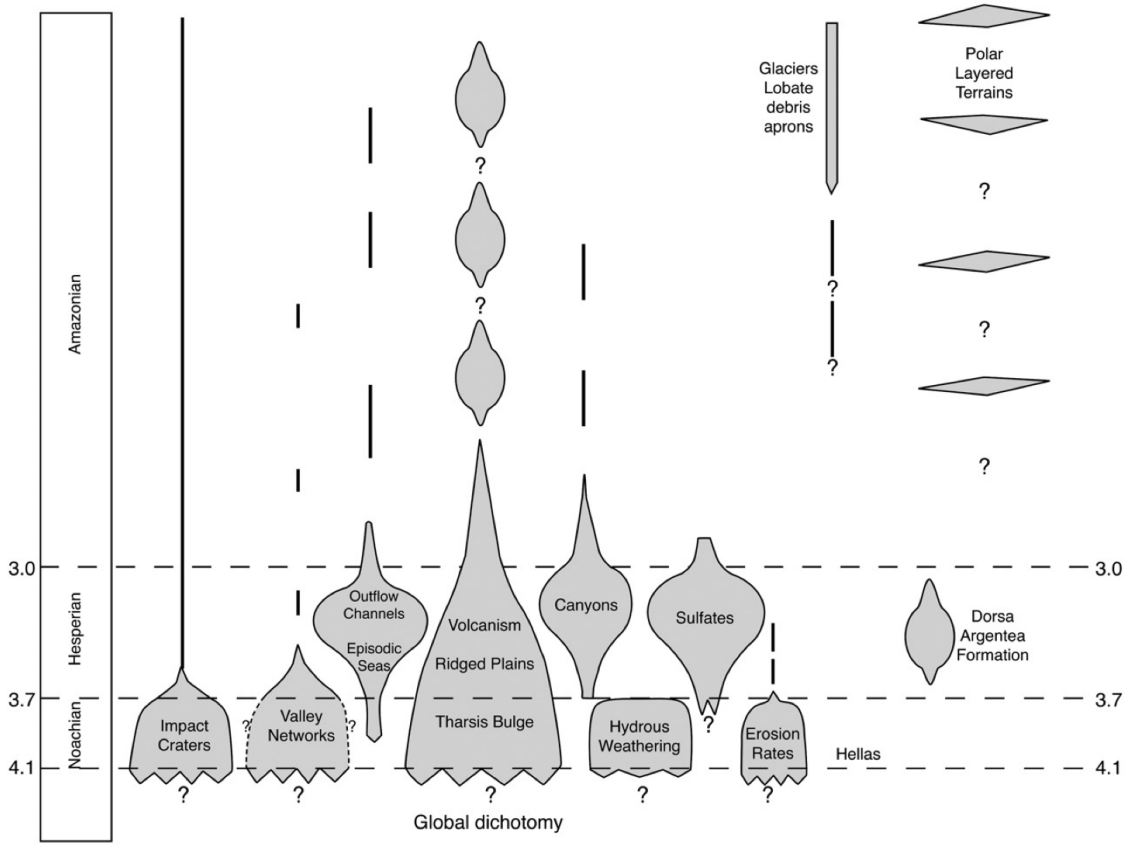

Figure 1.2: Geological activity as a function of time on Mars. The figure shows the relative importance of different processes, such as impact cratering and volcanism, the time and relative rates of formation of various features and units, such as valley networks and Dorsa Argentea Formation, and different types and rates of weathering, as a function of time. Also, the approximate boundaries of the major time periods of Mars's history are shown. [Carr and Head III, 2010].

In the Amazonian period, the surface geomorphological changes due to impact cratering, tectonism, and volcanism are modest compared with earlier periods. Much is also unknown about the evolution of Mars during this period. It is known that the volcanism during the Amazonian period was mainly in and peripheral to Tharsis and Elysium, and the eruption rates dropped significantly and were highly episodic [Carr and Head III, 2010]. The ice on Mars has played a significant role in the evolution of the Martian landscape. Changes in the Martian climate in the Amazonian period were followed by catastrophic flooding and/or glacial erosion [Chapman et al., 2010]. These could have resulted in the possibility that extensive ice deposits were left in low areas. The glacier's lobate debris aprons are adjacent to most steep slopes in the 30 to 55-degree bands in both the northern and southern hemispheres, and they are clear indicators of the presence of ice [Carr and Head III, 2010].

1.2. Research Questions

The Martian lithosphere has been the subject of various studies, but almost all use the assumption that the density of either the crust or mantle is uniform or both, but this is not very likely [Yuan et al., 2001]. The goal of this research is, therefore, to create a model which studies the lateral density variations. First, the crustal thickness will be calculated with isostasy models assuming a uniform crustal and mantle density. Next, a synthetic planet will be created to study the behavior of the model.

The main research question for this thesis research is:

Can lithospheric density models, obtained by gravity inversion, be related to the Martian geological history?

The sub-questions that need to be answered to be able to answer this main research question are:

1. **What types of lithosphere models are available?**
    - What types of isostasy models are used in literature?
    - What is the difference between local isostasy models and regional isostasy models?
    - How can these models be implemented in MATLAB, using the GSH package?
    - What is the effect of changing the input parameters of these isostasy models?
2. **How can synthetic planets be modeled realistically?**
    - What methods can be used to model synthetic planetary topographies and densities?
3. **What is the available topography and gravity data of Mars?**
4. **How can the lateral density variations be computed using an inversion model?**
    - How can the inversion be implemented?
    - How can the crustal and mantle density be obtained from a single inverted density?
    - What is the effect of varying the different inversion parameters?
5. **What is the effect of changing the parameters of the synthetic planet on the inversion?**
    - What is the effect of adding topography and/or a crust-mantle boundary?
    - What is the effect of varying the input parameters of the reference model? These input parameters are: T_e, C, ρ_c, ρ_m, and E.
    - What is the effect of adding deep mantle density variations?
6. **What are the obtained density variations within the lithosphere of Mars?**
    - What are the effects of changing the parameters of the reference model? These input parameters are: T_e, C, ρ_c, ρ_m, and $\Delta\rho$.
7. **How does the obtained lithosphere model compare to the existing lithosphere models?**
    - What are the differences between the existing models and the obtained model?
    - How do the obtained density values compare to geological mapping?
    - How do the obtained density values compare to meteors believed to originate from Mars and Martian rock analysis from landers?
    - Which improvements can be made to the model?

In chapter 1 an introduction to Mars and its geological history was given. Also, the research questions were introduced. The available data, as well as an introduction to the theory, will be given in chapter 2. The methodology will be further explained in chapter 3. In chapter 4 the verification and validation of the data, as well as the model, will be performed. The results of the power spectrum analyses and two-layer model will be given in chapter 5. The results and discussion of the Martian inversion results will be given in chapter 6. In chapter 7 the obtained results will be concluded, and recommendations for further research will be given.

2

Theory

In this chapter, the theory behind this research will be introduced. The crust-mantle boundary will be calculated using isostasy methods. Two types of isostasy methods are available, local and flexural isostasy. These methods will be explained in section 2.1. The input for the isostasy will be the topography of the planet. The available topographic data for Mars is given in section 2.2. The Martian gravity data is given in section 2.3, which is used as the input for the inversion. Lastly, the power spectrum is explained in section 2.4.

2.1. Isostasy

In this research, an isostasy model will be used to create a crustal model for Mars. Different isostasy models can be used to relate the observed topography on planets to the crust-mantle boundary. The idea of isostasy is based on Archimedes' principle and the principle of buoyancy, where it is believed that the rigid crust 'floats' on the denser mantle. There are different kinds of isostasy models based on different assumptions. The oldest models are the Airy and Pratt isostasy models, dating back to around 1855 [Airy, 1855]. These are the so-called local compensation models, where it is assumed that when the topography of the planet is divided into different columns, the columns can move separately from each other without any friction. When this is assumed, the topographic features are compensated locally. Other models, where it is assumed that the different columns can not move separately from each other, are the regional compensation or flexural models. Where it is assumed that the lithosphere as a whole bends when a load is applied to it. Two of these models which will be explained are the infinite plate model and the thin shell model.

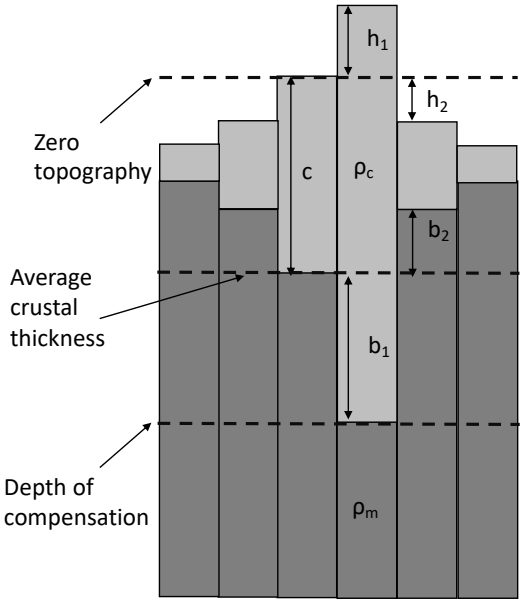

Figure 2.1: General representation of Airy isostasy.

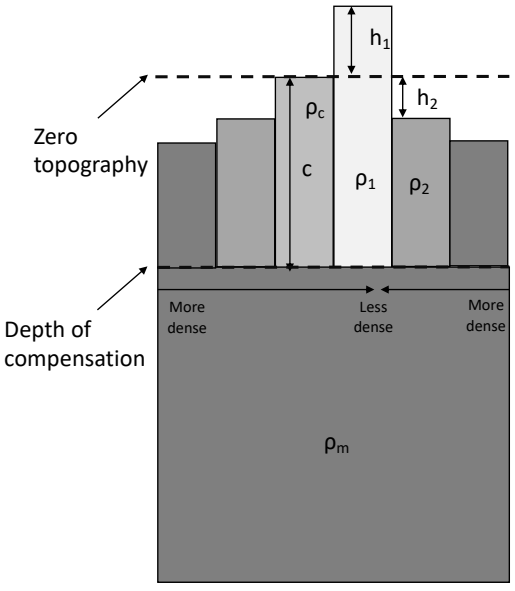

Figure 2.2: General representation of Pratt isostasy.

2.1.1. The Airy–Heiskanen Model

In Figure 2.1 the basic model of Airy isostasy is given. Airy isostasy assumes that the differences in the height of the topography are caused by differences in crustal thickness. A uniform crustal density and mantle density are assumed with variations in crustal thickness. From this, together with Pascal's law and the principle of buoyancy, the following equation can be obtained:

$$t_1\rho_1 = t_2\rho_2 = ... = t_n\rho_n. \tag{2.1}$$

In this equation t_1, t_2 and t_n are the thicknesses of the respective columns up to the depth of compensation, with corresponding densities ρ_1, ρ_2 and ρ_n. In Figure 2.1 h_1 is the difference between the topography and the reference ellipsoid, b_1 is the thickness of the crustal roots, c is the zero-load crustal thickness, ρ_c is the density of the crust and ρ_m is the density of the mantle. Therefore, where in Equation 2.1 c_n is the crustal thickness for the whole column, this can now be rewritten to: $c_n = h_1 + c + b_1$ for the middle column in Figure 2.1. With this information the following equation can be obtained:

$$(h_1 + c + b_1)\rho_c = c\rho_c + b_1\rho_m. \tag{2.2}$$

Rewriting this gives:

$$b_1(\rho_c - \rho_m) = -h_1\rho_c \qquad -> \qquad b_1 = \frac{h_1\rho_c}{\rho_m - \rho_c}. \tag{2.3}$$

The same calculation can be done for a ravine, as shown in the right column of Figure 2.1. In this figure h_2 is the deepness of the ravine and b_2 is the bulge caused by the rise of the mantle. It is assumed that the atmosphere can be neglected, for $\rho_{atm} << \rho_c$. This leads the following equation:

$$c\rho_c = b_2\rho_m + (c - h_2 - b_2)\rho_c + h_2. \tag{2.4}$$

Rewriting this gives Equation 2.5, which is equal to Equation 2.3.

$$h_2(\rho_c) = b_2\left(\rho_m - \rho_c\right) \qquad -> \qquad b_2 = \frac{h_2\rho_c}{\rho_m - \rho_c}. \tag{2.5}$$

Airy isostasy is based on local compensation, and when loads are applied, there is no resistance to bending. Each column in the Airy model can move without friction from the other columns. Watts [2001] introduces the flexural response function to describe the effect of the flexural models. This function is the ratio between the deflection of the lithosphere and the geological loads. Where the geological loads are the input and the deflection of the lithosphere is the output. Therefore the flexural response function can vary between 0 and 1, where 0 means no local compensation and 1 means fully local compensation. This results in the flexural response function, per spherical harmonic (SH) degree n, for Airy given by:

$$\Phi(n)_{\text{Airy}} = (1)^{-1}. \tag{2.6}$$

2.1.2. Pratt–Hayford Model

In Figure 2.2 the basic model of Pratt isostasy is presented. Pratt isostasy assumes that the differences in the height of the topography are caused by variations in the density of the crust. It, therefore, assumes a constant mantle density, a constant crust-mantle boundary, and varying crustal density. From this, the following equation can be obtained, again assuming that the density of the atmosphere can be neglected:

$$\rho_1 = \rho_c\frac{c}{h_1 + c}. \tag{2.7}$$

In this equation ρ_1 is the crustal density of segment 1, h_1 is the altitude of the segment above the reference ellipsoid, c is the crustal reference thickness, and ρ_c is the crustal density.

Each column in the Pratt model can also move without friction from each other, just as in the Airy model. This results in the flexural response function, per spherical harmonic degree n, given by:

$$\Phi(n)_{\text{Pratt}} = (1)^{-1}. \tag{2.8}$$

2.1.3. Regional/Flexural Isostasy

Regional or flexural models assume that the loads are compensated by regional instead of local displacement of the lithosphere. The load is therefore compensated by a larger area than in the Airy model, resulting in a smaller maximum crustal thickness. One parameter which is used in the flexural isostasy models is the effective elastic thickness of the lithosphere, T_e. This is a conceptual parameter that describes the strength of the lithosphere. A higher value of T_e corresponds to a stronger lithosphere. The elastic thickness can be related to the flexural rigidity D with the following equation:

$$D = \frac{E T_e^3}{12\left(1-\nu^2\right)}. \tag{2.9}$$

In this equation, E is Young's modulus, and ν is Poisson's ratio. The flexural rigidity gives a measure of the "stiffness" of the lithosphere. It relates a certain force to how much it would deflect a non-rigid structure, from which the thickness of the lithosphere and the viscosity of the mantle can be derived.

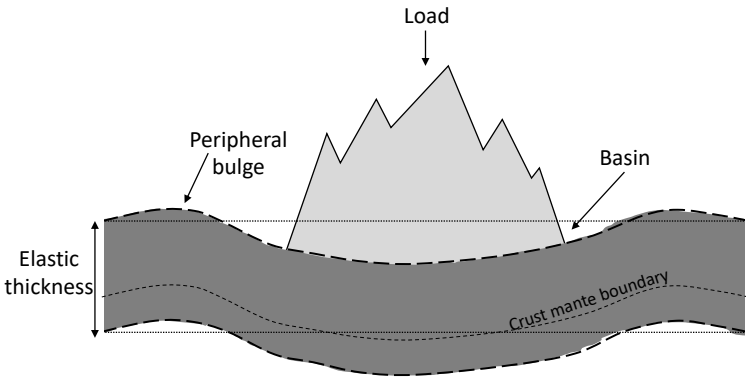

Figure 2.3: General representation of Vening Meinesz isostasy.

2.1.4. Infinite Plate Model

The infinite plate model is a simple and commonly used flexural mode. In this model, the lithosphere is simulated as an infinite plate, which is floating on a viscous mantle. The flexural response function per spherical harmonic degree n, for the infinite plate model, is given by Watts [2001]:

$$\Phi_{\text{Inf. plate}}(n) = \left[1 + \frac{D}{\left(\rho_m - \rho_c\right) g}\left(\frac{2n+1}{2R}\right)^4\right]^{-1}. \tag{2.10}$$

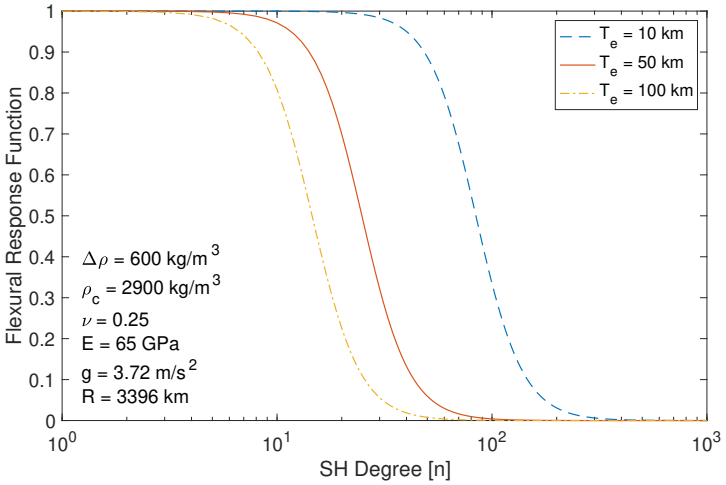

Figure 2.4: The flexural response function for the infinite plate model with varying values of the elastic thickness.

In Figure 2.4 the flexural response function for three different values of the elastic thickness is plotted. Visible is that the flexural response function produces a similar curve for the different elastic thicknesses but has a shift to

the left for increasing values of T_e. This means that for larger values of T_e the loads become less locally and more regionally compensated. From this, as well as from Equation 2.10, it can be found that when T_e reaches 0, the flexural response function for the infinite plate model is equal to that of the local compensation models.

2.1.5. Thin Shell Model

The infinite plate model is a representation that is more often used on Earth and gives a reasonably good representation for the shorter wavelength features. This is because the curvature of a planet does not have an influence on these shorter wavelengths, but for larger wavelengths, the curvature does have an effect. The radius of Mars is almost twice as small as that of Earth, and therefore Mars has a much larger curvature. The Gaussian curvature of a sphere would be $K = \frac{1}{r^2}$. This would mean that the Gaussian curvature on Mars would be four times the Gaussian curvature of Earth: $K_{\text{Mars}} = \frac{1}{(0.5R_{\text{Earth}})^2} = 4\frac{1}{R_{\text{Earth}}^2} = 4K_{\text{Earth}}$.

With the large features, such as the Tharsis region, and the small radius of Mars, this curvature is expected to have a significant effect and therefore can not be neglected, as is the case for the infinite plate model. A model where the curvature of a planet is taken into account is the thin shell model. The thin shell model was first derived by Harry Kraus [Kraus, 1967]. The flexural response function for the thin shell model is given by Qin [2021]:

$$\Phi_{\text{Thin shell}}(n) = \left[1 + \frac{D}{(\rho_m - \rho_c)g}\left(\frac{1}{R^4}\frac{[n(n+1)-2]^2}{1-\frac{1-\nu}{n(n+1)}} + \frac{12(1-\nu^2)}{T_e^2 R^2}\frac{1-\frac{2}{n(n+1)}}{1-\frac{1-\nu}{n(n+1)}}\right)\right]^{-1}. \tag{2.11}$$

The flexural response functions for the types of isostasy models are given in Table 2.1. A comparison of the two flexural isostasy models is given in Figure 2.5. Visible is that for smaller values of T_e, the two functions converge towards each other. This is because both converge towards the flexural response function of local isostasy when T_e approaches 0. The main difference between these two flexural response functions is the immediate drop (for $n > 1$) for the thin shell model. This is due to the large wavelength features, which correspond to the small spherical harmonic degrees, being compensated partially by the curvature of the planet. For larger spherical harmonic degrees, the two flexural response functions converge again. This is because the smaller wavelength features, or lack thereof, are compensated in a similar matter. This shows that the main difference between the two flexural response functions has to do with taking the curvature of the planet into account.

Table 2.1: The flexural response function for the different isostasy models. Both for local, Airy and Pratt, as well as flexural, infinite plate model and thin shell model, isostasy models the flexural response function is given.

Isostasy model		Flexural Response Function
Local isostasy	Airy and Pratt	$\Phi_{\text{local}}(n) = (1)^{-1}$
Flexural isostasy	Infinite plate model	$\Phi_{\text{Inf. plate}}(n) = \left[1 + \frac{D}{(\rho_m-\rho_c)g}\left(\frac{2n+1}{2R}\right)^4\right]^{-1}$
Flexural isostasy	Thin shell model	$\Phi_{\text{Thin shell}}(n) = \left[1 + \frac{D}{(\rho_m-\rho_c)g}\left(\frac{1}{R^4}\frac{[n(n+1)-2]^2}{1-\frac{1-\nu}{n(n+1)}} + \frac{12(1-\nu^2)}{T_e^2R^2}\frac{1-\frac{2}{n(n+1)}}{1-\frac{1-\nu}{n(n+1)}}\right)\right]^{-1}$

Looking at the equations in Table 2.1 for the flexural response function, it can be seen that they expand upon one another. The flexural response function of both the infinite plate model and the thin shell model features an additional term with respect to the local isostasy model. This term represents the bending of the lithosphere. For the flexural response function of the thin shell model, this extra term also represents the membrane stresses. In this model, the curvature of the planet is taken into account. The difference in adding this curvature to the flexural response function is visible in the lower spherical harmonic degrees in Figure 2.5. Visible is, next to the drop for degree 0, for degree 1, all FRF models are equal to 1.

These flexural response functions can be used to obtain the crust-mantle boundary from the Airy crust-mantle boundary. The flexural response function can be used as a filter to the spherical harmonic representation of the crust-mantle boundary obtained by Airy isostasy. This filtering was described by Mussini [2019]:

$$M_{lm} = A_{lm}\Phi(n). \tag{2.12}$$

In this equation M_{lm} is the spherical harmonic representation of the new crust-mantle boundary, A_{lm} is the spherical harmonic representation of the crustal thickness profile from the Airy model, and $\Phi(n)$ is the flexural response function of either the infinite plate model or the thin shell model, given in Equation 2.10 and Equation 2.11.

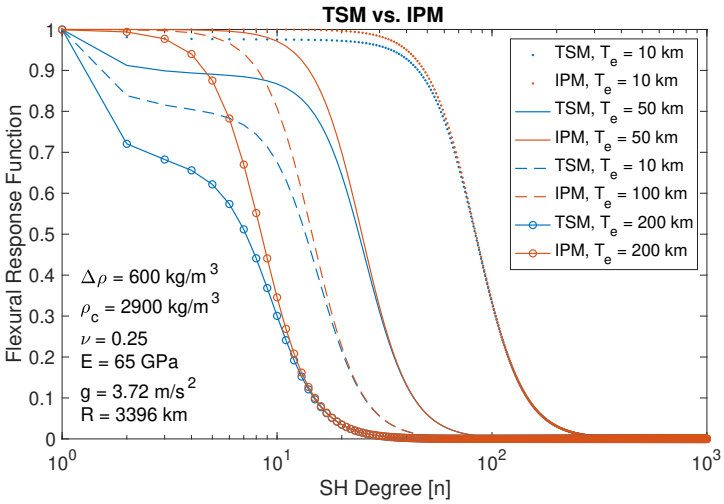

Figure 2.5: The flexural response function for the infinite plate model and thin shell model, with varying values of the elastic thickness.

2.2. Martian Topography

Current topographic models for Mars are mostly based on the Mars Orbital Laser Altimeter (MOLA). MOLA was launched in 1997 in the frame of the Mars Global Surveyor (MGS) mission [Delacourt et al., 2011]. During a period of four years (from 1997 to 2001), measurements were performed, which the current topography models use as their main data source. The most accurate topography data-set is MarsTopo2600 and goes up to spherical harmonic degree 2600 [Wieczorek, 2007]. The main limitation of this technique appears when a Digital Elevation Model (DEM) or a topographic map is required. To create such a map, an interpolation on individual MOLA measurements on regular grids is required, which requires very intensive computation and large disk capacities [Delacourt et al., 2011]. The MOLA instrument covered the surface of Mars with a dense network of precise measurements of surface elevation [Kreslavsk and Head III, 2000]. Other data was obtained by the High-Resolution Stereo Camera (HRSC) on board the European Space Agency's Mars Express (MEX) spacecraft. This data was combined to a resolution of 200 meters per pixel into the "Mars MGS MOLA - MEX HRSC Blended DEM Global 200m v2" data set.

The MOLA instrument fired infrared laser pulses downward ten times per second and measured the time it took for the reflected pulses to return from the surface. 600 million measurements were gathered by MOLA between 1999 and 2001. This originally had an average accuracy of ĩ00m for each point in the horizontal position, and the uncertainty in elevation is at least 3 m. This uncertainty in elevation is due to the global error in the areoid and regional uncertainties in its shape. MOLA produced a global topographic coverage with a spatial resolution at the equator of 300 m by 1000 m, and the resolution is even better near the poles. The MOLA topography is shown in Figure 1.1.

The MOLA topographic data used in this study was obtained from PDS Geoscience Node[1]. The used data type is the MOLA Mission Experiment Gridded Data Records (MEGDRs), which are global topographic maps of Mars created by binning altimetry values from the MOLA PEDR products acquired over the entirety of the MGS mission. These MEGDR maps are available in 4, 16, 32, 64, and 128 pixels per degree. Next to the topographic maps, different maps are available as well. These are elevation maps with respect to the areoid, a model for the equipotential surface of Mars, which is analogous to the so-called "sea level" on Earth and the planetary radius as recorded by the MOLA instrument. Next to this, also a map giving the counts, which is the number of observations used to construct the above-mentioned maps per cell in the map, is available. The topography is plotted in Figure 1.1 for 16 pixels per degree.

2.3. Martian Gravity

The first high-resolution gravity models of Mars were determined by combing the Mariner 9 and Viking 1 and 2 Orbiters S-band Doppler tracking data. This data was obtained from 1969 to 1979 [Smith et al., 1993]. This model was not uniform due to the high eccentricity of the missions [Konopliv et al., 2016]. The first global uniform gravity

[1]Last accessed 12-04-2022, https://pds-geosciences.wustl.edu/missions/mgs/megdr.html

model was determined by the Mars Global Surveyor (MGS). The MGS orbiter had an almost circular polar frozen orbit with a periapsis of approximately 380 km [Konopliv et al., 2016].

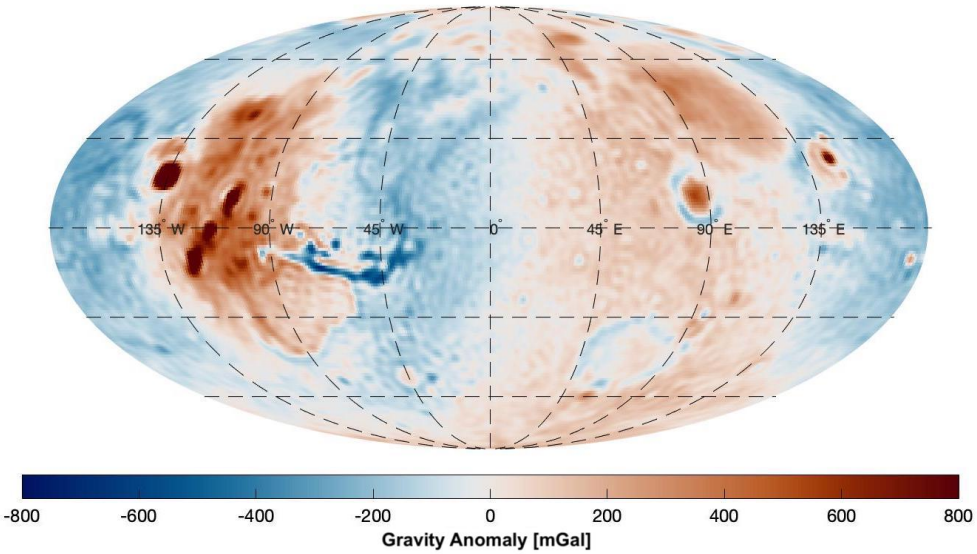

Figure 2.6: A global map of a Martian gravity anomaly based on the MRO120D gravity model. The gravity is corrected for the SH terms C_{00}, C_{10}, C_{11}, S_{11}, and C_{20} and is plotted up to SH degree 90. The colorbar is truncated for a gravity anomaly of ± 800 mGal. The MRO120D data is obtained from https://pds-geosciences.wustl.edu/mro/mro-m-rss-5-sdp-v1/mrors_1xxx/data/shadr/.

2.3.1. Gravity Representation

The aforementioned gravity models represent the gravity in its spherical harmonic form. In spherical harmonics, the gravity is represented in Stokes (C_{nm}) coefficients for varying degree (n) and order (m). The gravitational potential in spherical harmonic representation can be described with the following equation [Wieczorek, 2007]:

$$U(r) = -\frac{GM}{r}\sum_{n=0}^{\infty}\sum_{m=-n}^{n}\left(\frac{R_0}{r}\right)^n C_{nm}Y_{nm}(\theta,\phi), \tag{2.13}$$

where G is the gravitational constant, M is the mass of the body, r is the radial distance from the center of mass of the body at which the gravitational potential is measured, R_0 is the reference radius, and θ and ϕ are the planetocentric co-latitude and longitude respectively at position r. The stokes coefficients with negative order, $C_{n,-m}$, are also referred to as S_{nm}. In the equation $Y_{nm}(\theta,\phi)$ is the spherical harmonic function for degree n and order m described by:

$$Y_{nm}(\theta,\phi) = \begin{cases} \bar{P}_{nm}(\cos(\theta))\cos(m)\phi, & m \le 0 \\ \bar{P}_{n|m|}(\cos(\theta))\sin(|m|)\phi, & m < 0 \end{cases} \tag{2.14}$$

where $\bar{P}$ is the Legendre function after normalisation described by:

$$\bar{P}_{nm}(\mu) = \sqrt{(2-\delta_{0m})(2n+1)\frac{(n-m)!}{(n+m)!}}P_{nm}(\mu). \tag{2.15}$$

In the above equation $P_{nm}(\mu)$ are the de-normalized Legendre functions which are related to the Legendre polynomials as follows:

$$P_{nm}(\mu) = (1-\mu^2)^{\frac{m}{2}}\frac{d^m}{d^m}P_n(\mu), \tag{2.16}$$

$$P_n(\mu) = \frac{1}{2^n n!}\frac{d^n}{d\mu^n}\left(\mu^2-1\right)^n. \tag{2.17}$$

Equation 2.13 can be used to derive the gravitational vector in the radial direction (g_r). The gravitational vector is related to the gravitational potential as follows: $g = \nabla U$. The first derivative with respect to r needs to be taken to obtain:

$$g_r = \frac{GM}{r^2} \sum_{n=0}^{\infty} \sum_{m=-n}^{n} \left(\frac{R_0}{r}\right)^n (n+1) C_{nm} Y_{nm}(\theta, \phi). \tag{2.18}$$

In this equation, g_r is defined as positive downward. To obtain the gravitational tensor in the rr direction, the derivative with respect to r from Equation 2.18 needs to be taken to obtain Equation 2.19. The gravitational tensor is also defined as positive downward.

$$T_{rr} = -\frac{GM}{r^3} \sum_{n=0}^{\infty} \sum_{m=-n}^{n} \left(\frac{R_0}{r}\right)^n (n+2)(n+1) C_{nm} Y_{nm}(\theta, \phi). \tag{2.19}$$

2.3.2. MRO120D and GMM-3

One of the highest resolution gravity models of Mars at this moment is the MRO120D. This is a gravity model with a maximum spherical harmonic degree and order of 120, and the data from the Mars Reconnaissance Orbiter was used as the primary data. Next to this, data from the Mars Odyssey mission and the Mars Global Surveyor is included. Also, data from the Pathfinder, Viking Lander, and MER Opportunity are included. The MAVEN mission is one of the newer missions, launched in 2013, which have not been added to the current data-set yet, as well as data from the Mars InSight lander.

Another high-resolution gravity model is Goddard Mars Model-3 (GMM-3), available from Geosciences Node of the Planetary Data System. This model determined the static and time-varying gravity field of Mars by analyzing the radio tracking data of the three NASA orbiters: MGS, ODY, and MRO [Genova et al., 2016], just like the MRO12D model. Both use three different types of interplanetary radio links. 1-way Doppler is the direct transmission of the signal from the spacecraft to the Deep Space Network (DSN) station. With a 2-way Doppler, the transmission of the signal is done by a DSN station and sent coherently back to the same station by a transponder on the spacecraft. 3-way Doppler is similar to 2-way Doppler, with the only difference being that the transmitting and receiving antennas are on Earth [Genova et al., 2016].

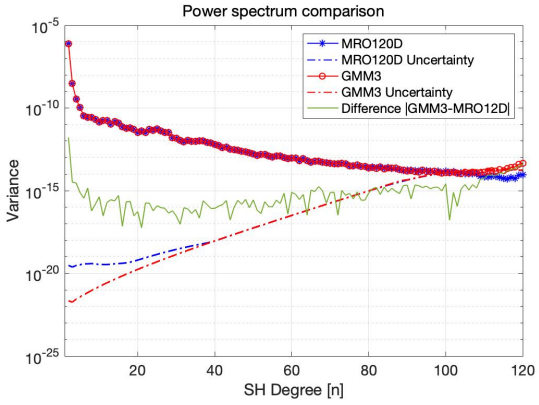

Figure 2.7: A power spectrum comparison of the GMM-3 and MRO120Dgravity data sets.

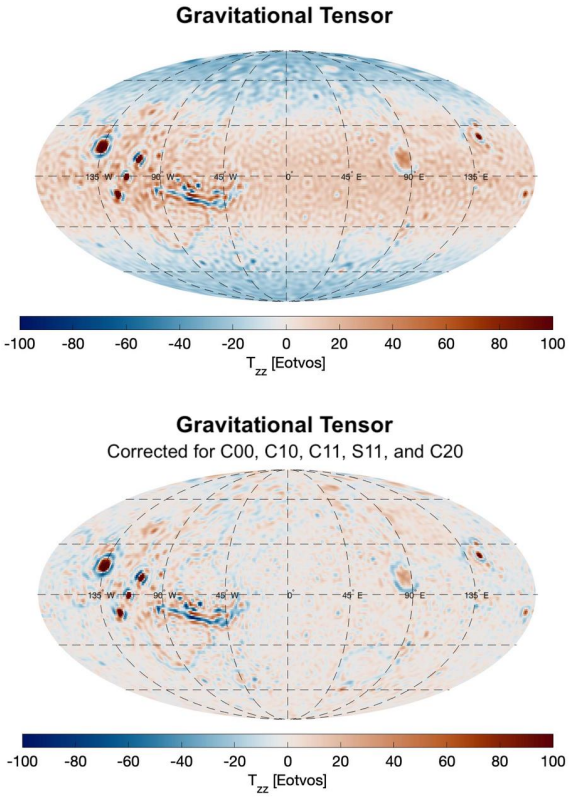

Figure 2.8: The gravitational tensor in the zz direction obtained from the MRO120D data set. The top plot shows the result from spherical harmonic degree 1 to 90 and the bottom plot shows the same plot, but with the spherical harmonic terms C_{00}, C_{10}, C_{11}, S_{11}, and C_{20} removed.

The resolution of the MRO120D data-set is up to a spherical harmonic degree 120, but the actual global resolution is close to degree 95 [Konopliv et al., 2016]. Around spherical harmonic degree 95, the standard deviation becomes larger than the actual data. This is also the case for the GMM-3 data set.

The data in this study was obtained from PDS Geoscience Node[2]. Both the GMM-3 as well as the MRO120D data set are available on PDS Geoscience Node. The power spectrum of both models are plotted in Figure 2.7. Visible is that up to approximately spherical harmonic degree 110, the models very closely follow each other, with differences approximately 5 orders lower than the actual signal. Because the models are only accurate up to degree 95, the parts that do differ from each other are anyways not included in the rest of the report.

The data will be converted using the SH toolbox, explained in subsection 2.3.4 from the spherical harmonic domain to the spatial domain. In this study, the MRO120D gravity data set will be used. The gravitational tensor in the zz direction, obtained after GSHS at the height of 150 km, is plotted in Figure 2.8. The spectrum is also plotted for 0 ° E to 360 ° E instead of the usual -180 ° E to 180 ° E. From now on, both the topography and the gravity plots will be plotted from -180 ° E to 180 ° E, which will be represented as 180 ° W to 180 ° E.

2.3.3. Gravity Anomaly

The gravitational field of a planet is directly related to its mass distribution. When a planet has relatively large masses on the surface, as for instance is the case for Mars with its large volcanoes, this mass can increase the gravity profile around these volcanoes. One way to get an insight into the planet is by performing gravity reductions based on the topography of the planet. The different spherical harmonic coefficients are connected to specific mass distributions of the planet. The spherical harmonic term with degree and order 0, C_{00}, represents the mass of the planet. The degree-1 terms, C_{10}, C_{11}, and S_{11}, give insights into the offset of the center of mass from the center of the planet. The degree-2 and order-0 term, C_{20}, represents the flattening of the planet [Wieczorek, 2007]. Therefore, when the crust and mantle are analyzed, often these mentioned coefficients are removed from the gravity signal, resulting in a gravity anomaly (GA). This is the gravity correction that has been used for the Martian gravity.

2.3.4. Forward Gravity Modelling

When the topography and density layers of a planet are known, a forward model can be used to derive the gravity of this planet. This forward model calculation can be performed using the toolbox provided by Root and Vermeersen [2016]. Using this toolbox, both Global Spherical Harmonics Synthesis (GSHS) and Global Spherical Harmonics Analysis (GSHA) can be conducted. With GSHS the data is converted from the spherical harmonic into the spatial domain. The GSHS software can be used to construct the components of gravitational fields(potential and vectors) and components of gravitational tensors from the data, together with several parameters of the planet. With GSHA this conversion can be performed the other way around. The data can be converted from the spatial into the spherical harmonic domain. Initially, the spherical harmonic toolbox was designed for Earth. With some adaptation, this toolbox can also be applied to other bodies as well as making the transformation between the spatial and spherical harmonic domain for other spatial-distributed parameters such as the topography or the crust-mantle boundary, as shown by De Backer. van der Tang [2021] also showed that this toolbox works for adding density anomalies to the mantle of a planet.

2.4. Power Spectrum

One possibility to relate the gravity to the topography of a planet is the comparison of the power spectrum [Watts and Moore, 2017]. The power spectrum is sometimes also referred to as the degree-variance and shows how much energy is stored per spherical harmonic degree.

2.4.1. Gravity Power Spectrum

The power spectrum for the gravity field, at a given degree n, can be calculated by summing the square of all coefficients as follows:

$$\sigma_{\mathrm{GA}}(n) = \sqrt{\sum_{m} C_{nm}^2 + S_{nm}^2}, \tag{2.20}$$

where C_{nm} and S_{nm} are the spherical harmonics coefficients of the gravity field model for degree n and order m.

[2]Last accessed 12-04-2022, https://pds-geosciences.wustl.edu/mro/mro-m-rss-5-sdp-v1/mrors_1xxx/data/shadr/

The coefficients in Equation 2.20 are not the Stokes coefficients but should be the spherical harmonic coefficients of certain mass anomalies. First, the correct coefficients need to be obtained. For the used gravity anomaly of Mars, the C_{00}, C_{10}, C_{11}, S_{11}, and C_{20} terms need to be removed. When these terms are removed from the data, the data then needs to be converted back to the Stokes coefficients using GSHS. Next, the radial component of the gravitational vector needs to be converted from the spatial to the spherical domain using GSHA.

2.4.2. Topography Power Spectrum

Similar to the gravity power spectrum, the topography power spectrum for spherical harmonic degree n is given by the following equation [Watts and Moore, 2017]:

$$\sigma_{\text{uncomp}}(n) = \left[4\pi G\rho_c \frac{n-1}{2n+1}\right]\sigma_{\text{topo}}\,. \tag{2.21}$$

Where σ_{topo} is the power spectrum of topography given by:

$$\sigma_{\text{topo}}(n) = \sqrt{\sum_m T_{nm}^2 + Y_{nm}^2}, \tag{2.22}$$

where T_{nm} and Y_{nm} are the spherical harmonics coefficients of the topography model for degree n and order m.

For Airy isostasy the power spectrum is given by:

$$\sigma_{\text{airy}}(n) = 4\pi G\rho_c \frac{n-1}{2n+1}\left[1-\left(\frac{R-D_c}{R}\right)^{n+2}\right]\sigma_{\text{topo}}\,. \tag{2.23}$$

And for flexure, either infinite plate of thin shell, the power spectrum can be obtained using the following equation:

$$\sigma_{\text{flexure}}(n) = 4\pi G\rho_c \frac{n-1}{2n+1}\left[1-\Phi(n)\left(\frac{R-D_c}{R}\right)^{n+2}\right]\sigma_{\text{topo}}\,. \tag{2.24}$$

The power spectrum for Airy isostasy is equal to the above equation, but with the FRF for Airy, $\Phi(n)_{\text{Airy}} = (1)^{-1}$, filled in. To obtain the power spectrum for the different isostasy models, the FRF of the corresponding model given in Table 2.1 needs to be filled in.

3

Methodology

In this study, a gravity inversion will be performed to obtain the lateral density variations within the lithosphere. The input for the inversion will be the gravity and topography data of a planet, as well as a reference planet for which the crust-mantle boundary needs to be obtained, and a lower boundary needs to be chosen. The output of the inversion will be the density of the crust and the mantle with lateral density variations. The goal is to perform this gravity inversion for Mars and obtain new insights into the Martian lithosphere. Firstly, different synthetic planets will be created, as will be explained in section 3.1. Synthetic planets consist of a modeled topography and crustal density pattern. These will be created with the Matérn covariance function, which will be explained in subsection 3.1.1. The topography will be used to calculate the crust-mantle boundary based on the isostasy methods explained in the previous chapter. The inversion will be explained in section 3.2. The crust and mantle density will be calculated from these inversion results, using the volumes of the crustal and mantle layer and a reference mass for each column, as will be explained in section 3.3. Different types of synthetic planets will be created to be able to determine for what type of planets this gravity inversion does or does not work. Lastly, the inversion modeling for Mars will be explained, given in section 3.4.

3.1. Creation of the Synthetic Planets

This section will go into how the synthetic planets will be created. First, the Matérn covariance function will be explained, which is used to obtain the topography and density variations for the synthetic planet. Next, the flexural modeling is explained, which is used to obtain the crust-mantle boundary.

3.1.1. The Matérn Covariance Function

Crustal profiles and density profiles need to be created to make a realistic model synthetic planet. One way to realistically model these profiles is through the Matérn isotropic class. In this study, this method will be used to create realistic topography and density profiles. In [Gneiting et al., 2010] the covariance function is defined as $\sigma^2 M(|\boldsymbol{h}|\nu,\alpha)$. In this $\sigma^2 > 0$ is the marginal variance and

$$M(|\boldsymbol{h}|\nu,\alpha) = \frac{\sigma^2 2^{1-\kappa}}{\Gamma(\kappa)}(\alpha\|\boldsymbol{h}\|)^{\kappa}\mathscr{K}_{\kappa}(\alpha\|\boldsymbol{h}\|) \tag{3.1}$$

is the spatial correlation at distance $|\boldsymbol{h}\|$. The spatial correlation equation is defined by the scale parameter $\alpha > 0$, the smoothness parameter $\kappa > 0$ and the gamma function of x, $\Gamma(x)$. $\mathscr{K}_{\kappa}(x)$ is the modified Bessel function and is given by the following equation

$$\mathscr{K}_{\kappa}(x) = \frac{\pi\left(\mathscr{I}_{-\kappa}(x) - \mathscr{I}_{\kappa}(x)\right)}{2\sin(\kappa\pi)}. \tag{3.2}$$

$\mathscr{I}_{\kappa}(x)$ is the Bessel function of the first kind and is given by

$$\mathscr{I}_{\kappa}(x) = \sum_{m=0}^{\infty}\frac{1}{m!\Gamma(m+\kappa+1)}\left(\frac{x}{2}\right)^{2m+\kappa}. \tag{3.3}$$

As stated above, the above equations are given in the spatial domain. In [Gneiting, 2013], it has been shown that the Matérn covariance function could be expressed on the sphere with the following equation

$$M(\psi) = \frac{\sigma^2 2^{1-\kappa}}{\Gamma(\kappa)}(\alpha\psi)^{\kappa}\mathscr{K}_{\kappa}(\alpha\psi). \tag{3.4}$$

In this equation ψ is the great circle distance, where $\psi \in [0, \pi]$. The constraints on the variance, scale parameter and smoothness parameter are respectively $\sigma^2 > 0$, $\alpha > 0$ and $0 < \kappa \leq \frac{1}{2}$. Equation 3.4 can be rewritten, using an alternate parametrization $\epsilon = \frac{2\sqrt{\kappa}}{\alpha}$, to

$$M(\psi) = \frac{\sigma^2 2^{1-\kappa}}{\Gamma(\kappa)} \left(\frac{2\sqrt{\kappa}}{\epsilon}\psi\right)^{\kappa} \mathscr{K}_{\kappa}\left(\frac{2\sqrt{\kappa}}{\epsilon}\psi\right). \tag{3.5}$$

This alternative parametrization is used because in Equation 3.4 there is mutual coupling because the behavior of α is coupled to κ. In Equation 3.5 ϵ solves this coupling problem, and this results in an easier interpretation of the parameters, which can be interpreted as follows: σ^2 represents the value which is approached when $\psi \to 0$, κ gives a measure of the smoothness around the origin, and ϵ, the decorrelation distance, represents the decay of the covariance function with ψ.

The constraint on κ, for the spherical representation of the Matérn covariance function, is a limiting constraint for many applications. This is due to the fields created with a low value of κ not being smooth. In [Guinness and Fuentes, 2016] a few different workarounds for the problem of limited smoothness in the spherical case are presented. One of these workarounds is the chordal Matérn covariance function $M_c(\psi)$. In this function, the great circle distance ψ is replaced by the Euclidian distance $2\sin(\frac{1}{2})$, resulting in the following equation:

$$M_c(\psi) = \sigma^2 \left(2\alpha \sin\frac{\psi}{2}\right)^{\nu} \mathscr{K}_{\kappa}\left(2\alpha \sin\frac{\psi}{2}\right). \tag{3.6}$$

Using again the alternate parametrization, $\epsilon = \frac{2\sqrt{\kappa}}{\alpha}$, the following equation can be obtained:

$$M_c(\psi) = \frac{\sigma^2 2^{1-\kappa}}{\Gamma(\kappa)} \left(\frac{4\sqrt{\kappa}}{\epsilon} \sin\frac{\psi}{2}\right)^{\kappa} \mathscr{K}_{\kappa}\left(\frac{4\sqrt{\kappa}}{\epsilon} \sin\frac{\psi}{2}\right), \tag{3.7}$$

with $\sigma^2 > 0$, $\epsilon > 0$ and $\kappa > 0$. In Figure 3.1 and Figure 3.2 the chordal Matérn covariance function is plotted for variations in ϵ and κ, respectively.

This chordal Matérn covariance function is used as input to the MATLAB function MVNRND, which generated a matrix of random vectors chosen from the multivariate normal distribution with mean a chosen average and the chordal Matérn covariance matrix as input for the covariance matrix. For this function, a random number generator is used. This random number generator will be set to a specific seed to be able to regenerate the obtained topography and densities. The output of this function is used to create the topography and density profiles for the synthetic planet.

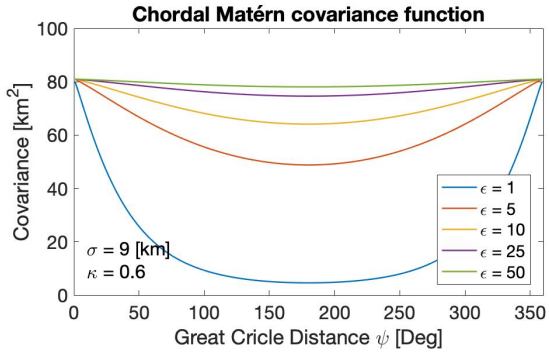

Figure 3.1: The chordal Matérn covariance function plotted for different values of ϵ.

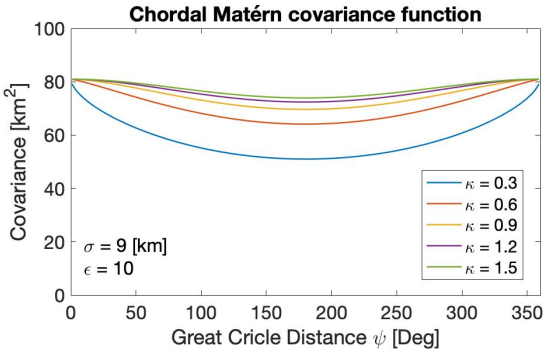

Figure 3.2: The chordal Matérn covariance function plotted for different values of κ.

3.1.2. Flexure modeling

The flexural response function (FRF) of the thin shell model is given in subsection 2.1.5. Using the flexural response function, a crustal model based on thin shell isostasy can be created. This will be done using the GSHA and GSHS toolbox explained in subsection 2.3.4. The spherical harmonic coefficients will be multiplied by the flexural response function corresponding to that specific degree. This step will be performed between GSHA and GSHS. In Figure 3.3, the flexural response function of the infinite plate model is applied, and in Figure 3.4, the flexural response function of the thin shell model is applied. The difference between the two plots, after the FRF

was applied to the original profile, is plotted in Figure 3.5. The parameters used for the Matérn covariance function, to obtain the original profiles in Figure 3.3 and Figure 3.4 with, were: $\sigma = 9$ km, $\kappa = 1.35$, and $\epsilon = 1$. The seed for the Matérn covariance function was set to 2. The parameters used for flexural response function of the thin shell model and infinite plate model, are: $T_e = 400$ km, $\nu = 0.25$, and $E = 100$ GPa.

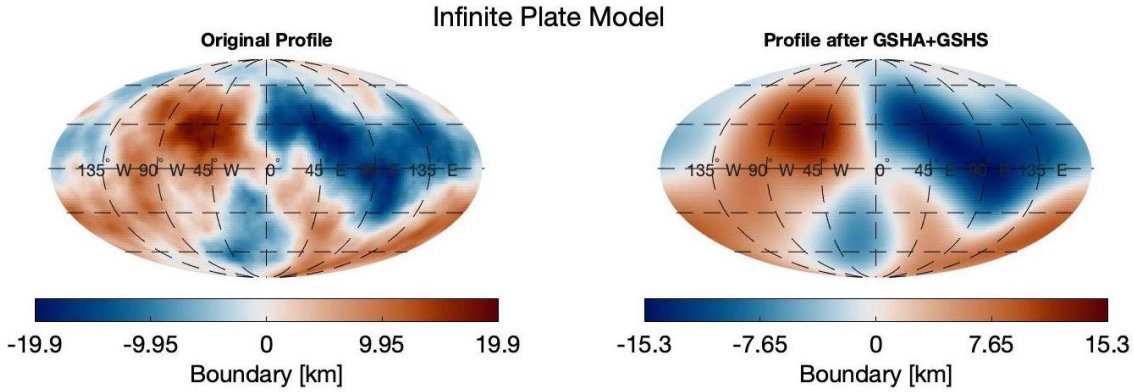

Figure 3.3: The left figure shows the crustal profile before application of the flexural response function. The right figure shows the same crustal profile after application of the flexural response function between GSHA and GSHS for the infinite plate model.

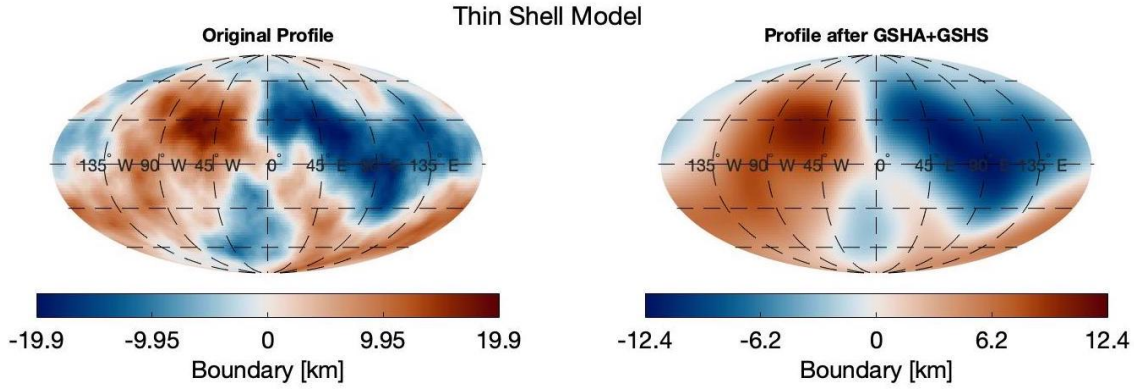

Figure 3.4: The left figure shows the crustal profile before application of the flexural response function. The right figure shows the same crustal profile after application of the flexural response function between GSHA and GSHS for the thin shell model.

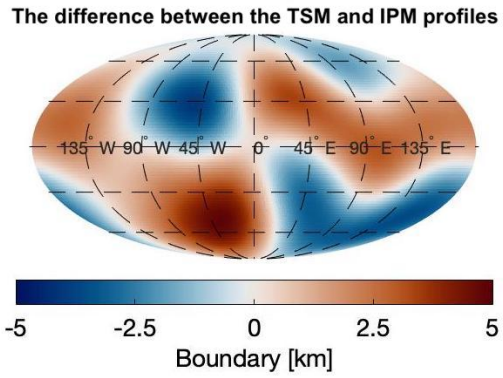

Figure 3.5: The difference between the boundary profiles, after GSHA and GSHS, of the thin shell model and the infinite plate model.

The difference plotted in Figure 3.5 shows some large wavelength patterns. These large patterns are expected when looking at the difference in the FRF, as shown in Figure 2.5. It is visible that for $T_e = 200$ km, the FRF starts to converge around SH degree 13. For $T_e = 400$ km, this conversion already happens around SH degree 8. Therefore, the differences observed in Figure 3.5 are represented by these lower SH degree terms. The main visible terms are the degree 3 and degree 4 terms, for which the difference in FRF is the largest.

3.2. Inversion

In this research, an inversion method will be used to calculate the crustal and upper mantle densities from gravity data. Inverse modeling is the reverse of forward modeling: $y = F(x)$. In the case of forward modeling, the model F is known, and the parameters x too, from which the observations, y, can be calculated in a forward manner. In the inverse model, the observations y are known, as well as the model F, and the parameters x need to be calculated. If the model is linear, a linear least-squares method can be used. In the next subsection, this method will be explained. The information was obtained from Schrama [2019].

3.2.1. Weighted Linear Least-Squares

The least-squares (LSQ) was invented by the German mathematician Carl Friedrich Gauss. He used this method to predict the position of Ceres in the asteroid belt [Gauss, 1887]. In this section, the linear least-squares method with an observation covariance matrix P_{yy} will be explained. A covariance matrix is a matrix with on the diagonal the variance of the observations, and the other elements of the matrix represent the covariance between the observations. If there is no correlation between the observations, the covariance matrix will only contain values on the diagonal. In the linear least-squares method, the observations are represented by the observation data vector $\bar{y}$, the model is denoted as the design-matrix or the information-matrix A, and parameters are represented in the parameter vector $\bar{x}$. The general formulation of the least-squares problem is:

$$\bar{y} = A\bar{x} + \bar{\varepsilon}. \tag{3.8}$$

With in this equation $\bar{\varepsilon}$ the error between the model and the observations, which need to be minimized. This is minimized with the cost function $J = \bar{\varepsilon}^t P_{yy}^{-1} \bar{\varepsilon}$. Equation 3.8 is rewritten into $\bar{\varepsilon} = \bar{y} - A\bar{x}$ and substituted into the cost function, resulting into:

$$J = \bar{y}^t P_{yy}^{-1} \left(\bar{y} - A\bar{x}\right) - \bar{x}^t A^t P_{yy}^{-1} \left(\bar{y} - A\bar{x}\right). \tag{3.9}$$

In order to minimize this cost function, a nonzero vector $\hat{x}$ needs to be found that minimizes the second term. This is because the first term on the right hand side cannot be minimized when $A\hat{x}$ approximates $\bar{y}$. This results in:

$$\hat{x}^t A^t P_{yy}^{-1} \left(\bar{y} - A\hat{x}\right) = 0. \tag{3.10}$$

This equation can be rewritten into:

$$A^t P_{yy}^{-1} A\hat{x} = A^t P_{yy}^{-1} \bar{y} \qquad -> \qquad \hat{x} = \left(A^t P_{yy}^{-1} A\right)^{-1} A^t P_{yy}^{-1} \bar{y}. \tag{3.11}$$

The above equation can be written as:

$$\hat{x} = \left(A^t P_{yy}^{-1} A\right)^{-1} A^t P_{yy}^{-1} \bar{y} = B\bar{y}. \tag{3.12}$$

Then the covariance matrix of the parameters, P_{xx}, can be written as: $P_{xx} = BP_{yy}^{-1} B^t$. Therefore, the parameter covariance matrix becomes:

$$P_{xx} = \left(A^t P_{yy}^{-1} A\right)^{-1} A^t P_{yy}^{-1} P_{yy}^{-1} P_{yy} A \left(A^t P_{yy}^{-1} A\right)^{-1} = \left(A^t P_{yy}^{-1} A\right)^{-1}. \tag{3.13}$$

3.2.2. Tikhonov Regularization

Using the Least squares method, it can happen that the Moment matrix ($A^t P_{yy}^{-1} A$) becomes near-singular. When this happens, the errors in the inversion significantly increase. One way to solve this is by using the Tikhonov regularization.

With Tikhonov regularization, a constant element is added to the diagonal of the Moment matrix. This results in the condition number being decreased. The condition number gives a measure of how much the output is changed for a small change in the input argument. The LSQ equation then becomes:

$$\hat{x} = \left(A^t P_{yy}^{-1} A + \lambda I\right)^{-1} A^t P_{yy}^{-1} \bar{y}. \tag{3.14}$$

In this equation, the ridge parameter needs to be optimized. One way to optimize this parameter is using the L-curve. An example of such an L-curve is shown in Figure 3.7. In the L-curve the solution norm, $||x_\lambda||$, is plotted against the residual norm, $||Ax_\lambda - b||$ for different values of the ridge parameter λ. The L-curve plots were first introduced by Hansen [2005]. In this paper, he describes the L-curve as: "The L-curve is a log-log plot of the norm

of a regularized solution versus the norm of the corresponding residual norm. It is a convenient graphical tool for displaying the trade-off between the size of a regularized solution and its fit to the given data, as the regularization parameter varies. The L-curve thus gives insight into the regularizing properties of the underlying regularization method, and it is an aid in choosing an appropriate regularization parameter for the given data.". The L-curve plot from Hansen [2005] is given in Figure 3.6. Visible is that for too large values of λ, the residual norm increases, but the solution norm decreases. For values of λ between 0.01 and 1, the solution norm stays almost the same, but the residual norm significantly increases. When λ becomes too small, $\lambda < 0.01$, the solution norm blows up. The optimal result is at the point where the combination of the solution norm and residual norm is minimal, in the horizontal turning point of the L, for $\lambda = 0.01$. When the result of the inversion is unknown, the L-curve is a tool to determine the optimal λ value.

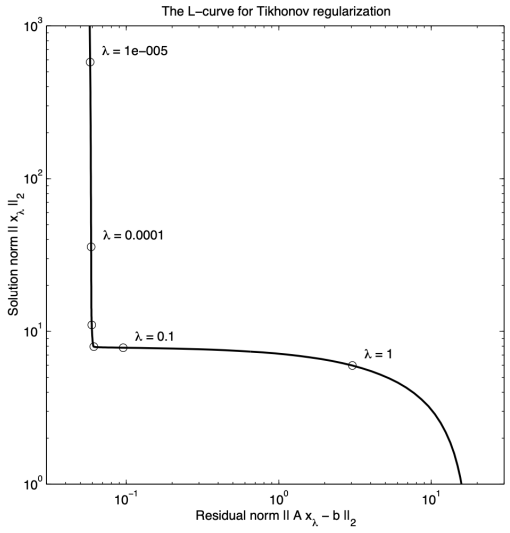

Figure 3.6: The generic L-curve for standard-form Tikhonov regularization with $x_0 = 0$; the points marked by the circles correspond to the regularization parameters = 105, 104, 103, 102, 101 and 1. Figure obtained from [Hansen, 2005]

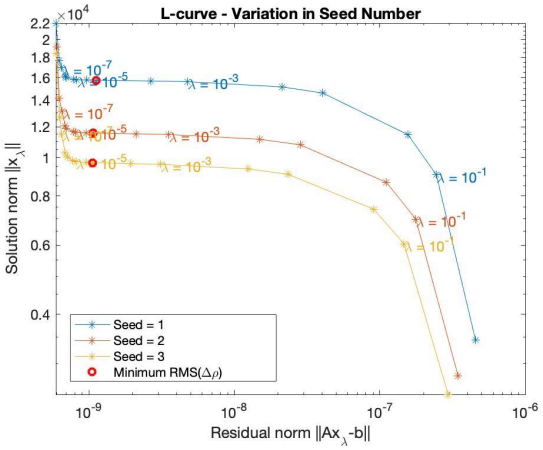

Figure 3.7: This figure shows 3 different L-curve plots corresponding to 3 different one-layer inversion models. In this figure the minimum RMS value between the obtained density variations of the inversion as well as the original density profile is given.

3.2.3. Inversion Implementation

In "Mass-density Green's functions for the gravitational gradient tensor at different heights" [Martinec, 2014], different forms of the tensor Green's function are derived for the gravitational potential, vector, and gradient tensor. These are used as a theoretical basis for geophysical interpretations of the GOCE-based gravitational gradients in terms of the Earth's mass-density structure. The Green's function for the gravitational gradient tensor, $\mathbf{G}$ = grad grad$\frac{1}{L}$, are derived in spherical coordinates (r,ϑ,φ). This Green's function is expressed in terms of the isotropic components. The function is:

$$\begin{aligned}\operatorname{grad}\operatorname{grad}\frac{1}{L} = \frac{1}{r^3}\Big[&K_{rr}(t,x)\boldsymbol{e}_{rr} + 2K_{r\Omega}(t,x)\left(\cos\alpha\,\boldsymbol{e}_{r\vartheta} - \sin\alpha\,\boldsymbol{e}_{r\varphi}\right)\\ &+ K_{\Omega\Omega}(t,x)\left(\cos 2\alpha\left(\boldsymbol{e}_{\vartheta\vartheta} - \boldsymbol{e}_{\varphi\varphi}\right) - 2\sin 2\alpha\,\boldsymbol{e}_{\vartheta\varphi}\right) - \frac{1}{2}K_{rr}(t,x)\left(\boldsymbol{e}_{\vartheta\vartheta} + \boldsymbol{e}_{\varphi\varphi}\right)\Big].\end{aligned} \tag{3.15}$$

In this equation α is the azimuth, Ω represents the co-latitude ϑ and longitude φ of the computation point, $\Omega \equiv (\vartheta,\varphi)$, and $K_{rr}(t,x)$, $K_{r\Omega}(t,x)$ and $K_{\Omega\Omega}(t,x)$ are the three isotropic kernels. In these kernels $t = \frac{r'}{r}$, with r and r' the magnitudes of vectors $\vec{r}$ and $\vec{r}'$. $\vec{r}$ and $\vec{r}'$ are the computation point and integration point, respectively, and $x = \cos(\psi)$ with ψ the angular distance. The isotropic kernels are given by an infinite series of Legendre polynomials $P_{jm}(x)$ of the azimuthal order $m = 0$, 1 and 2, respectively, and their first and second derivatives, given in Equation 3.16.

$$\begin{aligned}K_{rr}(t,x) &= \textstyle\sum_{j=0}^{\infty}(j+1)(j+2)\,t^j P_j(x),\\ K_{r\Omega}(t,x) &= -\sqrt{1-x^2}\textstyle\sum_{j=0}^{\infty}(j+2)\,t^j\frac{dP_j(x)}{dx},\\ K_{\Omega\Omega}(t,x) &= \tfrac{1}{2}\left(1-x^2\right)\textstyle\sum_{j=0}^{\infty}t^j\frac{d^2P_j(x)}{dx^2}.\end{aligned} \tag{3.16}$$

These equations can be rewritten to the closed forms of the isotropic kernels of the mass-density Green's function for the gravitational gradient tensor. These equations are given in Equation 3.17.

$$\begin{aligned} K_{rr}(t,x) &= -\frac{1}{g^3} + \frac{3(1-tx)^2}{g^5}, \\ K_{r\Omega}(t,x) &= -\sqrt{1-x^2}\frac{3t(1-tx)}{g^5}, \\ K_{\Omega\Omega}(t,x) &= \frac{1}{2}\left(1-x^2\right)\frac{3t^2}{g^5}. \end{aligned} \tag{3.17}$$

In these equations $g \equiv g(t,x) = \sqrt{1+t^2-2tx}$, $-1 \leq x \leq 1$, $0 < t \leq 1$. These isotropic Kernels are plotted in Figure 3.8 for a computation-point heights of 250 km. It is visible that K_{rr} has its maximum for $\psi = 0$ degrees.

The gravitational gradient tensor can be decomposed into three second-order tensors:

$$\mathbf{\Gamma} = \mathbf{\Gamma}_{rr} + \mathbf{\Gamma}_{r\Omega} + \mathbf{\Gamma}_{\Omega\Omega}. \tag{3.18}$$

$\mathbf{\Gamma}_{rr}$ is the vertical-vertical gravitational gradient, $\mathbf{\Gamma}_{r\Omega}$ is the vertical-horizontal gravitational gradient and $\mathbf{\Gamma}_{\Omega\Omega}$ is the horizontal-horizontal gravitational gradient. They are given by the following equations:

$$\mathbf{\Gamma}_{rr} = D_{rr}\left[\boldsymbol{e}_{rr} - \frac{1}{2}\left(\boldsymbol{e}_{\vartheta\vartheta} + \boldsymbol{e}_{\varphi\varphi}\right)\right], \tag{3.19}$$

$$\mathbf{\Gamma}_{r\Omega} = 2D_{r\vartheta}\boldsymbol{e}_{r\vartheta} - 2D_{r\varphi}\boldsymbol{e}_{r\varphi}, \tag{3.20}$$

$$\mathbf{\Gamma}_{\Omega\Omega} = D_{\vartheta\vartheta\varphi\varphi}\left(\boldsymbol{e}_{\vartheta\vartheta} - \boldsymbol{e}_{\varphi\varphi}\right) - 2D_{\vartheta\varphi}\boldsymbol{e}_{\vartheta\varphi}. \tag{3.21}$$

Which are expressed by five radially dependent functions:

$$D_{rr}(r) = \frac{\kappa}{r^3}\int_V \varrho\left(\vec{r}'\right) K_{rr}(t,\cos\psi)\,dV, \tag{3.22}$$

$$\begin{Bmatrix} D_{r\vartheta}(r) \\ D_{r\varphi}(r) \end{Bmatrix} = \frac{\kappa}{r^3}\int_V \varrho\left(\vec{r}'\right) K_{r\Omega}(t,\cos\psi) \begin{Bmatrix} \cos\alpha \\ \sin\alpha \end{Bmatrix} dV, \tag{3.23}$$

$$\begin{Bmatrix} D_{\vartheta\vartheta\varphi\varphi}(r) \\ D_{\vartheta\varphi}(r) \end{Bmatrix} = \frac{\kappa}{r^3}\int_V \varrho\left(\vec{r}'\right) K_{\Omega\Omega}(t,\cos\psi) \begin{Bmatrix} \cos 2\alpha \\ \sin 2\alpha \end{Bmatrix} dV. \tag{3.24}$$

In these equations $\varrho\left(\vec{r}'\right)$ is the mass density function. These radially dependent functions show the dependency of $K_{rr}(t,\cos\psi)$, $K_{r\Omega}(t,\cos\psi)$ and $K_{\Omega\Omega}(t,\cos\psi)$ on, the depth of the mass element $dm = \varrho\left(\vec{r}'\right)dV$, the spherical distance ψ between the mass element dm and the computation point, and the azimuthal direction α of mass element dm with respect to the computation point.

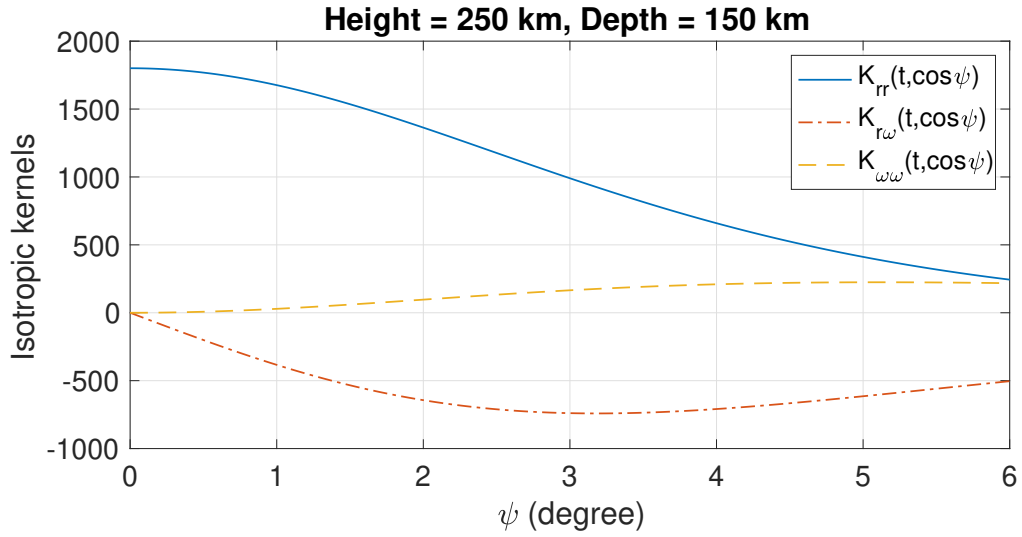

Figure 3.8: The sensitivity of the three different isotropic kernels for different angular distanced. A planetary radius of 3396 km is used, equal to the radius of Mars. The kernels are computed at a height of 250 km and a depth of 150 km and based on the closed form equations given in Equation 3.17.

As can be seen in Figure 3.8, only K_{rr} is sensitive for an angular distance of $\psi = 0$. The density underneath the computation of the gravity field needs to be calculated. Therefore the isotropic kernel, and gravitational tensor data, in the radial-radial direction will be used.

The design-matrix for the least-squares inversion can be related to the vertical-vertical gravitational gradient, which is related to the radially dependent function D_{rr}. The planet is divided into different columns. For each column, the density will be calculated. This will result in the density being obtained for each column, of which the volume is known. Because the volume is known, the vertical-vertical gravitational gradient then becomes:

$$T_{zz} = \frac{G}{r^3} \rho K_{rr} V. \tag{3.25}$$

This equation then needs to be split into the least-squares equation: $\bar{y} = A\bar{x} + \bar{\varepsilon}$. This results into $\bar{y} = T_{zz}$, $A = \frac{G}{r^3} K_{rr} V$, and the output $\bar{x} = \rho$. The input tensor is a matrix in which each value represents one column of the planet. The volume and density will have the same matrix representation.

This finally results into the following input and design matrix:

$$y = T_{\text{zz,input}}, \tag{3.26}$$

$$A = \frac{GVK_{rr}}{(R+h)^3}. \tag{3.27}$$

In these equations R is the radius of the planet and h is the computation height of the gravitational tensor input.

3.2.4. Inversion Iterations

A single inversion does not always result in a fully converted result. Depending on the input model, multiple iterations were sometimes needed to achieve a fully converted inversion. To solve this, the gravity of the inversion results will be subtracted from the initial input gravitational tensor. This can be described as follows:

$$\bar{y} = T_{\text{zz,input}} - T_{\text{zz,inversion}} \tag{3.28}$$

The same design-matrix was used for the inversion. The density output from the second iteration was then added to the density profile obtained from the first iteration. This was performed until $\bar{y}$ was smaller than a set threshold or a maximum number of iterations were performed.

3.2.5. Two-Layer Inversion

Next, the one-layer inversion is changed to a two-layer inversion. The inversion is called the two-layer inversion because the gravity of a planet with at least 2 layers is used as input.

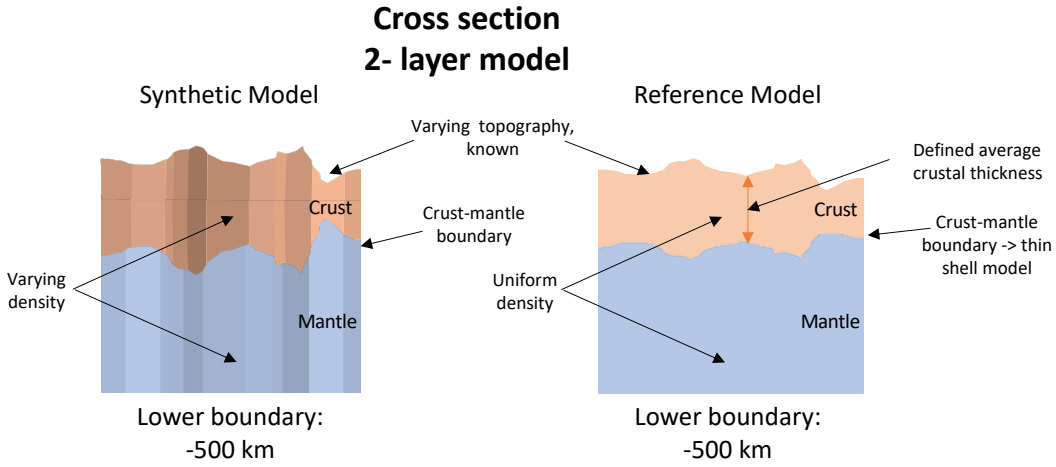

Figure 3.9: A schematic representation of both the synthetic planet and the reference model in the two-layer inversion.

The single layer output density was next used to calculate the density of both the crust and mantle. How the two densities, for the crust and mantle, are obtained from the single density output of the inversion is explained in

section 3.3. As input for the inversion, the gravity of the (synthetic) planet will be used. This could either be the gravitational potential, the gravitational vector in the z-direction, or the gravitational tensor in the zz direction. From the gravity field of the planet, the gravity of a chosen reference model will be subtracted. This reference model will be a two-layer model with uniform crustal and mantle density, as shown in Figure 3.9.

The topography of this reference model will be equal to the topography of the planet, and the crust-mantle boundary will be obtained using thin shell isostasy. The lower boundary will be set to a uniform depth. This will result in the following three observation data vectors:

$$\bar{y} = V_{\text{planet}} - V_{\text{ref}}, \quad \bar{y} = g_{\text{z,planet}} - g_{\text{z,ref}}, \quad \text{or} \quad \bar{y} = T_{\text{zz,planet}} - T_{\text{zz,ref}}. \tag{3.29}$$

This will result into three different design matrices respectively:

$$A = \frac{GVK}{(R+h)}, \quad A = -\frac{GVK_r}{(R+h)^2}, \quad \text{or} \quad A = \frac{GVK_{rr}}{(R+h)^3}. \tag{3.30}$$

The effect of using the different types of gravitational data will be studied, as well as the influence of varying the ridge parameter of the Tikhonov regularization, λ.

The output of this inversion method will be a single density. From this single density, the crust and mantle density will be obtained using the method explained in section 3.3. These new densities are used to calculate the gravity of the "new" reference model. This reference model is the same as the initial reference model, except that the uniform densities for both the crust and the mantle are changed to the densities obtained in the previous iteration. The iterations are run until the observation data vector becomes smaller than a set threshold.

It was found that for the inversion of the two-layer model, the signal was largely dampened. Therefore, many iterations were needed until the inversion converged. To speed up this process, the inversion result was multiplied by a multiplication factor. This new increased result was then used for the density calculations explained in the next section.

3.3. Density calculations

As explained above, the single density of the inversion output needs to be split into two densities. The idea is to split the single layer into two sections, the crust and the mantle, and place the mass of this volume in the center of mass of this volume. Splitting the crust and the mantle results in 2 volumes: V_c for the crust and V_m for the mantle. These volumes can be calculated with triple integrals in spherical coordinates:

$$V = \int\int\int dV \quad -> \quad V = \int\int\int r^2 \sin(\phi) \mathrm{d}r \mathrm{d}\phi \mathrm{d}\theta. \tag{3.31}$$

Using these integrals the volume of the crust and mantle, shown in blue and orange respectively in Figure 3.10, can be calculated. Integrating the above equation from θ_1 to θ_2, ϕ_1 to ϕ_2 and from r_1 to r_2, results into:

$$V = \int_{\theta_1}^{\theta_2}\int_{\phi_1}^{\phi_2}\int_{r_1}^{r_2} r^2 \sin(\phi) \mathrm{d}r \mathrm{d}\phi \mathrm{d}\theta \quad -> \quad V = \int_{\theta_1}^{\theta_2} \mathrm{d}\theta \int_{\phi_1}^{\phi_2} \sin(\phi) \mathrm{d}\phi \int_{r_1}^{r_2} r^2 \mathrm{d}r. \tag{3.32}$$

$$V = (\theta_2 - \theta_1)(\cos(\phi_1) - \cos(\phi_2)) \frac{1}{3} \left(r_2^3 - r_1^3\right). \tag{3.33}$$

Looking at Figure 3.10, the equations for r_1 and r_2 for the crustal volume can be derived, which are equal to: $r_1 = (R_M - c)$ and $r_2 = (R_M + h)$. Plugging these values into Equation 3.33 gives the following equation:

$$V_c = (\theta_2 - \theta_1)(\cos(\phi_1) - \cos(\phi_2)) \frac{1}{3} \left((R_M + h)^3 - (R_M - c)^3\right). \tag{3.34}$$

The equations for r_1 and r_2 for the mantle can also be derived from Figure 3.10, and are equal to: $r_1 = (R_M - d_{\text{ref}})$ and $r_2 = ((R_M - c)$. This gave the volume for the mantle to be equal to:

$$V_m = (\theta_2 - \theta_1)(\cos(\phi_1) - \cos(\phi_2)) \frac{1}{3} \leq \left((R_M - c)^3 - (R_M - d_{\text{ref}})^3\right). \tag{3.35}$$

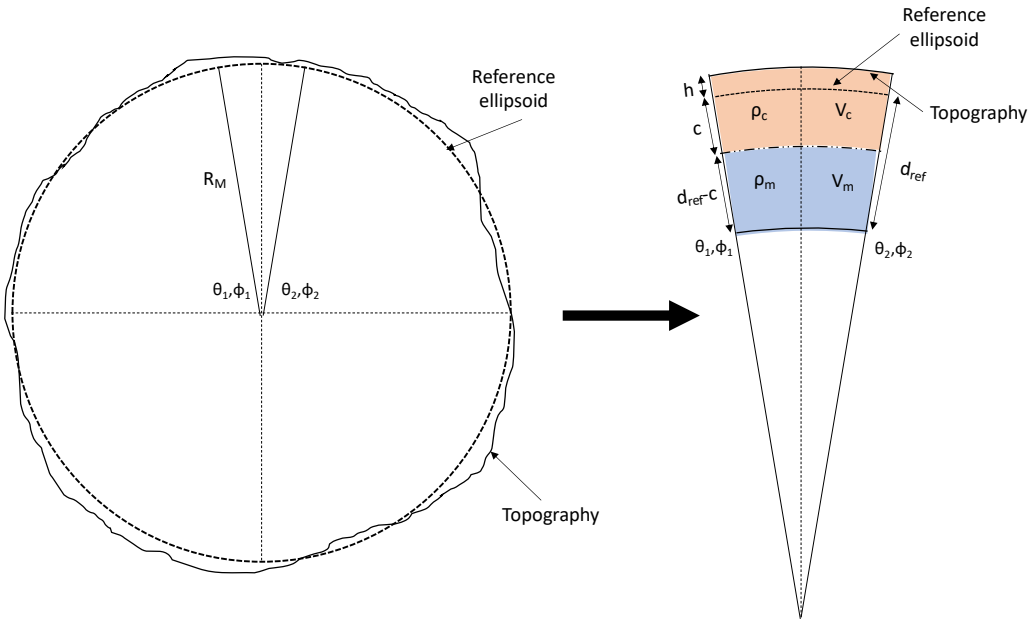

Figure 3.10: This figure shows how taking a grid from a planet with a crust, mantle and topography translates to the volumes of the crust and mantle.

Now that the volumes are known, the center of mass (CM) of both the crust and the mantle need to be calculated. Because the observed grid is symmetric, the CM will always be on the line from the center of the planet to the middle of the grid, the line of symmetry. Therefore only the z position of the CM needs to be calculated. The definition of the CM for a 3D sphere could be defined as:

$$z_{CM} = \frac{\int\int\int z' \mathrm{d}V}{\int\int\int \mathrm{d}V}. \tag{3.36}$$

In this equation $z' = r$, when the center of mass is in the radial direction of the planet. This gives the following equation for the z position of the CM:

$$z_{CM} = \frac{\int_{\theta_1}^{\theta_2} \mathrm{d}\theta \int_{\phi_1}^{\phi_2} \sin(\phi)\mathrm{d}\phi \int_{r_1}^{r_2} r^3 dr}{\int_{\theta_1}^{\theta_2} \mathrm{d}\theta \int_{\phi_1}^{\phi_2} \sin(\phi)\mathrm{d}\phi \int_{r_1}^{r_2} r^2 dr}. \tag{3.37}$$

$$z_{CM} = \frac{3}{4}\frac{\left(r_2^4 - r_1^4\right)}{\left(\left(r_2^3 - r_1^3\right)\right.}. \tag{3.38}$$

For the crust this gives a CM position of:

$$z_{CM} = \frac{3}{4}\frac{\left((R_M + h)^4 - (R_M - c)^4\right)}{\left((R_M + h)^3 - (R_M - c)^3\right)}, \tag{3.39}$$

and for the mantle this gives a CM position of:

$$z_{CM} = \frac{3}{4}\frac{\left((R_M - c)^4 - (R_M - d_{\mathrm{ref}})^4\right)}{\left((R_M - c)^3 - (R_M - d_{\mathrm{ref}})^3\right)}. \tag{3.40}$$

Now there are two equations with two unknowns:

$$\mathbf{g} = \frac{GM_{\mathrm{tot}}}{D_{\mathrm{tot}}^2} = \frac{Gm_c}{r_{cm_c}^2} + \frac{Gm_m}{r_{cm_m}^2}, \tag{3.41}$$

$$M_{\mathrm{tot}} = m_c + m_m. \tag{3.42}$$

In these equations, r_{cm_c}, r_{cm_m} and D_{tot} can be obtained when an isostasy method, as well as a depth of compensations, are set and the total mass M_{tot} can be obtained from gravity data. G is a constant which is known,

which results therefore in two equations with two unknowns: m_c and m_m, the masses of the crust and mantle, respectively. These masses can be rewritten in terms of density and volume: $m_c = \rho_c V_c$ and $m_m = \rho_m V_m$. Using these equations together with the one given above, the equations for the density of the crust and the mantle can be obtained.

Using the following two equations,

$$\frac{M_{\text{tot}}}{D_{\text{tot}}^2} = \frac{\rho_c V_c}{r_{cm_c}^2} + \frac{\rho_m V_m}{r_{cm_m}^2}, \tag{3.43}$$

$$M_{\text{tot}} = \rho_c V_c + \rho_m V_m, \tag{3.44}$$

the center of mass depth, D_{tot}, can be obtained. First Equation 3.43 can be rewritten to:

$$M_{\text{tot}} = D_{\text{tot}}^2 \frac{\rho_c V_c}{r_{cm_c}^2} + \frac{\rho_m V_m}{r_{cm_m}^2}. \tag{3.45}$$

Next this equation for M_{tot} needs to be filled into Equation 3.44, resulting into:

$$\rho_c V_c + \rho_m V_m = D_{\text{tot}}^2 \frac{\rho_c V_c}{r_{cm_c}^2} + \frac{\rho_m V_m}{r_{cm_m}^2}. \tag{3.46}$$

Rewriting this equation results into the following equation for D_{tot}:

$$D_{\text{tot}} = \sqrt{\frac{\rho_c V_c + \rho_m V_m}{\frac{\rho_c V_c}{r_{cm_c}^2} + \frac{\rho_m V_m}{r_{cm_m}^2}}}. \tag{3.47}$$

The current inversion model returns only one density layer, which could be interpreted as the density difference needed to achieve the obtained gravity field. This density difference could be rewritten into a displacement in the overall center of mass. This can be done by rewriting

$$\frac{\rho_{\text{ref.}} V_{\text{tot}}}{D_{\text{ref.}}^2} = \frac{\rho_{\text{inv.}} V_{\text{tot}}}{D_{\text{inv.}}^2}, \tag{3.48}$$

into,

$$D_{\text{inv.}} = D_{\text{ref.}} \sqrt{\frac{\rho_{\text{inv.}}}{\rho_{\text{ref.}}}}. \tag{3.49}$$

Now using this $D_{\text{inv.}}$ and rewriting Equation 3.43 and Equation 3.44, the density of both the crust and mantle can be calculated. First Equation 3.44 is rewritten in terms of ρ_c to:

$$\rho_c = \frac{M_{\text{tot}} - \rho_m V_m}{V_c} \tag{3.50}$$

Filling this back into Equation 3.43 results into a equation for ρ_m without any unknowns:

$$\rho_m = \left(\frac{M_{\text{tot}}}{D_{\text{inv.}}^2} - \frac{M_{\text{tot}}}{r_{cm_c}^2} \right) \left(-\frac{V_m}{r_{cm_c}^2} + \frac{V_m}{r_{cm_m}^2} \right)^{-1} \tag{3.51}$$

This equation for ρ_m can than again be used to calculate ρ_c using Equation 3.50.

3.3.1. Flowchart

A flowchart showing the two-layer iterative inversion process is given in Figure 3.11. On the left, the synthetic planet with its available data is given. The topographic data is used as input for the isostasy calculations for the crust-mantle boundary. The topography of the synthetic planet is also used as the topography of the reference model. The reference model also consists of the calculated crust-mantle boundary, a lower boundary of 500 km, and two uniform densities for the crust and mantle. The difference in gravity between the synthetic planet and the reference model is used as input for the inversion. From the output of the inversion, the density of the crust and mantle are calculated. These new densities are then inserted back into the reference model, and the inversion is performed again. This was done until a set number of iterations were performed.

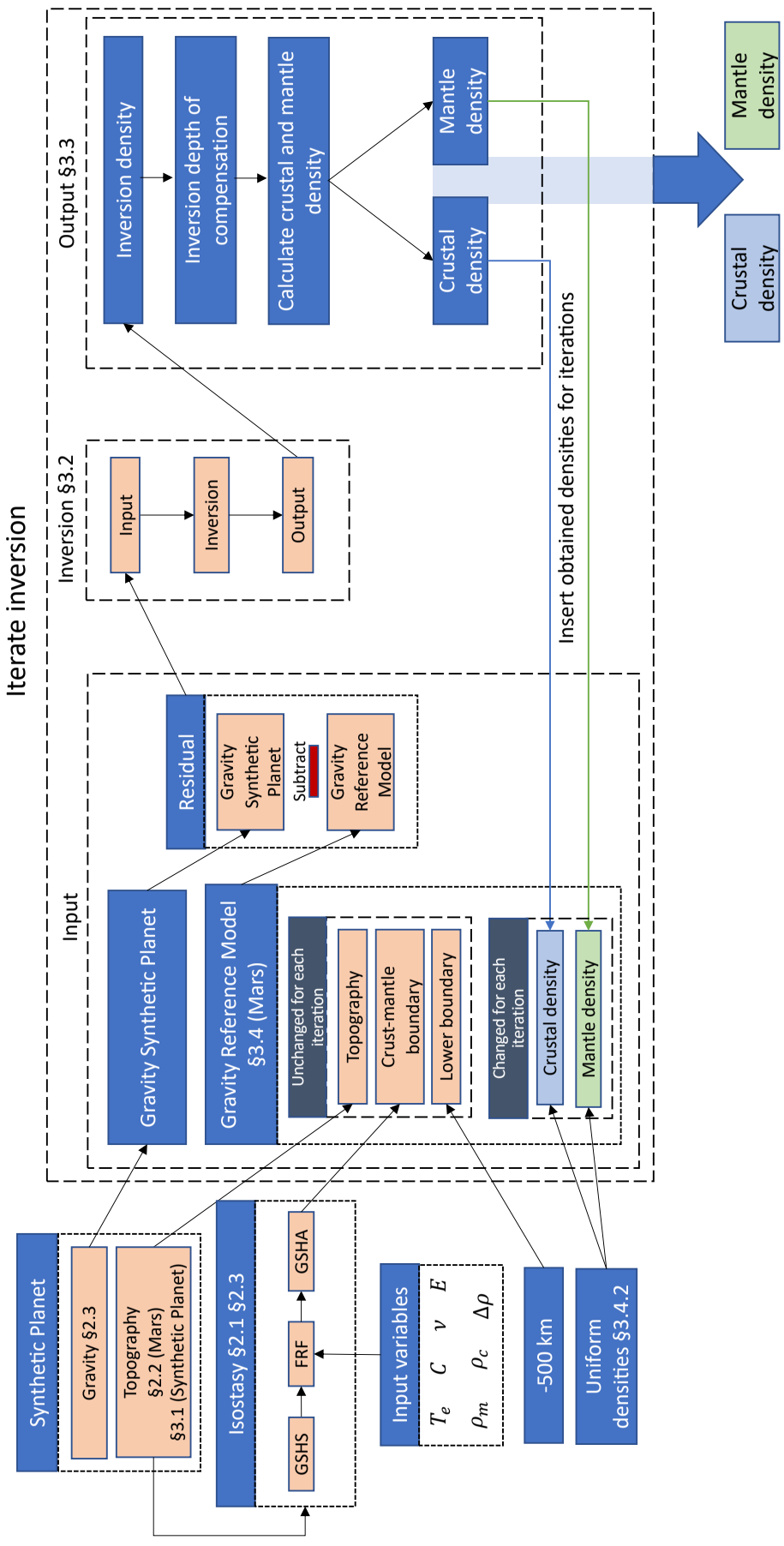

Figure 3.11: A flowchart given a schematic representation of the two-layer iterative inversion process.

3.4. Mars Inversion Modeling

The last step, when the two-layer inversion has been optimized and analyzed, is to change the model to fit the Martian inversion. The inputs for the inversion are the gravity data explained in section 2.3 and a reference model for Mars.

The reference model will be iterated to fit the Martian gravitational tensor. For every iteration, the densities of the reference model are changed to the obtained densities from the inversion. The gravity from this new reference model is then calculated, and the difference between the Martian gravity and the reference planet gravity will be used as input. This is re-iterated until a set number of iterations are performed.

3.4.1. Topography

The topography data which will be used for the reference model is the Martian MOLA topography data explained in section 2.2. The resolution of the topography will be changed to a 2 by 2-degree grid.

3.4.2. Crust-Mantle Boundary

The crust-mantle boundary for the reference model will be based on thin shell isostasy. Qin [2021] found that the thin shell model is the best fit for the Martian topography spectrum when looking at the SH degrees 4 to 17.

In Figure 3.12 the power spectrum of the Martian FAA, the uncompensated topography, the crust-mantle boundary obtained with local compensation (Airy), with the thin shell model, as well as the infinite plate model are given. It can be seen that the local compensation spectrum largely overcompensated the topography, resulting in a very low spectrum. For the larger spherical harmonic degrees, the infinite plate model also overcompensates the topography, underestimating the power spectrum. The thin shell model is the best fitting model between spherical harmonic degrees 4 and 17, and will therefore be used to create the crust-mantle boundary of the reference model.

As explained in section 2.1, there are different input parameters that can be changed in the isostasy model. These parameters are the: Poisson ration ν, the Young's modulus, E, the average crustal thickness, C, the elastic thickness, T_e, and the crustal and mantle densities, ρ_c, and ρ_m respectively.

To obtain a range for these different parameters, literature has been reviewed to obtain which values for these input parameters have been used previously in literature. Table 3.1 shows which studies used which input parameters. Based on this research, the parameter ranges given in the top row of Table 3.1 were chosen as the initial search space for the Martian reference models.

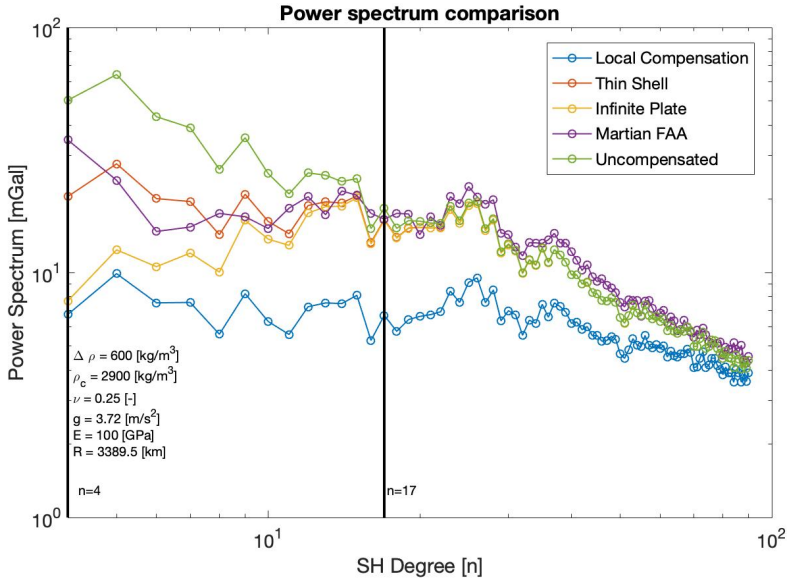

Figure 3.12: The power spectrum of the Martian gravity, the uncompensated topography, the crust mantle boundary obtained with local compensation (Airy) as well as with the infinite plate model and thin shell model.

3.4.3. Lower Boundary - Lithosphere

Based on the new Insight data, Khan et al. [2021] found that the Martian lithosphere reached up to a depth between 400 and 600 km. This is the seismic lithospheric thickness based on the seismic data obtained by the Insight mission. Based on these findings, the lower boundary for the lithosphere was set to a depth of 500 km, in the middle of what was found for the seismic lithosphere.

3.4.4. Plume Modeling

When looking at the Martian gravity power spectrum, there is a large peak for the lower spherical harmonic degrees. This is expected to be due to the Tharsis region, which is responsible for the largest gravity and topography features. Previous research suggests that the Tharsis region is mainly supported by the flexure of the lithosphere as well as partially by a deep mantle plume [Breuer et al., 1996] [Zhong, 2002]. Based on this, van der Tang [2021] modeled the Martian reference plume. In this study, a rectangular plume with a density variation of 400 kg/m^3 was found to be the optimal fit for the Martian gravity anomaly. They reached from a depth of 800 km up to a depth of 900 km. The plume was centered around [110°W 3°N] and had a longitudinal radius in both directions of 32° and a latitudinal radius in both directions of 30°, as shown in Figure 3.13. This density anomaly is very high and deemed too large for a mantle anomaly [van der Tang, 2021]. This yielded the best fitting result for a sensitivity study performed to find the best possible relationship between the depth, density, thickness, and size of the modeled anomaly. Because this yielded the best fitting results for the smaller SH degrees, this plume will also be added as a layer to the reference model.

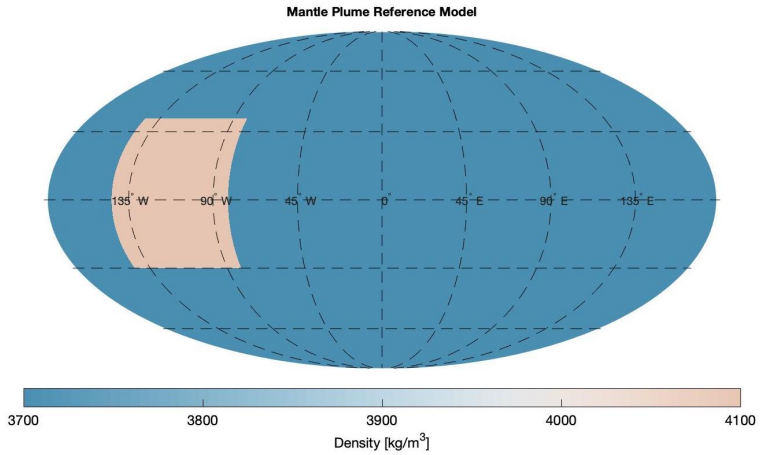

Figure 3.13: The mantle plume used in the reference model to fit the low Spherical Harmonic degrees in the power spectrum. The plume is modeled from a depth of 800km up to a depth of 900km. This plume was centerd around [110°W 3°N] with a longitudinal radius of 32° and a latitudinal radius 30°.

Table 3.1: A summary of the used/obtained crustal and mantle densities and crustal and lithospheric/elastic thicknesses

Paper	**Crustal Density** [kg/m^3]	**Mantle Density** [kg/m^3]	**Crustal Thickness** [km]	**Lithosphere /Elastic Thickness** [km]	**Young's modulus [Gpa]**	**Poisson Ratio** [-]
Initial analyzed ranges	[2700 - 3100]	[3400 - 3600]	[50 - 125]	[50 - 400]	100	0.25
[Goossens et al., 2017]	2582 ± 209	-	42	-	-	-
[Phillips et al., 1973]	3000 2670	3300 3270	50 50	-	-	-
[Wieczorek and Zuber, 2004]	2700–3100 2800–2900	3400–3550 3300–3400	>29 >39	-	-	-
[Zuber et al., 2000]	2900	-	50	0-100	-	-
[Neumann et al., 2004]	2900	3500	45	-	100	0.25
[Nimmo and Stevenson, 2001]	-	-	30-115	-	-	-
[Nimmo, 2002]	2000-3000 2500	-	1-111 1-75	21-113 37-89	-	-
[Turcotte et al., 2002]	2960±50	-	91.7 ±10	90 ± 10	-	-
[Yuan et al., 2001]	-	-	-	100 km	-	-
[McKenzie et al., 2002]	2350-2990	-	-	12.4-70	144	0.268
[Kiefer et al., 1996]	2900	3930	25-100	-	-	-
[Belleguic et al., 2005]	3050 ± 350 3270 ± 150 (Elysium region)	3500	60 ± 30	56 ± 20 to 105± 105 km	100	0.25
[Beuthe et al., 2012]	2950 ± 450 3000-34000 (large volcanoes)	3500	45	20-180	100	0.25
[Pauer and Breuer, 2008]	2400-3200	3500	-	-	-	-
[Grott and Breuer, 2008]	-	-	-	64±32	-	-
[Taylor et al., 2020]	3000 ± 500	3450 ± 150	-	40-170, mean 83.3	17.8	0.3 ± 0.2
[McGovern et al., 2004]	2900	3500	50	0-200	100	0.25
[Steinberger et al., 2010]	2950	3338	50	102	65	0.25
[Knapmeyer-Endrun et al., 2021]	2850 3100	3400	48 ± 24	-	-	-
[Khan et al., 2021]	2900	3500	65	400-600	-	-

4

Verification and Validation

In this chapter, the additional verification and validation steps will be explained. In the first section, the data will be verified and validated, first the topography data, and after that, the gravity data. In section 4.2 the one-layer model will be discussed, and in the last section, the two-layer model will be discussed.

4.1. Data

In this section, the topography (MOLA) and gravity (MRO120D) are validated by comparing the topography and gravity, together with their power spectra, to that what has been obtained in literature.

4.1.1. Topography

As explained in section 2.2, the topography data used in this study is the MOLA topography data obtained from PDS Geoscience Node[1]. The MOLA topography is plotted in Figure 1.1 but will also be validated based on the data presented in [Wieczorek, 2007]. In this study, the global topography is derived from the spherical harmonic shape model MarsTopo2600, referenced to the geoid. This MarsTopo2600 data is plotted in Figure 4.1. A similar plot is given in Figure 4.2, where the data used in this study is plotted.

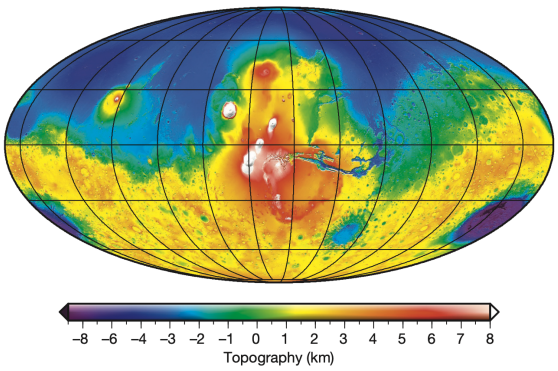

Figure 4.1: The global topography of Mars, which is derived from the spherical harmonic shape model MarsTopo2600, referenced to the geoid. This figure is in a Mollweide projection with a central meridian of 100° W longitude and is overlain by a gradient image derived from the topography model. [Wieczorek, 2007]

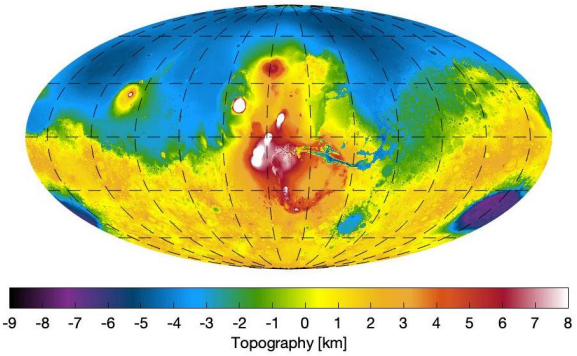

Figure 4.2: The global topography map is computed for the elevation difference between the planetary radius and the areoid. The data is obtained from PDS Geoscience Node. This figure is in a Mollweide projection with a central meridian of 100° W longitude.

There are small differences visible between the two plots in Figure 4.1 and Figure 4.2. This has to do with the fact that Figure 4.1 that the color bar is different from the one used in Figure 4.2. In the first figure, the color bar jumps from -8 to -6 km and from -6 to -4 km and then continues on linearly. For Figure 4.2 the color bar is linear from -9 km all the way up to 8 km. Next to these differences, the topography maps look nearly identical.

In [Wieczorek, 2007], next to the topography plot shown in Figure 4.1, also the power spectrum of the MarsTopo2600

[1]Last accessed 12-04-2022, https://pds-geosciences.wustl.edu/missions/mgs/megdr.html

data set is given. This spectrum is plotted in Figure 4.3. The power spectrum of both the MOLA data, used in this study, and the MarsTopo2600 data, used by Wieczorek [2007], are plotted in Figure 4.4. Visible is that both spectra are nearly identical, except for degree 2. The C_{20} term in the second spherical harmonic degree represents the flattening of the planet. The difference between these degrees in the power spectra might have to do with this term. This has to do with the fact that the MarsTopo2600 is a shape model, which does contain the flattening of the planet, while the MOLA data is a topography data set, which does not contain this flattening of the planet. Therefore the degree 2 power spectrum is lower for the MOLA data. When comparing the MarsTopo2600 spectrum plotted in Figure 4.4 to the figure given by Wieczorek [2007] in Figure 4.3, similar results are obtained. From the resemblance of the power spectra can be concluded that the data was processed correctly.

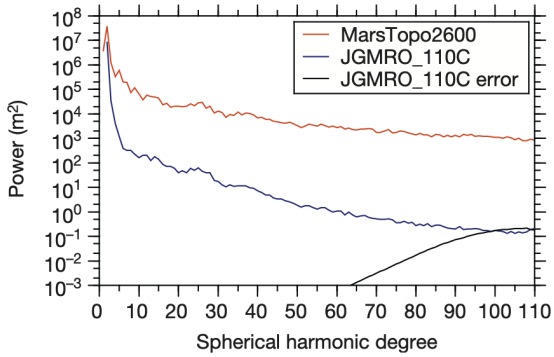

Figure 4.3: The power spectrum of the topography of Mars, which is derived from the spherical harmonic shape model MarsTopo2600. [Wieczorek, 2007].

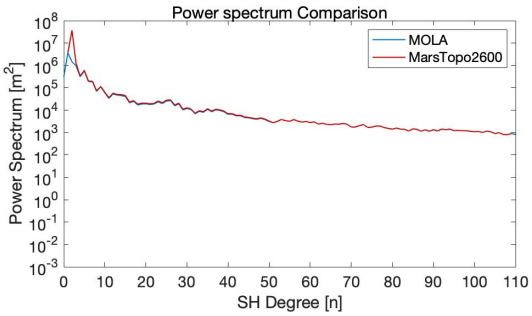

Figure 4.4: The power spectrum of the topography of Mars for both the MOLA data set, used in this study, and the MarsTopo2600 data set, used in [Wieczorek, 2007]. The MOLA data is obtained from PDS Geoscience Node and the MarsTopo2600 data is obtained from Zenodo.

4.1.2. Gravity

As explained in section 2.3, the gravity data used in this study is the MRO120D data set obtained from PDS Geoscience Node[2]. The power spectrum, together with the uncertainty, has been plotted in Figure 2.7. To validate the spectrum, the obtained power spectrum is again plotted in Figure 4.6 only for the MRO120D data set, and compared to the power spectrum given by [Gorski et al., 2018], shown in Figure 4.5. Visible is that these power spectra are identical to each other. The gravity is converted from the spherical harmonic domain into the spatial domain using the GSHS toolbox explained in subsection 2.3.4. This toolbox has already been validated and will therefore not be validated any further.

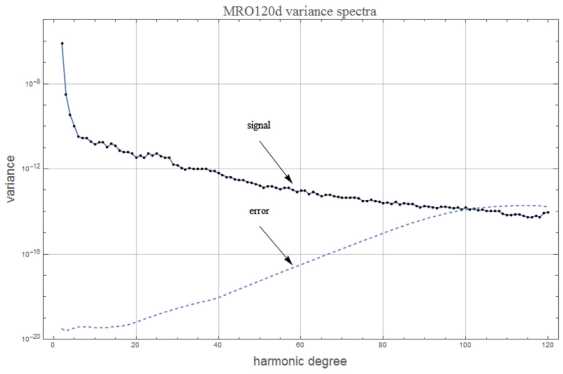

Figure 4.5: Variance spectra of signal and error for the Doppler-derived gravitational potential model MRO120d. [Gorski et al., 2018].

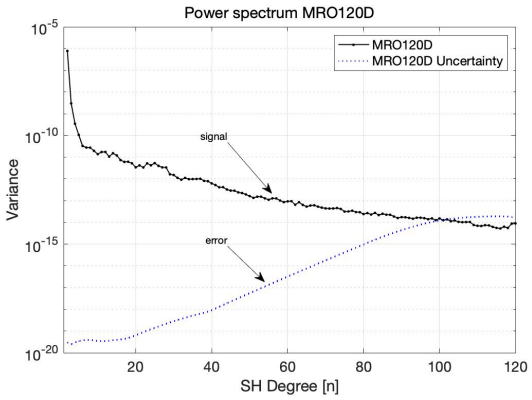

Figure 4.6: The power spectrum of the MRO120D data set plotted together with its uncertainty. The data is obtained from PDS Geoscience Node.

4.2. One-Layer Inversion

In this section, the inversion model will be validated, and the robustness will be analyzed. First, the single-layer inversion will be validated and understood, and its robustness will be analyzed. The inversion will be performed

[2]Last accessed 12-04-2022, https://pds-geosciences.wustl.edu/mro/mro-m-rss-5-sdp-v1/mrors_1xxx/data/shadr/

using a similar method as for the two-layer inversion. Therefore, the effect of the different inversion parameters, as well as the effect of different densities and topographies will be studied thoroughly. It needs to be studied whether the inversion works for a single layer without varying topography or lower boundary. Next, a varying topography boundary and a varying lower boundary will be added. The effect on the inversion for these single layers will be studied in the next subsection.

4.2.1. Height/Depth Analysis

As explained in subsection 3.2.3, an inversion height is used in the design-matrix. Next to this, a computation height and depth need to be chosen at which the isotropic kernels are obtained.

The depth of the inversion is chosen in approximately the center of mass of the layer. For the single-layer inversion, this was set to $D_{\text{inversion}} = 0.5 D_{\text{layer}}$.

A small analysis was performed on the variations in inversion height. The input data was also corrected for the inversion height. If a height of 250 km was chosen for the inversion and isotropic kernels, the input gravity was converted to the gravity which would be obtained at this inversion height. When the gravity is computed higher from the ground, the signal is dampened, but when the inversion is computed very close to the ground, the inversion is not sensitive enough to the data. Therefore, an optimal combination needed to be found. After a small analysis, it was found that a height of 150 km, yielded good results. From now on, unless mentioned otherwise, a computation height of 150 km will be used for both the one-layer and two-layer inversion.

4.2.2. Effect of Adding Topography and a Lower Boundary

Using the method described in subsection 3.2.4, three different one-layer models were used to analyze the influence of varying topography and lower boundary. A cross-section for each of these models is shown in Figure 4.7, and these models can be described as follows:

1. A 50 km layer with uniform topography of 0 km and a uniform lower boundary at -50 km.
2. A layer of approximately 50 km with a varying topography and a uniform lower boundary at -50 km.
3. A layer of approximately 50 km with a varying topography and a varying lower boundary.

The first model will study whether the inversion works when the easiest possible input model is used. When this works, the effect of varying topography and lower boundaries on the inversion are studied. For these inversion results a ridge parameter of $\lambda = 10^{-10}$ mGal was chosen and a weight of $W = \frac{1}{\sigma^2} = \frac{1}{(0.1*10^{-9})^2} = 10^{20}$ mGal. In subsection 4.2.6 the effect of varying σ and λ will be studied. The topography for the second and third models is given in Figure 4.8. The lower boundary used for the third model is given in Figure 4.9.

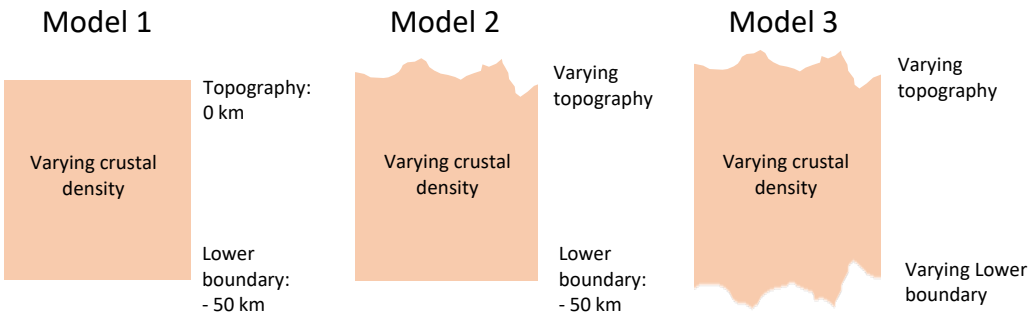

Figure 4.7: A cross section for each of the 3 one-layer models to study the effect of adding varying topography and lower boundary layers.

For every model, a computation height of 250 km is used. The used computation depth can be described by the following equation: $D_{\text{computation}} = \text{mean}\left(\frac{t-d}{2}\right)$. In this equation, t is the used topography of the layer, equal to 0 km for model 1, and the topography shown in Figure 4.8 for models 2 and 3 and d is the lower boundary, equal to -50 km for models 1 and 2 and equal to the lower boundary given in Figure 4.9 for model 3.

When a single run was performed, there was still a residual between the two gravity fields. Due to this residual, an iterative inversion process explained in subsection 3.2.4 was performed. The inversion was iterated until a maximum of 4 iterations or until the standard deviation of the difference between the two tensors in the zz direction was smaller than $2 \cdot 10^{-3}$ Eotvos for model 2, and $5 \cdot 10^{-3}$ Eotvos for model 3.

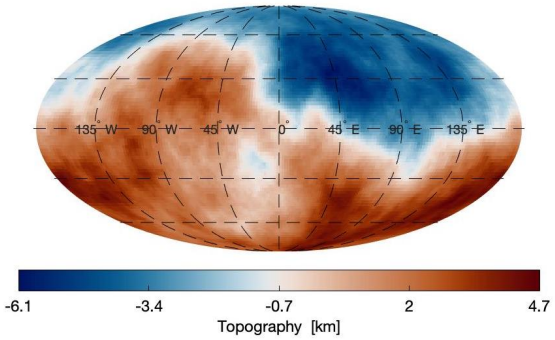

Figure 4.8: The topographic boundary for the one-layer inversion model. This varying upper boundary is used in the second and third model.

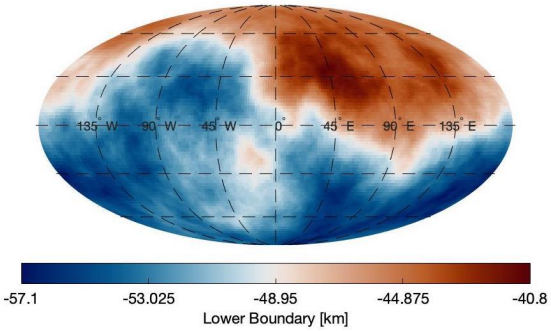

Figure 4.9: The Lower boundary for the one-layer inversion model. This varying lower boundary is used in the third model.

4.2.3. Model 1 - Uniform Layer

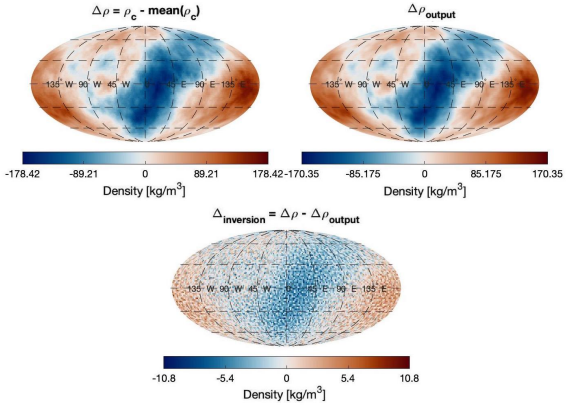

Figure 4.10: inversion results Model 1. This model is a 50 km layer with varying density, a constant upper boundary of 0 km, and a constant lower boundary of -50 km. The left top plot shows the input density difference, the top right plot shows the output density difference, and the bottom plot shows the difference between the two top plots.

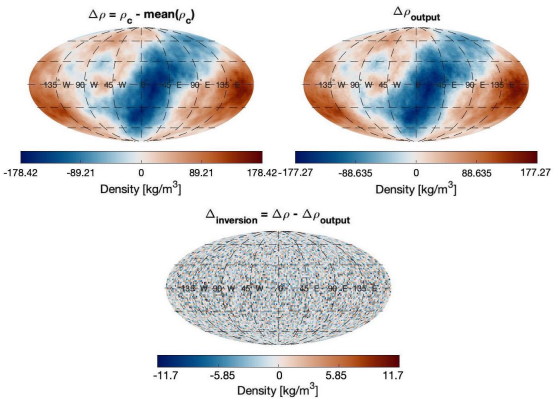

Figure 4.11: Inversion results Model 1 after multiple iterations. This model is a 50 km layer with varying density, a constant upper boundary of 0 km, and a constant lower boundary of -50 km. The left top plot shows the input density difference, the top right plot shows the output density difference, and the bottom plot shows the difference between the two top plots.

The results for the first model are given in Figure 4.10. In the top left figure, the input density variations are shown, and in the top right plot, the output density variations from the inversion are shown. In the bottom figure, the difference between the input and output density differences is given. When iterations were performed, no density pattern remained visible in the residual, as can be seen in Figure 4.11.

4.2.4. Model 2 - Varying Topography

The results for the second model are given in Figure 4.12. Visible is that larger errors occur when a varying topography is added. Visible in the residual is there still remain density patterns within the residual. Therefore, the iterative process, as explained in subsection 3.2.4, was introduced. The density result after iterations is shown in Figure 4.13. The residual is largely reduced, and no clear density patterns are visible anymore.

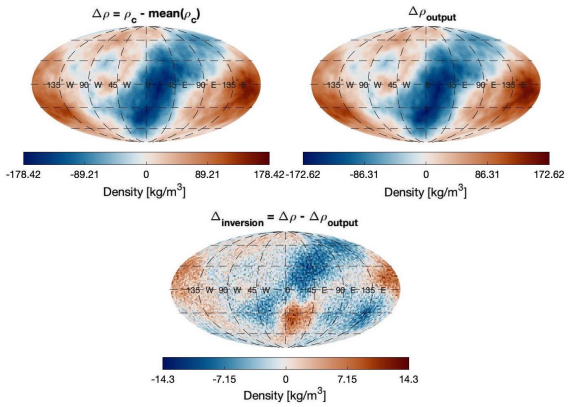

Figure 4.12: Inversion results Model 2. This model is approximately a 50 km layer with varying density, a varying upper boundary shown in Figure 4.8 and a constant lower boundary of -50 km. The left top plot shows the input density difference, the right top plot shows the output density difference, and the bottom plot shows the difference between the two top plots.

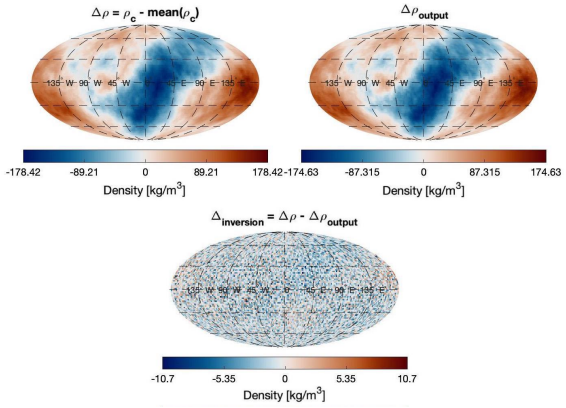

Figure 4.13: Inversion results Model 2 after multiple iterations. This model is approximately a 50 km layer with varying density, a varying upper boundary shown in Figure 4.8 and a constant lower boundary of -50 km. The left top plot shows the input density difference, the right top plot shows the output density difference, and the bottom plot shows the difference between the two top plots.

An extra study was performed on the effect of changing the topography on the residuals in the fit. These results are given in the Appendix. Ten different topography patterns were combined with twelve different density distributions, generated by varying the seed number of the Matèrn covariance function. This resulted in 120 different synthetic planets. Again, the iterative process was used. The standard deviation between the input tensor and inversion tensor is plotted in Figure A.1 against the RMS between the input density minus the inversion output density divided by the maximum input density. Visible on the y-axis is that after 3-4 iterations, a maximum percentile error of around 10% for model 2 was achieved. The percentile error of the RMS instead of the maximum of the density difference was used because after some iterations, polar errors occurred.

4.2.5. Model 3 - Varying Topography and Lower Boundary

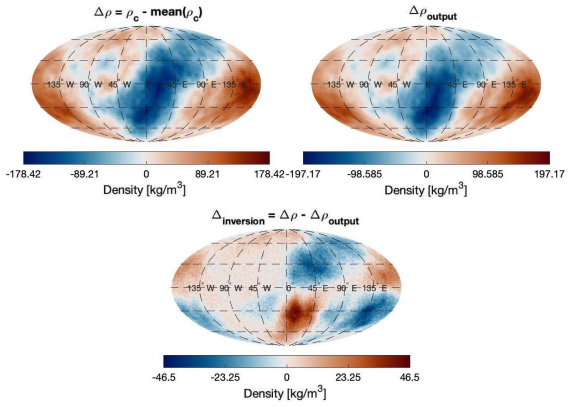

Figure 4.14: Inversion results Model 3. This model is approximately a 50 km layer with varying density, a varying upper boundary shown in Figure 4.8 and a varying lower boundary shown in Figure 4.9. The left top plot shows the input density difference, the right top plot shows the output density difference, and the bottom plot shows the difference between the two top plots.

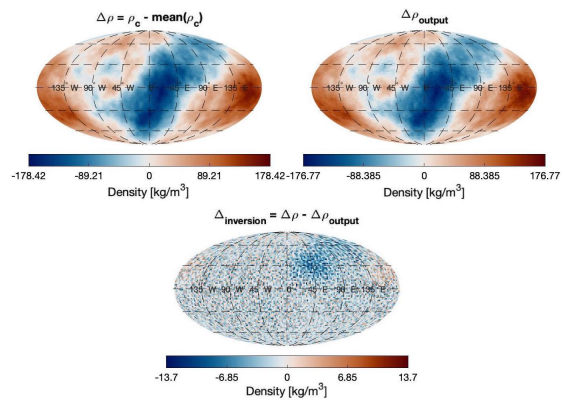

Figure 4.15: Inversion results Model 3 after multiple iterations. This model is approximately a 50 km layer with varying density, a varying upper boundary shown in Figure 4.8 and a varying lower boundary shown in Figure 4.9. The left top plot shows the input density difference, the right top plot shows the output density difference, and the bottom plot shows the difference between the two top plots.

The results for the third model are given in Figure 4.14. Similar to what was observed for model 2, is that for a single run of the inversion, there is still a large residual with clear density patterns. When multiple iterations were performed, the density converted to the input density, as can be seen in Figure 4.15. The residual is largely reduced, and no clear density patterns are visible anymore.

A similar analysis was performed for this model as for model 2, with 120 different synthetic one-layer planets,

again given in the Appendix. In Figure A.1 next to model 2, also the results of model 3 are plotted. When looking at the y-axis, it can be seen that after 3-4 iterations, a maximum percentile error of around 12% for model 3 was achieved.

4.2.6. One-Layer Inversion: $\lambda - \sigma$ Analyses

In this section, the optimal combinations of the ridge parameter, λ, and variance, σ^2 are studied. The ridge parameter is used for the Tikhonov regularization, as explained in subsection 3.2.2. The weights are dependent on σ as follows: $W = 1/\sigma^2$. This behavior is studied so that an understanding can be obtained of how this optimal combination behaves for different types of one-layer models. This understanding will help to choose an optimal combination of $\lambda - \sigma$ for the two-layer model later on.

As explained in subsection 3.2.2, the L-curve is one way to optimize the λ value when the results are unknown. For the synthetic planet, the results are known, but it is studied how the optimal λ value based on the L-curve corresponds to the optimal value based on the residuals. λ was varied from 10^{-1} to 10^{-8} and the σ value was set to $\sigma = 10^{-10}$. These results are given in the Appendix. When looking at the L-curve for varying the magnitude of the density variations, shown in Figure A.9, λ varied between 10^{-3} up to 10^{-5} for small to a large magnitude within the variations respectively. The seed number did not have an effect on the optimal λ value, with $\lambda = 10^{-4}$ yielding the optimal results, as visible in Figure A.12. The thicker the layer, the smaller the λ value, from $\lambda = 10^{-2}$ up to $\lambda = 10^{-5}$ for a 20 km to a 200 km layer, respectively, as can be seen in Figure A.3. When both the center of mass and the layer thickness were varied, as can be seen in the L-curve in Figure A.7, the optimal λ value of 10^{-4} was obtained. A more in-depth analysis is given in section A.2.

For the two-layer inversion, the layer will stretch from the topography up to a depth of 500 km. Therefore this can be compared to the analyses of varying both the CM-depth and the layer thickness, for which a ridge parameter value of $\lambda = 10^{-4}$ gave the optimal results. The ridge parameter is related to the value of σ, and therefore the weights. The relationship between σ and λ can be expressed with the following equation: $\sigma = \lambda^{0.5} \cdot 10^{-x}$ or $\lambda = \sigma^2 \cdot 10^{2x}$, with x to be chosen to optimize the inversion. This has to do with the relation between the weights, which is dependent on σ, and the ridge parameter λ. $W = \frac{1}{\sigma^2}$, which can be rewritten into $\sigma^2 = \frac{1}{W}$. The above relationship can therefore be can be rewritten to: $\frac{1}{W} = \lambda \cdot 10^{-2x}$ which, when rewritten again, results into the following relation: $\lambda W = 10^{2x}$.The general relation can be explained when looking at the equations for the Tikhonov regularization: $\hat{x} = \left(A^t P_{yy}^{-1} A + \lambda I\right)^{-1} A^t P_{yy}^{-1} \bar{y}$. In this equation $P_{yy}^{-1} = WI = \frac{1}{\sigma^2} I$, resulting into: $\hat{x} = \left(WA^t A + \lambda I\right)^{-1} WA^t \bar{y}$. Looking at the diagonal of the new moment matrix, it becomes clear that there is an optimal relation between λ and W. A λ value of 10^{-4} will from now be used for the inversion, but will be scaled based on σ, using the above equations.

4.3. Two-Layer Inversion

Next up, the robustness of the two-layer inversion is analyzed. As explained in subsection 3.2.5, there are three different types of input data that can be used: the gravitational potential, V, the gravitational vector in the z-direction, $\vec{g}_z$, or the gravitational tensor in the zz direction, T_{zz}. The use of the different types of input types starts to play an important role in the two-layer inversion because the different types are sensitive to radial density variations in a different manner. For the two-layer models, there is a mass that is contributed to the mantle and a mass that is contributed to the crust. Because of this, the analysis is performed to analyze which type of input data is optimal for the two-layer inversion. The analyses of these different input types are performed in the next subsection. For each of the inversions, a multiplication factor of 30 was used, and 25 iterations were performed. This was found to be the optimal combination. If a larger multiplication factor was used, the inversion diverged for multiple iterations. For a smaller multiplication factor, many more iterations were needed, increasing the run time.

4.3.1. Difference between Gravitational Potential, Vector, and Tensor

In this subsection, the inversion is performed for the three different input types. For each input data, the same input planet and reference model were used. The only differences between the inversions were the input data, the σ value, and the ridge parameter (λ). These different parameters are given in Table 4.1.

The difference between the density for the crust and mantle, obtained using the inversion, and the input crustal and mantle densities are shown in Figure 4.17 for V, $\vec{g}_z$, and T_{zz} as input data for the inversion. Visible is that using the gravitational potential as input data yields the largest differences and some small wavelength patterns

which are still present. This is also visible in the power spectrum, shown in subplot (a) of Figure 4.16. In this plot, the power spectrum of the inversion model only fits the input power spectrum up to approximately spherical harmonic degree 15, which is only a few degrees more than the power spectrum of the reference model. The density differences are shown in subplot (b) of Figure 4.16, which are obtained using the gravitational vector in the z-direction as input data for the inversion, show that there are still some small wavelength differences visible, but the overall difference is much smaller. This is also visible in the power spectrum, subplot (c) of Figure 4.16, where the spectrum of the inversion planet fits the input spectrum up to approximately spherical harmonic degree 30, which is almost 20 degrees higher than the spectrum of the reference planet.

Table 4.1: The different input parameters used in the inversion, for the 3 different types of input data.

Gravitational potential V	Gravitational vector $\vec{g}_z$	Gravitational tensor T_{zz}
$\sigma = 10\ [J]$	$\sigma = 10^{-5}\ [m/s^2]$	$\sigma = 10^{-11}\ [E]$
$\lambda = 100$	$\lambda = 100$	$\lambda = 1000$

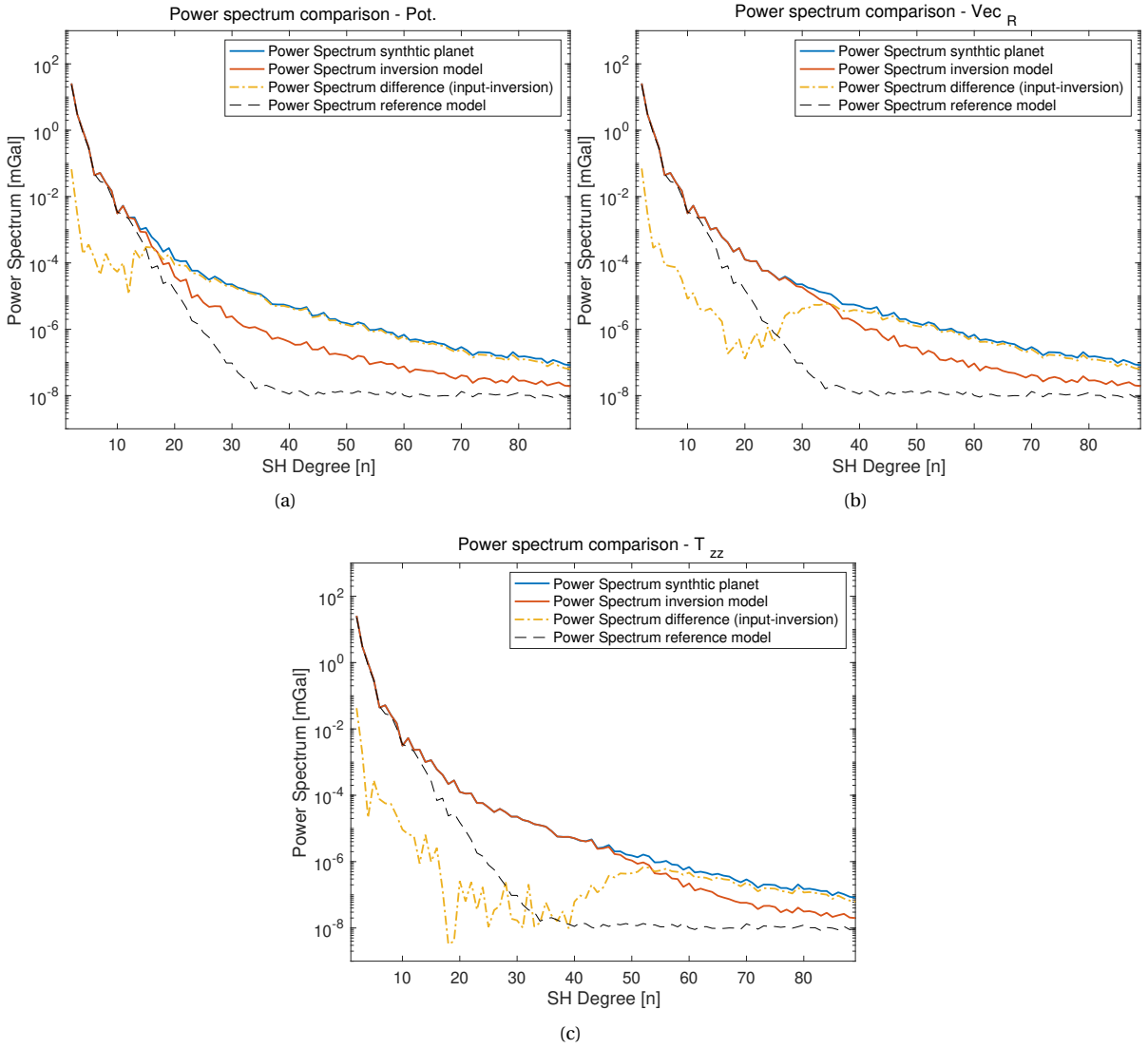

Figure 4.16: The power spectrum of the inversion planet obtained using the reference planet with the densities changed to the densities obtained from the inversion. Subplot (a) shows the results using the gravitational potential as input data for the inversion, (b) for the gravitational vector in the z direction, and (c) for the gravitational tensor in the zz direction.

The best overall fit of the power spectrum was obtained using the gravitational tensor in the zz direction as input data. The density differences for this input data are shown in subplot (c) of Figure 4.17 and the power spectrum is shown in subplot (c) of Figure 4.16. The power spectrum plot shows that the spectrum of the inversion model

fits the input power spectrum up to approximately spherical harmonic degree 50. This is also visible in subplot (c) of Figure 4.17, where small density patterns are visible. In subplot (c) of Figure 4.17 there also remains a long wavelength signal, which corresponds to the long wavelength signal of the input density pattern, as shown in Figure A.16. This residual was reduced when more iterations were performed, as can be seen in Figure A.18.

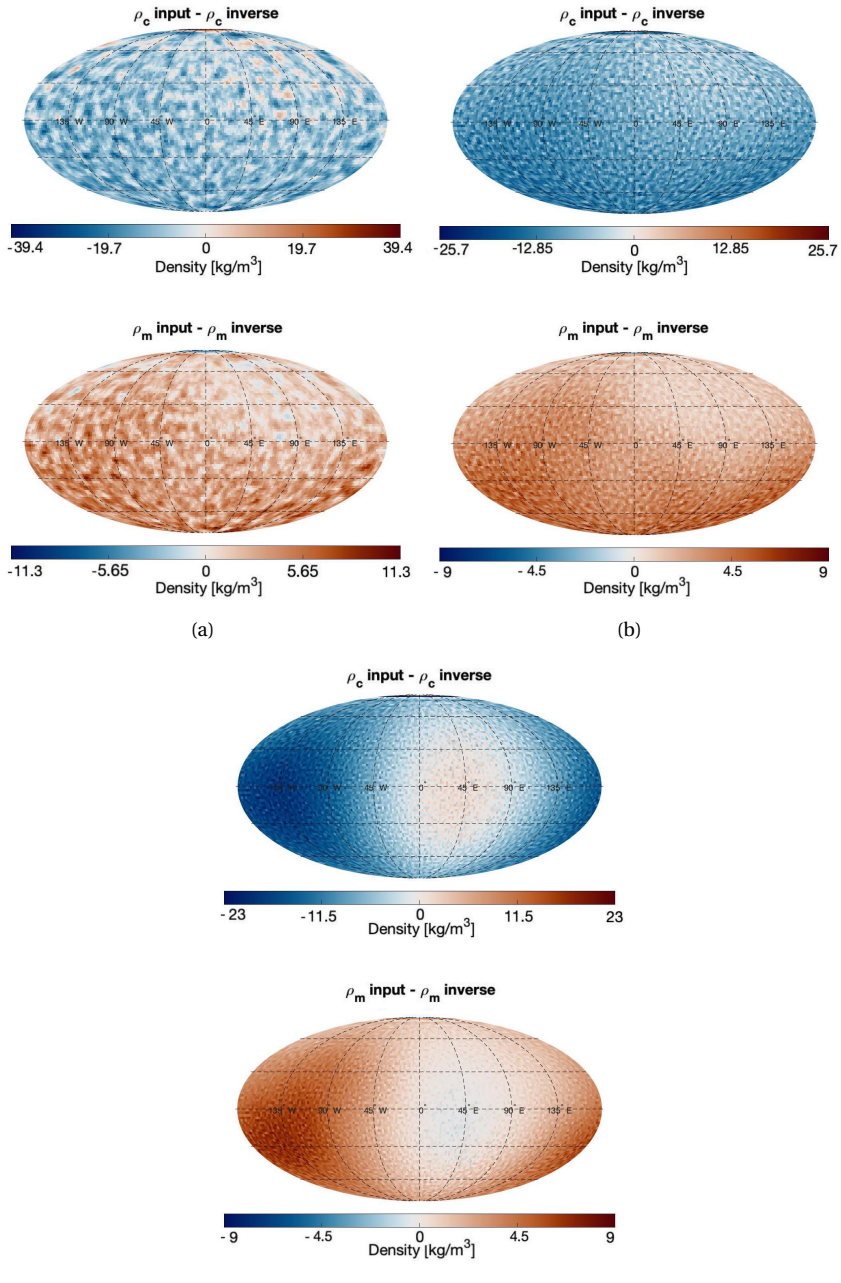

Figure 4.17: For each subplot, the top plot shows the difference between the input crustal density, ρ_c input, and the crustal density obtained using the inversion method, ρ_c inverse. The bottom plot shows the same plot, but for the mantle density instead of the crustal density. Subplot (a) shows the results using the gravitational potential as input data for the inversion, (b) for the gravitational vector in the z direction, and (c) for the gravitational tensor in the zz direction.

For these results, 25 iterations were performed. It could be possible that the inversion converges faster or slower, depending on the input type used. Therefore, the number of iterations was increased to 50 iterations to analyze how the different input types converge. The results after 50 iterations are given in section A.3. Similar behaviors for the three different input types were found. The power spectrum for all input types was fitted slightly better, around 5 SH degrees, but the gravitational tensor in the zz direction still fitted the power spectrum up to the highest SH degree.

5

Power Spectrum and Two-Layer Results

In this chapter, the power spectrum and two-layer model will be analyzed. In the first section the effect of changing different parameters of the synthetic planet on the power spectrum will be given. In the next section the effect of changing different parameters of the reference model, on the inversion density results are given.

5.1. Power Spectrum Analysis for Varying Input Variables

In this section, the influence of varying the density and topography of the synthetic planet on the power spectrum is studied. When the inversion is performed for Mars, the power spectrum of both the input gravity, as well as the power spectrum of the obtained reference planet, will be plotted. This analysis can be used later on when differences between the reference power spectrum and input power spectrum are observed to analyze what might cause the difference.

To be able to study the effect of changing a specific input parameter on the power spectrum, the remaining input parameters were kept constant. The parameters used for the topography of these planets are set to the following default values $\sigma = 9$ km, $\kappa = 0.6$, and $\epsilon = 10$, when not analyzed. An average topographic altitude of 3.6 km was used, with an average crustal thickness, c, of 125 km and a compensation depth of 500 km. The default values for the parameters the Matèrn covariance matrix used for the lateral density variations of the crust are set to: $\sigma = 100$ kg/m^3, $\kappa = 0.6$, and $\epsilon = 10$, when their effect was not studied. A (mean) density for the crust of 2900 kg/m^3 and a (mean) density for the mantle of 3500 kg/m^3 are used. A set seed is defined for the random number generator of the Matèrn covariance function. The seed of the crustal density variations was set to 2, and for the mantle density variations, the seed was set to 4.

5.1.1. Synthetic Planets

Different synthetic planets will be created, based on the Airy isostasy model, and the thin shell model. Three different planets will be analyzed based on Airy isostasy, and one planet will be analyzed based on the thin shell model. These models are:

- **Airy1**
  A two-layer model based on Airy isostasy with two uniform density layers. The topography for this model will be created using the Matèrn covariance function, explained in subsection 3.1.1.

- **Airy2**
  A two-layer model based on Airy isostasy with lateral density variation in both the crust and the mantle. The density variation will be correlated between the crust and the mantle, so that every column has an equal mass. The density of the mantle layer can be calculated using Figure 5.1. Each column needs to have an equal mass, from which the following equation can be obtained:

$$c\rho_{c,1} + (D_c - c)\rho_{m,1} = (h + c + b)\rho_{c_2} + (D_c - c - b)\rho_{m,2}. \tag{5.1}$$

  Rewriting this equation gives the following equation, from which the mantle density of the second column can be calculated.

$$\rho_{m,2} = \frac{c\rho_{c,1} + (D_c - c)\rho_{m,1} - (h + c + b)\rho_{c_2}}{D_c - c - b} \tag{5.2}$$

The topography and the crustal density variations for this model will be created using the Matèrn covariance function.

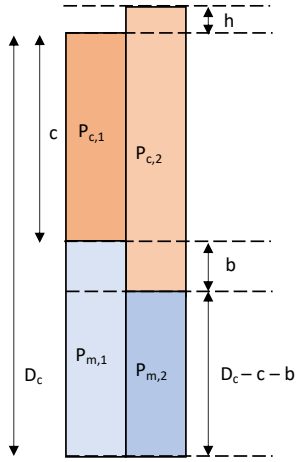

Figure 5.1: Airy for lateral density variations within the crust and mantle, now referred to as Airy2.

- **Airy3**
  This model will be similar to Airy2, also a two-layer model based on Airy isostasy with lateral density variation in both the crust and the mantle. But now, instead of a full correlation between the crustal and mantle density, there is a slight variation. This results in slight mass differences between each column.

  The topography, as well as the crustal density variations for this model, will be created using the Matèrn covariance function. The density difference in the mantle is created by adding an extra density layer, also created using the Matèrn covariance function.

- **TSM1**
  A two-layer model based on the thin shell model with two uniform density layers. The topography for this model will be created using the Matèrn covariance function.

5.1.2. Crustal Thickness Variations

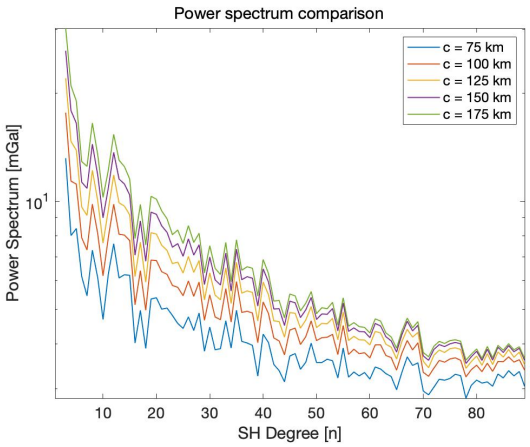

Figure 5.2: The power spectrum plotted for different values of average crustal thickness, c, for the synthetic planet Airy1.

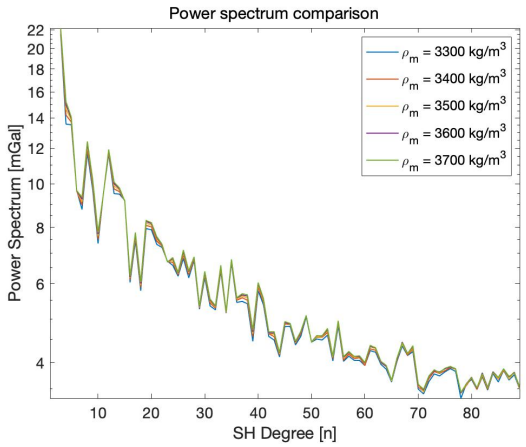

Figure 5.3: The power spectrum plotted for varying density differences between the crust and the mantle, $\Delta\rho$, for the synthetic planet Airy1. The crustal density was set to 2900 kg/m^3. This resulted into density variations between 400 and 800 kg/m^3.

The crustal thickness can be changed using two input parameters: by changing the average crustal thickness, c, or by changing the density difference between the crust and the mantle, $\Delta\rho$. Changing c will result in an increase or decrease of the whole crustal thickness while changing $\Delta\rho$ will enlarge the differences within the crustal thickness. In Figure 5.2 different power spectra are plotted for varying crustal thickness. Visible is that the thicker the crustal thickness, the higher the power spectrum. When the crustal thickness is increased, the topography becomes more dominant within the spectrum. This is because the compensation is lower within the crust. When the crust is infinitely thick, there would be no compensation, and the spectrum would be represented by the topography. If the crust were infinitely thin, the spectrum would be fully compensated. This effect is visualized in Figure 5.4. In this plot, the power spectrum of only the topography and the spectrum for a synthetic planet with a crust of 3380 km, which is almost equal to the planet's radius, is shown. Visible is that the power spectra closely approximate each other. In Figure 5.3 the different power spectra are plotted for varying density differences between the crust and mantle. This is done by changing the mantle density but keeping the crustal density constant. Visible is that the larger the density difference, the higher the spectrum for specific spherical harmonic degrees. When the density difference is increased, the differences in thickness within the crust decrease. Increasing the mantle density, and, therefore, the density difference, result in smaller thickness differences within the crust. This results in the topography being compensated closer to the average crustal thickness. This means that the negative topographic features will be compensated deeper in the mantle, while the positive topographic features will be compensated less deep in the mantle. Some spherical harmonic degrees will therefore be better, or worse, compensated, resulting in the shift for some spherical harmonic degrees.

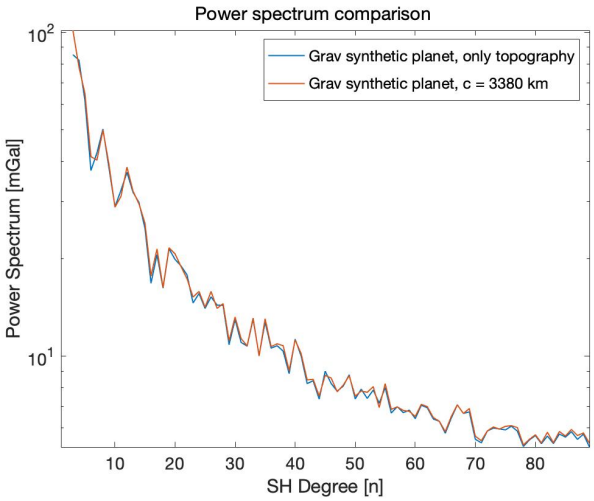

Figure 5.4: The power spectrum plotted for only the crust of the synthetic planet and for a planet with a crust of 3380 km.

5.1.3. Input Parameters Matèrn Covariance Function of the Topography

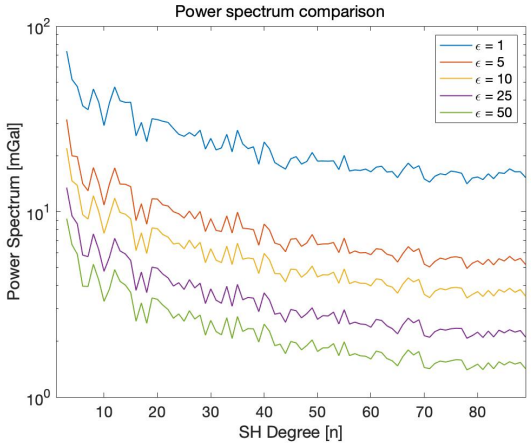

Figure 5.5: The power spectrum plotted for different values of the decorrelation distance, ϵ, for the synthetic planet Airy1.

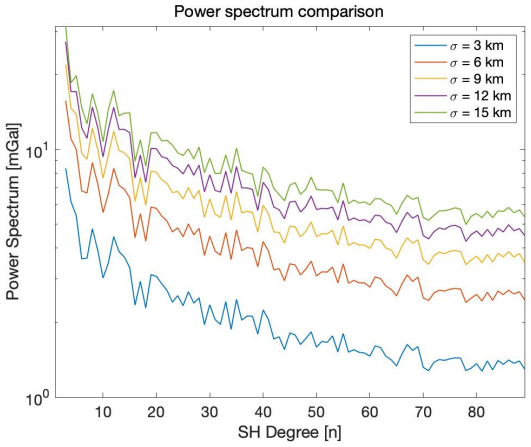

Figure 5.6: The power spectrum plotted for different values of the square-root of the variance, σ, for the synthetic planet Airy1.

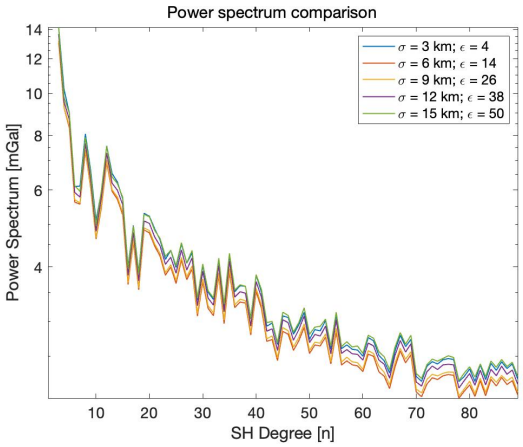

Figure 5.7: The power spectrum plotted for different values of the square-root of the variance, σ, and the for the decorrelation distance, ϵ, for synthetic planet Airy1.

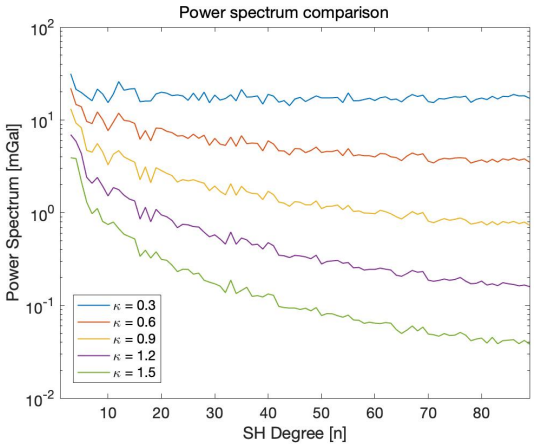

Figure 5.8: The power spectrum plotted for different values of the smoothness parameter, κ, for the synthetic planet Airy1.

The studied input parameters of the Matèrn covariance function of the topography are the decorrelation distance, ϵ, the variance, σ^2 and the smoothness parameter, κ, which can be seen as a measure of the smoothness around the origin. In Figure 5.5 the effect of changing ϵ on the power spectrum is visible. It can be seen that the larger ϵ, the lower the overall power spectrum. Increasing ϵ decreases the minimum and maximum altitude of the topography. Therefore smaller values of ϵ will result in larger differences within the crust-mantle boundary, which results in the deepest compensation of the topography being compensated lower up in the planet. This is visible in Figure 5.9. The power spectrum will therefore become smaller for larger values of ϵ. Another input parameter is the variance, σ^2. Increasing the variance means increasing the altitude differences within the topography, resulting in the power spectrum shifting up for increasing variance, as is visible in Figure 5.6. σ and ϵ seem to have an opposite effect on the power spectrum. To test this, both input parameters were varied, as is plotted in Figure 5.7.

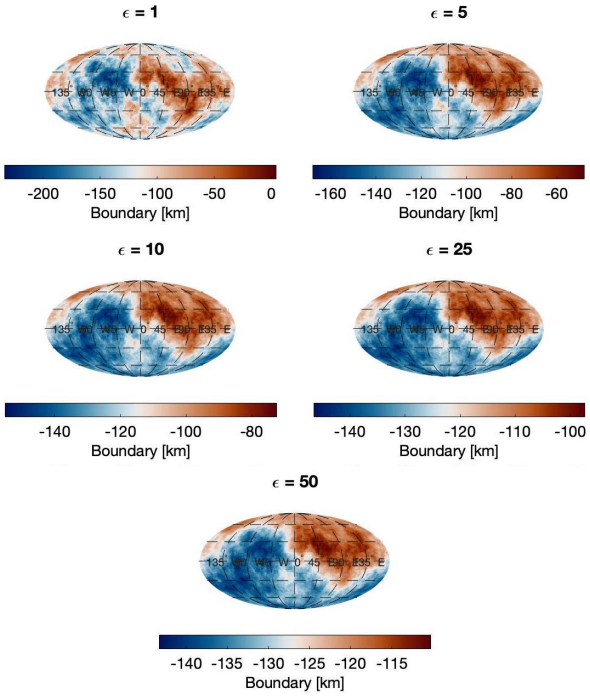

Figure 5.9: The effect of changing the input parameter ϵ of the Matèrn covariance function on the crust-mantle boundary. From the left to right, and top to bottom, these plots are obtained using $\epsilon = 1$, $\epsilon = 5$, $\epsilon = 10$, $\epsilon = 25$, and $\epsilon = 50$.

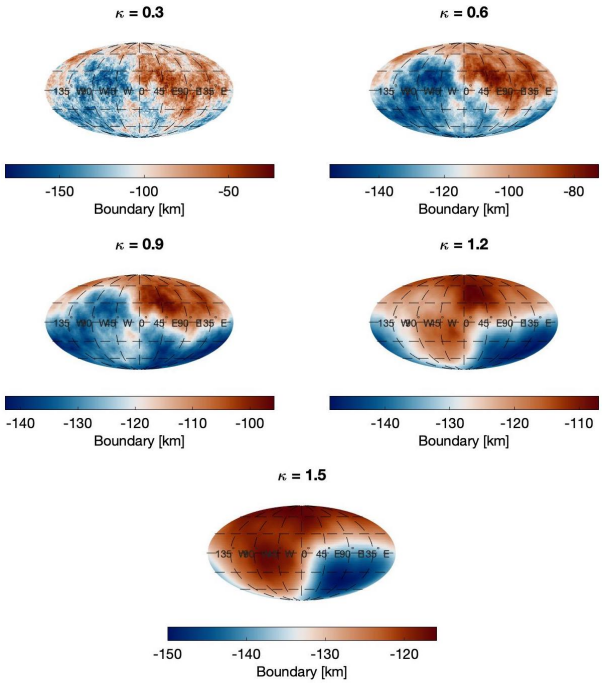

Figure 5.10: The effect of changing the input parameter κ of the Matèrn covariance function on the crust-mantle boundary. From the left to right, and top to bottom, these plots are obtained using $\kappa = 0.3$, $\kappa = 0.6$, $\kappa = 0.9$, $\kappa = 1.2$, $\kappa = 1.5$.

Visible is that when both are varied. Their effects are opposite, and therefore, almost canceled out when a correct

relation is used. This is an almost linear relation of $\epsilon = 4\sigma - 10$. A relation between σ and ϵ is expected, when looking at the effect in Figure 5.9. Larger values for ϵ result in smaller boundary variations. When σ is increased, these boundary variations are again increased.

The last analyzed input parameter is κ, with its behaviour shown in Figure 5.8. The larger κ, the larger the wavelength pattern of the crust and the smaller the altitude differences in the topography. This effect is visible in Figure 5.10. Therefore, the larger κ, the lower the power spectrum. Another phenomenon visible in Figure 5.8 is that for larger values of κ, the power spectrum for the smaller SH degrees decreases much less compared to the larger SH degrees. This is because when κ is increased, the wavelength pattern of both the topography and the crust mantle is increased.

5.1.4. Density Variations of the Mantle

Varying the density within the mantle can be achieved by altering different parameters of the Matèrn covariance function of the crustal density. First, κ is changed, which influences the wavelength pattern. The higher κ for the crustal density, the longer the wavelength features of the density pattern within both the crust and mantle. The effect of changing κ on the power spectrum is shown in Figure 5.11. When κ is increased, the power spectrum moves down slightly, but for κ values larger than 0.6, the power spectrum stays almost the same. κ has a similar effect on the density variations as on the crust-mantle boundary shown in Figure 5.10. Therefore, the larger κ, the smaller the density variations, and the longer the wavelength patterns within these variations. The power spectrum, therefore, moves down for increasing values of κ. When the density variations are very large and show small wavelength patters, these variations are not fully compensated, increasing the power spectrum especially for the larger SH degrees. For values of κ larger than 0.6, these variations can be compensated and further changes have no clear effect on the power spectrum.

Another way to vary the density within the mantle is by changing the variance of the Matèrn covariance function. This results in higher or lower density variations within the mantle. The effect of this on the power spectrum is shown in Figure 5.12. Visible is that overall, the higher the density difference within the mantle, the higher the spectrum, which means that the topography is compensated less.

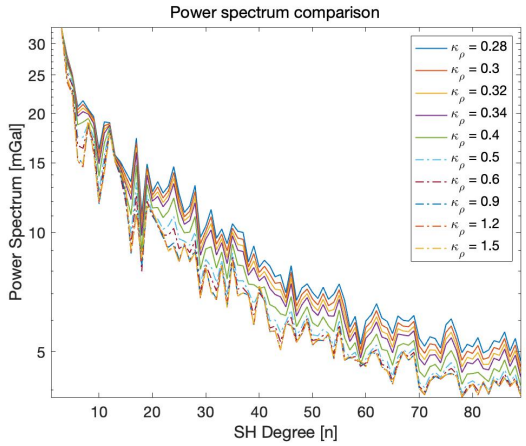

Figure 5.11: The power spectrum plotted for different values of the smoothness parameter for the density, κ, for the synthetic planet Airy2.

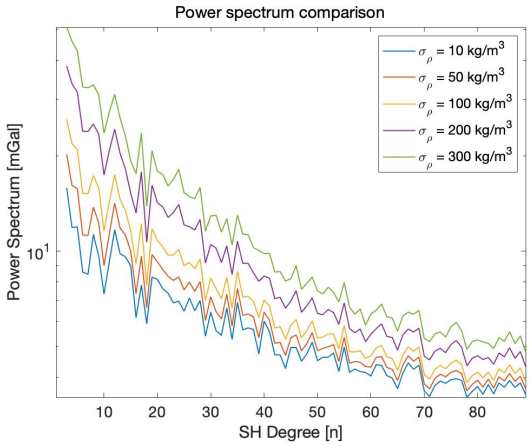

Figure 5.12: The power spectrum plotted for varying density differences within the crust, by changing σ, for the synthetic planet Airy2.

5.1.5. Mass Variations between columns

In this section the result of not fully correlating the mantle density and crustal density is studied, such that there is a mass variations between the different columns. Visible in Figure 5.13 is that for small increases in mass differences between the columns, the spectrum is better compensated for the larger SH degrees. To vary the mass of the different columns, extra density is added/subtracted to/from the mantle. The added/subtracted density has a similar pattern to the mantle density. Therefore for small changes, because the compensation takes place deeper inside the mantle, extra mantle density seems to compensate the crust better for the smaller wavelengths. When the added density results in an increase of the column mass above 15%, this effect seems to disappear, as is visible in Figure 5.14. This is to be expected because there is less compensation of the crust, resulting in an increase in the power spectrum. This effect is also only the case for the larger SH degrees and not for the smaller SH degrees.

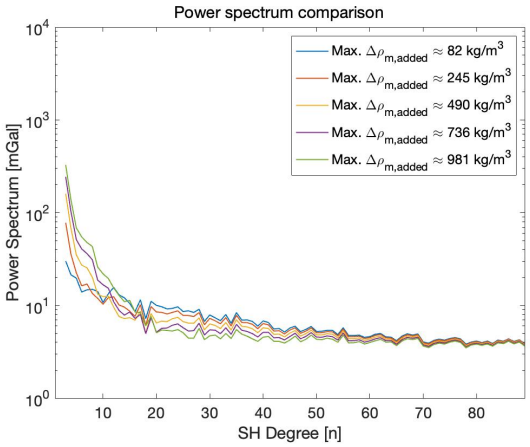

Figure 5.13: The power spectrum plotted for variations within both the crust and the mantle, with mass differences between the columns, plotted for the synthetic planet Airy3.

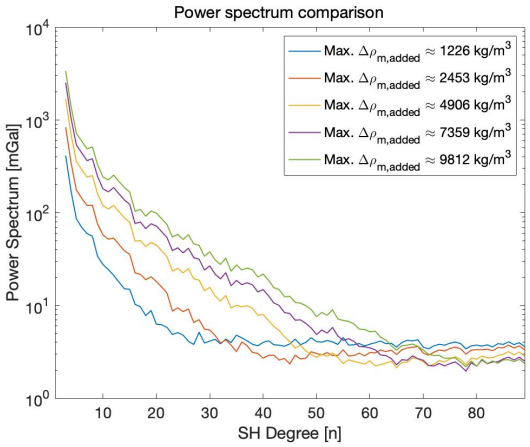

Figure 5.14: The power spectrum plotted for variations within both the crust and the mantle, with mass differences between the columns, plotted for the synthetic planet Airy3.

5.1.6. Input Parameters of the Flexural Response Function

In this section, the effect of changing the input parameters of the flexural response function on the power spectrum is studied. These input parameters are the elastic thickness, T_e, the Poisson ration, ν, and the Elastic modulus, E.

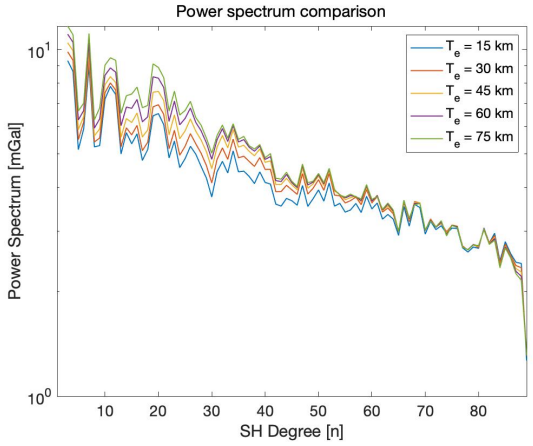

Figure 5.15: The power spectrum plotted for different values of the elastic thickness, T_e, for the synthetic planet TSM1.

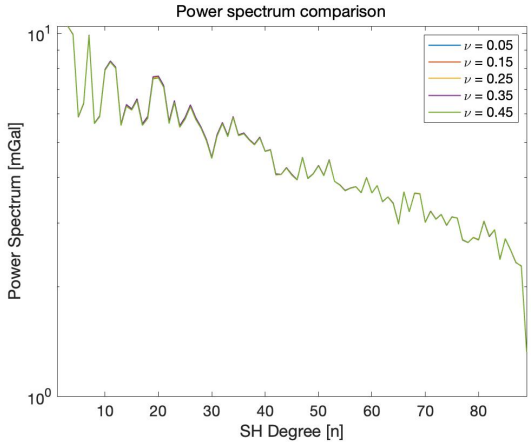

Figure 5.16: The power spectrum plotted for different values of the Poisson ratio, ν, for the synthetic planet TSM1.

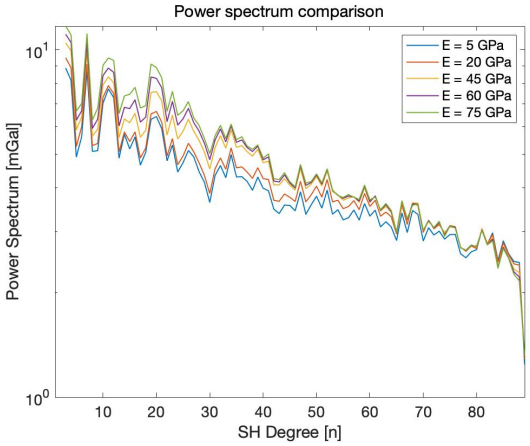

Figure 5.17: The power spectrum plotted for different values of the elastic modulus, E, for the synthetic planet TSM1.

The effect of changing T_e on the power spectrum is shown in Figure 5.15. The smaller T_e, the higher the power spectrum. The flexural response function is plotted in Figure 2.5. In this figure it is visible that for small values of T_e, around 10 km, the flexural response function stays close to 1, up to around spherical harmonic degree 30. The larger the spherical harmonic degree, the earlier the flexural response function drops off for increasing spherical harmonic degrees. Small wavelength features are represented by the large spherical harmonic degrees. Therefore, the thicker the elastic thickness, the less the smaller wavelength features are compensated. As visible in Figure 5.15, the power spectra start to deviate a lot for the smaller spherical harmonic degree and start to converge towards each other again for the higher spherical harmonic degrees. This has to do with the fact that after a certain spherical harmonic degree, the flexural response function has dropped to 0 for all values of T_e, resulting in no compensation of the topography. Therefore, for the larger spherical harmonic degrees, the topography signal becomes dominant again. In Figure 5.17 the effect of changing the Elastic modulus, E, on the power spectrum is plotted. Visible is that these results are very similar to those of the elastic thickness. This has to do with the fact that both E and T_e have a similar effect on the flexural response function of the thin shell model given in Equation 2.11. In Figure 5.16 the effect of changing the Poisson ratio, ν, is visible. It can be seen that varying this parameter has close to no influence on the power spectrum.

When looking at the equation for rigidity, $D = \frac{ET_e^3}{12(1-\nu^2)}$, increasing D would result into an upward shift of the power spectrum. Both the elastic thickness and Young's modulus are in numerator, therefore increasing their effects. The Poisson ratio is in the denominator, but showed no effect on the power spectrum. Therefore, similar effects will be seen for variations in the rigidity as for variations in both T_e and E.

5.2. Two-Layer Inversion

In this section the synthetic planet results will be analyzed, while the Martian two-layer inversion results are given in chapter 6. Also, the effect of adding deep mantle density variations is studied, as well as the effect of variations in input parameters of the reference model is studied. Lastly, the effect of adding additional mass to the crust and mantle is studied.

5.2.1. Inclusion of Deeper Mantle Density Variations

The used synthetic planets are two-layer planets, up to a depth of 500 km. It is assumed that beneath a depth of 500 km, the mantle has a uniform density. This assumption may not be realistic, so, therefore it is studied what the effect is when density differences are added to the deeper mantle from a depth of 500-1800 km. Because the different types of input data are affected differently by deep mantle density variations, the inversion is performed again for the gravitational potential, gravitational vector in the z direction, and the gravitational tensor in the zz direction.

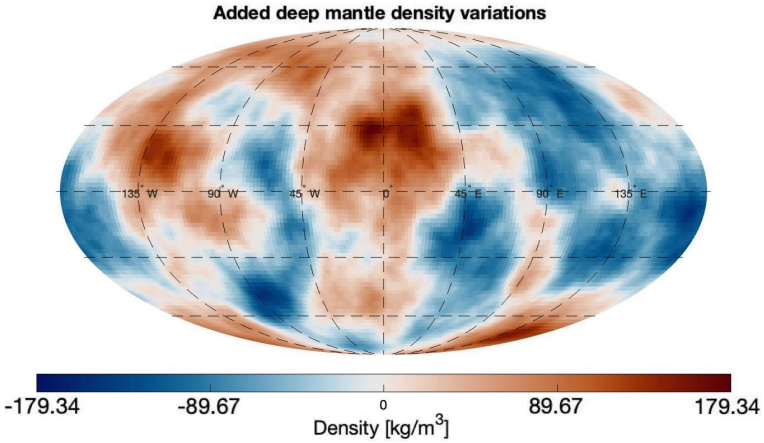

Figure 5.18: The density variations which were added to the two deep mantle layers from a depth of 500 km up to the depth of 1800 km.

The deep mantle was split into two different layers with different mean densities. From a depth of 500 km up to 1100 km, a mean density of 3700 kg/m^3 was used. From a depth of 1100 up to 1800 km, a mean density of 4000 kg/m^3 was used. The same density variations were used for these two-layers, shown in Figure 5.18.

When the density variations shown in Figure 5.18 were used, the obtained densities for both the crust and man-

tle diverged, yielding highly unrealistic results. Because of this, only 10% of the density variations in Figure 5.18 were used, to be able to study the effect of small density variations in the deep mantle. This resulted in similar differences between the obtained densities through the inversion and those of the synthetic planet for the three different input data types. These differences are shown in Figure 5.19. The magnitude of these differences is similar between the different data types. There are some differences visible in the wavelength pattern of these differences, with the gravitational potential yielding more short wavelength differences and the gravitational tensor yielding almost only long wavelength patterns.

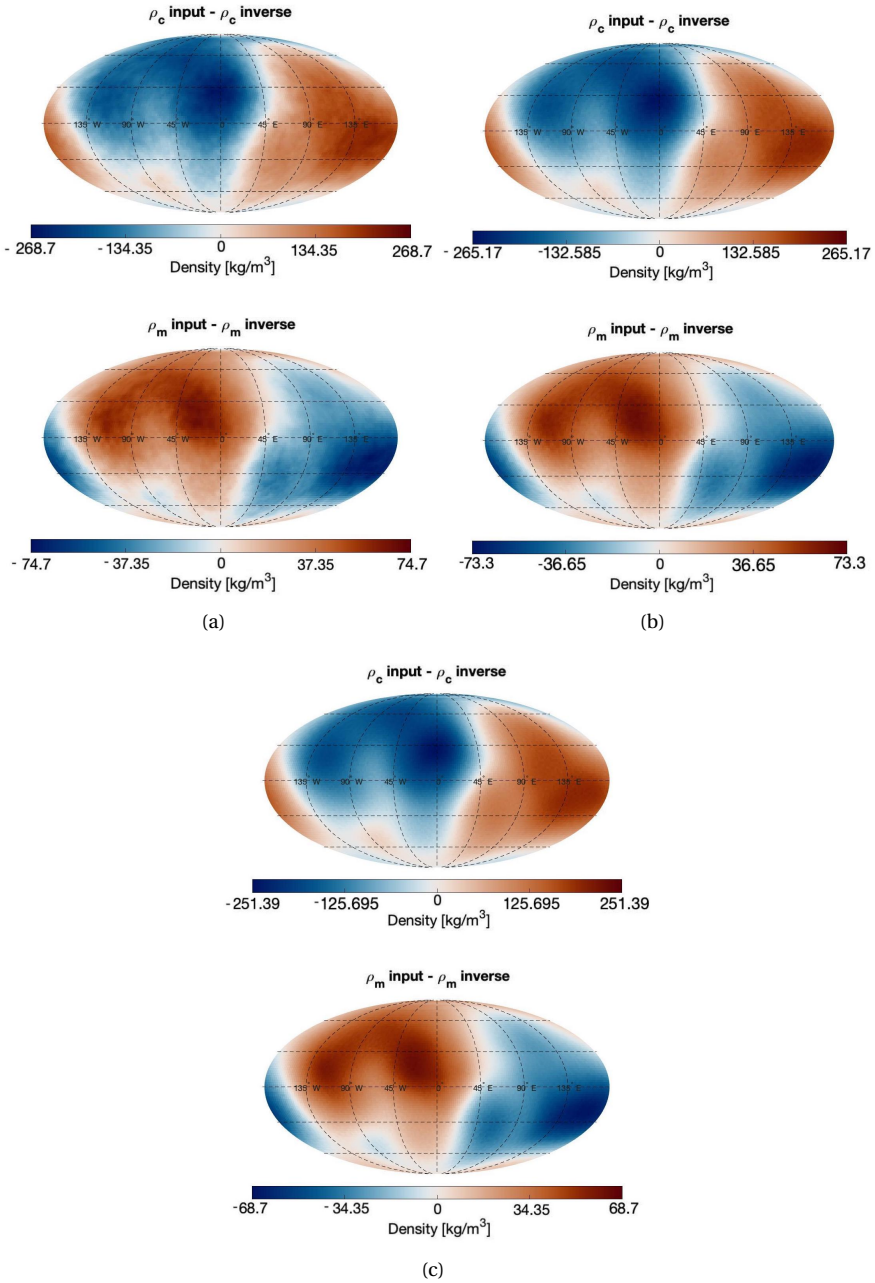

Figure 5.19: For each subplot, the top plot shows the difference between the input crustal density, ρ_c input, and the crustal density obtained using the inversion method, ρ_c inverse. The bottom plot shows the same plot, but for the mantle density instead of the crustal density. Deep mantle density variations were added to the input model reference planet. Subplot (a) shows the results using the gravitational potential as input data for the inversion, (b) for the gravitational vector in the z direction, and (c) for the gravitational tensor in the zz direction.

The main residual visible for all three input types, is the long wavelength pattern. This pattern corresponds the the long wavelength signal of the density variations shown in Figure 5.18. The density variations which occur in the mantle are of the order of approximately 4 times that of the input density variations in the deep mantle. The obtained density variations of the crust are inversely correlated to those used as input in the deep mantle.

The power spectra for the different data types, with the addition of deeper mantle density variations, yielded similar results for the different input data types as shown in Figure 4.16. Because of this, the gravitational tensor in the zz direction will now be used as data type for the input data for the remaining of this study. It as well shows that T_{zz} is the best type of input data for the analysis of the density variations within Mars. This has to do with the fact that it is not known whether the assumption that there are no lateral density variations within the deeper mantle holds.

5.2.2. Variation in Reference Model Input Parameters

In this section, the effect of varying the different input parameters for the reference model is studied. These different input parameters are: the crustal density ($\rho_{\text{c,ref}}$), the mantle density($\rho_{m,ref}$), the elastic thickness (T_e), the Young's modulus (E) and the crustal thickness (C). In section A.4 the crustal en mantle densities are plotted, for the limit case of each parameter.

In subplot (a) of Figure 5.20, the effect of varying the crustal density of the initial reference model is shown. Visible is that when an initial crustal density is larger than 5% of the mean density of the synthetic planet, the inversion diverges. For densities smaller than 95% of the mean density of the synthetic planet, the crust-mantle boundary becomes dominant in the inversion results for the density of both the crust and mantle. For $0.95 \cdot \text{mean}(\rho_{\text{c,input}}) < \rho_{\text{c,ref}} < 1.05 \cdot \text{mean}(\rho_{\text{c,input}})$ the inversion results yield some converted results, from which the original density profile could be obtained within a 50% error, with $\frac{\max(\Delta\rho_{\text{inp}} - \Delta\rho_{\text{inv}})}{\max(\Delta\rho_{\text{inp}})} < 50\%$. Both of these limit cases are plotted in Figure A.20.

In subplot (b) of Figure 5.20, the effect of varying the mantle density of the initial reference model. A similar, but opposite, behavior to the crustal density is visible, with too small initial mantle densities for the reference model resulting into the inversion to diverge. But when a too large initial density for the mantle was used in the reference model, $\frac{\max(\Delta\rho_{\text{inp}} - \Delta\rho_{\text{inv}})}{\max(\Delta\rho_{\text{inp}})} < 50\%$ for $\rho_{m,ref}$ up to $1.4 \cdot \text{mean}(\rho_{m,input})$. The average mantle density of the reference model can therefore vary from $0.95 \cdot \text{mean}(\rho_{m,input}) < \rho_{m,ref} < 1.4 \cdot \text{mean}(\rho_{m,input})$. The densities of these two limit cases are plotted in Figure A.21.

In subplot (c) and (d) of Figure 5.20, the effect of variations in elastic thickness, T_e, and Young's modules, E, on the inversion results are shown. Previously it was already shown that varying T_e and E yielded similar effects on the power spectrum of a planet. Visible in these figures is also that they yield almost the same results, with varying T_e only resulting into slightly larger differences. Varying T_e and E has an effect of the crust-mantle boundary of the reference model, varying from that of the synthetic planet. For $0.1 \cdot T_{e,input} < T_{e,ref} < 2 \cdot T_{e,input}$ as well as $0.1 \cdot E_{input} < E_{ref} < 2 \cdot E_{input}$ reasonable results were still obtained with $\frac{\max(\Delta\rho_{\text{inp}} - \Delta\rho_{\text{inv}})}{\max(\Delta\rho_{\text{inp}})} < 50\%$. When T_e and E were varied more, the variations in crust mantle boundary became dominant in the inversion. The densities of the two limit cases for T_e are plotted in Figure A.22, and for E in Figure A.23.

Lastly, varying the crustal thickness of the reference model was analyzed, shown in subplot (e) of Figure 5.20. The density pattern could already be obtained from $C_{ref} > 0.6 \cdot C_{input}$, but the magnitude of the density variations in the mantle and crust were quite larger, with $\frac{\max(\Delta\rho_{\text{inp}} - \Delta\rho_{\text{inv}})}{\max(\Delta\rho_{\text{inp}})} \approx 50\%$ for $C_{ref} = [0.6; 0.7; 0.8] \cdot C_{input}$. When the crustal thickness was increased above that of the synthetic planet, with $C_{ref} > 1.1 \cdot C_{input}$, the inversion blew up. Variations up to this increase yielded results with $\frac{\max(\Delta\rho_{\text{inp}} - \Delta\rho_{\text{inv}})}{\max(\Delta\rho_{\text{inp}})} < 50\%$, as can be seen for the densities plotted in Figure A.24.

These analyses will be used to optimize the input parameters for the reference model of Mars. The effects which are observed by varying the input parameters of the reference model of Mars, will be compared to the effects found in this analysis. Based on the similarities, the reference model input parameters can be analyzed and discussed.

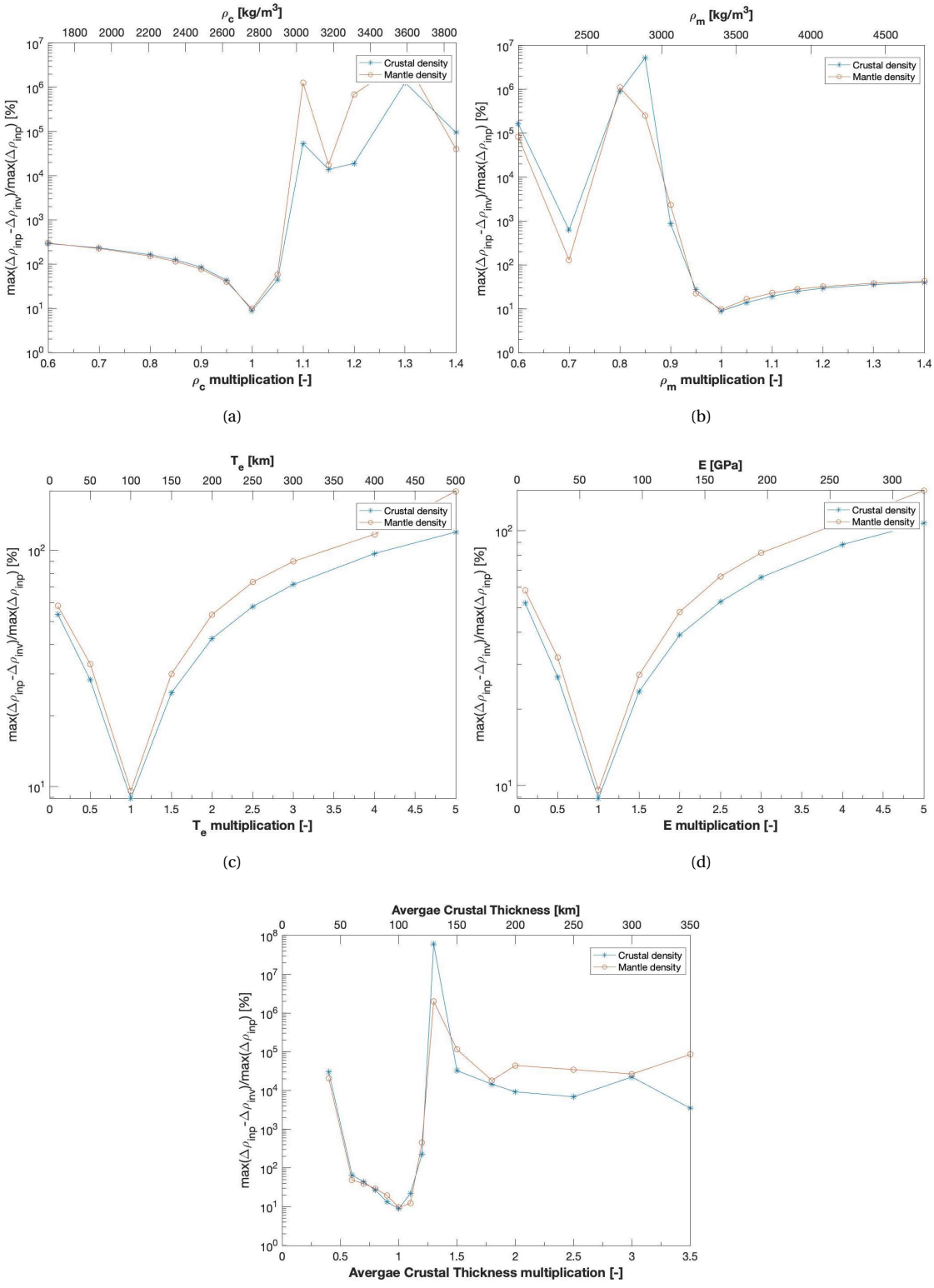

Figure 5.20: The effect of changing multiple input parameters for the reference model, on the obtained crustal and mantle density from the inversion. F0r subplot (a), the crustal density is varied, for (b), the mantle density is varied, for (c) the elastic thickness is varied, for (d), the Young's modulus is varied, and for (e), the average crustal thickness is varied.

5.2.3. Influence of Additional Crustal Mass

One of the assumptions that are made in this research is that each column has the same mass. This assumption is one of the assumptions that is required to be able to calculate the crust-mantle boundary using isostasy and to conclude that at a certain "depth of compensation", the pressure from each column is the same.

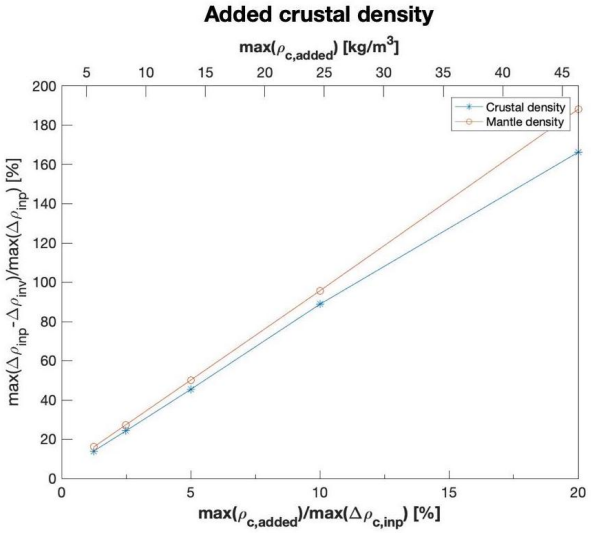

Figure 5.21: Effect of adding extra density variations to the crust of the synthetic planet.

In Figure 5.21 it can be seen that there is for both the crust and mantle a near-linear relation between the maximum added density variations to the crust and the maximum percentile error between the input density variations and the the density variations from the inversion results. This linear relation is approximately: $\frac{\max(\Delta\rho_{\text{inp}}-\Delta\rho_{\text{inv}})}{\max(\Delta\rho_{\text{inp}})} \approx 9 \cdot \max(\rho_{\text{c,added}})$.

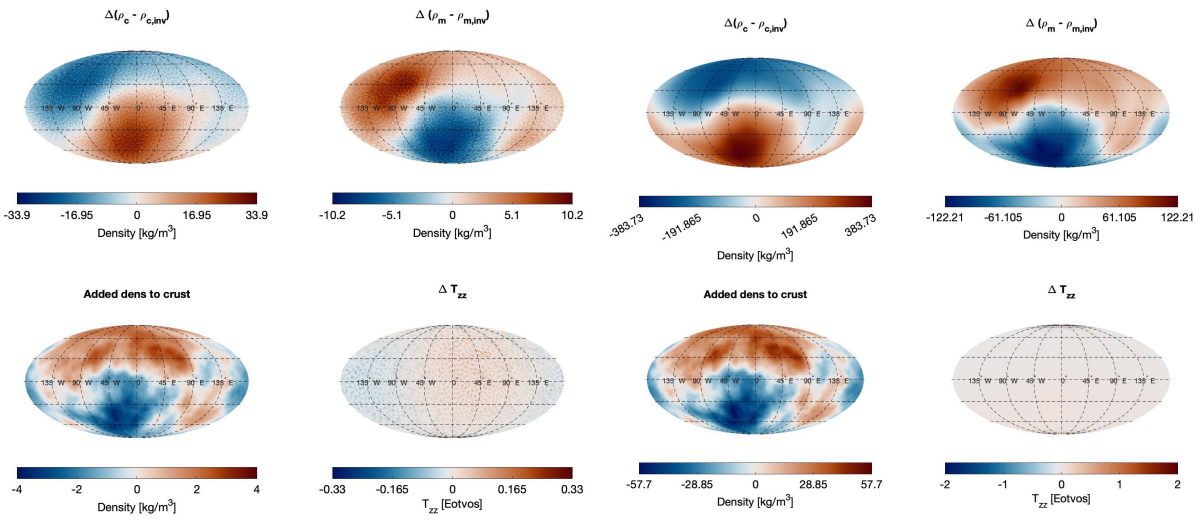

Figure 5.22: A closer look at the effect of adding extra density variations to the crust of the synthetic planet, equal to a maximum magnitude of 1.25% of the original density variations. The top left figure shows the difference between the density of the crust for the synthetic planet and the inversion results. The top right figure shows the same but for the mantle density variations. The bottom left figure shows the added density to the crust, and the bottom right figure shows the residual gravitational tensor (T_{zz}).

Figure 5.23: A closer look at the effect of adding extra density variations to the crust of the synthetic planet, equal to a maximum magnitude of 20% of the original density variations. The top left figure shows the difference between the density of the crust for the synthetic planet and the inversion results. The top right figure shows the same but for the mantle density variations. The bottom left figure shows the added density to the crust and the bottom right figure shows the residual gravitational tensor (T_{zz}).

Figure 5.22 and Figure 5.23 show a more in-depth view of the inversion results for the case of $\max(\rho_{\text{c,added}})$ equal to 1.25% and 20% respectively. Visible is that the residuals for both the crust and mantle density, shown at the top

of the two figures, correspond to the long wavelength pattern of the added crustal density, shown in the bottom left. What also can be seen is that when the added density is positive, the density residual for the crust is negative: if $\rho_{c,added} > 0$, then $\Delta(\rho_{c,input} - \rho_{c,inverse}) < 0$, and vice versa. The exact opposite is the case for the mantle. Visible in the bottom right of the two figures, is that the residual of the gravitational tensor (T_{zz}) is for both $\max(\rho_{c,added})$ equal to 1.25% and 20% similar in magnitude, when the polar regions are ignored, and contain almost only noise.

In the calculations, it is assumed that the mass of every column on the planet is equal. Because of this, the density variations in the crust result in opposite density variations in the mantle. This can be seen as if these densities "compensate" each other in the gravity field. When extra density variations are added to the crust, which are not represented in the mantle, this compensation does not take place in the gravity field. Therefore this added density to the crust will show up in large in the density results and also show up in the mantle when they are only added to the crust. Very small additions will already result in very large differences. When only approximately 1.25% is added, the density variations obtained through the inversion still closely resemble those of the input model, with a maximum error of approximately 18%. This corresponds to approximately ± 34 kg/m^3 for the crust and approximately ± 10 kg/m^3 for the mantle, as can be seen in the top two plots of Figure 5.22. When these added density variations become larger than approximately 5% (≈ 15 kg/m^3), they become dominant in the inversion and the input density variations, yielding unusable results for both the crustal and mantle density.

5.2.4. Influence of Additional Mantle Mass

Similar results where obtained for adding extra density variations to the mantle as were obtained for adding extra density variations to the crust.

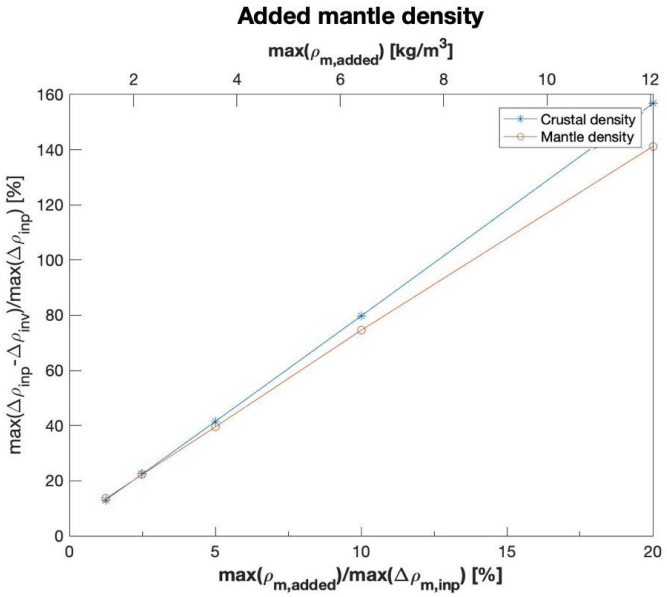

Figure 5.24: Effect of adding extra density variations to the mantle of the synthetic planet.

Figure 5.24 shows that there is for both the crust and mantle a near-linear relation between the maximum added density variations to the mantle and the maximum percentile error between the input density variations and the the density variations from the inversion results. This linear relation is approximately: $\frac{\max(\Delta\rho_{inp}-\Delta\rho_{inv})}{\max(\Delta\rho_{inp})} \approx 8 \cdot \max(\rho_{m,added})$. Figure 5.25 and Figure 5.26 show a more in-depth view of the inversion results for the case of $\max(\rho_{m,added})$ equal to 1.25% and 20% respectively. Similar to adding extra density variations to the crust, when the magnitude of the added density variations to the mantle exceed approximately 5% (≈ 4 kg/m^3), they become dominant yielding unusable results for both the crustal and mantle density.

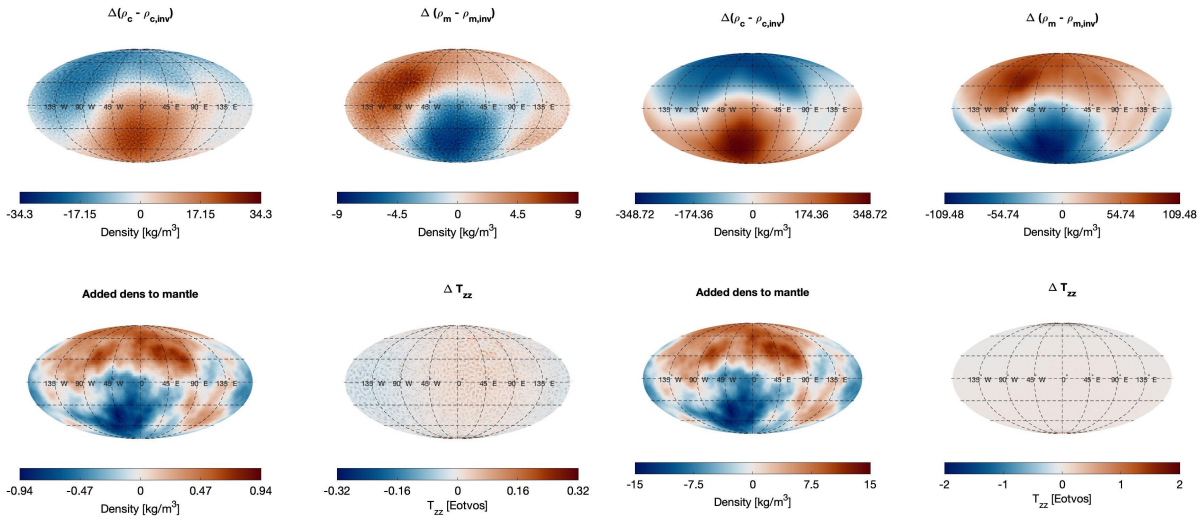

Figure 5.25: A closer look at the effect of adding extra density variations to the mantle of the synthetic planet, equal to a maximum magnitude of 1.25% of the original density variations. The top left figure shows the difference between the density of the crust for the synthetic planet and the inversion results. The top right figure shows the same but for the mantle density variations. The bottom left figure shows the added density to the mantle, and the bottom right figure shows the residual gravitational tensor (T_{zz}).

Figure 5.26: A closer look at the effect of adding extra density variations to the mantle of the synthetic planet, equal to a maximum magnitude of 20% of the original density variations. The top left figure shows the difference between the density of the crust for the synthetic planet and the inversion results. The top right figure shows the same but for the mantle density variations. The bottom left figure shows the added density to the mantle and the bottom right figure shows the residual gravitational tensor (T_{zz}).

5.2.5. Influence of Additional Mantle and Crustal Mass

In this section, the effect is studied of adding uncorrelated density variations to both the crust and the mantle. The additional density for both the crust and the mantle has been varied from 1.25% of the original density variations, up to 20%. Visible in Figure 5.27 is that when uncorrelated density variations are added to both the crust and mantle, the error diverges very fast, as is expected. This has to do with the fact that the method used to split the single layer density result into two-layers. It is assumed that the crust and mantle density are fully correlated to each other.

In this section it was analyzed how the crustal and mantle density outputs of the inversion change when the input parameters of the reference model were changed from the true parameters of the synthetic planet. It was found that when the crustal density of the reference model was set larger than that of the synthetic planet, the inversion results started to diverge very fast. Looking at varying the mantle density, this behavior was observed to be reversed. For too small mantle densities compared to that of the synthetic planet. Changing the elastic thickness, T_e, and the Young's modulus, E, yielded similar results. While for the average crustal thickness of the reference model, it was found that when it was set to a smaller average crustal thickness than that of the synthetic planet, the results deviated much less than when it was increased to above the average crustal thickness of the reference model.

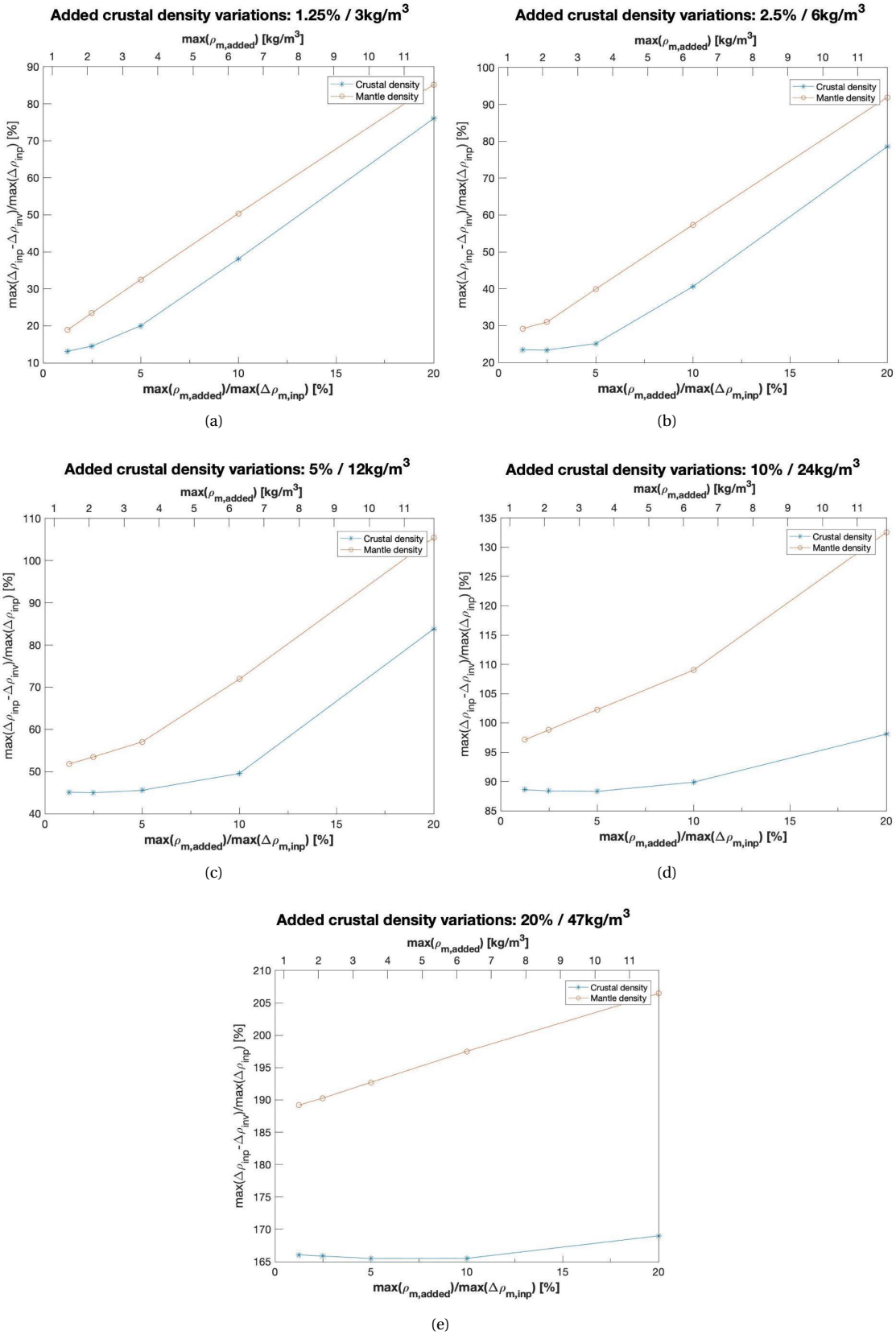

(a) (b) (c) (d) (e)

Figure 5.27: Analysis of the effect of adding extra density variations to both the crust and the mantle. These plots are plotted for variable mantle variations, and constant crustal density variations. The crustal maximum added crustal density variations are for subplot (a) 1.25%, (b) 2.5%, (c) 5%, (d) 10%, and (e) 20%.

6

Mars Inversion Results & Discussion

In this chapter, the inversion results for Mars will be given. A reference model is created based on the Martian topography, as given in section 2.2. The residual between this reference model and the Martian gravity, given in section 2.3, is used as input for the inversion.

In the first section, the initial analysis was performed. In this analysis, the effect of varying multiple input parameters of the reference model on the inversion results is analyzed. This analysis is split into three phases. The analysis is performed for 100 different reference models in the first phase. From this analysis, a more narrowed search space was obtained. In the second phase, the effect of varying the crustal thickness and elastic thickness on the inversion was studied for a set density difference between the crust and the mantle of the initial reference model. In the last phase, the effect of changing the density of the crust and mantle, as well as the density difference between the crust and the mantle, on the inversion, for varying elastic thicknesses was studied. In chapter 5 it was analyzed how the density outputs changed when the input parameters of the reference model were changed from the true parameters of the synthetic planet. These results will be compared to the Martian results.

In the next section, the optimal inversion results for Mars are given. After that, the obtained densities and crustal thickness are analyzed and compared to what has previously been found in literature. In section 6.4, the gravity of the inversion model will be compared to the gravity of Mars, and in section 6.5, the model assumptions will be discussed. Lastly, in section 6.6 the obtained crustal density variations will be compared to the geological map given by Tanaka et al. [2014].

6.1. Mars Parameter Analysis

In this section, the input parameters for the Martian reference model are analyzed. Based on the robustness analyses performed in chapter 5, the input parameters for the inversion are changed to fit the Martian gravity in three phases. A reference model will be used, as explained in section 3.4. In Table 3.1 the ranges for the different input parameters used for the initial Martian reference model are given. The next section will show the results of the initial analysis based on these parameter variations.

6.1.1. First Phase - General Analyses

As mentioned above, the variation of the different parameters is given in Table 3.1. The different combinations of these parameters used for this initial analysis are as follows:

Table 6.1: The chosen range for each of the different input parameters for the thin shell model, which will be used as input for the different reference models.

Crustal & Mantle Density [kg/m^3]	Crustal Thickness [km]	Elastic Thickness [km]	Young's modulus [Gpa]	Poisson Ratio [-]
2700 & 3600	50	50	100	0.25
2800 & 3500	75	150	-	-
2900 & 3500	100	250	-	-
3000 & 3400	125	400	-	-
3100 & 3400	150	-	-	-

Each range in Table 6.1 is combined in every possible combination, which results into $5 \cdot 5 \cdot 4 \cdot 1 \cdot 1 = 100$ different combinations. For each of the inversions with the different reference models, a multiplication factor of 30 was used, and 25 iterations were performed. This combination yielded converged results for the synthetic planet analysis. The resulting density for the crust was next analyzed and is plotted in Figure 6.1. Large density variations within the crust gave an indication of a non-optimal combination of input parameters, as was obtained by the analyses of the synthetic planets. Because of this, the maximum density variation in the crust, $\Delta\rho_c$, is plotted against the average crustal thickness for different combinations of ρ_c and ρ_m of the reference model. From the synthetic planet analysis, it was found that the smaller the obtained density variations, the closer the obtained density results to the input density, as long as the inversion tensors converged to the Martian tensor. In subsection 5.2.2, it was found that when the wrong input parameters were chosen, the density variations significantly increased. When the input parameter differed significantly from the parameter of the reference model, between $\pm$ 10% for ρ_c and ρ_m, +25% for C, and +250% for T_e, the differences between the inversion and input density increased up to 100% of the input density differences. Therefore, based on these synthetic planet results, it can be concluded that when the wrong input parameters are used, the inversion results either diverge or are significantly overestimated.

In Figure 6.1, the average crustal thickness is plotted against the maximum crustal density variations for varying density differences between the crustal and mantle density for the 100 different combinations for the reference model. Four subplots were made for the different elastic thicknesses. When analyzing these first results, it can be seen that the density variation of $\Delta\rho = 900$ kg/m^3 yields the best results for all four variations of the elastic thickness, the dark blue line, with the smallest max($\Delta\rho_{\text{c,inversion}}$). Figure 6.1 has been presented in a similar manner to the synthetic planet results given in Figure 5.20. Next to the results given in Figure 6.1, a heatmap of the same results is also created. This heatmap is given in Figure A.29. Visible in both Figure 6.1 and Figure A.29 is that the larger the elastic thickness, the larger the optimal average crustal thickness. For both $T_e = 50$ km and $T_e = 150$ km, the optimal crustal thickness lays somewhere around the 75 km for the different density variations. For $T_e = 250$ km as well as $T_e = 400$ km, this shifts to an optimal average crustal thickness of around a 100 km. As explained above, an important result is the density variations of the obtained crustal density. For $T_e = 50$ km, the optimal combination of parameters results into density variations in the crust of around 1060 kg/m^3. For $T_e = 150$ km this is around $\Delta\rho_{\text{c,inversion}} = 850$ kg/m^3 and for $T_e = 250$ km this is around $\Delta\rho_{\text{c,inversion}} = 750$ kg/m^3. Lastly, for $T_e = 400$ km, this is $\Delta\rho_{\text{c,inversion}} = 670$ kg/m^3. Therefore, it is more likely that the elastic thickness will be on the thicker side, somewhere around the 250 km up to above the 400 km thickness.

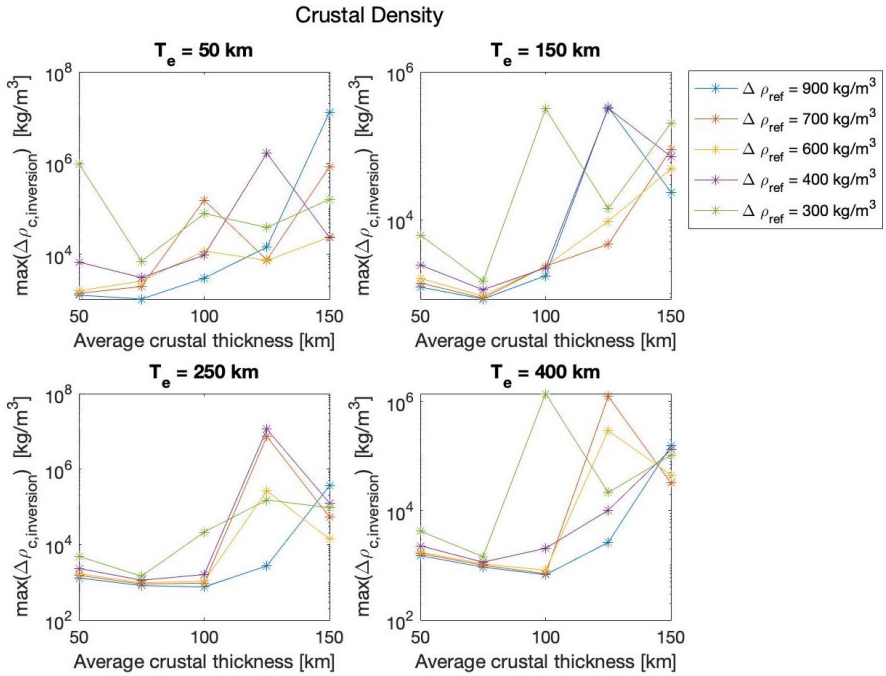

Figure 6.1: The first analysis of the different combinations of input parameters for the initial reference planets. The average crustal thickness is plotted against the density differences in the crustal density, for variations in elastic thickness between the four subplots. From top left, to bottom right, these figures show the results for elastic thicknesses of $T_e = 50$ km, $T_e = 150$ km, $T_e = 250$ km, and $T_e = 400$ km.

6.1.2. Second Phase - Crustal and Elastic Thickness Analysis

For the next analysis, the crustal thickness variation between the input density of the crust and mantle of the reference model will be set $\Delta\rho = 900$ kg/m^3. Next, the average crustal thickness of the reference model will be varied around 100 km, from 90 up to 115 km, with steps of 5 km. Also, T_e, is varied, from 150 km up to 550 km. These results are plotted in Figure 6.2. Also, for these results, a heatmap is created, given in Figure A.30.

The shift of the increasing optimal T_e when the average crustal thickness is increased is also visible when looking at Figure 6.2 and Figure A.30. The optimal combination of input parameters for this analysis is a crustal thickness of 105 km, with an elastic thickness of 425 km. When the crustal thickness increases beyond the optimal point, the results start to diverge. This is similar behavior to what was observed in subplot (e) of Figure 5.20, where the crustal thickness of the reference model was varied from the synthetic planet analyses.

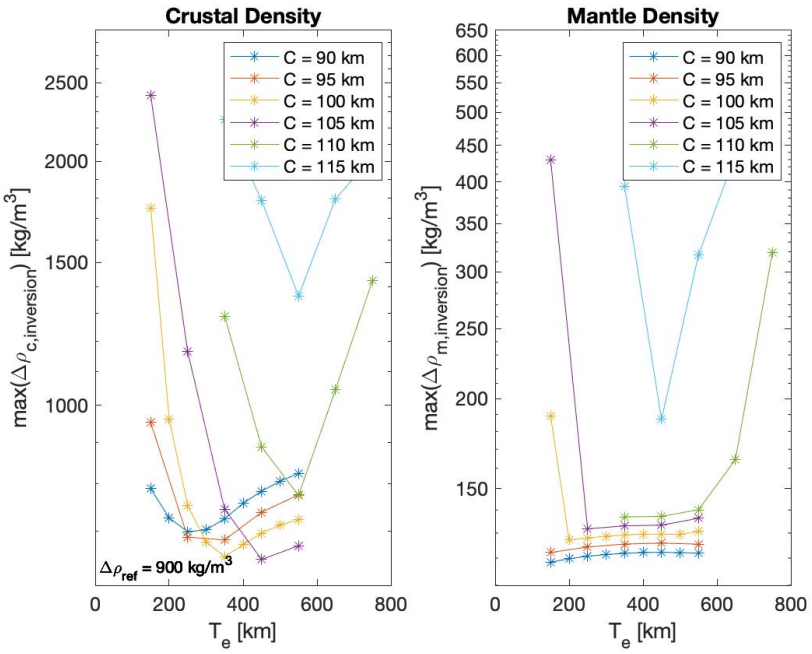

Figure 6.2: Results for a set density difference between the crustal and mantle density of the reference model of 900 kg/m^3, and variations in the average crustal thickness and elastic thickness. The elastic thickness is plotted against the density differences in the crustal, left subplot, and mantle, right subplot, density.

6.1.3. Third Phase - Crustal and Mantle Density Variations

Next, the density variations were studied for this optimal combination of C and T_e. The average crustal thickness was set to 105 km, with the elastic thickness varied from 400 km to 475 km in steps of 25 km. The density difference between the crust and mantle of the reference model was varied from 700 kg/m^3 to 1100 kg/m^3 with steps of 100 kg/m^3. Also, the mantle and crustal density combination was varied for constant density difference between them. Only the density difference has an influence on the crust-mantle boundary calculation, but the set density for the crust and mantle does have an influence on the inversion. Both the crustal density and density difference have an influence on the root of the Airy crust-mantle boundary. Therefore, the crustal and mantle density combinations given in Table 6.2 were used as input for the initial densities of the reference model for the next test. The combinations given in Table 6.2 were the initially used combinations. It was found that for those results, a density difference of 900 kg/m^3 was optimal. Therefore, density differences of 1000 and 1100 kg/m^3 were added too, as well as increasing the range up to 3800 kg/m^3 for the density difference of 800-1100 kg/m^3. Lastly, for a density difference of 900 and 1000 kg/m^3, the mantle density of 3550 and 3650 kg/m^3, and 3650 and 3750 kg/m^3 respectively, were added to narrow the search field around these optimal values of 3600 and 3700 kg/m^3 respectively. These results are shown in Figure 6.3 with the mantle density plotted on the horizontal axis and in Figure 6.4 with the crustal density plotted on the horizontal axis. For both the reference mantle density and the crustal reference density, heatmaps are created as well, shown in Figure A.31 and Figure A.32 respectively.

Table 6.2: Combinations of crustal and mantle density as input for the reference model used in the analysis of Figure 6.3.

	$\Delta\rho = 700$ kg/m^3			$\Delta\rho = 800$ kg/m^3			$\Delta\rho = 900$ kg/m^3		
ρ_c [kg/m^3]	2700	2800	2900	2600	2700	2800	2500	2600	2700
ρ_m [kg/m^3]	3400	3500	3600	3400	3500	3600	3400	3500	3600

Table 6.3: The second set of combinations of crustal and mantle density as input for the reference model used in the analysis of Figure 6.3.

	$\Delta\rho = 800$ kg/m^3		$\Delta\rho = 900$ kg/m^3		$\Delta\rho = 1000$ kg/m^3					$\Delta\rho = 1100$ kg/m^3			
ρ_c [kg/m^3]	2900	3000	2800	2900	2400	2500	2600	2700	2700	2400	2500	2600	2700
ρ_m [kg/m^3]	3700	3800	3700	3800	3400	3500	3600	3700	3700	3500	3600	3700	3800

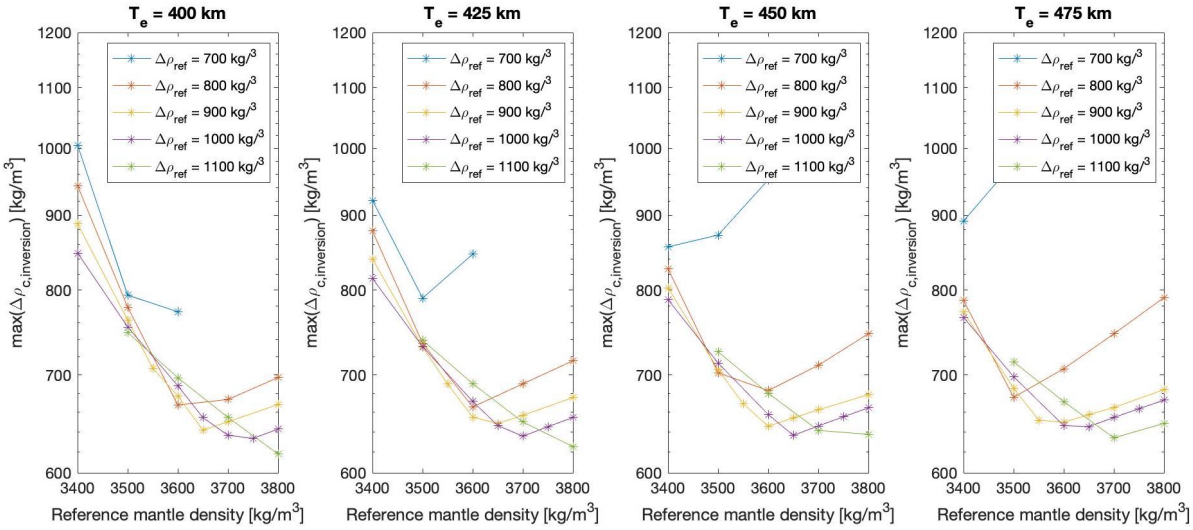

Figure 6.3: Results for a set average crustal thickness for the reference model of 105 km and variations in the elastic thickness and density difference between the crust and mantle of the reference model. The mantle reference density is plotted against the density differences in the crustal for different density differences. From left to right, subplot 1 shows the results for an elastic thickness of 400 km, subplot 2 for 425 km, subplot 3 for 450 km, and subplot 4 for 475 km.

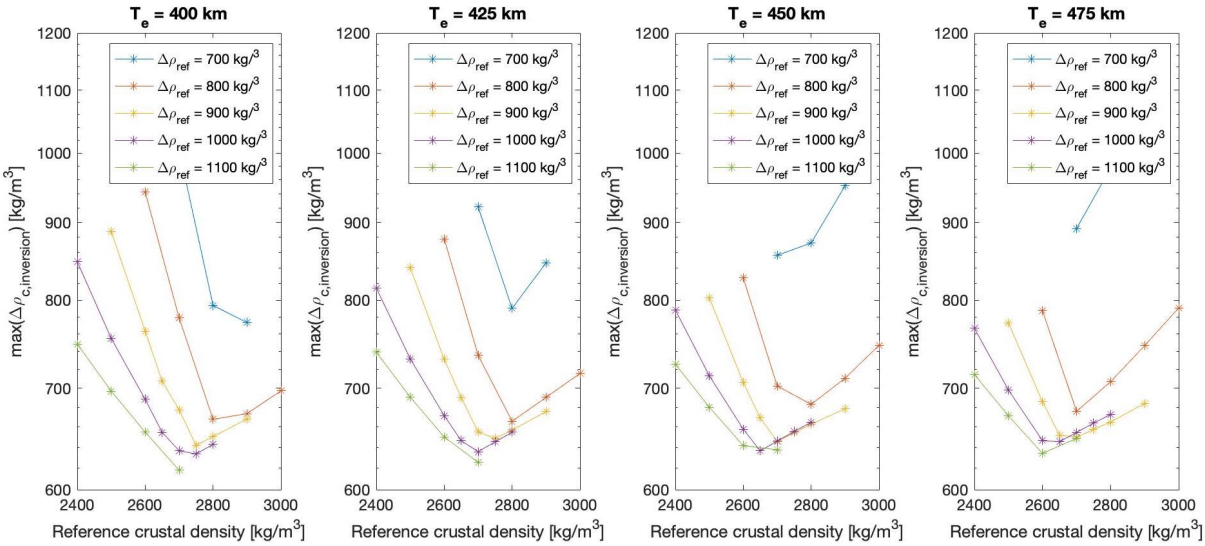

Figure 6.4: Results for a set average crustal thickness for the reference model of 105 km and variations in the elastic thickness and density difference between the crust and mantle of the reference model. The crustal reference density is plotted against the density differences in the crustal for different density differences. From left to right, subplot 1 shows the results for an elastic thickness of 400 km, subplot 2 for 425 km, subplot 3 for 450 km, and subplot 4 for 475 km.

Looking at the results in Figure 6.3 and Figure A.31, it can be concluded that, for the used ranges, larger $\Delta\rho_{\text{ref}}$ will result into smaller max($\Delta\rho_{\text{c,inversion}}$) values. The only exception is for T_e: the results of $\Delta\rho_{\text{ref}}$ = 1000 kg/m^3 gives a slightly better result than $\Delta\rho_{\text{ref}}$ = 1100 kg/m^3, but this probably has to do with the used ranges. The optimal value for $\Delta\rho_{\text{ref}}$ = 1100 kg/m^3 most likely lays somewhere between 3700 and 3800 kg/m^3. The optimal value for T_e = 450 km, is for $\Delta\rho_{\text{ref}}$ = 1100 kg/m^3, but with $\rho_{\text{m,ref}}$ is somewhere between the 3700 and 3800 kg/m^3. Another trend that is visible, is that, for the minima in max($\Delta\rho_{\text{c,inv}}$), smaller T_e resulted in larger mantle density for the reference model. No large differences in the minimum value for the max($\Delta\rho_{\text{c,inv}}$) are visible, for the different values of T_e. Also it is visible that the higher the $\Delta\rho_{\text{ref}}$, the higher the reference mantle density for the minimum max($\Delta\rho_{\text{c,inv}}$).

6.1.4. Discussion on Variations in Elastic Thickness

First, the effect of varying the elastic thickness, T_e, will be discussed. The trend visible in Figure 6.2 is the "V" like shape for each average crustal thickness when T_e is varied. In subsection 5.2.2 a similar "V" like shape was found for variations around the synthetic planet value. What was also found was that for large deviations, from approximately 0.1, up to 2 times the input elastic thickness of the synthetic planet, the error in the obtained density stayed below 60%. This still yielded results from which the original pattern of the density variations could be obtained. This was also visible in the Martian results, where from T_e = 150 km, up to T_e = 475 km, similar density patterns were obtained, but with varying magnitudes. For T_e = 50 km, the inversion did not converge, as can be seen in the top left plot of Figure 6.1. It is therefore assumed that the elastic thickness of 50 km is too small, yielding unrealistic results.

6.1.5. Discussion on Variations in Average Crustal Thickness

The effect of varying the average crustal thickness for the synthetic planet analyses, given in subsection 5.2.2, showed that when the crustal thickness was chosen too small, up to $C_{\text{ref}} = 0.6C_{\text{input}}$, the error in the obtained density stayed below 50%. When a too large average crustal thickness was chosen, the inversion diverged very fast, only yielding somewhat usable results up to $C_{\text{ref}} = 1.1C_{\text{input}}$. This trend was already visible in the first analysis results for Mars, shown in Figure 6.1, which showed that for $C > 100$ km, the inversion results diverged. In the second analysis, it was found that for $C < 110$ km, there were still combinations of input parameters possible for which converged results, with reasonably small $max(\Delta\rho_{\text{c,inversion}})$, were obtained. When the crustal thickness was increased up to 115 km, this was not the case anymore, and the inversion started to diverge. The optimal crustal thickness was found to be in the range of 100 to 105 km. For a value of C = 115 km, the inversion diverged. From the synthetic planet analyses, it was found that for $C_{\text{ref}} > 1.1C_{\text{input}}$, the inversion started to diverge. From this can be concluded that C = 115 km is at least 10% larger than the average crustal thickness of Mars. This would mean that C_{Mars} is somewhere between 100 and 105 km, equal to for which the smallest maximum density variations were found.

6.1.6. Discussion on Variations in Crustal and Mantle Density

Ranges from 300 kg/m^3 up to 900 kg/m^3 were initially studied and later increased up to 1100 kg/m^3. For all these ranges, different combinations of input parameters could be obtained for which the inversion converged. In the third analysis, shown in Figure 6.3, both variations in crustal density, mantle density, as well as the density variation were studied. It was found that the larger T_e, the smaller the mantle density for the smallest $max(\Delta\rho_{\text{c,inversion}})$. In subplot (b) of Figure 5.20, the variations of the mantle density for the synthetic planet have been analyzed. Visible is that when the mantle density was chosen too small, the inversion results diverged. When the mantle density was set to a value above a certain threshold, above $\Delta\rho_{\text{m,ref}} = 1.4\Delta\rho_{m,input}$, the inversion only diverged from the true density variations in a slow manner. In the Martian results, a similar trend was observed. When $\rho_{\text{m,ref}}$ was chosen too small, large $max(\Delta\rho_{\text{c,inversion}})$ values were found.

In Figure 6.1 it is visible that the density variation of $\Delta\rho$ = 900 kg/m^3 yields the best results for all four variations of the elastic thickness. This is the largest density difference used in this analysis. In Figure 6.3, it is also visible that the largest density difference between the crust and mantle of the reference model, in that specific analysis equal to 1100 kg/m^3, showed the best results for all except T_e = 450 km. This has probably to do more with the chosen interval, where the optimal value is located somewhere between ρ_m = 3700-3800 kg/m^3, but the spacing of the data points was too large. From this can be concluded that large density differences yielded the best results. The density difference has a clear influence on the obtained crust-mantle boundary, which was obtained using the following Airy equation,

$$b = \frac{h\rho_c}{\rho_m - \rho_c}, \tag{6.1}$$

where b is the depth/height of the root with respect to the average crustal thickness, h is the height/depth of the topography, ρ_m is the mantle density, and ρ_c is the crustal density. If the topography is positive, the root is positive down with respect to the crust-mantle boundary, and if the topography is negative, the root is negative up with respect to the crust-mantle boundary. Therefore, the larger the density difference between the crust and mantle, the smaller the roots. This, together with the large value for T_e that has been obtained, is the basis for the conclusion that the small wavelength topographic features are compensated through density differences, and only the large wavelength features are compensated isostatically.

6.2. Optimal Inversion Results Mars, Smallest max($\Delta\rho_{\mathbf{c,inv}}$)

The different density profiles for the smallest max($\Delta\rho_{\mathrm{c,inv}}$) for the different T_e values performed very similar behavior. In section A.5 the results are given for all four values of the elastic thickness. The combinations of the input parameters for each of these elastic thickness values, are given in Table 6.4. In this section only the results for T_e = 400 km is given.

Table 6.4: The combination of input parameters for the minimum max($\Delta\rho_{\mathrm{c,inv}}$) for each elastic thickness used in subsection 6.1.3.

T_e [km]	C [km]	$\Delta\rho_{\mathrm{ref}}$ [kg/m^3]	$\rho_{\mathrm{m,ref}}$ [kg/m^3]	$\rho_{c,ref}$ [kg/m^3]
400	105	1100	3800	2700
425	105	1100	3800	2700
450	105	1000	3650	2650
475	105	1100	3700	2600

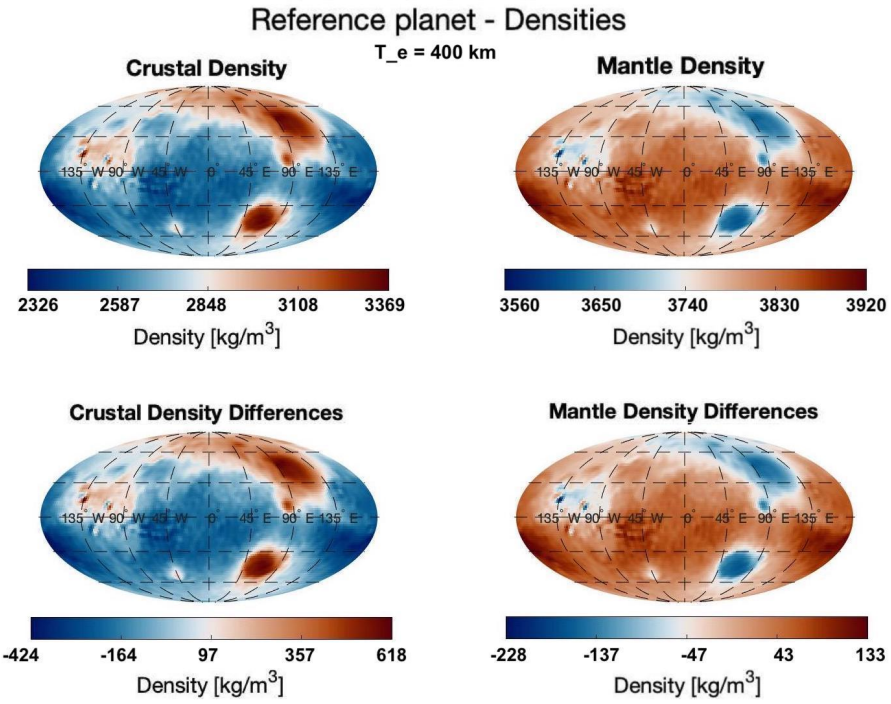

Figure 6.5: The crustal and mantle density and density variations obtained through the Martian inversion. For the inversion, a multiplication factor of 30 and 25 iterations were used. These results were obtained for a reference model with the topography and crust-mantle boundary shown in Figure 6.6, for the same subplots, respectively.

In the obtained densities, shown in Figure 6.5, some topographic features are clearly visible. These features are Hellas Basin, Utopia Basin, Vastitas Borealis, and the Tharsis Region. Also, the slightly smaller topographic features of Isidis Basin and Argyre Basin are visible, as well as Valles Marineris. The volcanoes Alba Mons and Elysium Mons are two topographic features that are not clearly visible in the obtained densities. In the density differences, for both the crust and mantle, no large differences are visible between the different elastic thickness results. The topography and the obtained crust-mantle boundary are plotted for each T_e, as well as the obtained crustal and mantle densities and density variations in the next sections. In the crust-mantle boundary, shown in the right

plots of Figure 6.6, the Martian dichotomy is clearly visible. Next to the Martian dichotomy, the thin crust underneath Hellas Basin is visible. The crust is the thickest underneath the Tharsis region, and the thin crustal regions are underneath Utopia Basin and goes up to Vastitas Borealis and then down to Chryse Planitia. No large differences are visible between the different crust-mantle boundaries.

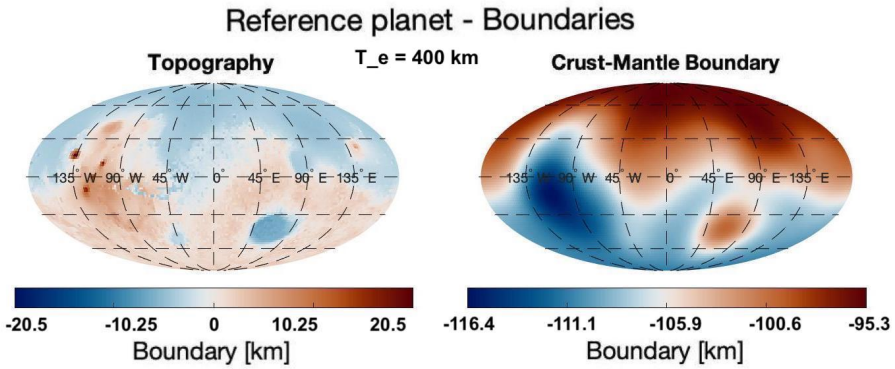

Figure 6.6: The topography and crust-mantle boundary used for the reference model for the Martian inversion. This is obtained with C = 105 km, E = 100 GPa, ν = 0.25, ρ_c = 2700 kg/m^3, ρ_m = 3800 kg/m^3, and T_e = 400 km.

6.3. Density and Crustal Thickness Analyses

For each T_e the results with the minimum density variations in the crust were plotted in section A.5. The obtained variations between the results for the different T_e values were very similar, only deviating slightly in magnitude. It was found that, overall, a density difference for the reference model of 1100 kg/m^3 between the crust and mantle density yielded the smallest $max(\Delta\rho_{\text{c,inversion}})$. This large density difference between the crust and the mantle has an influence on the crust-mantle boundary. The crust-mantle boundary was obtained by applying the flexural response function, as given in Equation 2.11, to the crust-mantle boundary obtained with Airy isostasy, given by Equation 2.3. As can be seen in this equation, the larger the density difference between the crust and mantle, the smaller the root. From the combination of the large obtained elastic thickness, and the large density difference between the crust and mantle, it can be concluded that for the inversion, large differences within the crust-mantle boundary were deemed unrealistic.

In previous research, most often, a crust-mantle boundary based on Airy isostasy was used. Qin [2021] already looked at the different isostasy methods and the effect of the power spectrum of Mars. In this research, it was also found that the thin shell method yielded the best fit for the Martian power spectrum. One of the main assumptions of Airy is that the density for both the crust and the mantle is uniform. When an impact crater is created, the material is crushed together, resulting in a higher density in the crust. Airy assumes that the lower topography would affect the crust-mantle boundary instead of assuming that impact craters are more isostatically compensated using Pratt. This would result in a lower topography, with a denser crust, underneath the impact crater, but the crust-mantle boundary would not be affected. Because the FRF is applied to a crust-mantle boundary obtained with Airy, it makes it very difficult to correctly model the crust-mantle boundary around impact craters. This may be the reason for the very large crustal density values observed near the impact craters. This is because the topography near impact craters is lower, resulting in a thinner crust than would be the case for Pratt isostasy. Because of the thinning of the crust underneath impact craters, more mass is located in a smaller volume, resulting in higher densities. This may also be the reason that large values for the elastic thickness, and the large density differences, yielded the best results. Large T_e and $\Delta\rho_{\text{ref}}$ yield small deflections in the crust-mantle boundary and, therefore also, less thinning of the crust underneath the impact craters. From this, it can be concluded that the large impact craters on Mars, such as Hellas, Utopia, Isidis, and Argyre basin, are more likely to be compensated by applying the thin shell FRF to a crust-mantle boundary which is obtained with Pratt isostasy.

Based on the reference model with T_e = 400 km, C = 105 km, $\rho_{c,ref}$ = 2700 kg/m^3 and $\rho_{\text{m,ref}}$ = 3800 kg/m^3, which resulted into the result with the smallest $max(\Delta\rho_{\text{c,inversion}})$, now referred to as the Martian inversion result, a density difference for the final inversion results of approximately 1000 kg/m^3 between the crust and mantle was obtained. A mean crustal density of approximately 2750 kg/m^3 and the mean mantle density of approximately 3750 kg/m^3 were found. The elastic thickness, if chosen uniformly, most likely lays somewhere between the 450 $\pm$ 50 km and the uniform crustal thickness somewhere between 100 $\pm$ 10 km.

Based on the results of the Martian inversion result, a mean crustal thickness of 103.5 km was found, with crustal thickness values ranging from approximately 90 km, underneath Utopia Basin and Vastitas Borealis, up to approximately 125 km, underneath Olympus Mons. In the next subsections, a more in-depth analysis and comparison of the crustal thickness beneath specific topographic features will be given. An optimal lithospheric thickness of 450 ± 50 km was obtained in this research. Up until the recent findings, based on the Insight data, previous research found a lithospheric thickness somewhere between the 50-150 km [Zuber et al., 2000] [Nimmo, 2002] [Turcotte et al., 2002] [Belleguic et al., 2005] [Beuthe et al., 2012] [Taylor et al., 2020] [McGovern et al., 2004] [Steinberger et al., 2010]. In the most recent study [Khan et al., 2021], based on the seismic data obtained through the Insight mission, a lithospheric thickness between the 400 and 600 km was found. The elastic thickness for this study is fully based on the T_e value as used in Equation 2.11, the flexural response function for the thin shell model. In this model, there is a correlation between the elastic thickness and the Young's modulus. These two parameters give a measure of how easy the lithosphere 'bends'. The Young's modulus has been taken as constant in this study, 100 GPa, and only the elastic thickness value is varied. One way to solve this is by looking at the flexural rigidity parameter, D, as explained in section 2.1, which relates the elastic thickness to both the Young's modulus as well as the Poisson ratio.

In [Nimmo and Stevenson, 2001] it is demonstrated that the crustal thickness of the southern highlands is unlikely to be larger than 125 km and is more probably smaller than 100 km. When it is assumed that the topographic features in the southern highlands, such as Hellas, are supported by Airy isostasy, it is found that the crustal thickness can not be less than approximately 40 km. These bounds translate into a mean planetary crustal thickness of approximately 30-115 km, resulting in a crustal thickness range that encloses the findings obtained in this thesis project. In [Nimmo, 2002], the upper layer of the crust was taken as variable. This resulted in the mean crust lying in the range of 1–111 km. The obtained average crustal thickness range for this thesis research lies within this range. In [Turcotte et al., 2002], a mean crustal density of 2960 kg/m^3 and a crustal reference thickness of 91.7 km were assumed. Based on the scatter in the data, this would result in an error of $\pm$50 kg/m^3 in the crustal density and $\pm$10 km error in crustal thickness. It was also found that even though the Hellas area is locally compensated, much of the topography on Mars is not. The average crustal thickness of 2960 $\pm$50 kg/m^3 is 8% larger than the obtained crustal density of 2750 kg/m^3. The crust of 91.7 $\pm$10 km is 11% lower than the obtained average crustal thickness of 103.5 km. The lower crustal density found by Nimmo [2002] might be the reason for the larger average crustal density.

The densities of the meteorites, which are believed to originate from Mars, were found to have densities between the 3100 and 3700 kg/m^3 Coulson et al. [2007]. Based on igneous rocks at Gusev crater, located 14.5 degrees south and 175.4 degrees east, the crustal density was calculated to lie somewhere between the 3100 and 3600 kg/m^3 [Baratoux et al., 2014]. Most of the found densities for the impact crater lie within these ranges. It is believed that the meteorites originate from the Martian impact craters, being ejected due to the impact. [Baratoux et al., 2014] also found that these higher densities are compatible with the measured mass of Mars and the moment of inertia factor for average crustal thickness values approaching 100 km, similar to what was found in this study.

Based on the shergottites, nakhlites, and chassignites (SNC) meteorites, Sohl and Spohn [1997] found that Mars is overlain by a 100 up to 250 km thick basaltic crust. The present thermal lithosphere was estimated to be about 500 km thick, similar to the seismic lithosphere found by Khan et al. [2021]. The lithosphere is subdivided into a 300 km thick outer lithosphere [Sohl and Spohn, 1997].

In Figure 6.5, some topographic features are clearly visible. Especially the impact craters are clearly visible: Hellas Basin, Utopia Basin, Isidis Basin, and Argyre Basin. Next to the craters, the Tharsis region is also visible. When looking at the densities, it becomes clear that the impact crater features are more clearly represented in the obtained densities than the large volcanoes on Mars. Volcanoes such as Alba Mons and Elysium Mons are not clearly distinguishable in the obtained densities. This has likely to do with the fact that it is difficult to correctly model impact craters, as explained above. Volcanoes were not formed by impact but through internal mechanisms. Therefore, the density was not externally pressured together, and the crust-mantle boundary-based in Airy isostasy, together with the applied FRF, might be a more realistic compensation for volcanoes than for large impact craters.

6.3.1. Hellas Basin, Utopia Basin, and other impact craters

In this subsection, the obtained densities and crustal thickness are analyzed, as well as compared to what has already been found in literature for the different topographic features. For this analysis the cross-sections shown in subsection 6.3.3 are used. The cross-sections were made for only the Martian inversion result. In Table 6.5 the

crustal thickness, crustal density, and mantle density obtained for the Martian inversion result are given.

In the model used by Zuber [2001], a crustal density of 2900 kg/m^3 and a mantle density of 3500 kg/m^3 is assumed. This is consistent with plausible crustal compositions and with bulk composition models [Dreibus and Wanke, 1985]. A mean crustal thickness of approximately 50 km is obtained. This model assumes an average crustal and mantle density, with a constant density difference of 600 kg/m^3. This is a much smaller density difference than was obtained for the Martian inversion result.

Table 6.5: The mean crustal thickness, mean crustal density, and mean mantle density obtained for some of the Martian surface features, specifically basins and low elevation areas, for the Martian inversion result.

Topographic feature	Crustal thickness [km]	Crustal Density [kg/m^3]	Mantle Density [kg/m^3]
Hellas Basin	93	3345	3630
Utopia Basin	90	3300	3640
Isidis Basin	97	3200	3650
Argyre Basin	105	2870	3740

In [Zuber, 2001], a much thinner crustal thickness is obtained than for the Martian inversion model, approximately 5-10 km versus 90 km, respectively. When the crustal thickness is small, the mean density of the column would be almost equal to the mantle density. The crustal thickness in [Zuber, 2001] is based on Airy isostasy, which would result in a very thin crust. Because this assumes uniform crustal and mantle thickness, this can also be translated to different crustal thickness variations, with variations in both crustal and mantle density. In [Zuber, 2001] the mass of a column can be seen as follows:

$$\begin{aligned} c\rho_c + (x-c-h)\rho_m &= 5\cdot 2.9 + (x-5-8)\cdot 3.5, \\ &= 14.5 + (x-13)\cdot 3.5, \\ &= 3.5x - 31, \end{aligned}$$

with c the crustal thickness, ρ_c the crustal density, x the depth of compensation, h the topographic height/depth and ρ_m the mantle density. For the Martian inversion model the mass beneath Hellas basin for one column is:

$$\begin{aligned} c\rho_c + (x-c-h)\rho_m &= 93\cdot 3.345 + (500-93-8)\cdot 3.63, \\ &= 311 + (500-101)\cdot 3.63, \\ &= 311 + 1448 = 1759. \end{aligned}$$

This would mean a depth of compensation for the model of Zuber [2001] for $3.5x - 31 = 1759 -> x = 494$ km. The crustal thickness underneath the Hellas basin would need to be equal to 30 km to result in a depth of compensation of 500 km. When the columns can not move without friction from each other, as is the case for the thin shell model, the crustal thickness would increase underneath Hellas basin. Combining this all, it can be concluded that even though these results seem quite different, they can be interpreted in a similar manner.

If Hellas basin was compensated through Pratt isostasy instead of thin shell isostasy, there would be no crustal thinning underneath Hellas basin. Therefore, the crust would be between 6 and 7 km thicker. This would increase the crust from 93 km up to approximately 100 km. If this were the case, the density underneath Hellas basin would be of the order $\frac{93\cdot 3345}{100} = 3110$ kg/m^3. This is more than 200 kg/m^3 less than the current crustal density found underneath Hellas basin.

Another effect might be that there is a mantle plume underneath Utopia basin. When looking at the Martian topography, as shown in Figure 1.1, Hellas Basin is clearly visible, but for Utopia Basin not as much. There is no clear rim or significant lowering of the topography near Utopia basin compared to the surrounding Northern Lowlands. Therefore, there is also no clear crustal thinning visible underneath Utopia basin, as visible in subplot (e) of Figure 6.7. The crustal thinning is clearly visible underneath Hellas Basin, as is visible in subplot (d) of subsection 6.3.3. Therefore, this large gravity signal for Utopia Basin might be due to a mantle plume.

6.3.2. Tharsis Region, Olympus Mons, and the other Large Volcanoes

In Table 6.6 the crustal thickness, crustal density, and mantle density obtained for the Martian inversion result are given. In [Zuber et al., 2000] it was found that Olympus Mons and the other volcanoes on Mars in the Tharsis region have an elastic thickness larger than 100 km. In [McKenzie et al., 2002] a crustal density of 2970 ± 40 kg/m^3

was found for the Tharsis region, which is substantially greater than the terrestrial value of 2670 kg/m^3 and is about 10% less than the density of the meteorites believed to come from the Martian crust. If the rock density of Mars is 3320 kg/m^3, equal to that of the meteorites believed to come from the Martian crust [McKenzie et al., 2002], these meteorites could originate from the high elevation, volcanic areas of Mars. These meteorite densities fall within the crustal density range for the Tharsis region.

In [Pauer and Breuer, 2008] a mantle density of 3500 kg/m^3 is used and a range for the crustal density between 2400 and 3200 kg/m^3 is used. To satisfy the constraint that the minimum crustal thickness should be smaller or equal to the mean crustal thickness, a maximum crustal density of 3020 ± 70 kg/m^3 was obtained. For the volcanoes such as Olympus, Elysium, Arsia, Pavonis, and Ascraeus Mons, a load density of 3200 ± 100 kg/m^3 was found, which was studied with gravity/topography and was much higher than the maximum density obtained for the southern crust. The higher crustal densities in this thesis study were mainly found near the large impact basins (Hellas, Utopia, Isidis, and Argyre), the Tharsis region and Olympus Mons, and the northern highlands. The other large volcanoes, Alba Mons and Elysium Mons, were found to be very well isostatically compensated using the thin shell method.

Table 6.6: The mean crustal thickness, mean crustal density, and mean mantle density obtained for some of the Martian surface features, specifically volcanoes and high elevation areas, for the Martian inversion result.

Topographic feature	Crustal thickness [km]	Crustal Density [kg/m^3]	Mantle Density [kg/m^3]
Tharsis Region	120-130	2770-3370	3750-3560
Olympus Mons	127	3370	3560
Alba Mons	112	2660	3810
Elysium Mons	100	2770	3780

Belleguic et al. [2005] found that the densities of the Martian volcanoes are generally well constrained with values of 3200 ± 100 kg/m^3. This is similar to the densities found for the volcanoes in the Tharsis region. The other large volcanoes, such as Alba Mons and Elysium Mons were found to be well compensated by thin shell isostasy, and crustal densities of 2660 and 2770 kg/m^3 were found, respectively, which is much lower than was found by Belleguic et al. [2005]. The density was only constrained for the Elysium rise to 3270 ± 150 kg/m^3, which is almost 20% higher than was found in this study. This smaller crustal density for the volcanoes outside the Tharsis rise might have to do with the fact that this thesis study uses the thin shell model, in which the curvature of the planet compensates part of the loads. The volcanoes outside of the Tharsis region are more stand-alone volcanoes, which are easier compensated by the curvature than the large volcanic region, which is the Tharsis region.

6.3.3. Cross-Sections

Different cross-sections of the reference model with the densities obtained through the inversion were made to better see the correlation and anti-correlation between the found density differences, the topography, and crust-mantle boundary. The cross-sections are made with the density results and input boundaries for the elastic thickness of 400 km. For T_e = 400 km, the result with the smallest max($\Delta\rho_{c,inv}$) was found. In the previous sections, it was shown that varying the elastic thickness did not have a significant influence on the obtained densities for the smallest max($\Delta\rho_{c,inv}$). Therefore, the cross-sections are only given for one reference model. Six of these cross-sections have been made and are shown in Figure 6.7. These cross-sections are obtained with the density variations given in Figure 6.5 and the topography and crust-mantle boundary shown in Figure 6.6.

In subplot (a) of Figure 6.7, the cross-section is made for the longitude line of -134 degrees, which shows the Southern Highlands, Olympus Mons, and the Northern Highlands. In subplot (b), the cross-section is made for the longitude line of -114 degrees, where the Southern Highlands as well as the Tharsis Montes, Alba Mons, and the Northern Highlands can be seen. In the next cross-section, subplot (c), the Argyre Basin, Valles Marineris, and the Northern Lowlands can be seen at the longitude line of -44 degrees. On the longitude line of 80 degrees, shown in subplot (d), Hellas Basin, Hesperia Planum, Isidis Basin, and the Northern Lowlands can be seen. The next cross-section shows the cross-section of the 120-degree longitude line, subplot (e), and shows the Southern Highlands as well as Utopia Basin. The last cross-section is for longitude line 148 degrees, shown in subplot (f) and shows the southern Highlands, Elysium Mons, and the Northern Lowlands.

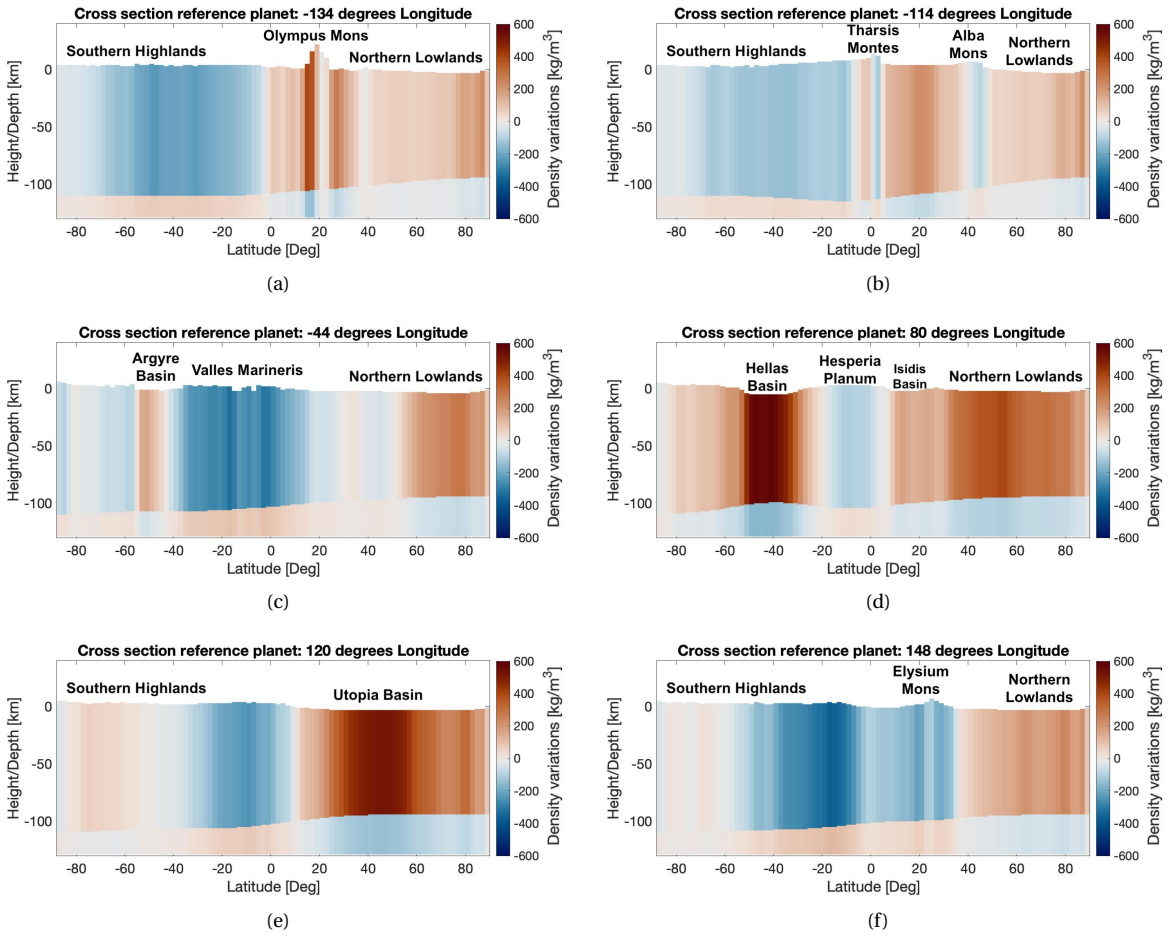

Figure 6.7: A cross section of the reference model based on the densities given in Figure 6.5 and the boundaries given in Figure 6.6. The subplot shows the longitude line of (a) -134 degrees, (b) -114 degrees, (c) -44 degrees, (d) 80 degrees, (e) 120 degrees, and (f) 148 degrees.

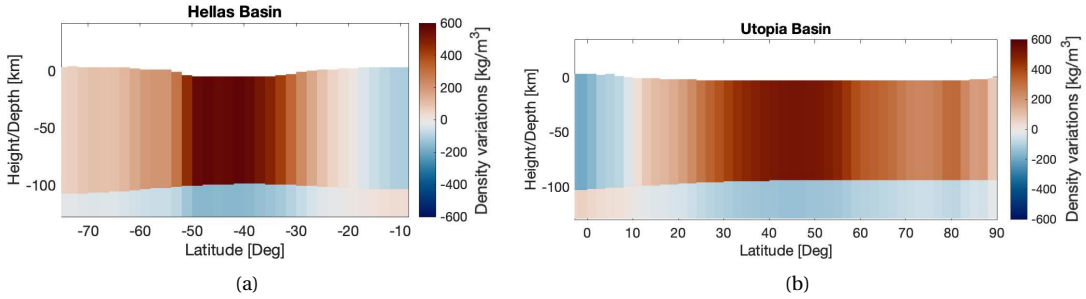

Figure 6.8: A more zoomed in cross section of the reference model based on the densities given in Figure 6.5 and the boundaries given in Figure 6.6. The subplot shows the cross-section for (a) Hellas Basin and (b) Utopia Basin.

6.4. Gravity of the Inversion Model

The gravity for the reference model with uniform densities, the reference model with the densities obtained through the inversion, and of Mars are given in the next subsections. First, the gravity anomaly will be given, after which the gravitational tensor will be given.

6.4.1. Gravity Anomaly

In Figure 6.9 the gravity anomaly of the reference planet with the density of the crust and mantle obtained from the inversion is potted. In the top right, the gravity anomaly of Mars is plotted, and in the bottom plot, the residual between the two is plotted. The residual has a maximum of ± 3% of the input signal, with most of the residual

around the ± 1.5% of the input signal. The largest residuals are near the Tharsis region and Valles Marineris. There is also a degree 1 signal visible in the residual. This degree 1 signal corresponds to the long wavelength signal of the Martian dichotomy. The northern part of the gravity from the reference model with the obtained densities of the inversion has a smaller gravitational signal than the gravity of Mars. The gravity of the reference model has a higher gravity for the southern hemisphere.

The gravity anomaly of the reference model with uniform densities is plotted in the top right figure of Figure A.27. The residual between the reference model with uniform densities, and the gravity anomaly of Mars, is plotted in the bottom figure of Figure A.27. The gravity of the reference model is highly correlated to the martian topography due to the uniform densities. Therefore, the only variations in the reference model are due to the varying topography and crust-mantle boundary. The residual, shown in the bottom figure of Figure A.27, is highly correlated to the obtained density variations, as shown in Figure 6.5. This is expected because this residual is the input data for the inversion.

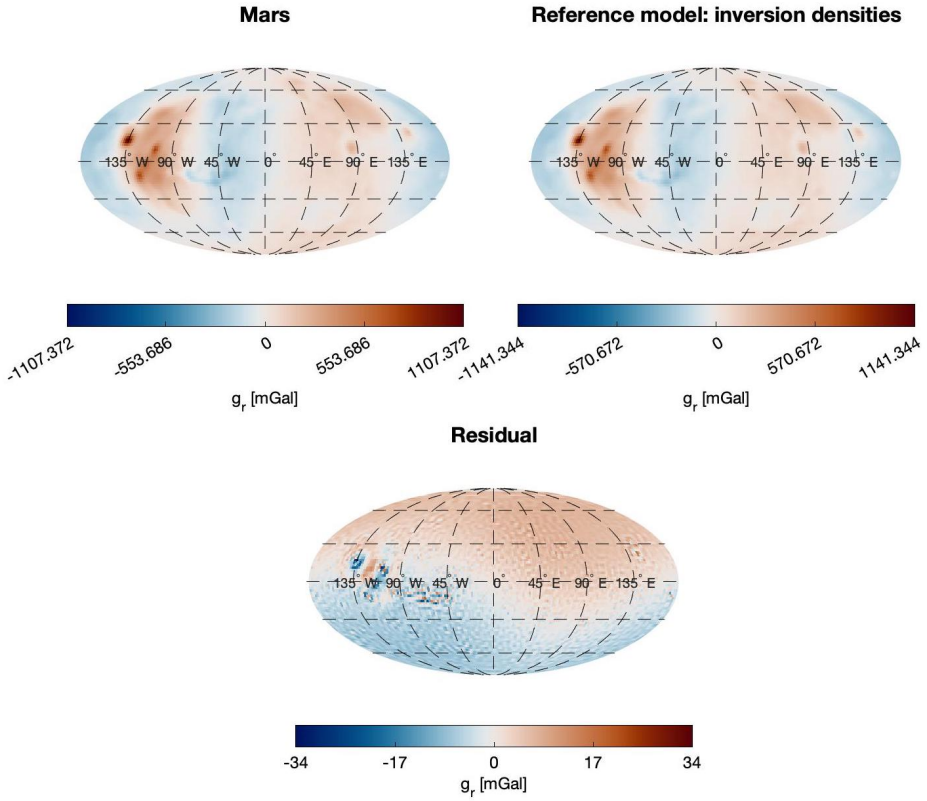

Figure 6.9: The top left figure shows the anomaly for Mars, the top right for the reference model with the obtained inversion densities, and the bottom figure shows the residual.

6.4.2. Gravitational Tensor

In Figure 6.10 the gravitational tensor of the reference planet with the density of the crust and mantle obtained from the inversion is plotted. In the top right, the input tensor of the Martian gravity is plotted, and in the bottom plot, the residual between the two is plotted. The residual has a maximum of ± 7% of the input signal, with most of the residual less than ± 1% of the input signal. The largest residuals are near the Tharsis region and Valles Marineris. The gravitational tensor in the zz direction of the reference model with uniform densities is plotted in the top right figure of Figure A.28. The residual between the reference model with uniform densities and Mars is plotted in the bottom figure of Figure A.28. This residual is used as input for the first iteration of the inversion.

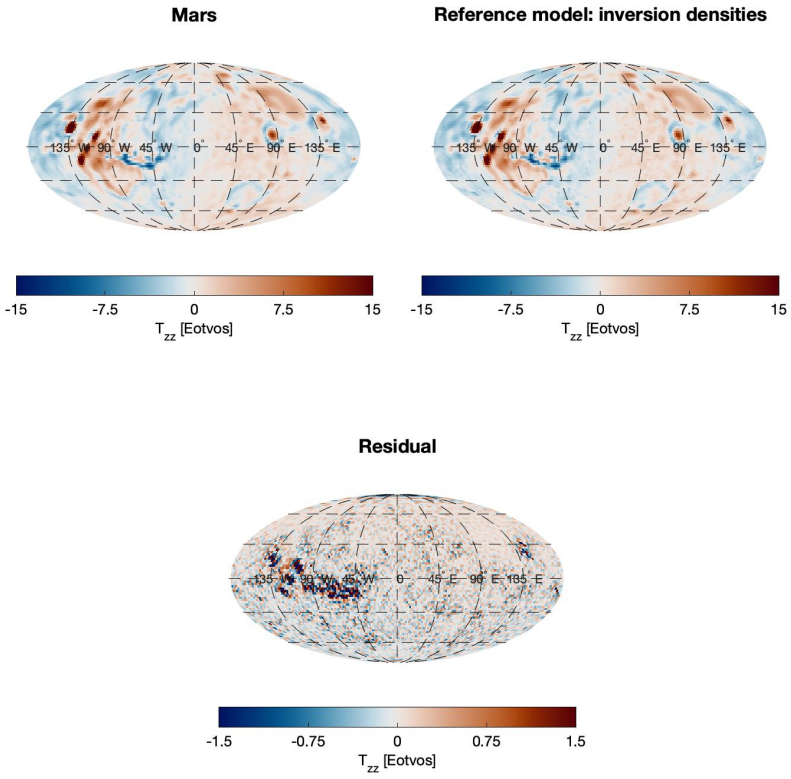

Figure 6.10: The top left figure shows the gravitational tensor in the zz direction for Mars, the top right for the reference model with the obtained inversion densities, and the bottom figure shows the residual. The two top plots are truncated for $T_{zz} = \pm$ 15 Eotvos and the bottom figure is truncated for $T_{zz} = \pm$ 1.5 Eotvos.

6.4.3. Power Spectrum

The power spectrum of the Martian gravity, the gravity of the reference model with uniform densities, and the reference model with the inversion densities are shown in subplot (a) of Figure 6.5. Visible in Figure 6.11 is that the power spectrum for degrees 1 and 2 is fitted very poorly. This has to do with the fact that these degrees are not fully taken into account in the inversion. The spherical harmonic terms C_{00}, C_{10}, C_{11}, S_{11}, and C_{20} are all set to 0, as explained in section 2.3. The reference model is a complete sphere, resulting in C_{20} already being very off. Therefore, the degrees need to be analyzed only for spherical harmonic degrees greater than 2. Visible is that the power spectrum for the reference model with uniform densities overestimated the Martian power spectrum for spherical harmonic degrees 3-15. These larger spherical harmonic degrees represent the large wavelength features of the planet. The large elastic thickness results in isostatic under-compensation of the large surface features. Therefore, the power spectrum of the reference model with uniform densities lies above the power spectrum of Mars for these spherical harmonic degrees. For these degrees, the reference model with the inversion densities very closely approximated the Martian power spectrum. The density variations can be seen as partially compensating for the large topographic features such as Hellas Basin, Utopia Basin, and Vastitas Borealis. The power spectrum of the inversion model closely follows the Martian power spectrum up to spherical harmonic degree 40, as can be seen in the zoomed-in plot in Figure 6.11. For larger spherical harmonic degrees, the power spectrum starts to wobble around the Martian power spectrum. From spherical harmonic degree 55, the inversion model, as well as the reference model with uniform densities, overestimates the Martian power spectrum. This might have to do with local compensation of small topographic features. The resolution of the model is too small to compensate for the small impact craters through the obtained densities. Therefore, the small wavelength features corresponding to the high SH degrees are overestimated for the reference model. Overestimation of the power spectrum means that there is more signal and, therefore, less compensation for these small wavelength features.

Looking at the power spectrum analysis for the synthetic planet, shown in subplot (c) of Figure 4.16, it is also visible that for the synthetic planet, the power spectrum is well fitted up to SH degree 45. For larger SH degrees,

the inversion power spectrum underestimates the synthetic planet power spectrum. For the Martian inversion, the opposite is the case. The power spectrum of the inversion model underestimates the Martian power spectrum for SH degrees > 55. This difference most likely has to do with the presence of small wavelength density variation within the crust and mantle of the synthetic planet and a lack of these small wavelength variations in the density of the crust and mantle of Mars. To further fit the power spectrum, a higher resolution than 2 by 2 degrees will be needed.

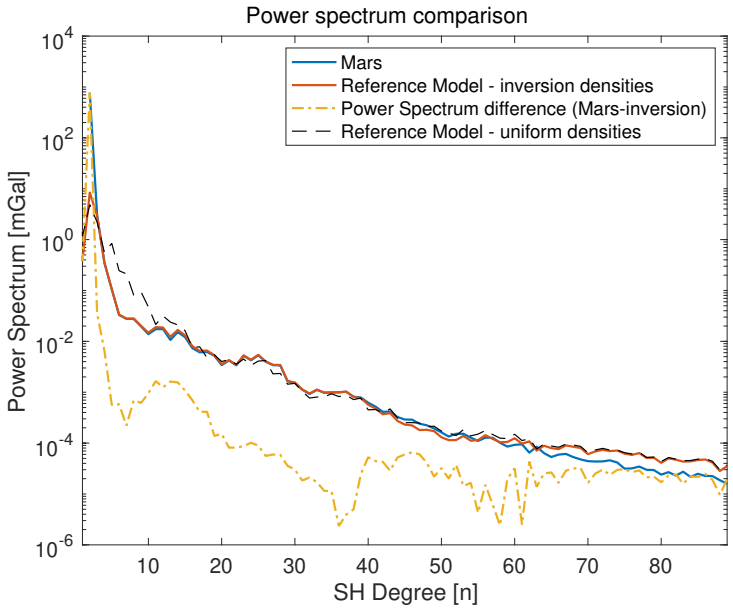

Figure 6.11: The power spectrum of the gravity of Mars, the reference model with uniform densities, ρ_c = 2700 kg/m^3 and ρ_m = 3800 kg/m^3, and the reference model with the density variations obtained through the inversion.

When looking at the power spectrum analyses performed in section 5.1, the effect of changing different parameters is shown. The power spectrum is well fitted up to SH degree 45, and the higher SH degrees are less well fitted. The effect of varying the elastic thickness on the power spectrum can be seen in Figure 5.15 and mainly has an effect on the smaller SH degrees. Based on this, varying the elastic thickness would most likely not yield a better fit for the larger SH degrees. Changing the wavelength pattern of the topography, or density, are the two parameters that have an effect on the larger SH degrees of the power spectrum. The topography is known and can, therefore, not be changed. Because of this, the misfit in the larger SH degrees most likely originates from small density variations. The resolution of the available gravity data is currently too low to be able to calculate these small wavelength density variations.

6.5. Model Assumptions

The Martian inversion model is based on many assumptions. For the two-layer model, a single obtained density from the inversion needs to be converted to two densities. This is explained in section 3.3. This conversion from one to two densities is based on multiple assumptions. The first assumption is that the mass of every column is equal. In subsection 5.2.3, subsection 5.2.4, and subsection 5.2.5, the effect of adding extra mass to the crust, the mantle, and both the crust and mantle has been studied. In this analysis, it was found that when extra mass was added to the crust and/or the mantle, the inversion started to diverge fast. The error was around 10 times the extra density variations when the density variations were added to only the crust or mantle and increased even more, when density variations to both the crust and mantle were added. Therefore, based on this analysis, it can be concluded that there are no large mass differences between the columns, but small density differences might be the case. The density differences of the crust were ± 650 kg/m^3 and for the mantle ± 230 kg/m^3. This would mean that a maximum density difference of 10% would be around ± 65 kg/m^3 for the crust and ± 23 kg/m^3 for the mantle. Also, looking at the power spectrum analysis shown in Figure 5.13, the power spectrum of the small SH degrees (up to ≈ 20) increases for small mass variations between the different columns. This increase in power spectrum up to SH degree 20 is not observed for the power spectrum of Mars.

Next to the calculations for the density, the model assumes a set crust-mantle boundary for the reference model.

The calculated crust-mantle density is based on a multitude of assumptions: 1) There is a uniform elastic thickness. 2) All topographic features are isostatically compensated using thin shell isostasy. 3) FRF applied to Airy isostasy crust-mantle boundary obtained with uniform densities.

In this study, a uniform elastic thickness was used to obtain the crust-mantle boundary. This elastic thickness was used in the flexural response function, given in Equation 2.11. This results in the elastic thickness used in this study being different from the elastic thickness used in most literature, which most often use Airy isostasy. This makes it difficult to compare the obtained elastic thickness in this thesis research to the ones obtained in literature. Using the flexural rigidity parameter, D, as explained in section 2.1, which relates the elastic thickness to both the Young's modulus as well as the Poisson ratio, instead of taking both ν and E constant and only varying the elastic thickness, might be a better option for future research.

The next assumption is that the topographic features are all isostatically compensated using thin shell isostasy. It was found by Qin [2021] that, when looking at the power spectrum of Mars as a whole, the thin shell model is the best approximation. This does not mean that the whole of Mars is compensated using the same isostatic model. Different regions might have different values for the elastic thickness or some regions might be isostatically compensated through Airy or Pratt isostasy. The thin shell FRF is applied to the crust-mantle boundary obtained with Airy isostasy. Based on the high densities for the large impact craters, Pratt isostasy might be the better option for these regions. Looking into a combination of isostasy methods could be a valuable addition to the model.

Lastly, the crust-mantle boundary is obtained using uniform densities for the crust and mantle. It was found that there are large density differences within the obtained crustal and mantle density. Therefore, a uniform density as input is not realistic for the crust-mantle boundary compared to the obtained results. Looking into changing the crust-mantle boundary for each iteration, based on the obtained density results, might be interesting to study for further research.

6.6. Evolution of Mars Based on the Obtained Densities

In this section, the obtained crustal density variations are compared to the geological map given by Tanaka et al. [2014], plotted in section A.8. This map has divided the Martian topography into different units and related them to the three historical periods of Mars, the Amazonian, Hesperian, and Noachian periods. In the obtained density, the large impact craters are clearly visible. In this section, specific topographic features are discussed. A separate plot of the obtained crustal density is given in Figure 6.12.

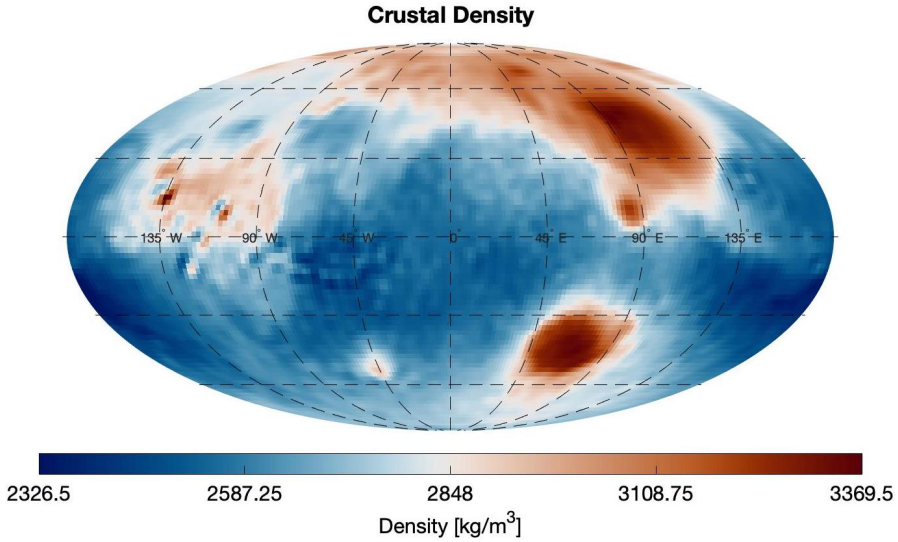

Figure 6.12: The crustal density obtained for the Martian inversion result, with T_e = 400 km, C = 105 km, $\rho_{c,ref}$ = 2700 kg/m^3 and $\rho_{m,ref}$ = 3800 kg/m^3.

Some of the map units used by Tanaka et al. [2014], as shown in section A.8, could be related to densities found in this study. The corresponding densities to these units are given in Table 6.7.

Table 6.7: A table relating the map units used in section A.8 by Tanaka et al. [2014], to the crustal densities found for the Martian inversion result, as shown in Figure 6.12.

Map Unit Name	Corresponding Crustal Density Range [kg/m^3]
Late Hesperian basin unit	3300-3350
Early Hesperian basin unit	3000-3100
Hesperian and Noachian basin unit	2850-2950
Noachian volcanic unit	2800-2900
Early Amazonian basin unit	3220-3350
Late Hesperian lowland unit	2950-3200
Amazonian volcanic edifice	3350-2900
Amazonian and Hesperian volcanic unit	2900-2950
Middle Noachian highland unit	2500-2700
Late Noachian highland unit	2500-2700
Early Noachian highland unit	2500-2700
Amazonian and Hesperian impact unit	2500-2700

6.6.1. Hellas Basin

According to [Tanaka et al., 2014], Hellas Basin is believed to originate from the late Hesperian period. The inner center is made out of the late Hesperian basin unit, which consists of Plains-forming deposits on the basin floor, finely layered in places and hundreds of meters thick. The eastern margins of Hellas are covered by the early Hesperian basin unit, and the western margins are formed by the Hesperian and Noachian basin unit, which are low-lying, plains-forming deposits, which have relatively low daytime IR brightness and have a thickness of at least hundreds of meters. In the obtained crustal density, as shown in Figure 6.12, it is visible that the center of Hellas Basin has the highest crustal density, around 3300-3350 kg/m^3. The eastern margins have a slightly lower density, around 3000-3100 kg/m^3, and the western margins have a density of around 2900-2950 kg/m^3. These different obtained crustal densities correlate to different periods in the Martian History.

To the southwest of the Hellas Basin, there is a slightly higher crustal density region, with densities between 2800 and 2900 kg/m^3. In the geological map, this region, marked the Malea Planum, consists of a Late Noachian volcanic unit, which is planar deposits tens of meters thick and tens to hundreds of kilometers across. The higher densities found in this region could correlate to the volcanic unit from a specific time period.

6.6.2. Argyre Basin

For the center of the Argyre Basin, a density between 2850 and 2900 kg/m^3 was found. According to Tanaka et al. [2014], it is believed that this region consists of the Hesperian and Noachian basin unit, similar to the western margins of Hellas Basin. For the Hellas basin regions, believed to consist of similar Basin units, slightly higher densities were found, around 50 kg/m^3, but in a similar range.

6.6.3. Utopia Basin, Isidis Basin, and Vastitas Borealis

Utopia Basin and Vastitas Borealis were found to have high density values in Figure 6.12, from 3220-3350 kg/m^3 for Utopia, to 2950-3100 kg/m^3 for Vastitas Borealis. For Isidis basin, crustal densities between 2950 and 3200 kg/m^3 were found. The impact crater part of Utopia Basin is believed to be made out of the early Amazonian basin unit [Tanaka et al., 2014], similar to a very small region on the western side of Hellas Basin. Near this region, densities of 3180 kg/m^3 were found for the crustal density of the Martian inversion result. This is slightly lower than what has been found near Utopia Basin but deviates only slightly, between the 2% up to 5%. Tanaka et al. [2014] believes that the vast majority of the Northern plains are made out of Late Hesperian lowland unit with smaller regions distributed within Vastitas Borealis made up of the Middle Amazonian lowland unit. Isidis Basin is also believed to be made out of the Late Hesperian lowland unit, and showed in Figure 6.12 similar densities to that of the northern plains and Vastitas Borealis.

6.6.4. Olympus Mons and the Tharsis region

The large volcanoes in the Tharsis region and Olympus Mons are believed to consist of the Amazonian volcanic edifice, which are shield-like edifices hundreds of kilometers across; made up of lobate flows. Towards the northwest of the large volcanoes, the late Amazonian apron unit was found, which are concentrically ribbed, knobby lobes extending as much as 500 km from shield-like edifices [Tanaka et al., 2014]. In Figure 6.12 high densities

were found for the large volcanoes in this region, but also lower densities were found to the north-west of these volcanoes, corresponding to the late Amazonian apron unit. The bulk of the Tharsis region is made out of Amazonian and Hesperian volcanic unit, which are stacked, gently sloping lobate flows. The higher density region, with densities between 2900 and 2950 kg/m^3, towards the north of the Tharsis region, can be related to these regions. Tanaka et al. [2014] also found the Deadalia Planum to be made out of the Amazonian and Hesperian volcanic unit, but the findings could not be related to what was found for the crustal densities of the Martian inversion result.

6.6.5. Arabia Terra down to the Noachis Terra

Lastly, the large region from the Arabia Terra down to the Noachis Terra was analyzed. This region does not contain any large volcanoes or impact craters but is heavily cratered with small impact craters, as can be seen in Figure 1.1. Densities between 2500 kg/m^3 and 2700 kg/m^3 were found. The topography of the Arabia Terra is around 4 km lower than that of the Noachis Terra, but no significant differences in the obtained crustal density were found between these regions. This region is believed to consist mainly of the Middle Noachian highland unit, as well as the Late Noachian highland unit and Early Noachian highland unit, and the Amazonian and Hesperian impact unit [Tanaka et al., 2014]. The impact units are all believed to be made out of the Amazonian and Hesperian impact unit. The impact craters in this region are relatively small impact craters when compared to Hellas, Argyre, and Isidis. The resolution of the used gravity is too low to observe density differences on such a small scale. It is, therefore, not possible to distinguish between the units found in [Tanaka et al., 2014].

7

Conclusions and Recommendations

This thesis study was performed to study the lateral density variations in the lithosphere of Mars. In previous studies, either the crustal density, mantle density, or both have been taken as uniform. This assumption is not likely to hold [Yuan et al., 2001], and therefore the density variations in both the crust and mantle are studied in this thesis research. The main research question was:

Can lithospheric density models, obtained by gravity inversion, be related to the Martian geological history?

By comparing the obtained densities to the geological map presented by Tanaka et al. [2014], a relation between specific map units, materials originating from a specific period of the Martian history, is made. Due to the lack of resolution in the Martian gravity data, it was not possible to relate densities to smaller regions. Only the large areas corresponding to specific map units could be related to the obtained density variations.

Different lithosphere models were studied. These models were all based on the thin shell isostasy model. It was found by Qin [2021], as well as by this research, that when looking at the power spectrum, the thin shell model is the best fitting isostasy model between SH degrees 4 and 17. Different parameters could be varied for these lithosphere models. The isostasy model could be implemented by applying the flexural response function to the Airy obtained crust-mantle boundary. This was done using the GSH package provided by Root and Vermeersen [2016]. Using this package, the boundaries could be converted from the spatial domain to the spherical domain and vice versa. The FRF is dependent on a few parameters: the elastic thickness, T_e, the Young's modulus, E, the Poisson ration, ν, and the density difference between the crust and mantle, $\Delta\rho$. Based on previous research, the Young's modulus was set constant to 100 GPa, and the Poisson ratio was set constant to 0.25. A larger value of the elastic thickness resulted in more global and less local compensation of the topographic features. For the Martian analyses, T_e was varied to study its behavior and the optimal value. To obtain the crust-mantle boundary with Airy isostasy, an average crustal thickness, C, a crustal density ρ_c, and mantle density ρ_m needed to be defined. If the difference between the crust and mantle density was increased, the roots of the crust-mantle boundary decreased.

The data used for this research were the gravity MRO120D data and the MOLA topography data. The gravity data has a resolution up to SH degree 120 but is only accurate up to SH degree 95. This is because the uncertainty in the data becomes larger than the actual data above SH degree 95. This low resolution of the gravity was the limiting factor of this research. A 2 by 2-degree grid was used, which corresponds to SH degree 89.

Different synthetic planets were created to analyze and better understand the inversion model. The topography and density variations of this synthetic planet were created using the Matérn covariance function. This is a method to calculate the covariance between two great circle points.

The gravity inversion was performed using a linear-least squares inversion. This resulted in a single density variation as output. This single density variation needed to be split into two density variations. This was done using two assumptions. Firstly, it is assumed that the mass of each column is equal. Second, it is assumed that the gravity of each column can be split into two point masses. One point mass is located in the center of mass of the crust, and the other is located in the center of mass of the mantle.

Varying the different input parameters of the synthetic planet on the inversion were studied. This was done to gain a better understanding of the final Martian inversion results and how to optimize the reference model. It was found that when ρ_c of the reference model was set larger than ρ_c of the synthetic planet, the output density started to diverge largely from the input density. For smaller values of ρ_c, the output results diverged much slower from the input. This was the opposite of what was observed for ρ_m, where too small values resulted in the output to diverge fast from the input density. Too large values of ρ_m for the reference model resulted in the output density to diverge much slower from the input. For variations in T_e, the output diverged slowly, both for smaller and larger values of T_e than the T_e of the synthetic planet. It was found that when the average crustal thickness was chosen too large, compared to C of the synthetic planet, the output diverged very fast. For too small values of C, the output diverged much slower. These insights were used for the optimization of the Martian reference model.

The optimal result for Mars, with the smallest density variations and gravitational tensor residual, was obtained for a reference planet with T_e = 400 km, C = 105 km, $\rho_{c,ref}$ = 2700 kg/m^3 and $\rho_{m,ref}$ = 3800 kg/m^3. When these input parameters were used for the inversion of Mars' gravity field, a final density difference of approximately 1000 kg/m^3 between the crust and mantle was obtained. A mean crustal density of approximately 2750 kg/m^3 and mean mantle density of approximately 3750 kg/m^3, were found. The density variations in the crust varied from -424 up to 618 kg/m^3 around the mean crustal density, and -228 and 133 kg/m^3 around the mean mantle density. The elastic thickness obtained through the inversion was found to lay somewhere between the 450 ± 50 km and the uniform crustal thickness between 100 ± 10 km. The crustal thickness is on the larger side of the crustal thickness used in previous research, between the 30 and 115 km. The elastic thickness is much larger than what was previously used in literature, most often around 70-100 km. This study uses a different isostasy model compared to previous literature, the thin shell model. The large lithospheric thickness and the large difference between the crustal and mantle density both resulted in small differences within the crust-mantle boundary. This also meant a thicker crust underneath the impact basins, compared to smaller density differences are a thinner elastic thickness. This, together with the large crustal densities obtained underneath the impact craters, was the basis for the conclusion that this method may not be correct in modeling the densities underneath impact craters. For the synthetic planet analyses, no impact craters were added. Therefore, it was not possible to study if these methods correctly work for modeling impact craters.

A summary of the crustal thickness and crustal and mantle densities of some topographic features are given in Table 7.1. Large crustal densities were found for the impact craters, which, together with the large obtained elastic thickness and density difference between the crust and mantle, led to the conclusion that the large impact craters may be compensated using a different isostasy method. The volcanoes outside the Tharsis region were found to be well compensated using the thin shell method, and small densities were found compared to the volcanoes in the Tharsis region, as well as what has been found in previous literature. The smaller densities for these stand-alone volcanoes might have to do with the compensation of these volcanoes due to the curvature of the planet, which is taken into account with the thin shell isostasy model. This has not been used previously in the literature studies analyzed in this thesis study.

Table 7.1: The mean crustal thickness, mean crustal density, and mean mantle density obtained for some of the Martian surface features.

Topographic feature	Crustal thickness [km]	Crustal Density [kg/m^3]	Mantle Density [kg/m^3]
Hellas Basin	93	3345	3630
Utopia Basin	90	3300	3640
Isidis Basin	97	3200	3650
Argyre Basin	105	2870	3740
Tharsis Region	120-130	2770-3370	3750-3560
Olympus Mons	127	3370	3560
Alba Mons	112	2660	3810
Elysium Mons	100	2770	3780

It was found that the Martian power spectrum could be fitted up to SH degree 40. In the analyses for the synthetic planet, it was also found that the inversion power spectrum could only fit the synthetic planet power spectrum up to SH degree 45. To fit the larger SH degrees, a higher resolution gravity field would be needed.

Recommendations

As explained in chapter 6, multiple assumptions have been made for the reference model. To further improve the model, a better reference model will need to be created. One of the options is to use a combination of different isostasy methods. For instance, a study could be performed into the possibilities of Pratt isostasy for the impact craters, as well as different elastic thickness values. It is also recommended to use the flexural rigidity parameter, D, as explained in section 2.1, which relates the elastic thickness to both the Young's modulus as well as the Poisson ratio, instead of taking both ν and E constant and only varying the elastic thickness.

It would also be interesting to look into changing the reference model in-between iterations. For this study, the densities of the reference model were changed, but the boundaries were not changed between iterations. Large density variations within the crust were found, while the obtained crust-mantle boundary assumed uniform densities for the crust and mantle and, therefore, also uniform density differences. Including the obtained densities from the previous iteration in the calculation of a new crust-mantle boundary could therefore improve the model.

For the so-called two-layer inversion, actually, only one layer was inverted. One density for the whole layer was obtained, from which a variation in the center of mass was obtained. This resulted in part of the signal being lost, and many iterations, as well as a multiplication factor, were needed. To make the inversion more realistic, a new study could be performed which could rewrite the density inversion to obtain a center of mass shift. This center of mass could then immediately be used instead of obtaining it from the single-layer density.

Another option would be to rewrite the inversion to an actual two-layer inversion. This would result in no signal being lost in the inversion process. This is a difficult task, but when improved, it could improve the number of iterations needed and possibly disregard the use of the multiplication factor.

A

Appendix

A.1. One layer inversion - models 2 and 3

An extra study was performed on the effect of changing the topography and density variations, on the residuals in the fit. In this 10 different topographies (10 different seed numbers for the Matèrn covariance function) and 12 different density distributions (also for varying seed numbers) were combined, resulting into 120 different synthetic planets. Initially, the residual was slightly correlated with the variations within the topography and/or density, when only 1 iteration was used. When the number of iterations was increased, this correlation vanished and the results converted. A maximum of 4 iterations were performed or until the difference between the input tensor and inversion tensor was smaller than smaller than 2e-3 Eotvos for model 2, and 5e-3 Eotvos for model 3. The standard deviation between the input tensor and inversion tensor is plotted in Figure A.1 against the RMS between the input density minus the inversion density divided by the maximum input density. Visible on the y axis is that after 3-4 iterations, a maximum percentile error of around 10% for model 2 was achieved. The percentile error of the RMS of the density difference was used, because after some iterations, polar errors occurred. When a varying lower boundary was added, for model 3, the maximum percentile error increased slightly up to around 12%.

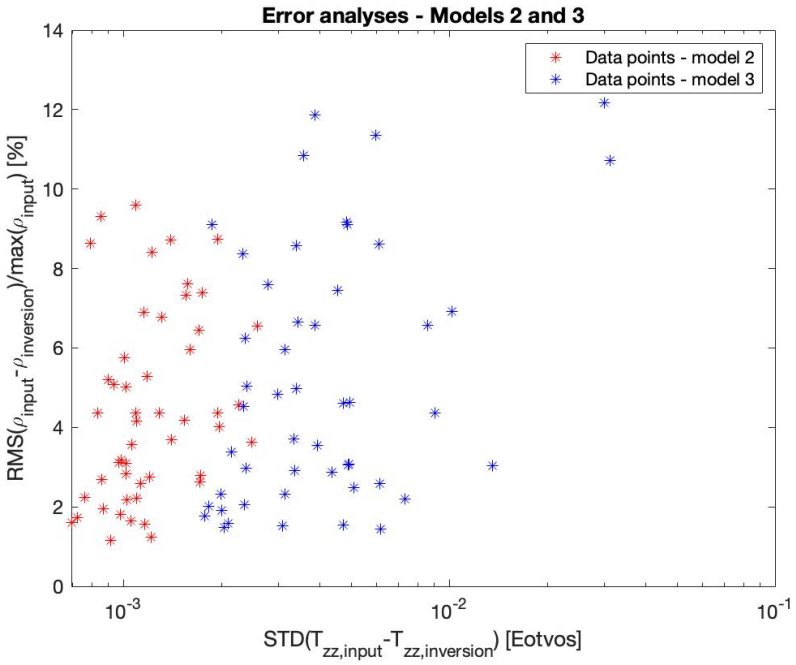

Figure A.1: The RMS between the input density minus the inversion density divided by the maximum input density plotted against the standard deviation between the input tensor and inversion tensor for 120 different 1-layer inversion models, both for model 2 and model 3.

A.2. $\lambda - \sigma$ analyses

A.2.1. Variation in layer thickness

First the influence of varying the thickness of the layer, while keeping the Centre of Mass at a constant depth, is analyzed. All models had a constant Centre of Mass at -50 km depth. First a layer ranging from -40 to -60 km was used, second a layer ranging from -25 to -75 km was used, and lastly a layer ranging from 0 to -100 km was used. The $\lambda - \sigma$ plots are shown in Figure A.2.

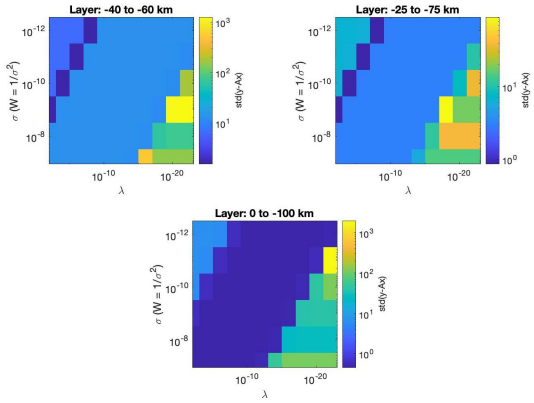

Figure A.2: $\lambda - \sigma$ analyses plot for variation in layer thickness.

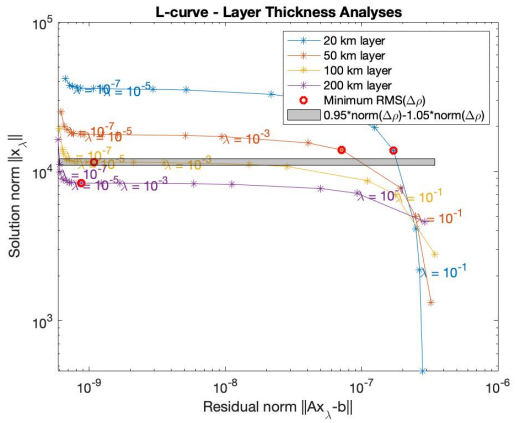

Figure A.3: L-curve for both variation in layer thickness.

In this figure it is visible, that for the 20 km and 50 km layers, there is only 1 optimal line with combinations for $\lambda - \sigma$. For the thickets layer, of 100 km, there are 7 times as many combinations possible, which still yield good results. The optimal relation between λ and σ for the 20 km and 50 km layer is: $\sigma = \lambda^{0.5} \cdot 10^{-8}$ or rewritten this becomes: $\lambda = \sigma^2 \cdot 10^{16}$. For the 100 km layer, there is a wider range, and slightly shifts to the right: $\sigma = \lambda^{0.5} \cdot [10^{-7} \quad 10^{-2}]$ or rewritten this becomes: $\lambda = \sigma^2 \cdot [10^{14} \quad 10^{4}]$.

A.2.2. Variation in layer Centre of Mass

For variations in the CM, a reversed result is visible to the variation in layer depth. Three different CM depths were analyzed, all with a 50 km layer. For the CM depth of 25 km, a layer from 0 to -50 km was used. For the CM depth of 50 km, a layer from -25 to -75 km was used. And lastly, for a CM depth of 75 km, a layer from -50 to -100 km was used.

In Figure A.4 is visible that for CM = -50 km and CM = -75 km, there is only 1 optimal relation line. For a more shallow depth of CM = -25 km, there is a wider range of optimal relations between λ and σ.

The optimal relation between λ and σ for a CM depth of 50 km and 75 km is: $\sigma = \lambda^{0.5} \cdot 10^{-8}$ or rewritten this becomes: $\lambda = \sigma^2 \cdot 10^{16}$. For the CM depth of 25 km, there is a wider range, and slightly shifted to the right: $\sigma = \lambda^{0.5} \cdot [10^{-7} \quad 10^{-5}]$ or rewritten this becomes: $\lambda = \sigma^2 \cdot [10^{14} \quad 10^{10}]$.

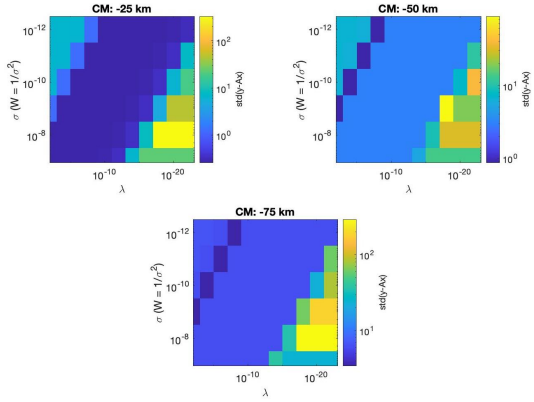

Figure A.4: $\lambda - \sigma$ analyses plot for variation in CM depth.

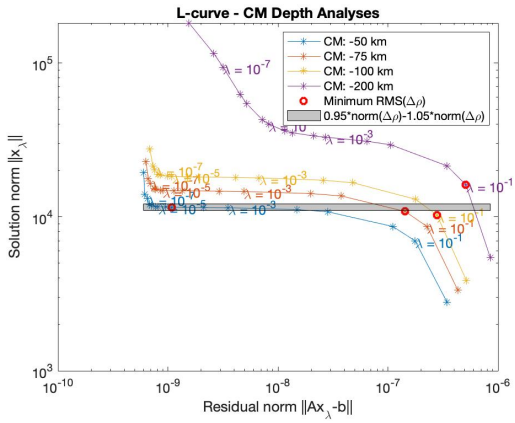

Figure A.5: L-curve for both variation in CM depth.

A.2.3. Variation in both layer Centre of Mass and Thickness

After this both the depth of the CM and the layer thickness were varied. This was done to observe the dominant behavior, or to study how the two behaviors influence each other.

The optimal relation between λ and σ for the 0 to -25 km layer is: $\sigma = \lambda^{0.5} \cdot 10^{-6}$ or rewritten this becomes: $\lambda = \sigma^2 \cdot 10^{12}$. For the 0 to -50 km layer, there is a wider range: $\sigma = \lambda^{0.5} \cdot [10^{-7} \quad 10^{-5}]$ or rewritten this becomes: $\lambda = \sigma^2 \cdot [10^{14} \quad 10^{10}]$. For the 0 to -100 km layer, the range is the widest, with the optimal given bu the following 2 equations: $\sigma = \lambda^{0.5} \cdot [10^{-7} \quad 10^{-2}]$ or rewritten this becomes: $\lambda = \sigma^2 \cdot [10^{14} \quad 10^{4}]$.

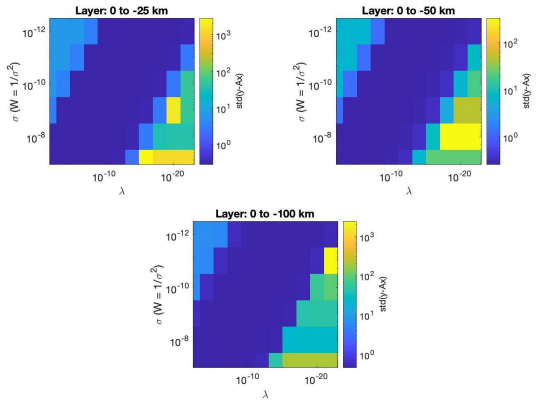

Figure A.6: $\lambda - \sigma$ analyses plot for variation in both layer thickness and variation in CM depth.

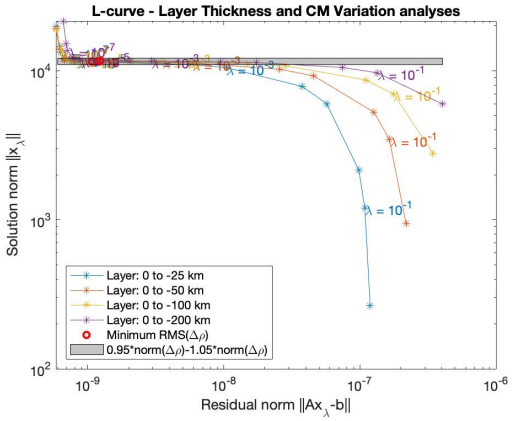

Figure A.7: L-curve for both variation in layer thickness and CM depth.

A.2.4. Variation in $\Delta\rho$

Next up the changes in density variations, $\Delta\rho$, are analyzed. Small $\Delta\rho$ variations have maximum density variations of $\pm$ 5 kg/m^3, medium $\Delta\rho$ variations have maximum density variations of $\pm$ 50 kg/m^3, and large $\Delta\rho$ variations have maximum density variations of $\pm$ 500 kg/m^3.

Looking at the overall profiles, shown in Figure A.8, they are not largely influenced by the different density variations. The smaller the density variations ($\Delta\rho$), the larger the optimal range for λ and σ. The optimal relation for small density variations is:$\sigma = \lambda^{0.5} \cdot [10^{-7} \quad 10^{-2}]$ or rewritten this becomes: $\lambda = \sigma^2 \cdot [10^{14} \quad 10^{4}]$. For medium density variations, this range becomes slightly smaller: $\sigma = \lambda^{0.5} \cdot [10^{-7} \quad 10^{-5}]$ or rewritten this becomes: $\lambda = \sigma^2 \cdot [10^{14} \quad 10^{10}]$. And for larger density variations, this range stays the same, but a more optimal line of $\sigma = \lambda^{0.5} \cdot 10^{-6}$ or rewritten this becomes: $\lambda = \sigma^2 \cdot 10^{12}$ becomes visible.

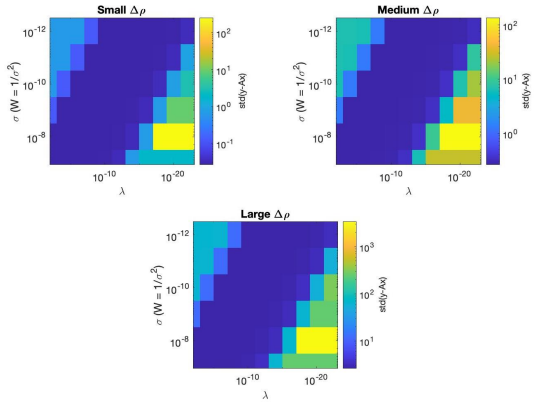

Figure A.8: $\lambda - \sigma$ analyses plot for variation in the density differences within the 1-layer model.

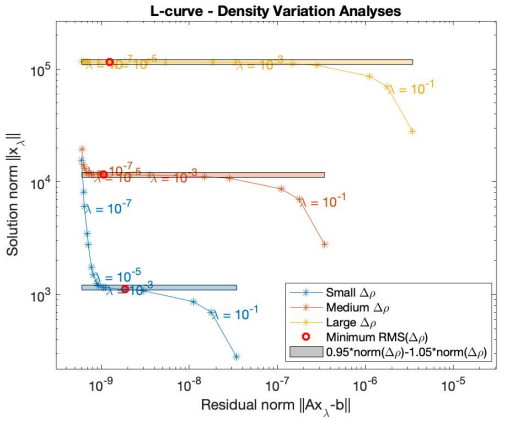

Figure A.9: L-curve for variation in the maximum density variations of the inversion layer.

A.2.5. Variation in Seed Number

Now the effect of changing the density pattern is analyzed. This density pattern can be changed by varying the seed numbers of the Matèrn covariance function. The different obtained profiles are shown in Figure A.10.

The overall pattern is not largely influenced by the 3 different seed numbers, as is visible in Figure A.11. The overall optimal range is between: $\sigma = \lambda^{0.5} \cdot [10^{-7} \quad 10^{-2}]$ or rewritten this becomes: $\lambda = \sigma^2 \cdot [10^{14} \quad 10^{4}]$.

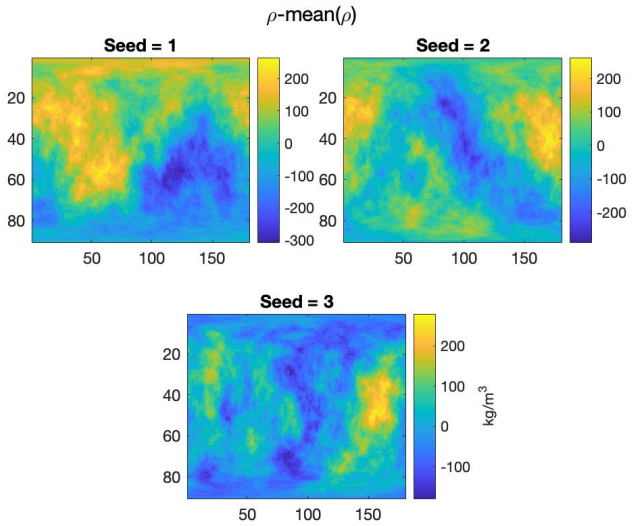

Figure A.10: The density variations corresponding to the different seed numbers, used in the Matèrn covariance function, to obtain the $\lambda - \sigma$ plots shown in Figure A.11.

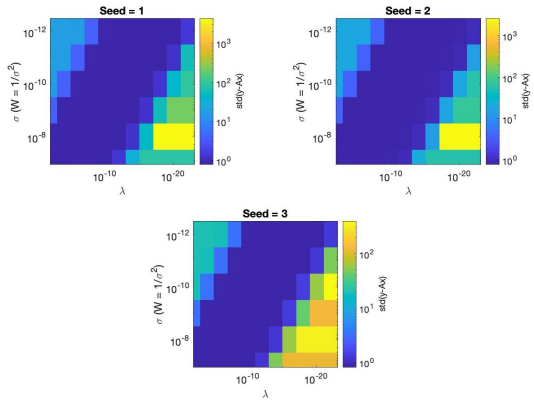

Figure A.11: $\lambda - \sigma$ analyses plot for variation in seed numbers with which the density profile was obtained using the Matèrn covariance function.

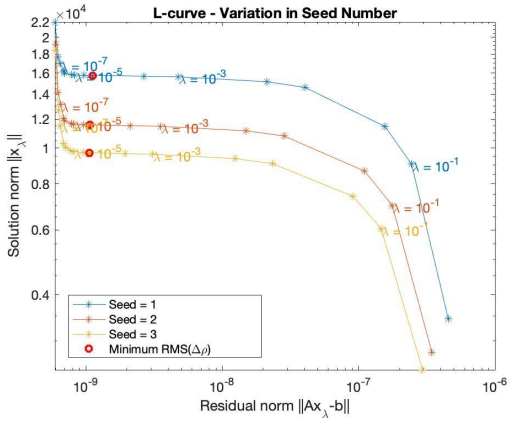

Figure A.12: L-curve for variation in seed number for the Matèrn covariance function of the density variations, which influence the density pattern.

A.2.6. Variation in κ

Lastly, varying the wavelength patterns of the density profiles, are analyzed. This can be done by changing the smoothness parameter of the Matèrn covariance matrix. The different density profiles are given in Figure A.13.

Similar to changing the seed number, the overall pattern in the $\lambda - \sigma$ plots is not largely influenced by changing the smoothness parameter, κ, as is visible in Figure A.14. The overall optimal relation is between: $\sigma = \lambda^{0.5} \cdot [10^{-7} \quad 10^{-2}]$ or rewritten this becomes: $\lambda = \sigma^2 \cdot [10^{14} \quad 10^{4}]$. For smaller wavelength patterns in the density profile, $\kappa = 0.3$, the optimal relation is: $\sigma = \lambda^{0.5} \cdot 10^{-6}$ or rewritten this becomes: $\lambda = \sigma^2 \cdot 10^{12}$. For medium wavelength patterns in the density profile, $\kappa = 0.9$, the optimal relation is: $\sigma = \lambda^{0.5} \cdot [10^{-6} \quad 10^{-5}]$ or rewritten this becomes: $\lambda = \sigma^2 \cdot [10^{12} \quad 10^{10}]$. For large wavelength patters in the density profile, $\kappa = 1.5$, the optimal relation is: $\sigma = \lambda^{0.5} \cdot [10^{-6} \quad 10^{-3}]$ or rewritten this becomes: $\lambda = \sigma^2 \cdot [10^{12} \quad 10^{6}]$.

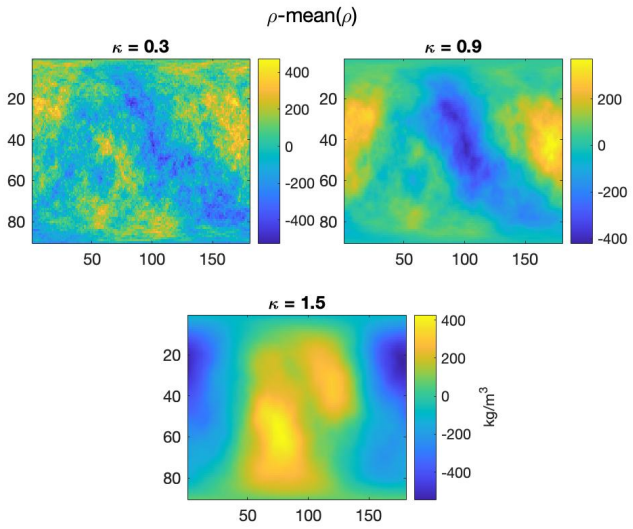

Figure A.13: The density variations corresponding to the different κ values, used in the Matèrn covariance function, to obtain the $\lambda - \sigma$ plots shown in Figure A.14.

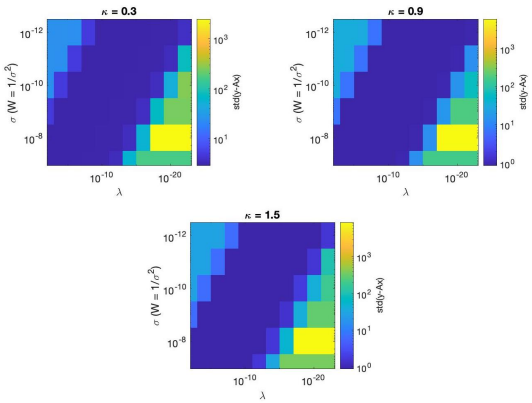

Figure A.14: $\lambda - \sigma$ analyses plot for variation in kappa value, used to obtain the density difference for the Matèrn covariance function.

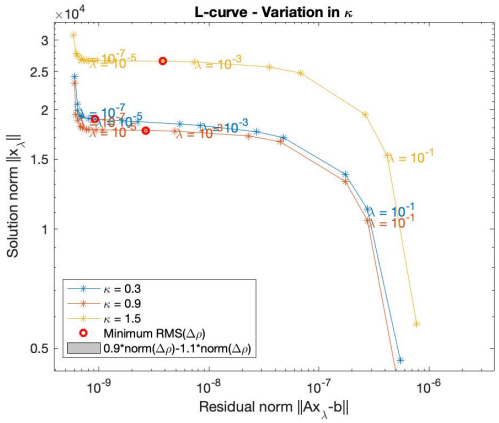

Figure A.15: L-curve for variation in κ for the Matèrn covariance function of the density variations, which influence the wavelength pattern of the density variations.

A.3. Two-Layer Inversion - Input Type Analyses 50 iterations

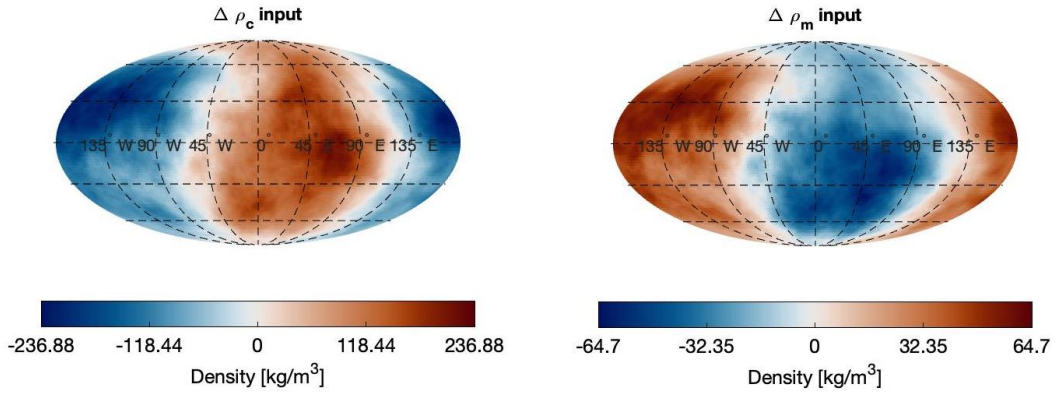

Figure A.16: The input crustal and mantle density variations. These density variations are used as input for the analyses of the different input gravity data types.

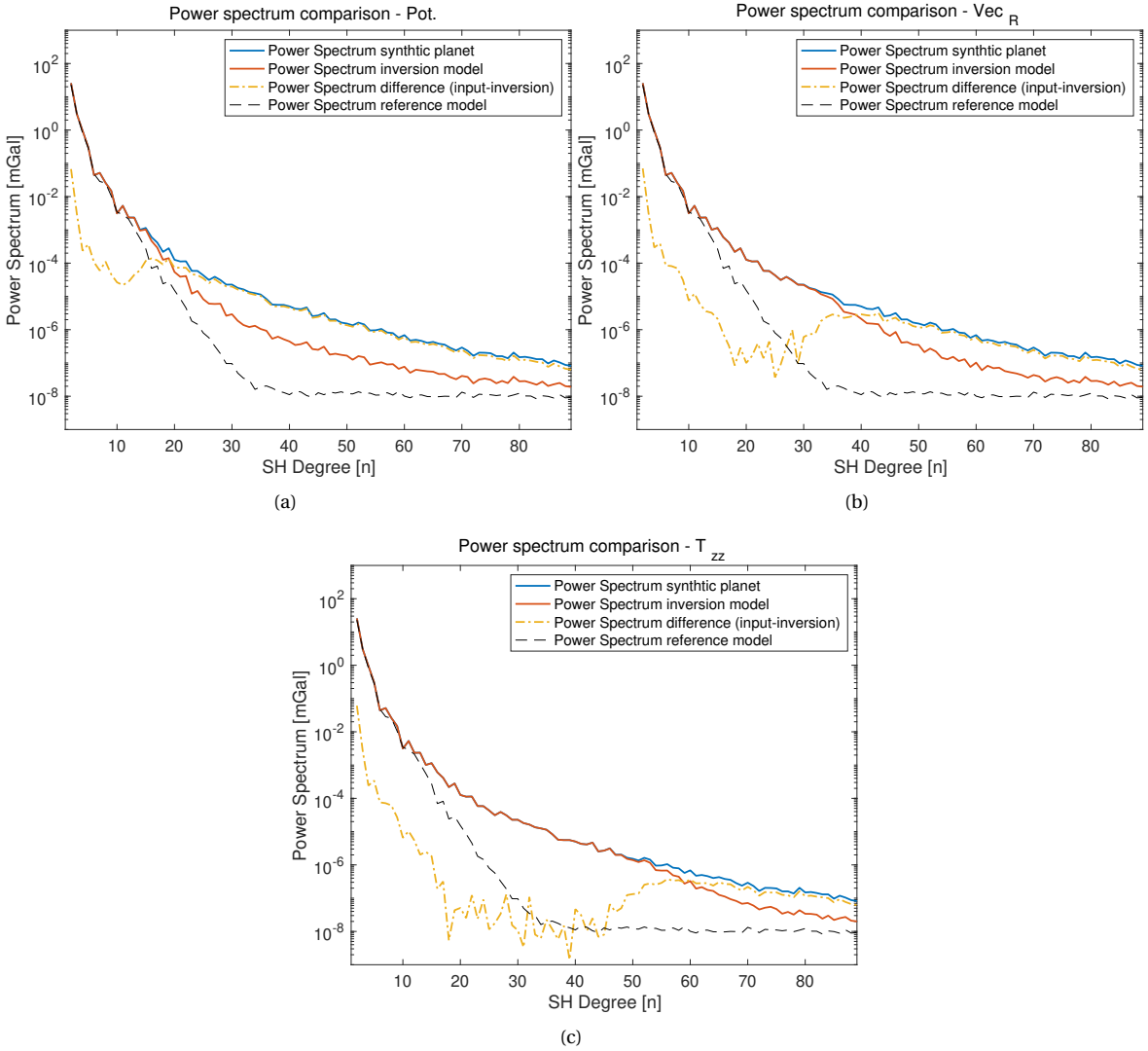

Figure A.17: The power spectrum of the inversion planet obtained using the reference planet with the densities changed to the densities obtained from the inversion. Subplot (a) shows the results using the gravitational potential as input data for the inversion, (b) for the gravitational vector in the z direction, and (c) for the gravitational tensor in the zz direction.

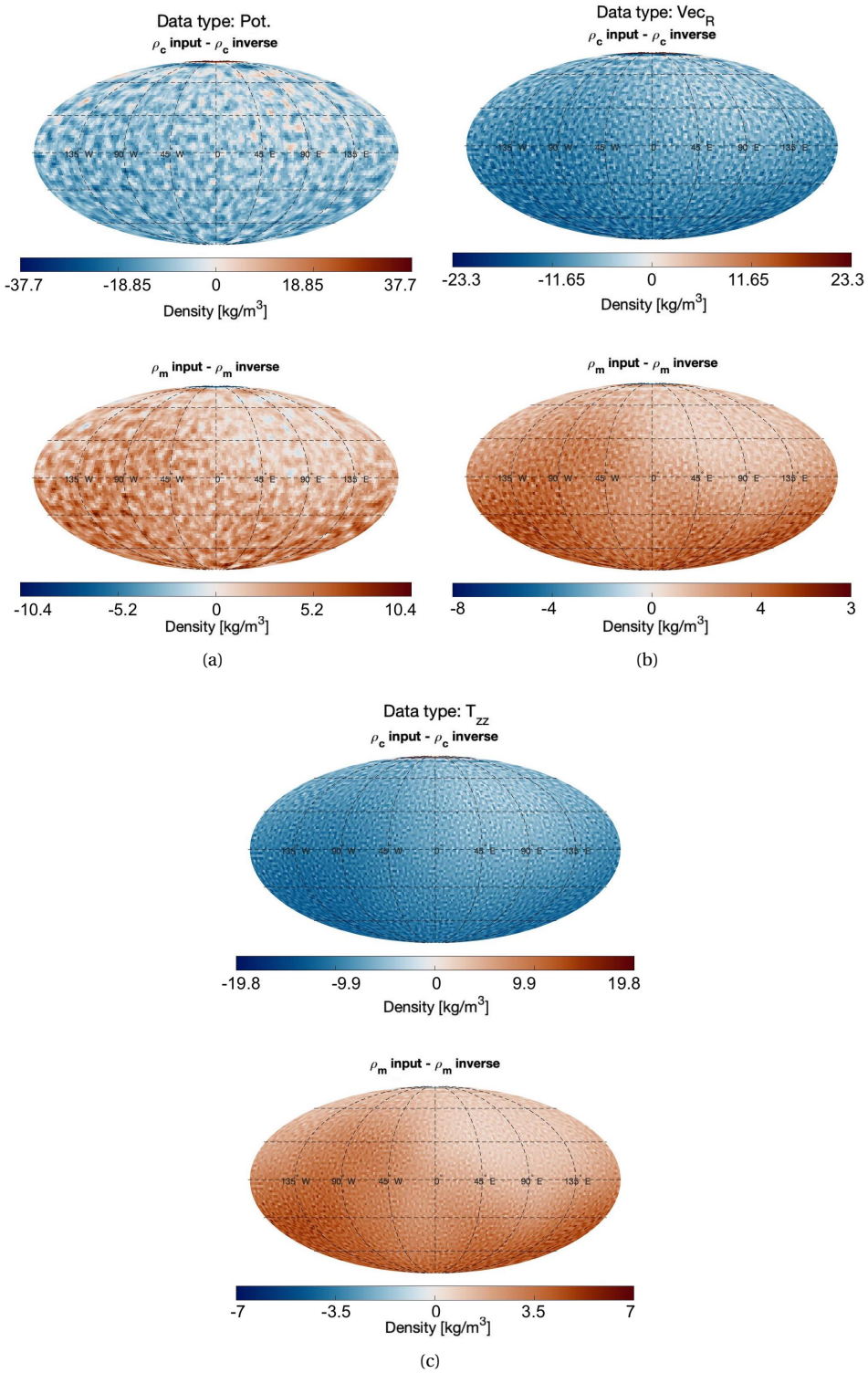

Figure A.18: For each subplot, the top plot shows the difference between the input crustal density, ρ_c input, and the crustal density obtained using the inversion method, ρ_c inverse. The bottom plot shows the same plot, but for the mantle density instead of the crustal density. Subplot (a) shows the results using the gravitational potential as input data for the inversion, (b) for the gravitational vector in the z direction, and (c) for the gravitational tensor in the zz direction.

A.4. Plots Variation Input Parameters Reference Model

For each input parameter analyses, two plots are made for which $max(\Delta\rho_{inp} - \Delta\rho_{inv})/max(\Delta\rho_{inp} \approx 50\%$. One of these plots is for the minimum multiplication factor, for which the maximum difference is approximately 50%, and the other is for the maximum multiplication factor for which this is still the case. In Figure A.19 the crustal and mantle input density, as well as inversion density, when all input parameters were chosen equal to the input parameters of the synthetic planet.

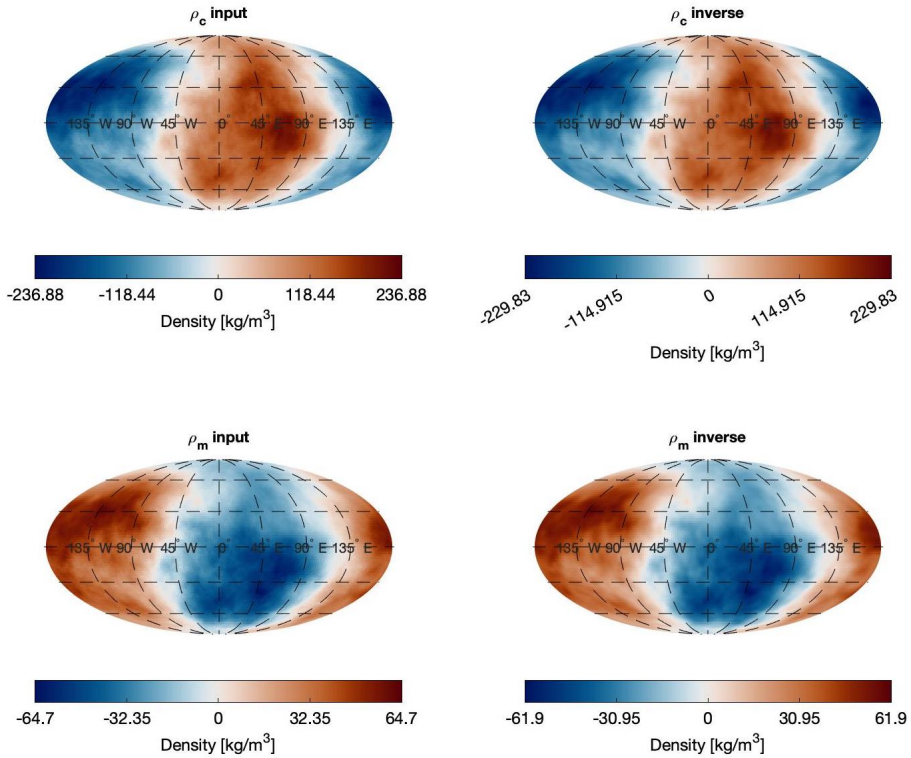

Figure A.19: The left plots shows the input crustal and mantle density, and the left plots the obtained crustal and mantle density from the inversion with the correct input parameters for the reference model.

82 A. Appendix

A.4.1. Crustal Density Variation

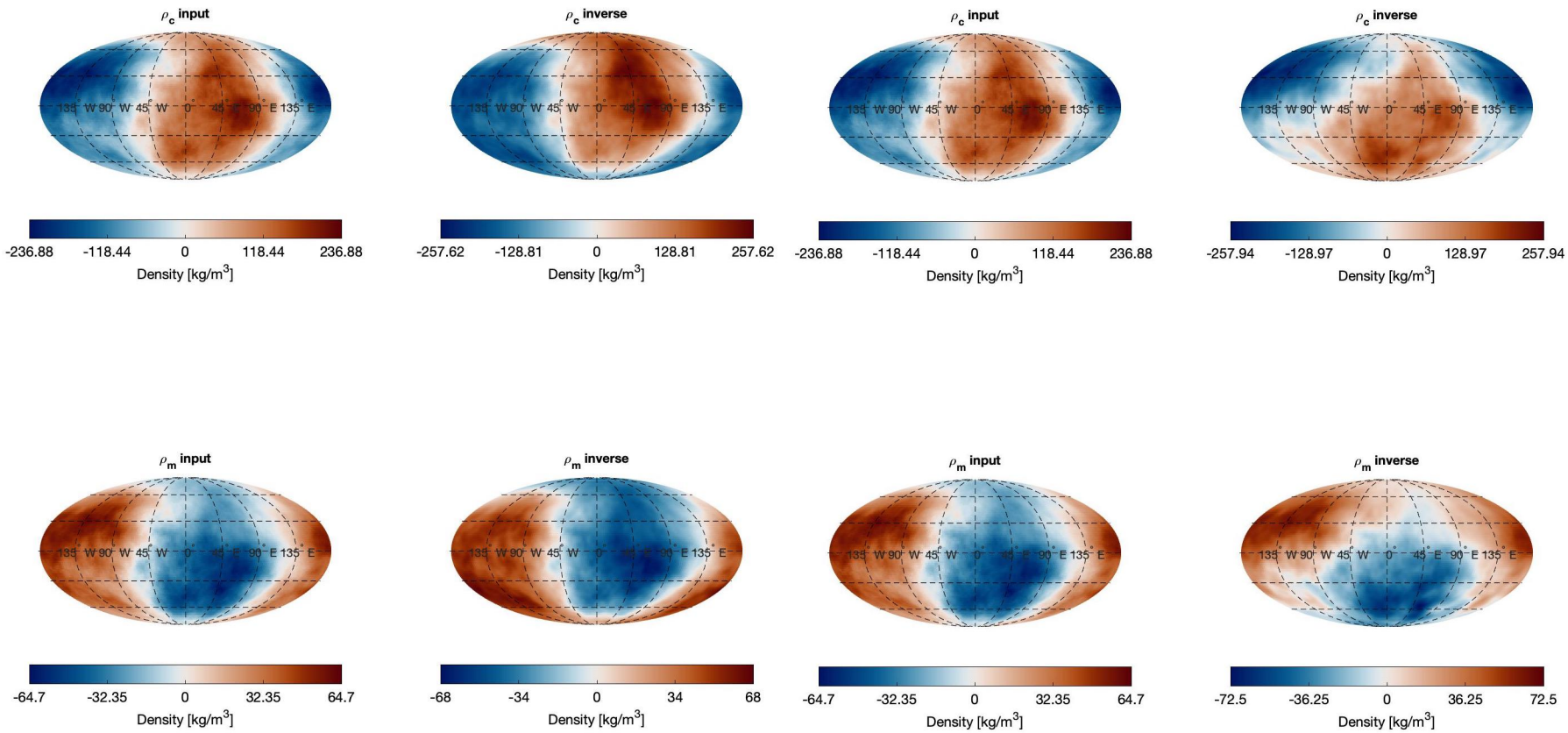

Figure A.20: Each subplot shows the input crustal and mantle density, as well as the obtained crustal and mantle density from the inversion. Subplot (a) shows the results for $\rho_c = 0.95\rho_{c,inp}$, and (b) shows the results for $\rho_c = 1.05\rho_{c,inp}$.

A.4.2. Mantle Density Variation

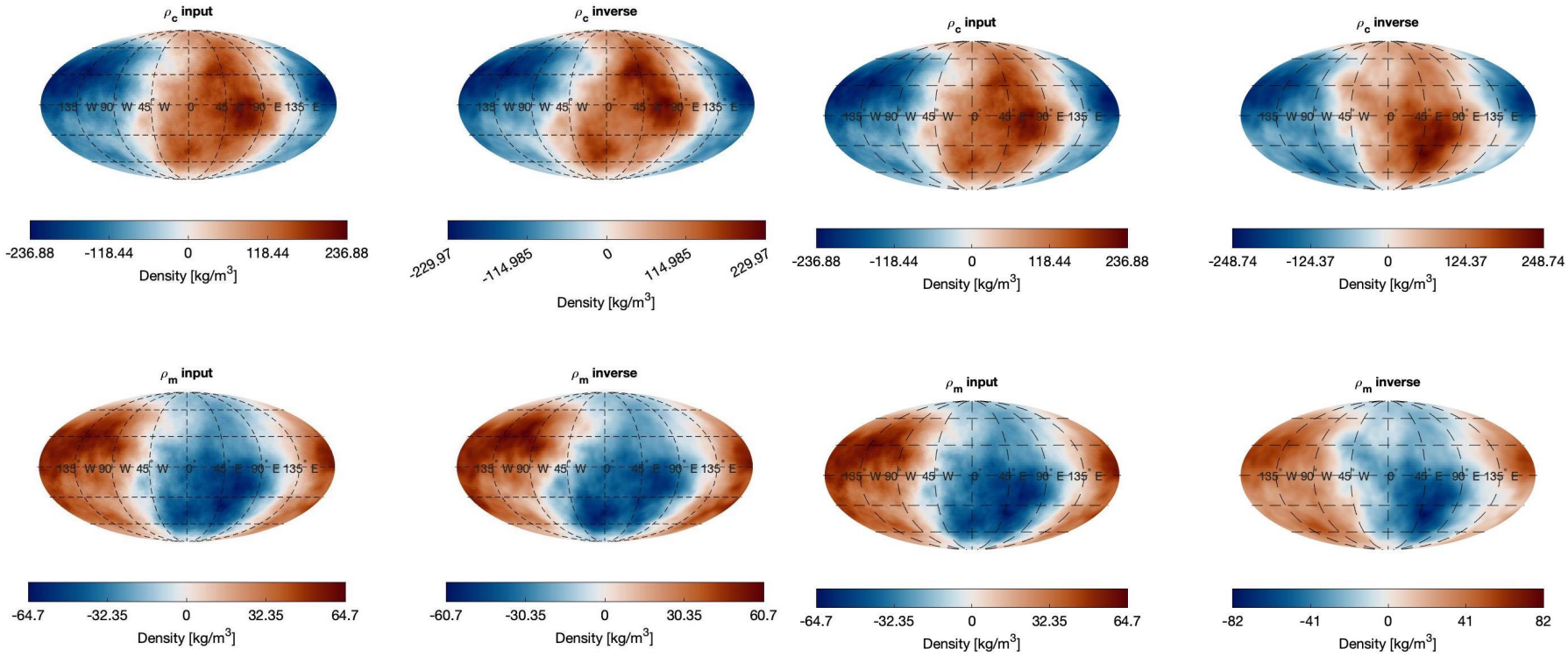

Figure A.21: Each subplot shows the input crustal and mantle density, as well as the obtained crustal and mantle density from the inversion. Subplot (a) shows the results for $\rho_m = 0.95 \cdot \rho_{m,inp}$, and (b) shows the results for $\rho_m = 1.4 \cdot \rho_{m,inp}$.

A.4.3. Elsatic Thickness Variation

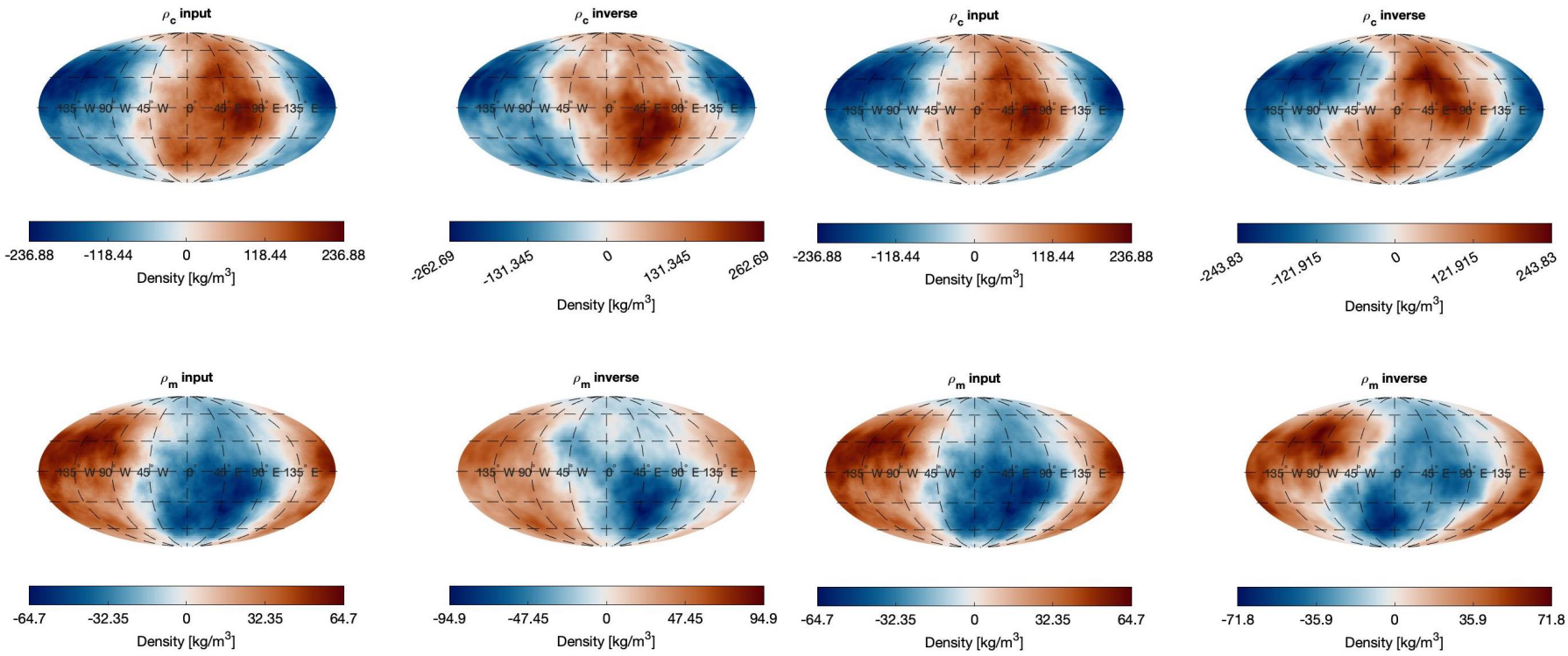

Figure A.22: Each subplot shows the input crustal and mantle density, as well as the obtained crustal and mantle density from the inversion. Subplot (a) shows the results for $T_e = 0.1\,T_{e,inp}$, and (b) shows the results for $T_e = 2\,T_{e,inp}$.

A.4.4. Young's Modulus Variation

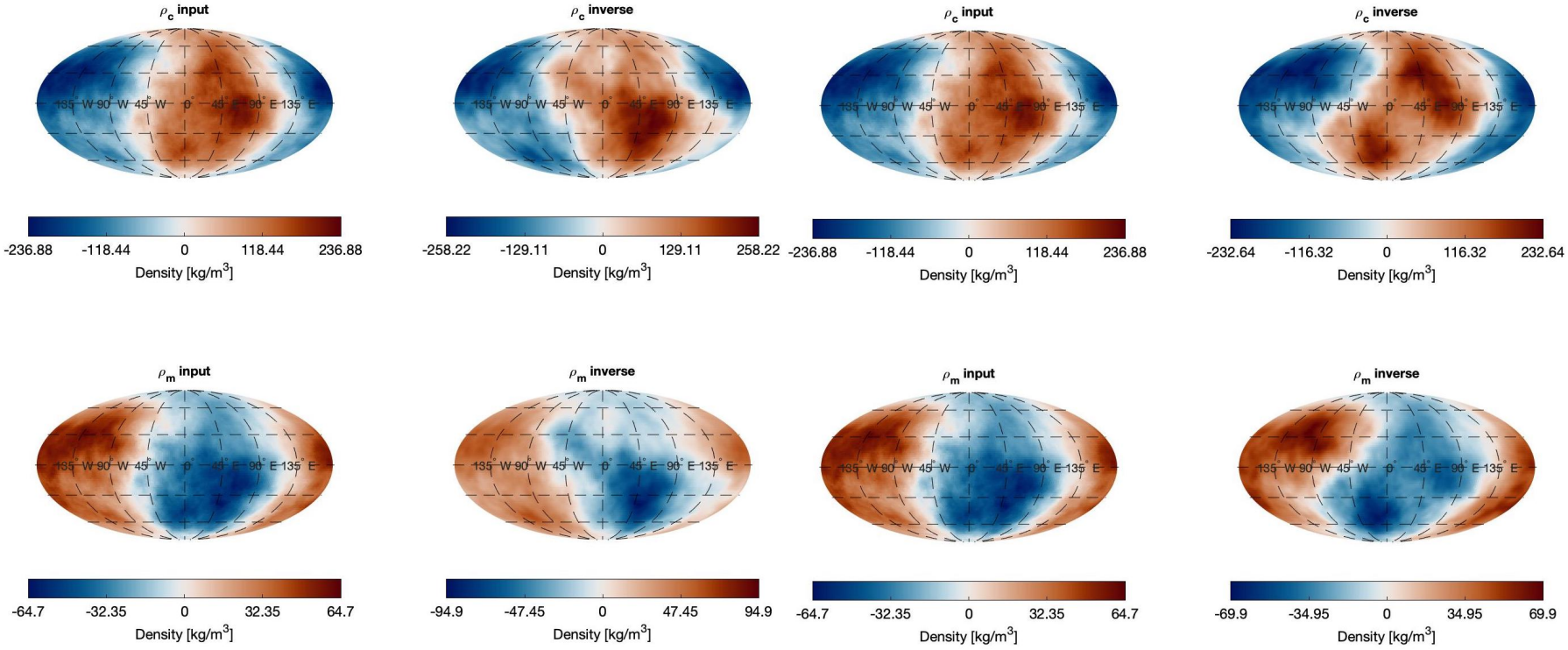

Figure A.23: Each subplot shows the input crustal and mantle density, as well as the obtained crustal and mantle density from the inversion. Subplot (a) shows the results for $E = 0.1E_{inp}$, and (b) shows the results for $E = 2E_{inp}$.

A.4.5. Average crustal Thickness Variation

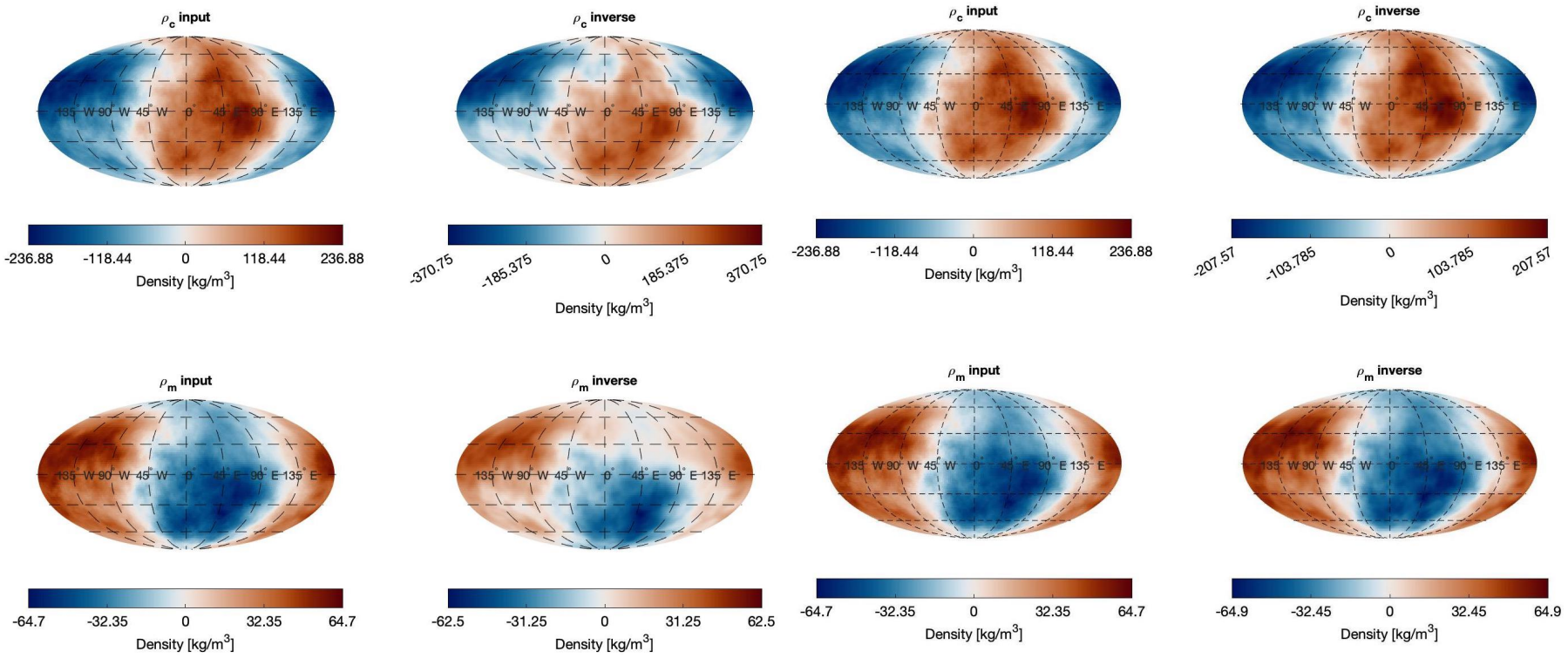

Figure A.24: Each subplot shows the input crustal and mantle density, as well as the obtained crustal and mantle density from the inversion. Subplot (a) shows the results for $C = 0.6C_{inp}$, and (b) shows the results for $C = 1.1C_{inp}$.

A.5. Density and crust-mantle boundary results for minimum $max(\Delta\rho_{c,inv})$

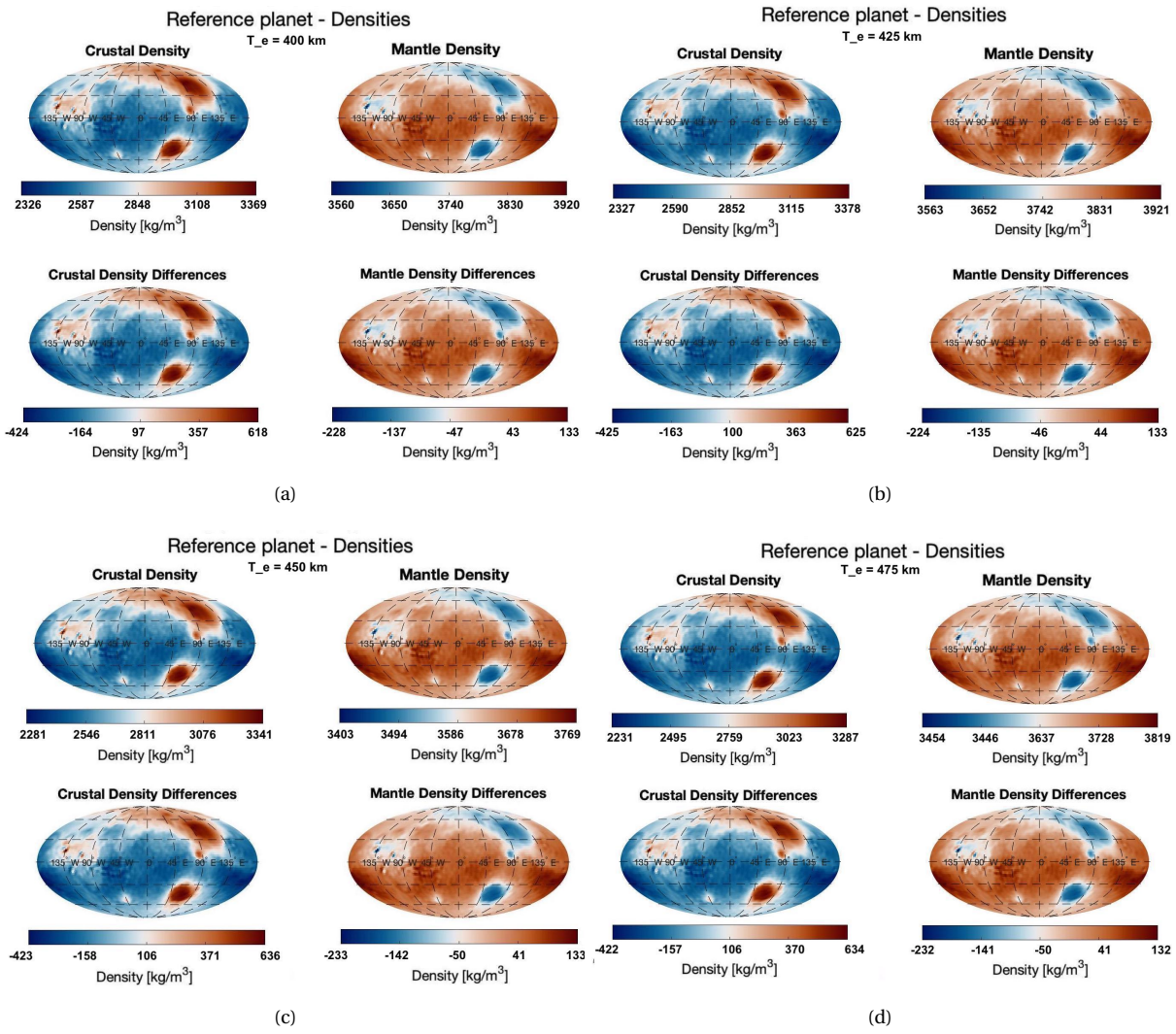

Figure A.25: The crustal and mantle density and density variations obtained through the Martian inversion. For the inversion a multiplication factor of 30 and 25 iterations were used. These results were obtained for a reference model with the topography and crust-mantle boundary shown in Figure 6.6, for the same subplots respectively.

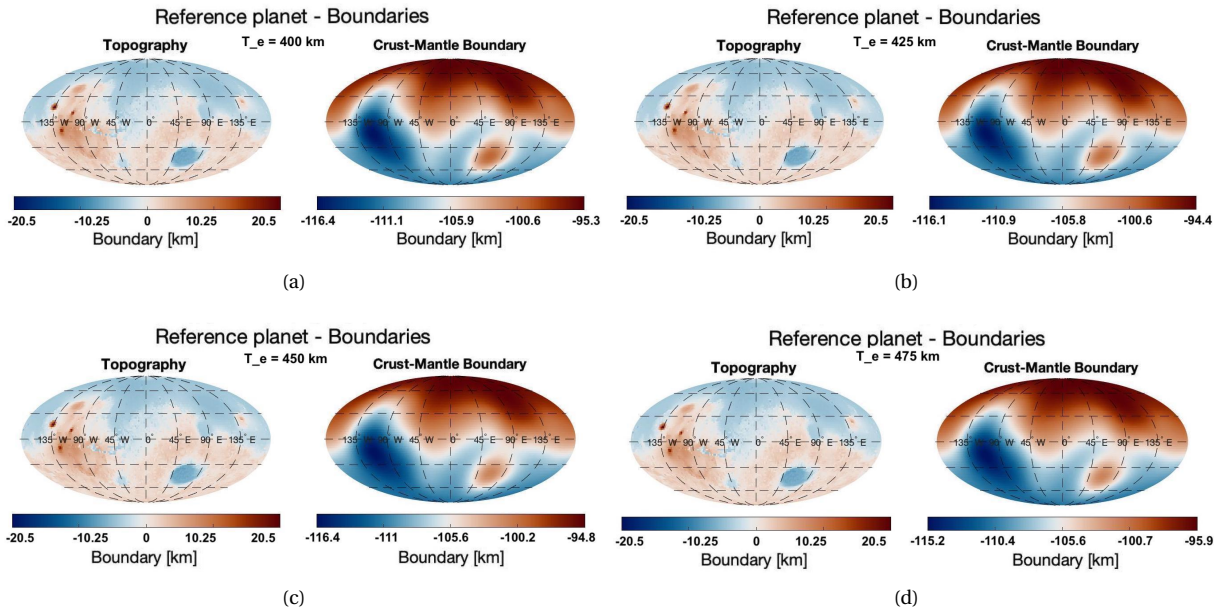

Figure A.26: The topography and crust-mantle boundary used for the reference model for the Martian inversion. This is obtained with $C = 105$ km, $E = 100$ GPa, $\nu = 0.25$, and varying elastic thickness for the subplots. Subplot (a), (b) and (d) use $rho_c = 2700$ kg/m^3, $\rho_m = 3800$ kg/m^3, and subplot (c) uses $rho_c = 2650$ kg/m^3, $\rho_m = 3650$.

A.6. Gravity Input Inversion

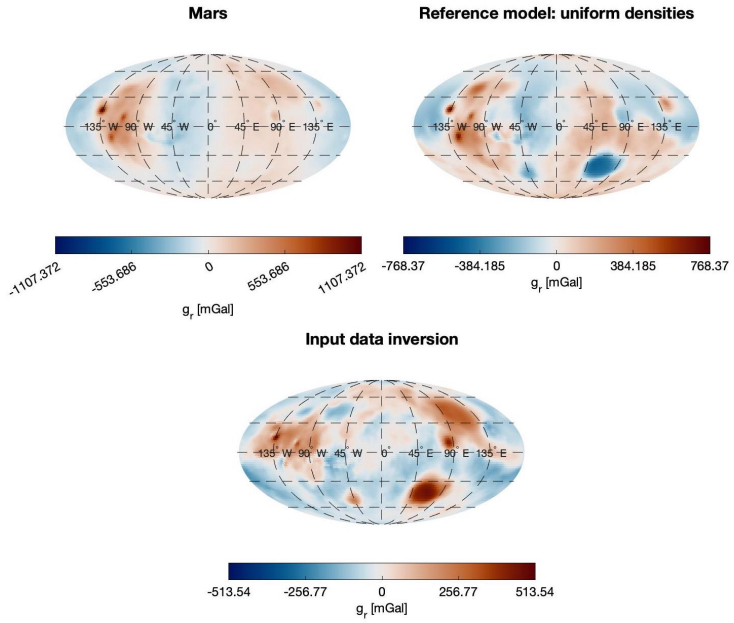

Figure A.27: The top left figure shows the anomaly for Mars, the top right for the reference model with uniform densities, and the bottom figure shows the residual, which is used as the input data for the inversion.

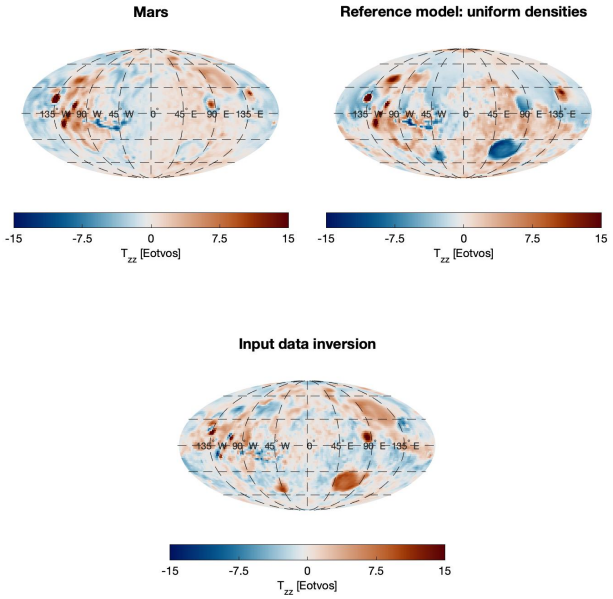

Figure A.28: The top left figure shows the gravitational tensor in the zz direction for Mars, the top right for the reference model with uniform densities, and the bottom figure shows the residual, which is used as the input data for the inversion. The two top plots are truncated for $T_z z = \pm 15$ Eotvos and the bottom figure is truncated for $T_z z = \pm 1.5$ Eotvos.

A.7. Heatmap Results

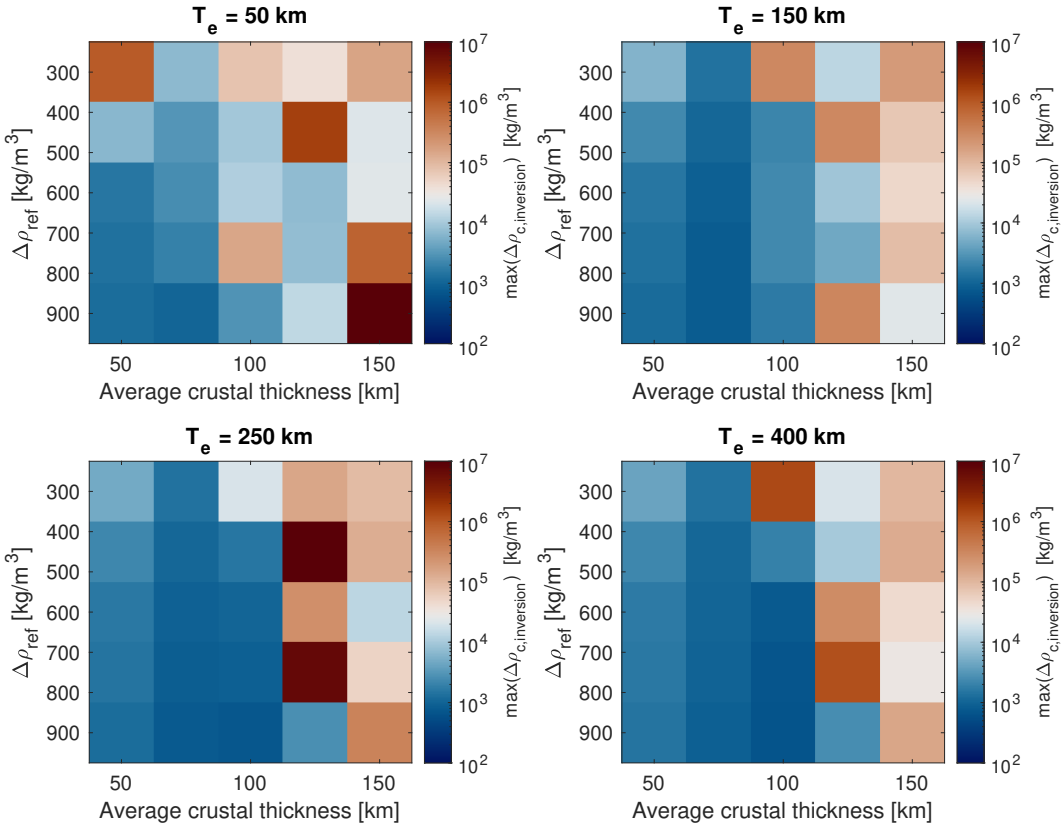

Figure A.29: The heatmaps for the first analyses of the different combinations of input parameters for the initial reference planets. The average crustal thickness is plotted against the density differences in the crustal density, for variations in elastic thickness between the four subplots. From top left, to bottom right, these figures show the results for elastic thicknesses of $T_e = 50$ km, $T_e = 150$ km, $T_e = 250$ km, and $T_e = 400$ km.

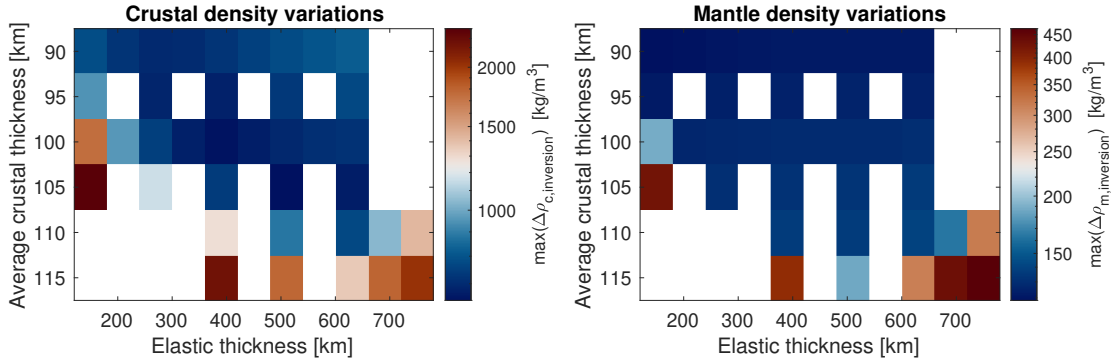

Figure A.30: The heatmaps showing the results for a set density difference between the crustal and mantle density of the reference model of 900 kg/m^3, and variations in the average crustal thickness and elastic thickness. The elastic thickness is plotted against the density differences in the crustal, left subplot, and mantle, right subplot, density.

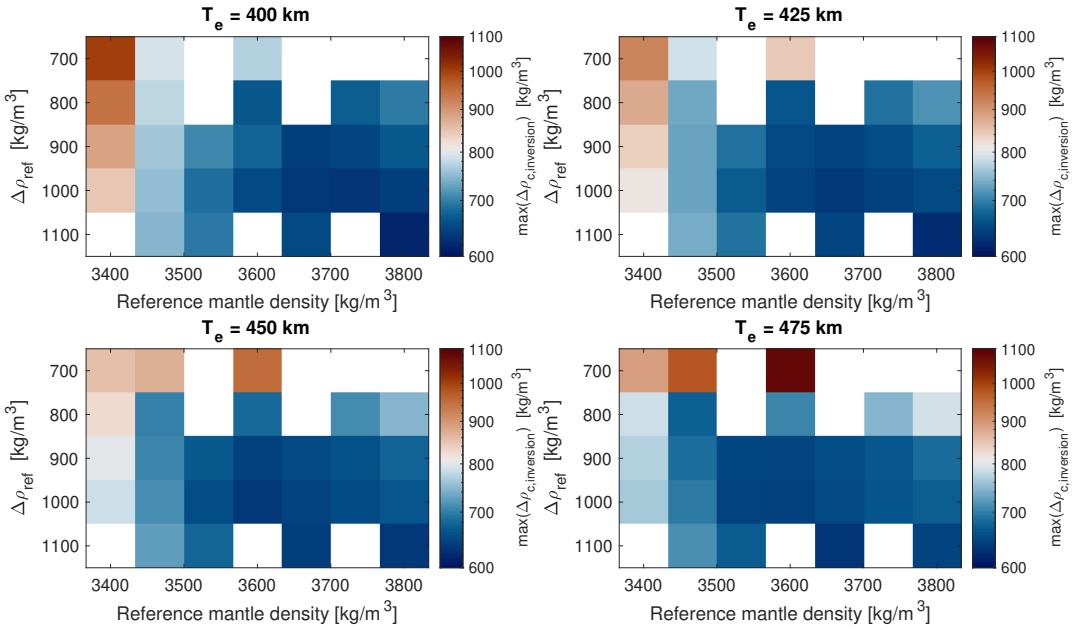

Figure A.31: The heatmaps showing the results for a set average crustal thickness for the reference model of 105 km and variations in the elastic thickness and density difference between the crust and mantle of the reference model. The mantle reference density is plotted against the density differences in the crustal for different density differences. From left to right, subplot 1 shows the results for an elastic thickness of 400 km, subplot 2 for 425 km, subplot 3 for 450 km, and subplot 4 for 475 km.

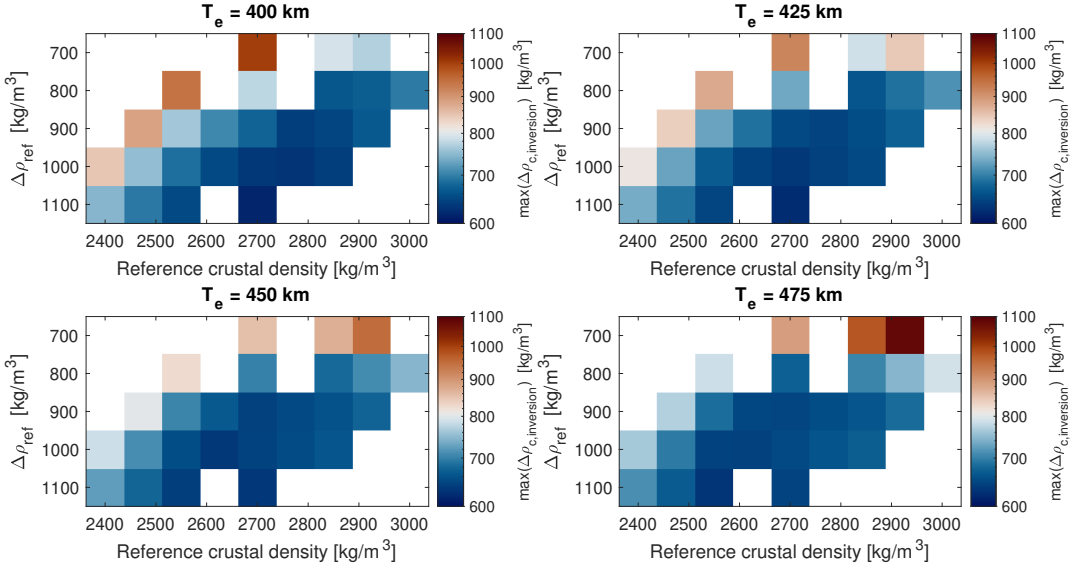

Figure A.32: The heatmaps showing the results for a set average crustal thickness for the reference model of 105 km and variations in the elastic thickness and density difference between the crust and mantle of the reference model. The crustal reference density is plotted against the density differences in the crustal for different density differences. From left to right, subplot 1 shows the results for an elastic thickness of 400 km, subplot 2 for 425 km, subplot 3 for 450 km, and subplot 4 for 475 km.

A.8. Geologic Map of Mars

The geological map of Mars from [Tanaka et al., 2014].

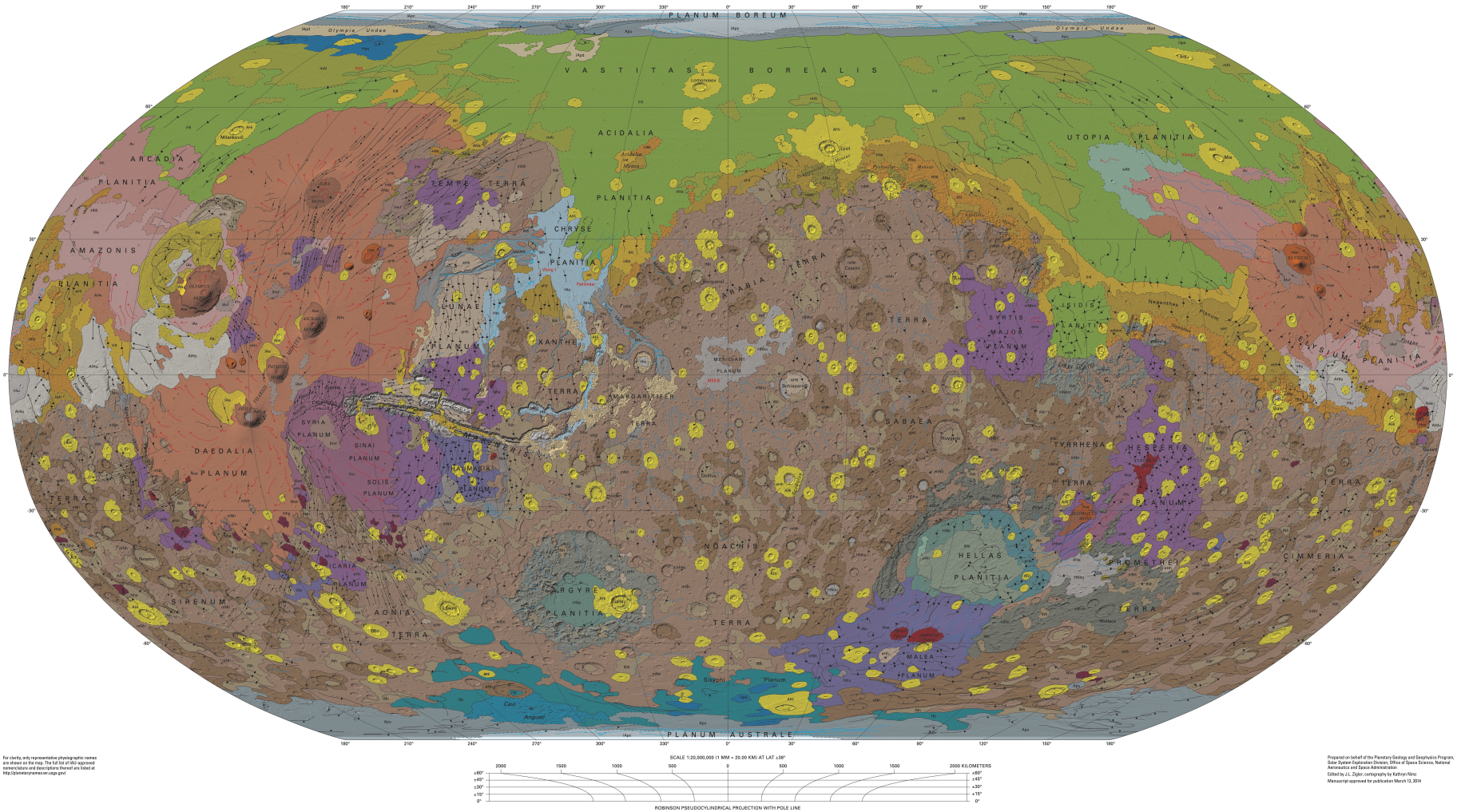

CORRELATION OF MAP UNITS

[Cumulative crater-densities for epoch boundaries at 1, 5, or 16 km diameters are from Werner and Tanaka (2011); see table 1 for model absolute-ages for the epoch boundaries. Map unit ages are resolved to nearest epoch; hachured box edges indicate possible, extended durations. The determinations rely on both stratigraphic relations as documented in the Description of Map Units and crater size-frequency distributions provided in tables 2, 3, and D1 and by other workers as referenced in the Geologic History section. See Age Determinations section of text for methodology discussion. Determination of ages from crater densities is complicated by the geologic history of the unit of interest, including size-dependent degradation and resurfacing, such that different crater diameter ranges (and the associated N(1), N(5), and N(16) values) may provide different age estimates for a given geologic unit; see tables 2 and D1 for examples of formation and resurfacing ages for some localities]

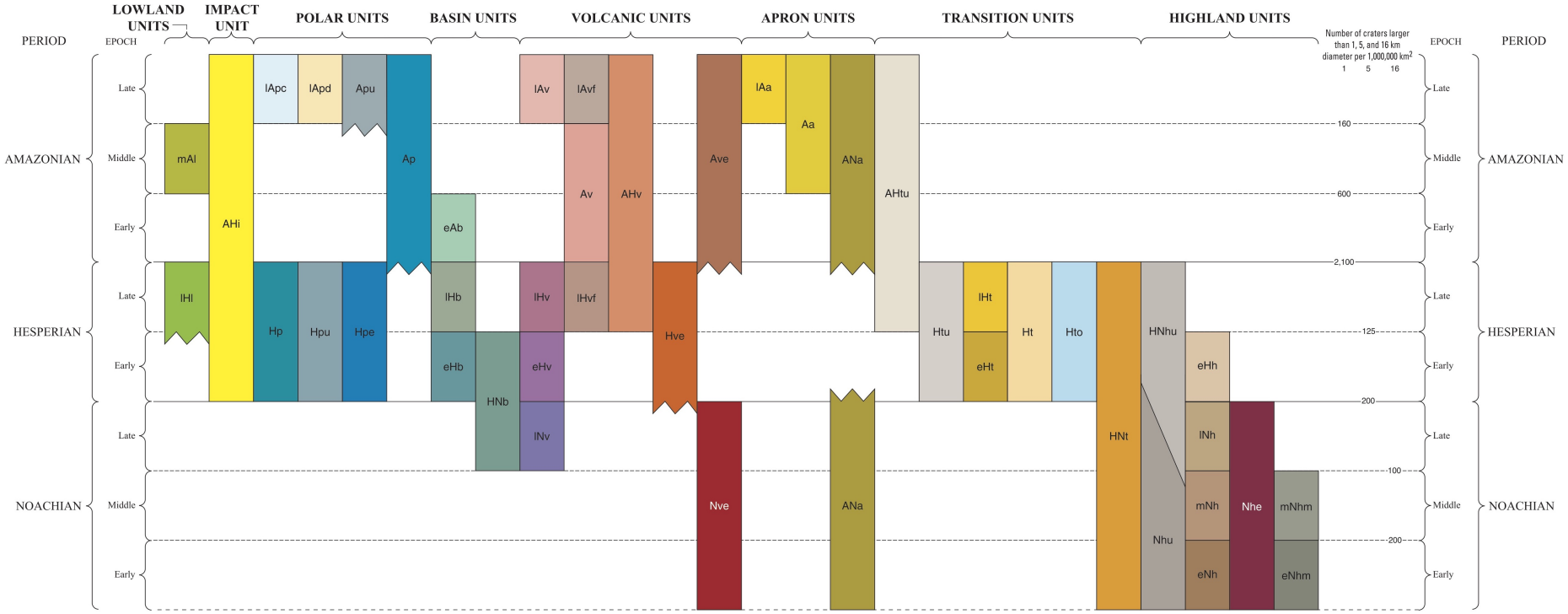

Figure A.33: "This global geologic map of Mars, which records the distribution of geologic units and landforms on the planet's surface through time, is based on unprecedented variety, quality, and quantity of remotely sensed data acquired since the Viking Orbiters. These data have provided morphologic, topographic, spectral, thermophysical, radar sounding, and other observations for integration, analysis, and interpretation in support of geologic mapping. In particular, the precise topographic mapping now available has enabled consistent morphologic portrayal of the surface for global mapping. Also, thermal infrared image bases used for this map tended to be less affected by atmospheric haze and thus are reliable for analysis of surface morphology and texture at even higher resolution than the topographic products." [Tanaka et al., 2014]

94

A. Appendix

Bibliography

Airy, G. B. Iii. on the computation of the effect of the attraction of mountain-masses, as disturbing the apparent astronomical latitude of stations in geodetic surveys. Philosophical Transactions, 145:101–105, 1855. doi: 10.1098/rstl.1855.0003.

Banerdt, W. B., Golombek, M. P., and Tanaka, K. L. Stress and tectonics on mars. Mars, pages 249–297, 1992.

Baratoux, D., Samuel, H., Michaut, C., Toplis, M. J., Monnereau, M., Wieczorek, M., Garcia, R., and Kurita, k. Petrological constraints on the density of the martian crust. Journal of Geophysical Research: Planets, 119: 1707–1727, 2014. doi: https://doi-org.tudelft.idm.oclc.org/10.1002/2014JE004642.

Belleguic, V., P., L., and Wieczorek, M. A. Constraints on the martian lithosphere from gravityand topography data. Journal of Geophysical Research: planets, 110(E11), 2005. doi: https://doi.org/10.1029/2005JE002437.

Beuthe, M., Le Maistre, S., Rosenblatt, P., Pätzold, M., and Dehant, V. Density and lithospheric thickness of the tharsis provincefrom mex mars and mro gravity data. Journal of Geophysical Research: Planets, 117, 2012. doi: 10.1029/2011JE003976.

Borg, L. E., Nyquist, L. E., Wiesmann, H., Shih, C.-Y., and Reese, Y. The age of dar al gani 476 and the differentiation history of the martian meteorites inferred from their radiogenic isotopic systematics. Geochimica et Cosmochimica Acta, 67:3519–3536, 2003. doi: https://doi.org/10.1016/S0016-7037(03)00094-2.

Breuer, D., Zhou, H., and Yuen, D. A. Implications for the planet's volcanic history stability. Journal of Geophysical Research, 101:7531–7542, 1996.

Carr, M. H. and Head III, J. W. Geologic history of mars. Earth and Planetary Science Letters, 294:185–203, 2010. doi: https://doi.org/10.1016/j.epsl.2009.06.042.

Chapman, M., Neukum, G., Dumke, A., Michael, G., van Gasselt, S., Kneissl, T., Zuschneid, W., Hauber, E., and Mangold, N. Amazonian geologic history of the echus chasma and kasei valles system on mars: New data and interpretations. Earth and Planetary Science Letters, 294:238–255, 2010. doi: https://doi.org/10.1016/j.epsl.2009.11.034.

Comer, R. P., Solomon, S. C., and Head, J. W. Mars' thickness of the lithosphere from the tectonic response to volcanic loads. Reviews of Geophysics, 23:61–92, 1985. doi: https://doi.org/10.1029/RG023i001p00061.

Coulson, I. M., Beech, M., and Nie, W. Physical properties of martian meteorites: Porosity and density measurements. Meteoritics Planetary Science, 42:2043–2054, 2007. doi: https://doi.org/10.1111/j.1945-5100.2007.tb01006.x.

Davies, M. E. Photogrammetric measurements of olympus mons on mars. Icarus, 12, 1974. doi: https://doi.org/10.1016/0019-1035(74)90037-2.

De Backer, L. Seismic analysis of mars using gravitational potential stresses - insight. MSc. Thesis. URL https://repository.tudelft.nl/islandora/object/uuid%3A9b62bef7-b3a0-4dd3-8a84-462bdd07b720, year={2018}.

Delacourt, C., Gros, N., Allemand, P., and Baratoux, D. Online mars digital elevation model derived from profiles. Eos, Transactions American Geophysical Union, 84:583, 2011. doi: https://doi.org/10.1029/2003EO520003.

Dreibus, G. and Wanke, H. Mars, a volatile-rich planet. Meteoritics, 20:367–381, 1985.

Gauss, C. F. Abhandlungen Zur Methode Der Kleinsten Quadrate. Berlin: Dr. A. Börsch Dr. P. Simon, 1887.

Genova, A., Goossens, S., Lemoine, F. G., Mazarico, E., Neumann, G. A., Smith, D. E., and Zuber, M. T. Seasonal and static gravity field of mars from mgs, mars odyssey and mro radio science. Icarus, 272:228–245, 2016. doi: https://doi.org/10.1016/j.icarus.2016.02.050.

Gneiting, T., Kleiber, W., and Schlather, M. Matern cross-covariance functions for multivariate random fields. Journal of the American Statistical Association, 105:1167–1177, 2010. doi: 10.1198/jasa.2010.tm09420.

Gneiting, T. Strictly and non-strictly positive definite functions on spheres. Bernoulli, 19:1300–1342, 2013. doi: 10.3150/12-BEJSP06.

Goossens, S., Sabaka, T. J., Genova, A., Mazarico, E., Nicholas, J. B., and Neumann, G. A. Evidence for a low bulk crustal density for marsfrom gravity and topography. Geophysical Research Letters, 44:7686–7694, 2017. doi: https://doi.org/10.1002/2017GL074172.

Gorski, K. M., Bills, B. G., and Konopliv, A. S. A high resolution mars surface gravity grid. Planetary and Space Science, 160:84–106, 2018. doi: https://doi.org/10.1016/j.pss.2018.03.015.

Grott, M. and Breuer, D. The evolution of the martian elastic lithosphere and implications for crustal and mantle rheology. Icarus, 193:503–515, 2008. doi: https://doi.org/10.1016/j.icarus.2007.08.015.

Guinness, J. and Fuentes, M. Isotropic covariance functions on spheres: Some properties and modeling considerations. Journal of Multivariate Analysis, 143:143–152, 2016. doi: https://doi.org/10.1016/j.jmva.2015.08.018.

Hansen, P. C. The l-curve and its use in the numerical treatment of inverse problems. 2005. URL https://www.sintef.no/globalassets/project/evitameeting/2005/lcurve.pdf.

Khan, A., Ceylan, S., van Driel, M., Giardini, D., Lognonné, P., Samuel, H., Schmerr, N. C., Stähler, S. C., Duran, A. C., Huang, Q., and et al. Upper mantle structure of mars from insight seismic data. Science, 373:434–438, 2021. doi: 10.1126/science.abf2966.

Kiefer, W. S., Bills, B. G., and Nerem, R. S. An inversion of gravity and topography for mantle and crustal structure on mars. Journal of Geophysical Research, 101:9239–9252, 1996. doi: https://doi.org/10.1029/95JE03699.

Knapmeyer-Endrun, B., Panning, M. P., Bissig, F., Joshi, R., Khan, A., Kim, D., Lekić, V., Tauzin, B., Tharimena, S., Plasman, M., and et al. Thickness and structure of the martian crust from insight seismic data. Science, 373: 438–443, 2021. doi: 10.1126/science.abf8966.

Konopliv, A. S., Park, R. S., and Folkner, W. M. An improved jpl mars gravity field and orientation from mars orbiter and lander tracking data. Icarus, 274:253–260, 2016. doi: 10.1016/j.icarus.2016.02.052.

Kraus, H. Thin Elastic Shells: An Introduction to the Theoretical Foundations and the Analysis of Their Static and Dynamic Behavior. 1967.

Kreslavsk, M. A. and Head III, J. W. Kilometer-scale roughness of mars- results from mola data analysis. Journal of Geophysical Research, 105(E11):26695–26711, 2000.

Leonard, G. J. and Tanaka, K. L. Geologic map of the hellas region of mars. Geological Survey, 2001.

Martinec, Z. Mass-density green's functions for the gravitational gradient tensor at different heights. Geophysical Journal International, 196:1455–1465, 2014. doi: doi:10.1093/gji/ggt495.

McGovern, P. J., Solomon, S. C., Smith, D. E., Zuber, M. T., Simons, M., Wieczorek, M. A., Phillips, R. J., Neumann, G. A., Aharonson, O., and Head, J. W. Correction to "localized gravity/topography admittance and correlation spectra on mars: Implications for regional and global evolution". Journal of Geophysical Research: planets, 109 (E7), 2004. doi: https://doi.org/10.1029/2004JE002286.

McKenzie, D., Barnett, D. N., and Yuan, D. N. The relationship between martian gravity and topography. Earth and Planetary Science Letters, 195:1–16, 2002. doi: https://doi.org/10.1016/S0012-821X(01)00555-6.

Mouginis-Mark, P. J., Wilson, L., and Head III, J. W. Explosive volcanism on hecates tholus, mars' investigation of eruption conditions. Journal of Geophysical Research: Planets, 87, 1982. doi: https://doi.org/10.1029/JB087iB12p09890.

Mussini, J. An anisotropic fexural isostasy method for investigating the martian lithosphere. MSc. Thesis, 2019. URL https://repository.tudelft.nl/islandora/object/uuid%3A5d77cc6e-a4c5-433e-b898-d5e8b9f4d58d.

Neumann, G. A., Zuber, M. T., Wieczorek, M. A., McGovern, P. J., Lemoine, F. G., and Smith, D. E. Crustal structure of mars from gravity and topography. Journal of Geophysical Research: planets, 109(E8), 2004. doi: https://doi.org/10.1029/2004JE002262.

Nimmo, F. Admittance estimates of mean crustal thickness and density at the martian hemispheric dichotomy. Journal of Geophysical Research: Planet, 107, 2002. doi: https://doi.org/10.1029/2000JE001488.

Nimmo, F. and Stevenson, D. Estimates of martian crustal thickness from viscous relaxation of topography. Journal of Geophysical Research Atmospheres, 106(E3):5085–5098, 2001. doi: 10.1029/2000JE001331.

Pauer, M. and Breuer, D. Constraints on the maximum crustal density from gravity–topography modeling: Applications to the southern highlands of mars. Earth and Planetary Science Letters, 276:253–261, 2008. doi: https://doi.org/10.1016/j.epsl.2008.09.014.

Phillips, R. J., Saunders, R. S., and Conel, J. E. Mars: Crustal structure inferred from bouguer gravity anomalie. Journal of Geophysical Research: Solid Earth, 78(23), 1973. doi: https://doi.org/10.1029/JB078i023p04815.

Qin, W. Mars surface stress modeling, investigation on the crustal structure of mars with finite element method. MSc. Thesis, 2021. URL https://repository.tudelft.nl/islandora/object/uuid%3A74eb3038-2de4-44b9-bac7-07d94becd48e.

Root, N. P. D. D. K. M. v. d. W. W., B.C. and Vermeersen, L. On a spectral method for forward gravity field modelling. Journal of Geodynamics, 97:22–30, 2016. doi: https://doi.org/10.1016/j.jog.2016.02.008.

Schrama, E. J. O. Lecture notes on planetary sciences and satellite orbit determination. Delft University of Technology, 2019.

Smith, D. E., Lerch, F. J., Nerem, R. S., Zuber, M. T., Patel, G. B., Fricke, S. K., and Lemoine, F. G. An improved gravity model for mars: Goddard mars model 1. Journal of Geophysical Research, 98(E11):20871, 1993. doi: 10.1029/93je01839.

Sohl, F. and Spohn, T. The interior structure of mars: Implications from snc meteorites. Journal of Geophysical Research: Planets, 102:1613–1635, 1997. doi: https://doi-org.tudelft.idm.oclc.org/10.1029/96JE03419.

Solomon, S. C. and Head, J. W. Heterogeneities in the thickness of the elastic lithosphere of mars: Constraints on heat flow and internal dynamics. Journal of Geophysical Research: Solid Earth, 95:61–92, 1990. doi: https://doi.org/10.1029/JB095iB07p11073.

Steinberger, B., Werner, S. C., and Torsvik, T. H. Deep versus shallow origin of gravity anomalies, topography and volcanismon earth, venus and mars. Icarus, 207:564–577, 2010. doi: https://doi.org/10.1016/j.icarus.2009.12.025.

Tanaka, K. L. and Kolb, E. J. Geologic history of the polar regions of mars based on mars global surveyor data: I. noachian and hesperian periods. Icarus, 154:3–21, 2001. doi: https://doi.org/10.1006/icar.2001.6675.

Tanaka, K. L., Skinner Jr., J. A., Dohm, J. M., Irwin III, R. P., Kolb, E. J., Fortezzo, C. M., Platz, T., Michael, G. G., and Hare, T. M. Geologic map of mars. 2014. URL https://pubs.usgs.gov/sim/3292/pdf/sim3292_map.pdf.

Taylor, N. C., J. H. Johnson, J. H., Herd, R. A., and Regan, C. E. What can olympus mons tell us about the martian lithosphere? Journal of Volcanology and Geothermal Research, 402:106981, 2020. doi: https://doi.org/10.1016/j.jvolgeores.2020.106981.

Thomson, B. J. and Head III, J. W. Utopia basin, mars: Characterization of topography and morphology and assessment of the origin and evolution of basin internal structure. Journal of Geophysical Research: Planets, 106:23209–23230, 2001. doi: https://doi-org.tudelft.idm.oclc.org/10.1029/2000JE001355.

Turcotte, D. L., Shcherbakov, R., Malamud, B. D., and Kucinskas, A. B. Is the martian crust also the martian elastic lithosphere? Journal of Geophysical Research: planets, 107(E11), 2002. doi: https://doi.org/10.1029/2001JE001594.

van der Tang, Y. The origin of tharsis: A deep mantle gravity study. MSc. Thesis, 2021. URL https://repository.tudelft.nl/islandora/object/uuid%3A9eb2c215-a23e-4d8a-9696-f0a09603bbe1.

Watts, A. B. Isostasy and Flexure of the Lithosphere. Cambridge University Press, 2001. ISBN 0-521-622727.

Watts, A. B. and Moore, J. D. P. Flexural isostasy: Constraints from gravity and topography power spectra. Journal of Geophysical Research: Solid Earth, 122:8417–8430, 2017. doi: 10.1002/2017JB014571.

Wieczorek, M. A. 10.05 - gravity and topography of the terrestrial planets. Treatise on Geophysics, 10:165–206, 2007. doi: https://doi.org/10.1016/B978-044452748-6.00156-5.

Wieczorek, M. A. and Zuber, M. T. Thickness of the martian crust: Improved constraints from geoid-to-topography ratios. Journal of Geophysical Research, 109, 2004. doi: 10.1029/2003JE002153.

Yuan, D. N., Sjogren, W. L., Konopliv, A. S., and Kucinskas, A. B. Gravity field of mars: A 75th degree and order model. Journal of Geophysical Research, 106(E10):23377–23401, 2001. doi: 10.1029/2003JE002153.

Zhong, S. Effects of lithosphere on the long-wavelength gravity anomalies and their implications for the formation of the tharsis rise on mars. Journal of Geophysical Research: Planets, 107, 2002. doi: https://doi-org.tudelft.idm.oclc.org/10.1029/2001JE001589.

Zuber, M. T. The crust and mantle of mars. Nature, 412:220–227, 2001. doi: https://doi.org/10.1038/35084163.

Zuber, M. T., Solomon, S. C., Phillips, R. J., Smith, D. E., Tyler, G. L., Aharonson, O., Balmino, G., Banerd, W. B., Head, J. W., Johnson, C. L., Lemoine, F. G., McGovern, P. J., Neumann, G. A., Rowlands, D. D., and Zhong, S. Internal structure and early thermal evolution of mars from mars global surveyor topography and gravity. Science, 283:1788–1793, 2000. doi: 10.1126/science.287.5459.1788.